Directed assembly of colloidal rods, spheres and their mixtures

Cover: Edited polarized light microscopy image of a binary smectic phase made using a full wave retardation plate. Colors are stretched to optimize contrast. For aesthetic reasons the image was edited with Gimp 2.8 using a mosaic filter.

PhD thesis, Utrecht University, the Netherlands, February 2017.
ISBN: 978-90-393-6696-7
A digital version of this thesis is available at http://www.colloid.nl

Directed assembly of colloidal rods, spheres and their mixtures

---

Gerichte organisatie van colloïdale staven, bollen en hun mengsels

(met een samenvatting in het Nederlands)

Proefschrift

ter verkrijging van de graad van doctor aan de Universiteit Utrecht op gezag van de rector magnificus, prof. dr. G. J. van der Zwaan, ingevolge het besluit van het college voor promoties in het openbaar te verdedigen op maandag 13 februari 2017 des middags te 2.30 uur

door

Henriëtte Elisabeth Bakker

geboren op 15 januari 1987 te Warnsveld

Promotor:	Prof. dr. A. van Blaaderen
Copromotor:	Dr. A. Imhof

This work is part of the *Stirring of light!* research programme of the Foundation for Fundamental Research on Matter (FOM), which is part of the Netherlands Organisation for Scientific Research (NWO).

Contents

1 Introduction 1
1.1 Soft Matter 1
1.2 Colloidal Model Systems 3
1.3 Colloids Influenced by External Fields 6
1.4 Colloidal Assembly: Applications 7
1.5 Quantum Confinement 9
1.6 Thesis Outline 9

2 Particle Synthesis, Characterization and General Techniques 11
2.1 Introduction 12
2.2 Particles 12
2.3 Dispersion Properties 18
2.4 Imaging Colloidal Dispersions 19
2.5 Acknowledgments 23

3 Phase Diagram of Binary Colloidal Rod-Sphere Mixtures from a 3D Real-space Analysis of Sedimentation-Diffusion Equilibria 25
3.1 Introduction 26
3.2 Methods 26
3.3 Simulations 30
3.4 Results & Discussion 30
3.5 Conclusion 37
3.6 Acknowledgments 38
Appendix 3 39

4 Dynamics of Sedimentation of Binary Colloidal Rod-Sphere Mixtures 51
4.1 Introduction 52
4.2 Sedimentation of Rods and Spheres 53
4.3 Methods 54
4.4 Results & Discussion 57
4.5 Conclusion 74
4.6 Acknowledgements 75
Appendix 4 76

5 Micro-electrophoresis of Silica Rods and Spheres using Confocal Microscopy 79
5.1 Introduction 80
5.2 Theoretical Framework 81
5.3 Methods 84
5.4 Results & Discussion 88
5.5 Conclusion 100
5.6 Acknowledgements 101
Appendix 5 102

6 Assembly of Thin Films of Silica Rods or Spheres 109
6.1 Introduction 110
6.2 Theoretical Framework 111
6.3 Methods 113
6.4 Results & Discussion 117
6.5 Conclusion 139
6.6 Acknowledgments 140
Appendix 6 141

7 Shape-Dependent MultiExciton Emission and Whispering Gallery Modes in Supraparticles of CdSe/MultiShell Quantum Dots 143
7.1 Introduction 144
7.2 Methods 145
7.3 Results & Discussion 146
7.4 Conclusion 156
7.5 Acknowledgements 156

References 157

Summary 175

Samenvatting voor een breed publiek 177

Dankwoord 185

List of Peer-Reviewed Publications 187

About the author 189

1

Introduction

1.1 Soft Matter

In daily life we are surrounded with *soft matter*; think of paint, shampoo, milk, mayonnaise, blood, soap, rubber and the liquid crystalline display in your smartphone. But also the cells inside your own body are composed of soft matter[*], proteins, DNA, RNA, membranes and polysaccharides. When we study a block of metal or water with an electron microscope, which has a resolution of a few nanometers ($1\,\mathrm{nm} = 10^{-9}\,\mathrm{m}$), such materials appear to be homogeneous. In the case of *soft matter* we will observe an inhomogeneous structure when studied with the same microscope. Soft matter systems are structured on *mesoscopic* length scales. Their characteristic length scales are between the atomic world and the macroscopic world, which are between the nanometers and micrometers range ($1\,\mathrm{nm} - 1\,\mu\mathrm{m} = 10^{-9}\,\mathrm{m} - 10^{-6}\,\mathrm{m}$).

The term soft matter (in french: matière molle) was first introduced by the french physicist Madeleine Veyssié as a joke around 1970, it has a double meaning in french [1]. Later, Pierre-Gilles de Gennes, who had worked together with Veyssié, introduced the term soft matter to wide public in his Nobel laureate lecture 1991 [2].

Soft matter materials have the following special features in common. These materials are structured on mesoscopic lengths scales, as such they often have a large interfacial surface area. Therefore, the chemical and physical properties of these *interfaces* often determine the properties of the material. The structures are generally *soft*. The energies associated with deformation of the bonds in these structures are on the order of thermal energy k_BT, with k_B Boltzmann's constant and T the absolute temperature. Therefore, these structures *respond* easily to external fields and are easily deformed by external fields. Due to the low amounts of energies associated with interactions in soft matter, random fluctuations and Brownian motion are important. Brownian motion is the erratic motion that soft matter materials encounter due to the random kicks of liquid or gas molecules surrounding the material. This motion was first observed by Robert Brown in 1827, when he studied the pollen of *Clarkia pulchella* dispersed in water with an optical microscope [3]. Soon, he discovered that also inanimate fine particles of clay and sand exhibit the same erratic motion. Hence, soft matter systems are constantly in motion due to *thermal*

---

[*] Human bodies itself are 'Soft Machines' as William S. Burroughs already pointed out in 1961.

fluctuations. Finally, soft matter often exists of *self-assembled* material. Because of the interplay between thermal fluctuations and interactions, which are both on the order of k_BT, material can self-assemble into organized structures and reach thermodynamic equilibrium. When the responsiveness and self-assembly are combined to overcome kinetic barriers in structuring, this is called *directed assembly.*

The soft matter systems we use in this thesis are colloids. Colloids are particles with a mesoscopic size which are dispersed in a continuous phase. Think of the fat droplets and proteins floating inside milk. Both the colloid and the continuous phase can be made of either a gas, a liquid or a solid. In this thesis we study the directed self-assembly of colloids external fields such as gravity, electric fields and shear flow.

The knowledge and use of colloidal dispersions dates already a long way back. The inks used by Egyptians $4000-300$ B.C. to write on papyrus were colloidal dispersions made of fine grains of carbon black or cinnabar in solution, which were stabilized by a biopolymer such as gum arabic. Also, in the seventeenth century alchemists produced colloidal dispersions from gold chloride solutions treated with reducing agents. The scientific history of colloids starts in the middle of the nineteenth century with Selmi [4] and Graham [5]. They are often named the founding fathers of colloid science, as they were the first to thoroughly investigate the stabilization, preparation and characterization of colloids. The term *colloid* (in Greek glue = $\kappa o \lambda \lambda \alpha$) was first coined by Thomas Graham in 1861 [5]. He studied diffusion through a parchment membrane and found a gluey substance that remained on the membrane, which he coined colloid. In 1902 Zsigmondy developed the ultramicroscope together with Siedentopf, while he investigated colloidal dispersion of Purple Cassius [6, 7]. The ultramicroscope uses Tindall scattering to observe and determine the size of colloids that were smaller than the wavelength of light, which could not been done with a normal optical microscope. Five years later Jean Baptiste Perrin [8] used the ultramicroscope to follow the movement of uniform gamboge particles. With his experiments he verified the molecular nature of Brownian motion and the existence of atoms. A theoretical explanation on Brownian motion was given two years before by Albert Einstein and Marian von Smoluckowski [9–11].

Not only did Perrin study Brownian motion, but he was also able to determine Avagadro's number by studying the sedimentation profile of a dilute suspension of the same particles [8]. Colloids that are heavier than the solvent they reside in will settle and form a sediment. In sedimentation-diffusion equilibrium, the rate of sedimentation is balanced by the diffusion, due to Brownian motion, in the upward direction. A density gradient is present along the axis of sedimentation. Perrin showed that in equilibrium at the top of the sediment the density gradient resembles the barometric height distribution of ideal gasses. He concluded that the ideal gas law, which was already extended by van 't Hoff to solutions, was still valid for dilute colloidal suspensions. These findings were important for the development of statistical mechanics.

1.2 Colloidal Model Systems

When colloidal particles are made monodisperse, they show the same thermodynamic phase behavior as atoms and molecules [12]. For example, spherical colloids that that have a hard-core particle potential, e.g. they act as billiard balls, can form a fluid and a crystal depending on the concentration [13, 14]. As colloids are much bigger than atoms and molecules, colloids can be easily investigated and manipulated. Therefore, monodisperse colloids can serve as model system for their much smaller counterparts. This is also what we used them for in Chapters 3 and 4.

Colloids are relatively large and slow, and therefore, colloids can easily be studied with an optical microscope. With the confocal laser scanning microscope it is possible to obtain quantitative data on the single particle level about the 3D structure and dynamics [15, 16]. In contrast to atomic and molecular systems, for which more advanced techniques such as atomic force microscopy (AFM) and electron tomography are needed.

Spheres The most famous colloidal model system consists of spherical particles with a hard-core particle potential, in short hard spheres. Theoretically, these spheres have an infinite potential energy at contact, but zero otherwise. Hence, the internal energy is constant at constant temperature and the phase transition is purely entropy driven, and no attractions between particles are needed. The equilibrium phase diagram consists of only a fluid and a crystal phase [13, 14] and is dictated by the density of the spheres. Early experiments in the 1960s with hard spheres used granular ball bearings [17], but these bearings have negligible thermal motion in contrast to colloids, which undergo Brownian motion. In the 1980s, sterically stabilized poly(methyl methacrylate) (PMMA) spheres were prepared that act as nearly hard spheres and showed equilibrium phase behavior [18] and crystal nucleation was studied [19]. Later in the 1990s, the whole equation of state was obtained of a suspension of nearly hard spheres, with one single measurement of the sedimentation-diffusion equilibrium profile [20–22]. Using confocal microscopy local processes can be studied on the single particle level, such as crystal nucleation [23] and melting [24]. Hard-core colloidal particles that can be used in confocal microscopy studies are silica spheres [25, 26] and PMMA spheres [27, 28].

Although many interesting models can be tested experimentally, colloidal hard spheres synthesized in laboratory differ from the idealized theoretical model [29]. In experimental systems, colloidal spheres do not all have the same size, but a distribution of sizes exist, the colloids are affected by gravity and there is always a degree of softness, e.g. the billiard balls are a bit squishy. For sterically stabilized colloids, this softness can arise from the compressibility of the polymer hairs grafted onto the colloid. For charge stabilized colloids, the charged surface causes a different interaction potential. However, with the addition of salt, electric charge can be screened such that the range of interaction is much smaller than the diameter of the particle. By using an effective diameter for these particles, their phase behavior can be mapped onto the hard sphere phase diagram [15, 29–31]. Next, colloids are affected by gravity. This effect can be diminished by matching the solvent mass density with the particle mass density. However, this is not possible for all systems and sometimes makes imaging these systems difficult. Hence, colloids will either cream or sediment over the course of time. At last, the relative width of the size distribution of the particles, or polydispersity, can influence phase behavior, as it affects the fluid-crystal coexistence density [32]. Also, for spherical particles with over 7% polydispersity no crystal phase exists [18]. Apart from using spherical colloids as model systems for simple atoms, a wealth of different shapes and interaction potentials can be synthesized in laboratory [33–36]. This allows for investigating colloids that mimic simple molecules. In addition, a wider variety of (complex) colloidal structures can be made than just the simple face centered cubic (fcc) or hexagonal close packed (hcp) structure formed by hard spheres.

Liquid Crystals By only changing the shape of a hard-core spherical particle to a rod shape, a wealth of different phases can already be formed [37]. Rods are anisotropic, therefore next to positional order, also orientational order determines the phase behavior. Due to the additional degrees of freedom, sufficienly long rod-like particles form liquid crystalline phases. Liquid crystalline phases, also called mesophases, exhibit order in between that of a liquid and the long-range positional order of a crystal. These intermediate phases have different mechanical responses and optical properties compared to simple fluids.

The scientific history of molecular liquid crystals starts in 1888, when the Austrian botanical physiologist Friedrich Reinitzer discovered that a compound named cholesteryl benzoate has two melting points, and thus behaved differently from other compounds he knew [38]. Together with Otto Lehmann, who in 1904 coined the name cholesteric liquid crystals, he discovered that between the two melting points the fluid was crystalline, but also that it had a different interaction with light [39]. Reinitzer and Lehmann were the first who became aware that phases exist that have symmetry properties in between those of a liquid and a crystal. Later, in 1922 Georges Friedel published his classification of mesomorphic states of matters as he called liquid crystals [40]. He classified three phases, namely the nematic, cholesteric and smectic-A phases. It took until 1977 before columnar phases were discovered by Sivaramakrishna Chandrasekhar [41].

Lars Onsager was the first in 1949 to predict with theory an entropy-driven phase transition, that occurred in a system of long hard rods [42]. When the density of rods is increased, the system undergoes a phase transition from a disordered isotropic phase to the nematic phase, for which the rods on average point in the same direction, the nematic director $\hat{\boldsymbol{n}}$. By aligning, the rods lose rotational entropy, but this is outweighed by a gain in translational entropy. Later, computer simulations have shown that a system of sufficiently long hard rods not only forms a nematic phase, but also a smectic phase [43].

Silica rods are a simple experimental model system for monodisperse colloidal hard rods that form liquid crystalline phases [44, 45]. Silica rods can form the nematic phase, the smectic phases and crystal phases, next to the isotropic liquid phase, see Fig. 1.1. In the nematic phase rods do not show positional order, but rods are all oriented in on average the same direction. When Georges Friedel observed nematic phases with the microscope, he observed defects that looked like threads (in Greek thread = $\nu\eta\mu\alpha$). In the smectic phase rods are, in addition to being aligned, arranged into layers. Friedel noticed that the mechanical properties of the Smectic-A phase were similar to that of soap (in Greek soap = $\sigma\mu\eta\gamma\mu\alpha$). In what way the rods are arranged inside the layers depends on the type of smectic. There exist many types of smectic phases from smectic-A until

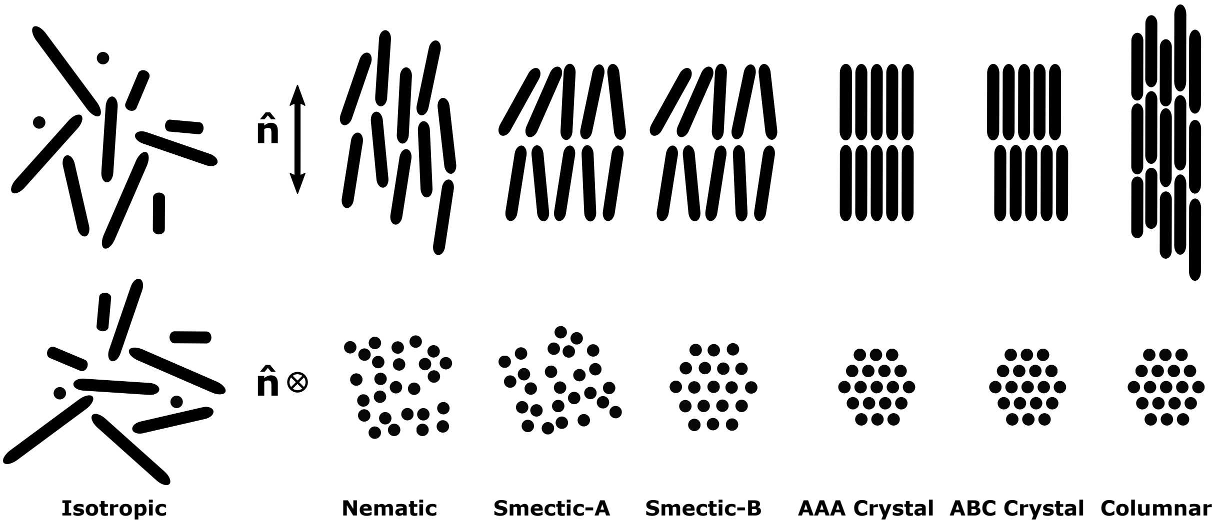

Figure 1.1 Schematic of liquid crystalline phases for hard spherocylinders discussed in this chapter. The phases are depicted parallel to the director $\hat{\boldsymbol{n}}$ (average alignment) and perpendicular to $\hat{\boldsymbol{n}}$.

smectic-K. For silica rods, with a hard-core potential, only the smectic-A phase is expected theoretically [37], but in experiments also the smectic-B phase was observed [46]. In the smectic-A phase, the rods are arranged in layers, but there is no order within the layer. In the smectic-B phase, the rods are hexagonally ordered within the layers. However, there is no correlation of particle position between the layers. When long-range correlation between the different layers exists a crystal is formed. The rods can either stack in an ABC crystal or in an AAA crystal, see Fig. 1.1. In the ABC crystal, rods in the next layer are positioned in alternate interstices of the former rod layer, like the way spheres stack in an fcc lattice. In the AAA crystal, rods are aligned tip to tip. Furthermore, if the rods are sufficiently polydisperse also a columnar phase exists [47]. In the columnar phase the rods are hexagonally ordered and aligned tip to tip, but the rods do not order in layers, such that the rods can slide along each other.

Silica rods are a different type of liquid crystal than the molecules studied by Reinitz and Lehmann. Silica rods are *lyotropic* and depending on their density form different phases. In contrast, the molecules studied by Reinitz and Lehmann formed different phases depending on the temperature, and therefore, are *thermotropic* [48]. Still, silica rods can serve as a model system to investigate structure and dynamics inside liquid crystals.

The first rod-like colloids were observed in the 1920s, when vanadium pentoxide particles were shown to form the nematic phase [49]. Later, in the 1930s the nematic phase was observed in a system of rod-like tobacco mosaic virus (TMV) [50]. It took until the 1950s before the smectic phase was observed in the same system [51]. At the moment, many rod-like colloids are available in a range of different materials. This includes bio-organic particles such as *fd*-virus [52], but also poly(methyl methacrylate) PMMA ellipsoids [53], polystyrene ellipsoids [54], goethite (α-FeOOH) [55], gibbsite ($Al(OH)_3$) [56, 57], nickel dimethylglioxime rods [58] and the silica rods used in this thesis [44]. Some of these systems can be used in confocal microscopy studies, such that it allows for quantitative 3D studies of the behavior of anisotropic particles, these include PMMA ellipsoids [59, 60], core-shell polystyrene-poly(N-isopropylacrylamide) ellipsoids [61], silica ellipsoids [62], silica dumbbells [63, 64] and the silica rods [44, 45] used in this thesis. The the phase behavior of these rods could be mapped on the theoretical phase diagram of hard spherocylinders, by the addition of effective shell around the particles [46]. Recently, the equation of state of hard silica rods was measured for the first time in experiment, using sedimentation-diffusion equilibrium and confocal microscopy [65].

1.3 Colloids Influenced by External Fields

Due to their relatively large size colloids are easily influenced by external fields, such as gravity, electric fields and shear-flow. Self-assembly of colloids into colloidal crystals can be guided by external fields, to overcome kinetic barriers that prevent the system to get in the state of lowest free energy. This process is usually called *directed assembly*.

The additional rotational degrees of freedom of anisotropic particles makes the formation of new structures possible, compared to spherical isotropic particles. However, these rotations can also frustrate the kinetics of self-assembly. Therefore, when preparing colloidal crystals of anisotropic particles without external fields, this often results in structures with multiple domains all having different orientations. Which makes them unsuitable as photonic crystals, as for this periodic structures over large scale are needed. The alignment of anisotropic particles with external field can help to overcome kinetic barriers to obtain colloidal crystals with long-range orientation and which are periodic on a large-scale. This can be done either by flow alignment of particles [66], magnetic fields [67–69], or by using ac electric fields [64, 70, 71].

If for instance the colloids are lighter or heavier than the solvent they reside in, they will either cream or sediment. Hence, *gravity* acts as an external field on the particles. Gravity can be used as a tool to probe all phases in a sediment. For thick enough sediments, the sedimentation profile of a single component system will contain all possible phases of the system, as a density gradient is present along the gravitational axis of the sediment. In Chapter 3 and 4 we make use of the gravitational field to probe the phase behavior and sedimentation dynamics of a binary mixture of rods and spheres. Because there is a gradient in the density of both components, this is more complicated. In Chapter 3 we identify and characterize a binary smectic (Sm_2) phase in this system. In the Sm_2-phase rods are arranged in smectic layers, and spheres fill up the space in between the rods [72].

Colloids are also easily affected by electric fields. When applying a uniform dc electric field to a suspension of charged stabilized colloids, the colloids start to move relative to the fluid. This motion is called electrophoresis and is used in biological laboratories to separate macromolecules, such as proteins or DNA and RNA fragments, based on their size. Electrophoresis can also be used to determine the surface charge of monodisperse colloidal particle. The surface charge on a particle is a measure for the stability of a colloidal particle and determines the strength of the repulsive interaction between particles. Moreover, the driven-motion of colloidal particles under influence of an electric field is also used in e-readers [73]. Here, one pixel contains oppositely charged white and black particles, with electrodes at the bottom and top of the pixel. When an electric field is applied, the particles migrate to the negative or positive electrode, such that the pixel appears black or white. In Chapter 5 we investigate the electrophoresis of silica rods as a function of double layer thickness using dc electric fields.

When a high frequency ac electric field is applied to a colloidal dispersion, the colloids will not move. And the change in the electric field direction is faster than the response of the ions present in de double layer around the particles. However, the colloids will acquire a dipole, provided that the colloidal particles have a dielectric constant mismatch with the solvent they reside in. At low field strengths, the induced dipole can be used to orient particles with the electric field, as long as the particle is anisotropic in shape or has an anisotropic polarizability, due to the material it is composed of. Due to the anisotropic polarizability of the particle the electric field will exert a torque on the particles, such that the dipole of the particles will align with the field. This results in alignment of anisotropic particles over large distances [64, 70, 71]. At sufficiently strong fields, dipole-dipole interactions between the particles occur. At low particle densities this results in the formation of strings of particles [70, 74–76]. At high densities of spherical particles, the body-centered tetragonal (bct) phase [33, 77] can be observed. For high densities of rod-like particles, new phases were observed [64, 70, 78]. In Chapter 3 we show that we can align the Sm_2-phase over large areas using high frequency ac electric fields.

Colloidal suspensions can be easily deformed by shear. Shear can either induce ordering in colloidal suspensions, but can also induce melting of colloidal crystals [79–82]. Shear alignment of colloid crystals is used in the preparation of colloidal crystals with spin coating [83–85], doctor blade coating [66, 86], melt compression [87, 88], or bending-induced oscillatory shear technique [89]. When rod-like particles are subjected to shear-flow they can align with the shear field. Next to that, dense systems of rod-like particles in shear flow are known to exhibit rich dynamics [90, 91]. Depending on the initial conditions and the applied shear, rod-like particles can show periodic motions like ‘tumbling’, ‘kayaking’, and ‘wagging’. During these motions, the average alignment of the particles varies periodically in time. Experimentally, some of these time periodic motions were found in a system of *fd*-virus [92, 93]. This behavior was later confirmed by Brownian Dynamics computer simulations [94, 95]. In Chapter 6 we use shear alignment to direct the assembly of thin films of ordered silica rods or spheres.

1.4 Colloidal Assembly: Applications

Monodisperse colloids are able to form colloidal crystals for which the exact periodic structure depends on the interaction potential, the volume fraction and the shape of the colloids. Periodic structures with features on the nano- to micrometer scale are mainly of interest due to their interaction with visible light, which has wavelengths on the same scale. When colloids in a colloidal crystal have a different refractive index from that of the surrounding medium, a 3D structure is formed for which the refractive index varies periodically in space, i.e. they form a photonic crystal. Structuring on the nano- and micro-scale can be done using the bottom-up approach of self-assembly of colloids, but it can also be done top-down using lithography methods. However, the top-down approaches are usually more expensive and are more limited in the production of large quantities [96].

Colloidal photonic crystals can also be found in nature, such as precious opal, which are formed by highly monodisperse colloidal spheres of amorphous silica (SiO_2) [97]. Opal has a *stopband* in the [111] direction of the fcc lattice [98]. Therefore, light in a certain frequency range (color range) cannot propagate in that direction, which is observed as enhanced reflectivity from that direction. In the case of a photonic crystal with a full 3D photonic bandgap, light of a certain frequency range cannot propagate in any direction, regardless of its polarization [99, 100]. This allows for the control of the emission and propagation of light, which in turn allows for applications such as optical integrated circuits. Colloidal hard spheres order into a fcc or hcp crystal, just as precious opal, and this structure does not have a full photonic bandgap. This is one of the reasons, why a photonic colloidal crystal with a full bandgap has not been made yet. The inverse structure actually has a full photonic bandgap, if the refractive index contrast $n_c = n_{max}/n_{min} \gtrsim 3$ [101]. Using the colloidal crystal as a template for a high refractive index material like silicon, germanium or some II-VI semiconductors [96], such an inverted structure (inverse opal) can be made by chemical vapor deposition or atomic layer deposition [102–104].

In order to create colloidal photonic crystals with a full bandgap, different colloidal structures are needed than the colloidal fcc structure. Calculations have shown that colloids assembled in the diamond lattice and the pyrochlore lattice can possess a full bandgap with a relatively low refractive index contrast $n_c \sim 2$ [105]. Also colloidal structures assembled from dimers can poses a full bandgap at $n_c \sim 2.3$ [106]. For this reason, photonic crystals with a full bandgap can in principle be made from titania or zinc sulfide colloids. In order to obtain such structures, the research in preparing colloids with different shape and interaction potential is of great interest.

Without a full photonic bandgap, colloidal crystals have optical applications in displays [107, 108], chemical and biological sensors [36, 109–112], antireflection coatings [113–115] and security data encryption [116, 117]. And, because an inverse opal is highly porous, colloidal crystal template methods are also of interest in non optical applications to obtain structures for catalysis [118], filtration [86] and fuel cells [119].

A variety of techniques are available to fabricate and direct the assembly of colloidal crystals, such as assembly by sedimentation [120, 121], convective self-assembly [122–125], Langmuir-Blodgett techniques [126], assembly using external electric or magnetic fields [68, 71, 127, 128], shear alignment [87, 88], spin coating [83–85] and doctor blade coating (DBC) [66, 86, 129].

Another optical application for colloids, is as a scattering object inside thin film solar cells in order to increase the optical path length and enhance efficiency [130]. As such, the particles are dispersed in the medium evenly and at a low concentration, the long-range order is not important such as in photonic crystals. Due to the anisotropic shape, silica rods have shown to provide superior light trapping compared to spherical particles [131, 132] in these thin film solar cells.

In order to use colloidal crystals for applications, the structure needs to be made permanent. Typically, this is done by evaporation of the solvent from the colloidal crystal. However, during drying cracks form due to capillary stresses that arise upon evaporation of the solvent [133]. This is unfavorable as defects in photonic crystals can suppress bandgaps. To prevent crack formation, Jiang and McFarland used a liquid acrylate monomer to disperse the particles in and upon polymerization of the medium the structure became permanent [83, 134]. Using this method free standing colloidal films can be obtained [85]. With this in mind, we used a liquid monomer as the dispersion medium in Chapter 6 to directed assembly of thin colloidal films composed of rods or spheres.

1.5 Quantum Confinement

One example where the mesoscopic length scale of a particle defines its properties are semiconductor nanoparticles, or colloidal quantum dots. Quantum dots are made from semiconductor material, which have a conductance behavior between that of a metal and an insulator. In a semiconductor the valence and the conductance band are separated by an energy gap E_g. It takes an energy E_g to excite an electron into the conductance band, which leaves a hole behind in the valence band. In the conductance band the electron is unbound and free to move. Thus, when a quantum dot absorbs light electron-hole pairs are created, so-called excitons. The energy E_g is released, often in the form of photons (light), when an excited electron recombines with the hole. Due to the nanometer size of the quantum dots, with a typical size below $\sim 10\,\mathrm{nm}$, the wave function of an excited electron gets physically confined in three dimensions. Hence, energy levels are quantized due to extra kinetic energy of particle wave confinement, resembling more the energy levels of atoms or molecules than those of bulk semiconductor [135]. As a result, E_g increases as the particle size gets smaller, therefore, more energy is needed to create an exciton, and hence, more energy is released when an exciton recombines [136]. Due to this quantum confinement, quantum dots show a size dependent photoluminescence. For smaller particles, the photoluminescence is shifted to shorter wavelengths. Quantum dots are of interest in a variety of applications, such as displays [137, 138], LEDs [139, 140], biolabeling [141, 142] and solar cells [143, 144].

In Chapter 7 we investigate the optical properties of micron sized supraparticles assembled from core-multishell quantum dots. Although the quantum dots are closely packed together, they do not behave as bulk semiconductor and the quantum confinement effect is still present. This was due to the additional shells of semiconductor grown around the particle, which have a larger energy gap E_g.

1.6 Thesis Outline

In this thesis we describe the directed assembly of silica rods, spheres and mixtures of silica rods and spheres. In Chapter 2, the particle synthesis, colloidal dispersions and the imaging techniques are described that are used in this thesis. Chapter 3 and 4 describe the sedimentation of a binary mixture of silica rods and spheres. In Chapter 3 the experimental phase diagram, of a binary mixture of silica rods and spheres that form a Sm_2-phase, is determined from sedimentation-diffusion equilibria using confocal microscopy. The real-space results are compared with results from Monte Carlo simulations of hard spheres and hard rods in bulk. In Chapter 4, the sedimentation dynamics of binary mixtures of silica rods and spheres are followed over time. We compare two systems: in the first system the diameter of silica spheres is smaller than the diameter of the rods; in the second system the diameter of the silica spheres is larger than the diameter of the rod.

In Chapter 5, the electrophoresis of silica rods is investigated on the single particle level. The experimental results are compared with theoretical predictions. Next, we show that using crosscorrelation as an image analysis technique, we can decrease the measurement time of micro-electrophoresis experiments using confocal microscopy. In Chapter 6, shear alignment is used to direct the assembly of thin films of ordered silica rods or spheres. In the first part of the chapter spin coating is used to obtain colloidal rod films where the silica rods are aligned with the flow direction. In the second part of the chapter doctor blade coating is used to obtain crystalline colloidal films made of silica spheres. The process of doctor blade coating is followed in real time with a confocal microscope, such that we can investigate shear alignment and the flow behavior of the dispersion during doctor blade coating. Finally, in Chapter 7 the optical properties of supraparticles consisting of core-multishell quantum dots are investigated.

2

Particle Synthesis, Characterization and General Techniques

In this chapter, we describe the properties of the colloidal dispersions used in this thesis. Colloidal silica rods and spheres were used, these particles were dispersed in different solvents such as: a mixture of glycerol and water; a mixture of dimethylsulfoxide and water; cyclohexyl chloride (CHC) or a liquid monomer (ethoxylated trimethylolpropane triacrylate, ETPTA). We describe the synthesis of the silica spheres and rods. We also show the relation between the Debye screening length and the conductivity of the solvent. Finally, we discuss the basic principles of imaging using confocal laser scanning microscopy, which was used to follow the directed self-assembly.

2.1 Introduction

This thesis presents the results on directed assembly of colloidal silica spheres, of colloidal silica rods and their mixtures. Polar solvents were used for the directed assembly of mixtures of colloidal rods and spheres under the influence of gravity. The polar solvents consisted of mixtures of glycerol and water or dimethylsulfoxide (DMSO) and water. The same polar solvents were used to measure the angle dependent motion of silica rods during electrophoresis. Additionally, cyclohexyl chloride (CHC) was used as an apolar solvent to measure the angle dependent motion. As uncoated silica rods are unstable in CHC, the rods were coated with octadecyltrimethoxysilane (OTMOS), in order to obtain steric stabilization. A liquid acrylate monomer (ethoxylated trimethylolpropane triacrylate, ETPTA) was used for directed assembly using the shear of doctor blade coating (DBC) and spin coating. The particles used in this thesis were fluorescently labeled and dispersed in (nearly) refractive index-matched solvents or solvent-mixtures to allow for laser scanning confocal microscopy. Thus, we were able to acquire images up to $\sim 120\,\mu\mathrm{m}$ into the sample and record 3D data-stacks. Image analysis was performed on the recorded confocal microscopy images in order to follow the directed assembly in-situ. Next, we directed the assembly of the colloids using external fields such as gravity, shear and electric fields. In this chapter we describe the synthesis of the colloids used, the main properties of the solvents and the imaging methods that were used in this thesis. We first describe the synthesis of the particles and the general properties of the particles. After that, we describe the properties of solvents. Finally, we discuss the basic principles of confocal laser scanning microscopy and image formation.

2.2 Particles

2.2.1 Spherical Particles

Fluorescently labeled silica spheres (SiO_2, density $\rho_{SiO_2} = 1.9\,\mathrm{g\,cm^{-3}}$; dielectric constant $\epsilon_r = 4.5$, refractive index $n_D^{21} = 1.45$) described in this thesis were prepared via a modified Stöber synthesis [25, 26]. The particles were covalently labeled with a fluorescent dye either with rhodamine isothiocyanate (RITC) or with fluorescein isothiocyanate (FITC), using a silane coupling agent with an amine as the functional group. A non-fluorescent silica shell was grown around the silica spheres using the seeded growth method of Giesche [145]. The diameter D and polydispersity δ of the spheres were determined by transmission electron microscopy (TEM) images made with a Philips Tecnai 10 or 12 microscope (FEI company). Typically 80 particles were measured by hand in the program iTEM (Soft Imaging System GmbH, Version 5.0). The polydispersity is defined as $\delta_D = s_D \,/\, D$, with s_D the standard deviation of D. A list of the silica spheres used in this thesis is given in Table 2.1. Fig. 2.1 depicts TEM images of the silica spheres used in this thesis.

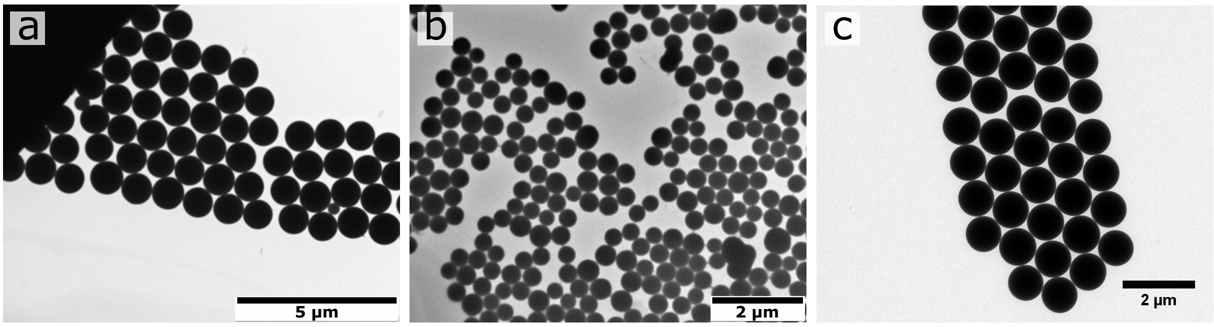

Figure 2.1 Silica spheres used in this thesis. **(a)** D930 silica spheres. **(b)** D385 silica spheres. **(c)** D970 silica spheres. See Table 2.1 for more information on the properties of silica spheres.

Table 2.1 Properties of silica spheres used in this thesis.
Here D is the diameter of the particles and δ_D the polydispersity. Both were determined from transmission electron microscopy (TEM).

	D µm	δ_D %	dye
D930	0.93	4	RITC
D385	0.39	9	RITC
D970	0.97	3	FITC

2.2.2 Rod-like Particles

In this thesis FITC fluorescently labeled silica rods were prepared according to a slightly altered method of Kuijk *et al.* [44, 45]. Rods were synthesized in a core-shell-shell fashion. First a non-fluorescent core was synthesized and around the core a fluorescently labeled silica shell was grown. In order to distinguish separate rods with the confocal microscope, the fluorescent parts of a pair of neighboring rods need to be separated by at least 200 nm in the lateral direction and 500 nm in the axial direction (the resolution of the confocal microscope). Therefore, an additional thick non-fluorescent silica shell was grown around the rods. However, this non-fluorescent shell did not need to be 250 nm thick, to obtain 500 nm separation. Also the repulsive interaction between charged silica rods accounts for additional spacing. This accounts for a separation around 120 nm in a solvent mixture of 85 wt% glycerol-water with 0.55 mM LiCl added, see Appendix 3.A. In our experience, a non-fluorescent shell thickness of 150 nm suffices to distinguish separate silica rods in dense sediments.

Growth of additional non-fluorescent shells around a silica rod gives rise to some hurdles. First, the growth of additional layers of silica makes the rods heavy. Hence, the gravitational length decreases and the Brownian dynamics gets slower. Second, the end-to-end length to diameter ratio L/D (or aspect ratio) of the rod decreases, which lowers the chances of finding liquid crystalline phases [37]. Figs. 2.2a-b show that rods with $L/D = 6.1$ were synthesized from non-fluorescent cores with $L/D = 14.5$. Fig. 2.2c depicts the decrease in aspect ratio with shell growth for rods with initial diameter of 255 nm. The solid lines depict the decrease in aspect ratio for initial aspect ratio's $L/D = 10.5$,

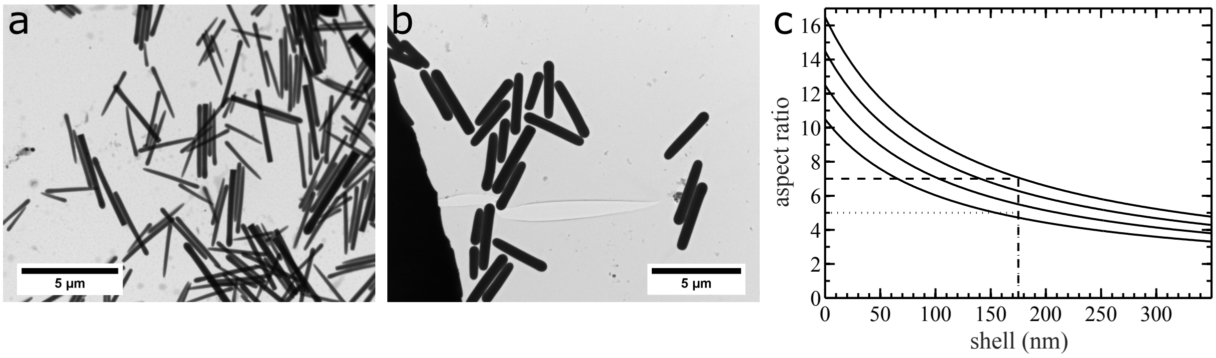

Figure 2.2 The effect of shell growth on the aspect ratio of a silica rod. **(a)** TEM images of cores of R2 rods with $L/D = 14.5$. **(b)** R2 rods, but now coated with a 184 nm shell, had $L/D = 6.1$. **(c)** The change of aspect ratio as function of shell growth for a rod with initial diameter $D = 255$ nm. The solid lines from top to bottom are initial L/D of 16.5, 14.5, 12.5 and 10.5 respectively.

12.5, 14.5, 16.5. The shell accounts for the fluorescent shell growth (*ca* 25 nm) and the non-fluorescent shell. Therefore, the minimum shell thickness needed is 175 nm. In order to obtain a stable smectic phase a final end-to-end aspect ratio $L/D > 5$ is needed. The dotted line shows that in order to obtain rods with $L/D = 5$, an initial $L/D = 11.2$ is needed. In order to obtain a stable nematic phase an even larger aspect ratio is needed. The dashed line shows that to obtain rods with $L/D = 7$, an initial $L/D = 16.3$ is needed. Due to the synthesis procedure of the silica rods [44, 45], the initial cores have a bullet shape, the rods are flat at one tip, and rounded at the other tip, see Fig. 2.2a and Fig. 2.4h. The rods used in experiments resemble more a spherocylinder, as the growth of additional silica shells made the rods more rounded, see Fig. 2.2b and Fig. 2.4i.

The standard recipe for silica rods yields non-fluorescent rods with $L/D \sim 7.5$ [44]. Therefore, we changed the recipe to obtain rods with larger aspect ratios. We reduced the concentration of both ammonia and water by $\sim 11\%$, performed the synthesis with a larger volume and waited for 72 h before ending the reaction. By sonication, 80.0 gram of poly(vinyl-pyrrolidone) (PVP, average molecular weight $\mathrm{M}_w = 40\,000\,\mathrm{g\,mol^{-1}}$, Sigma-Aldrich) was dissolved in 800.0 mL of 1-pentanol (99%, Sigma-Aldrich). After all PVP had been dissolved, 80.0 mL of absolute ethanol (Baker), 20.0 mL of ultrapure water (Milipore), 8.0 mL of 0.18 M sodium citrate dihydrate solution (99%, Sigma-Aldrich) were added and the flask was shaken by hand. Then 16.0 mL of aqueous ammonia solution (25 wt%, Merck) was added and the flask was shaken again. Next, 8.0 mL of tetraethylorthosilicate (TEOS, 98%, Sigma-Aldrich) was added. The mixture was shaken again and then allowed to react undisturbed for 72 h. The mixture was centrifuged at 900 g for 30 minutes (Hettich rotina 46s or Eppendorf 5810 centrifuge) to separate the silica rods. Afterwards, the silica rods were washed with ethanol twice, ultrapure water twice and ethanol twice, respectively. For each washing step, the rods were centrifuged at 500 g for 15 minutes.

To grow a fluorescent shell around the rods (*ca.* 25 nm), half of the prepared silica rods were dispersed into 400.0 mL ethanol containing 25.0 mL of ultrapure water and 30.0 mL of aqueous ammonia solution (25 wt%), under gentle magnetic stirring in a round-bottom flask. Subsequently, 0.750 mL of TEOS and 5.0 mL of a dye mixture were added. The reaction was stirred for 6 hours. The dye mixture was prepared the day before. For this mixture 25.0 mg (0.064 mmol) fluorescein isothiocyanate (FITC, isomer I, 90%, Sigma-Aldrich) was dissolved in 5.0 mL absolute ethanol by sonication. Subsequently, 37.0 µL (0.16 mmol) of 3-aminopropyltriethoxysilane (APS, 99%, Sigma-Aldrich) was added. The dye mixture was left to react overnight, before adding it to the reaction mixture. After the fluorescent shell growth, the silica rods were washed twice with ethanol, as described above. Additional non-fluorescent shells were grown using a similar procedure, but without the addition of the dye mixture. The procedure was repeated several (5 to 6) times such that a thick enough non-fluorescent shell was obtained. The final colloidal silica rods had a multi-layered structure: a non-fluorescent silica core, a fluorescently labeled silica shell (*ca.* 25 nm) and a non-fluorescent silica shell (*ca.* 145 nm).

The above described shell growth procedure is sensitive to aggregation. The TEOS is added in one step, which leads to a spike in the conductivity that can cause aggregation of particles [146]. Therefore, in the case of R10, R10-2 and R12 rods the synthesis procedure for the growth of silica shells was slightly altered. To reduce the chance of aggregation during synthesis, we added the TEOS over the course of two hours. Every half an hour 0.19 mL of TEOS was added to the mixture, reducing the increase in ionic strength caused by dissociating silanol groups. After all TEOS had been added, the mixture was left to react for another four hours, before the rods were washed twice with ethanol.

Polydispersity of the rods is unavoidable due the synthesis procedure. Although, with subsequent centrifugation steps, the polydispersity of the rods can be reduced. A benefit of the growth of an additional silica shell is that also the polydispersity of the rod δ_i decreases. Rod cores of R1 had initial polydispersities of $\delta_L \simeq 22\%$ and $\delta_D \simeq 14\%$, after the growth of an 153 nm thick shell, the polydispersity was reduced to $\delta_L \simeq 9\%$ and $\delta_D \simeq 9\%$. The same goes for rod cores of R2, which had initial polydispersities of $\delta_L \simeq 18\%$ and $\delta_D \simeq 18\%$, after the growth of an 183 nm thick shell, the polydispersity was reduced to $\delta_L \simeq 18\%$ and $\delta_D \simeq 10\%$. Please note, that the polydispersity in particle volume is larger, for R2 rods this is 30%. Hence, this can lead to size fractionation in samples. Moreover, a correlation exists between the length and diameter within a batch of synthesized rods [147]. Fig. 2.3 shows the measured length and corresponding diameter of 100 rods from particle system R2, which shows a correlation between the rod length and the particle diameter.

SR29 rods which were stable in cyclohexylchloride (CHC, > 98%, Merck), were coated with octadecyltrimethoxylsilane (OTMOS, 90%, Sigma-Aldrich) [148], see Chapter 5 for details.

The properties of the silica rods used for directed assembly experiments in this thesis can be found in Table 2.2 . The dimensions of the rods and the amount of shell growth were determined from TEM images, as described in Section 2.2.1. The thickness of the non-fluorescent (NF) shell is given in the last column. Fig. 2.4 depicts TEM images of the silica rods used in this thesis.

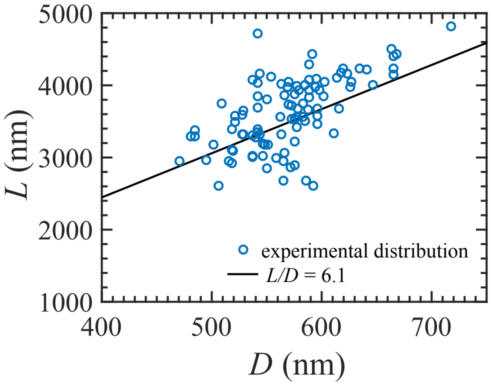

Figure 2.3 Correlation between length and diameter within R2 rods. The length of 100 R2 rods is plotted together with the corresponding diameter of the particle.

Table 2.2 Properties of silica rods used in this thesis.
Here L is the end-to-end length of the rods, D is the diameter of the particles, δ_i the polydispersity and L/D the aspect ratio, determined from transmission electron microscopy (TEM). The last column lists the thickness of the outer non-fluorescent shell.

	L µm	δ_L %	D µm	δ_D %	L/D	NF shell nm
R1	2.86	9	0.51	9	5.6	133
R2	3.59	18	0.59	10	6.1	145
SR29	2.29	6	0.60	8	3.8	100
R10	2.56	9	0.38	12	6.8	45
R10-2	2.40	11	0.36	15	6.6	40
R12	2.72	11	0.40	12	6.9	52
I02	1.42	14	0.24	21	6.1	5

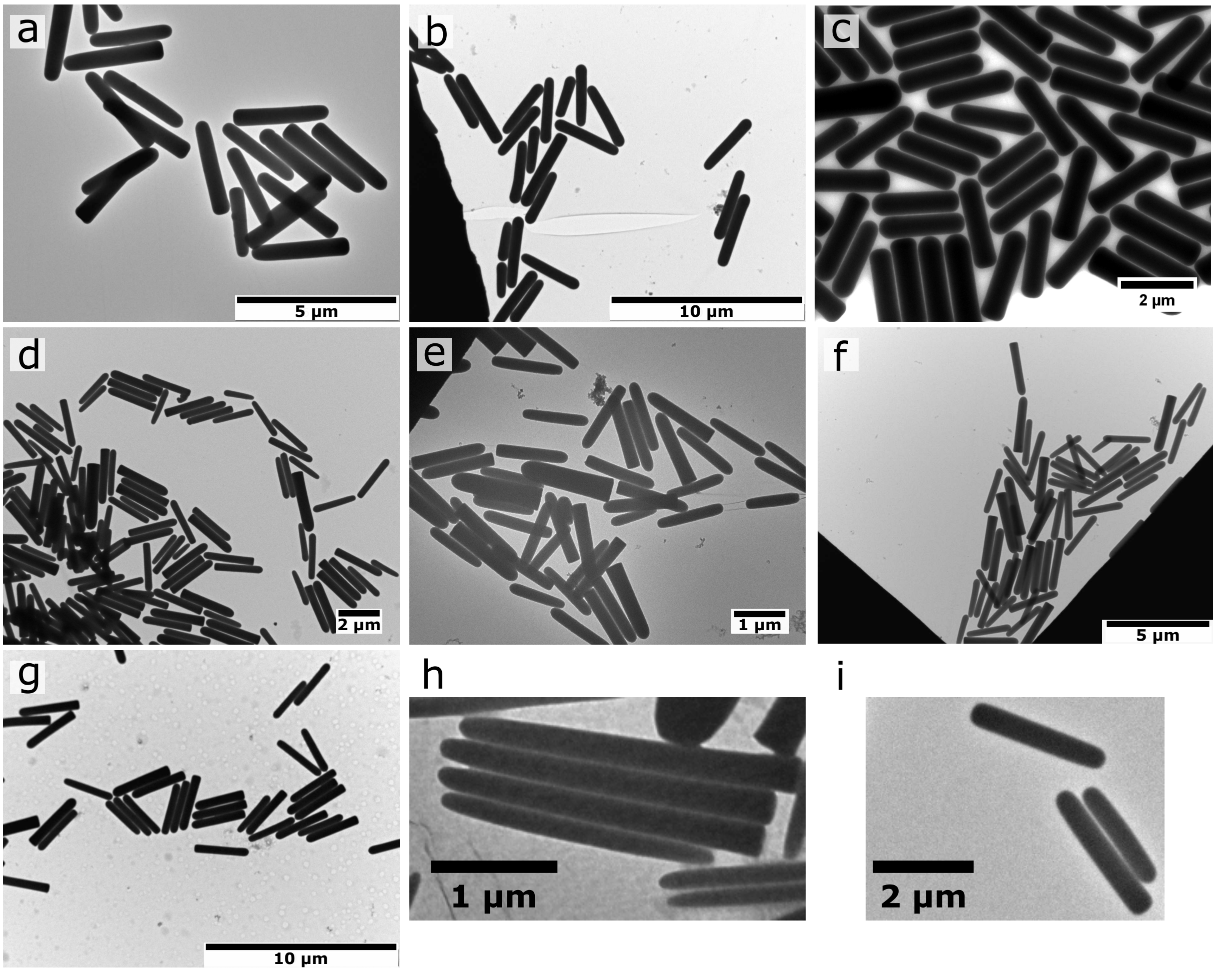

Figure 2.4 TEM images of silica rods used in this thesis. **(a)** R1 silica rods **(b)** R2 silica rods. **(c)** SR29 silica rods. **(d)** R10 silica rods. **(e)** R10-2 silica rods. **(f)** R12 silica rods. **(g)** I02 silica rods. **(h)** Particle cores of R1 rods ($L/D = 11.8$). **(i)** Zoom-in image of R1 rods after the growth of a 153 nm thick shell ($L/D = 5.6$). See Table 2.2 for more information on the properties of the silica rods used in this thesis.

2.3 Dispersion Properties

2.3.1 Solvent Properties

Silica rods and spheres were dispersed in (nearly) refractive index-matching solvents and solvent mixtures. General properties of the solvents used in this thesis are listed in Table 2.3. Refractive indices were measured with a refractometer (Atago 3T). The composition of the glycerol-water and DMSO-water mixtures were made to match the refractive index of the silica rods. This reduces the scattering in the sample, such that we can image relatively deep into the sample. In addition, it minimizes the attractive van der Waals interactions between the particles. The glycerol-water mixture ($\eta = 81\,\mathrm{mPa\,s}$) has a high viscosity, which slows down the dynamics of the particles. The downside of a high viscosity is that it takes longer to reach sedimentation-diffusion. The upside is that imaging of rods in the dilute phase is easier as images distortions, like bended rods, are prevented by the slow rotational diffusion. Therefore, the mixture is suitable to measure the sedimentation profile of mixtures of rods and spheres (see Chapter 3 and 4).

Table 2.3 Properties of solvents used in this thesis.
With ρ the density of the solution, n_D the refractive index of the solution, η the viscosity of the solution and ϵ_m the dielectric constant of the medium. Values marked with * are obtained from linear interpolation of literature values.

	ρ g mL^{-1}	n_D	η (mPa s)	ϵ_m
CHC	0.993 (25 °C) [149]	1.46265 (20 °C) [150]	1.5675 (25 °C) [149]	7.6 (25 °C) [151]
DMSO	1.096 (25 °C) [152]	1.477 (25 °C) [152]	1.99 (25 °C) [152]	48.4 (25 °C) [153]
Glycerol	1.258 (25 °C) [154]	1.474 (20 °C) [154]	1410 (20 °C) [154]	41.1 (20 °C) [155]
78 wt% DMSO/water	1.096* (25 °C) [152]	1.45 (22 °C)	3.542* (25 °C) [152]	56.1* (25 °C) [153]
85 wt% glycerol/water	1.219 (25 °C) [154]	1.45 (20 °C)	81 (25 °C) [156]	49.6* (20 °C) [155]
ETPTA	1.11 (25 °C) [85]	1.47 (20 °C) [85]	70 (25 °C) [85]	3 [157]

2.3.2 Electric Conductivity and the Debye Screening Length

To control the Debye screening length κ^{-1} in our samples we dissolved lithium chloride salt (LiCl, Merck) in the polar solvents used. Tetrabutylammonium chloride (TBAC, $\geq$ 97% Sigma-Aldrich) was dissolved in CHC to control κ^{-1}. For more details, see Chapter 3 and 5. In this thesis estimates for the Debye screening length, κ^{-1} were obtained from the measured conductivities of the used solvents. The conductivities of the polar solvents were measured with a CDM 230 conductivity meter (Radiometer Analytical). The conductivities of apolar solvents were measured using a Scientifica 627 conductivity meter. We assumed that ions contributing to the conductivity were monovalent and that ions migrated independently. The conductivity is then related to the concentration of dissociated salt, given by

$$\sigma = c\Lambda_0, \tag{2.1}$$

with σ the measured conductivity ($\mathrm{S\,m^{-1}}$), Λ_0 the limiting molar conductance of the salt at infinite solution ($\mathrm{S\,m^2\,mol^{-1}}$) in the given solvent and c is the concentration of dissociated salt.

Using Walden's rule, one can approximate Λ_0 for different solvents, using literature values of known species. Walden's rule states that the product of the limiting conductance and the viscosity is a constant for the same species in different solvents

$$\Lambda_0^A \eta^A = \Lambda_0^B \eta^B, \tag{2.2}$$

where the superscript denotes the particular solvent and η is the viscosity ($\mathrm{Pa\,s}$) of the solvent. In order to calculate Λ_0 for CHC, we used known literature values for the particular salt. Using the relation between the ionic strength and conductivity we can calculate κ^{-1} using the following relation, valid for monovalent ions:

$$\kappa^{-1} = \sqrt{\frac{\epsilon_m \epsilon_0 k_B T}{2 N_A c e^2}}, \tag{2.3}$$

with N_A Avogadro constant, c the concentration of dissociated monovalent salt in the solvent in $\mathrm{mol\,m^{-3}}$, ϵ_r the dielectric constant of the solvent, ϵ_0 the permittivity of vacuum, e is the elementary charge, k_B Boltzmann's constant and T the absolute temperature.

2.4 Imaging Colloidal Dispersions

Colloids and Confocal Microscopy Confocal laser scanning microscopy has been widely used in colloidal science to study the structure and dynamics [158]. Colloids are often used as model systems for atomic and molecular system to study crystallization [23, 31, 159], the glass transition [16] and shear induced melting and crystallization [80, 81]. Quantitative information can be obtained by using confocal microscopy to study colloidal dispersions in 3D and on the single particle level. This quantitative 3D ability was for the first time demonstrated in 1995 [16]. To resolve single particles with the confocal microscope, colloids need to be fluorescently labeled and their fluorescent parts need to be separated by at least the resolution of the microscope. Moreover, by refractive index-matching dense systems can be studied and images can be obtained deeper in the sample, such that wall effects do not play a role.

In this thesis, we used three different confocal microscopes to study colloidal dispersions, namely a Nikon C1, a Leica TCS SP2 and a Leica TCS SP8.

Confocal Laser Scanning Microscopy Marvin Minsky developed the confocal microscope in the 1950s in order to improve imaging on the nerve cells he was studying at the time [160, 161]. Confocal microscopy makes use of two principles: first, it excludes out of focus light by placing a pinhole aperture in the conjugated focal plane; second; the excitation light is limited to a point source by using a high numerical aperture lens in combination with a pinhole aperture placed in front of a bright light source. This is in contrast to normal fluorescence microscopy, where the entire field of view is illuminated, which can cause scattered light from elsewhere in the sample to be in the point of focus, causing noise in the image and significantly reducing contrast.

The first confocal microscope made by Marvin Minsky moved the sample to obtain a image and used a carbon-arc lamp for illumination, as lasers did not exist at the time. In 1969 the first confocal *laser* microscope was built [162]. In the 1980s faster imaging was obtained by scanning the laser beam over the sample instead of carefully moving the sample. This development was achieved simultaneously in several laboratories and led to the first commercially available confocal microscopes [163–166].

A schematic overview of a confocal laser scanning microscope is depicted in Fig. 2.5a. A 2D image is obtained by scanning the laser point-by-point, with a diffraction limited spot, over a 2D focal plane in the sample, with the use of rotating mirrors placed in the beam path. The same lens is used to pass the fluorescent light to the detector, in front of which a pinhole aperture is placed to reject out of focus light. This pinhole aperture is positioned in the plane optically *con*jugate to the focused spot, hence the name confocal [167]. This pinhole produces an optical sectioning effect, as out-of-focus light is rejected.

A 3D reconstruction of the sample can be made by moving the focus in the vertical direction, and making 2D images at different depths. This was done in Chapter 3 and 4. Here, we also used tracking algorithms [77, 168, 169] to determine the particle positions in the sedimentation profiles of mixtures of colloidal silica rods and spheres. Note, that the determination of the particle position is often more precise than the resolution of the microscope.

The use of a diffraction limited spot and pinhole aperture increases the resolution of a confocal microscope compared to conventional light microscopy. The resolution is limited by the point spread function (PSF) of the excitation spot size and the PSF of the detection spot. The excitation spot size imaged with a confocal microscope can be regarded as an ideal point source that is spread over three dimensions, which is known as the excitation PSF. In the lateral direction the PSF is given by the Airy function [170]

$$I_{xy}(v) = \left(\frac{2J_1(v)}{v}\right)^2, \tag{2.4}$$

with J_1 the Bessel function of the first kind of the first order, $v = 2\pi r NA/\lambda$ with r the distance from the center point, NA the numerical aperture of the objective and λ the wavelength of the excitation light. The area within the first minimum is called the Airy disk, with is radius given by: $r_{Airy} = 0.61\lambda/NA$. The Rayleigh criterion states that the intensity maxima of two point sources should be at least separated by the radius of their Airy disk.

In the axial direction, the excitation PSF is given by [170]

$$I_z(u) = \left(\frac{\sin\frac{u}{4}}{\frac{u}{4}}\right)^2, \tag{2.5}$$

with $u = 2\pi NA^2 z/(\lambda n)$, z the distance in the axial direction and n the refractive index of the sample. The distance to the first minimum is given is $z = 2\lambda n/NA^2$. A plot of I_{xy} and I_z is depicted in Fig. 2.5b.

The resolution for a conventional light microscope, not using a detection pinhole, can be found by filling in the experimental numbers: $\lambda = 488\,\mathrm{nm}$; $NA = 1.35$ and $n_D = 1.45$

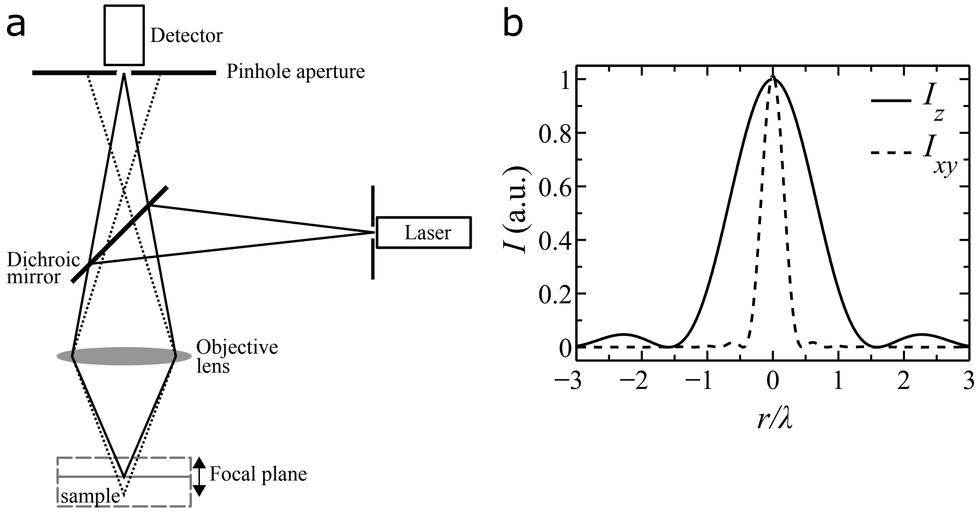

Figure 2.5 **(a)** Schematic overview of a confocal laser scanning microscope. Laser light gets directed via a dichroic mirror through the microscope objective and excites at one spot the fluorescent sample. The fluorescent emission passes back through the same objective and the dichroic mirror and hits the detector through a pinhole placed in the conjugate focal plane. **(b)** Intensity distribution of an idealized point source in the lateral direction I_{xy} (dashed line) and in the axial direction I_z (solid line). Intensity is plotted as function of distance from the center r/λ, for $n_D = 1.45$ and $NA = 1.35$.

for a refractive index-matched silica dispersion. A lateral resolution of 220 nm is found and an axial resolution of 777 nm. The resolution in the z-direction is more than three times less.

The PSF of the confocal microscope is a convolution of the PSF of the excitation spot size and the detection PSF [171]

$$PSF_{conf}(x,y,z) = PSF_{ext}\,(x,y,z) * PSF_{det}\,(x,y,z)\,. \tag{2.6}$$

Therefore, the resolution of a confocal microscope is in theory a factor $\sim \sqrt{2}$ better compared to light microscopy [167, 170]. But, in practice the improvement is less and a lateral confocal resolution of $\sim$ 200 nm is obtained [170]. In the axial direction still a resolution of $\sim$ 500 nm can be obtained.

An image f of an object obtained with a confocal microscope can be regarded as a convolution of the object function $f_0(x,y,z)$ and the $PSF_{conf}(x,y,z)$, together with noise ε

$$f(x,y,z) = f_0(x,y,z) * PSF_{conf}(x,y,z) + \varepsilon. \tag{2.7}$$

Deconvolution In order to improve the confocal-image quality, we deconvolved the confocal images in some cases with a theoretical point spread function (Chapter 3 and 4). In image processing deconvolution is used as a process that reverses the convolution process of the object with the PSF. However, as seen in equation 2.7, also noise is present in the recorded images. Therefore, the deconvolution process with just the theoretical PSF does not return the true object. Nevertheless, the deconvolution process results in clearer and sharper images.

Deconvolution on confocal images can be carried out if the images are recorded using at least the ideal Nyquist sampling density, such that the information of the microscope's PSF in the image is still available [172, 173]. For a confocal microscope using a 488 nm laser and a glycerol-objective ($n_D = 1.45$) with $NA = 1.35$, the ideal Nyquist sample distance is around 45 nm in the lateral (xy) direction and 138 nm in the axial (z) direction, or about 1/4 of the resolution of the microscope.

The deconvolved images presented in this thesis (Chapter 3 and 4) were carried out using commercially available Huygens SVI software (Version 14.10) using the classic likelihood estimation restoration method and a theoretical PSF that was dependent on the depth in the sample [174]. After deconvolution, particle fitting algorithms were used to find the particle positions and orientations in the confocal data [77, 168, 169].

Super-resolution Imaging Techniques In the last years new super-resolution techniques have been developed to beat the diffraction limit, examples are photo-activated localization microscopy (PALM) [175], stochastic optical reconstruction microscopy (STORM) [176] and stimulated emission depletion (STED) [177–179]. These techniques are not used in this thesis and therefore, are only briefly discussed here.

PALM and STORM are widefield techniques and use a two step approach to identify and localize individual molecules. The emission of two near-by emitters is separated in time, and many detection events are needed to obtain one image. Therefore these imaging techniques are too slow to capture fast Brownian dynamics in colloidal dispersions.

STED imaging is as fast as normal confocal microscopy. STED works by depleting the excited state using stimulated emission in the diffraction limited spot. This is done by the overlay of a second strong laser in the diffraction limited spot that has a wavelength matching the emission of the fluorophore. The spot of a second laser is designed in the shape of a donut in the lateral direction, such that it leaves a bright spot in the diffraction limited spot and depletes the emission of fluorophores in periphery of the diffraction limited spot. By also using an overlay along the axial direction, the emission can be depleted in 3D. Using 3D STED a lateral resolution of $20-80$ nm and an axial resolution of 100 nm can be obtained [180].

Due to the higher resolution in 3D STED, a less thick non-fluorescent shell is needed around the fluorescent rod-core to distinguish separate rods with STED. Therefore, single particle studies of rods, with relatively large L/D, that form a stable nematic phase become accessible.

Two-photon Microscopy In Chapter 7 we made use of two-photon microscopy (2PM). 2PM was for the first time demonstrated in 1990 [181]. The theory of two-photon excitation (2PE) was described by Maria Göppert-Mayer in 1931 [182]. After the development of the laser, this effect was demonstrated in practice by Kaiser and Garret in 1961 [183].

2PE is a nonlinear process, in where two photons are absorbed almost simultaneously, to induce a molecular transition to an excited state. The energy difference between the lower and excited state is equal to the sum of the energies of the two photons. From a quantum mechanics point of view, a first photon excites a molecule to a virtual intermediate state, and a second photon excites the molecule to the excited state. Two photon excitation depends on the square of the light intensity, hence, it is a nonlinear optical process. A high intensity light source is required for 2PE and usually a femtosecond laser is used.

As the fluorescence is dependent on the square of the intensity, the lateral excitation PSF for 2PE is given by [184]

$$I_{xy}^{2p}(v) = \left(\frac{2J_1(v/2)}{v/2}\right)^4, \tag{2.8}$$

assuming that λ is the emission wavelength and 2λ the excitation wavelength. In the direction along the optical axis the two photon PSF is given by [184]

$$I_z^{2p}(u) = \left(\frac{\sin\frac{u/2}{4}}{\frac{u/2}{4}}\right)^4. \tag{2.9}$$

Due to the square dependency of 2PE on the light intensity, 2PE only excites light inside the focused spot and a pinhole aperture in front of the detector is not needed to create an optical sectioning effect. Note, that the excitation is light is 2λ, which results in a larger diffraction limited spot compared to conventional confocal microscopy and therefore a lower resolution. Although, the resolution can be increased by combining 2PM with STED [185] or by using a pinhole [184].

Apart from the disadvantage of lower resolution, 2PM has four major benefits compared to conventional microscopy. First, longer wavelengths are used in 2PM compared to conventional microscopy. Therefore, photodamage is reduced inside samples. Second, longer wavelengths scatter less. Hence, images can be acquired deeper inside samples. Third, contamination of the fluorescent signal by excitation light is eliminated. Finally, 2PM can initiate photochemical reactions within the focused spot inside the sample. For example, two-photon polymerization is already been used as a 3D printer on the submicron scale for data storage or to create photonic structures [186–188]. In addition, the high peak powers can be used to modify the shape of individual nanoparticles [189]

2.5 Acknowledgments

Thijs Besseling is thanked for providing the SR29 rods. Judith Wijnhoven is thanked for the synthesis of the D970 spheres and Gülşen Heessels-Gürboğa is thanked for the synthesis of the D385 and D930 spheres. I also would like to thank Fabian Hagemans for taking some of the TEM images (Figs. 2.1c and 2.4c).

3

Phase Diagram of Binary Colloidal Rod-Sphere Mixtures from a 3D Real-space Analysis of Sedimentation-Diffusion Equilibria

Self-assembly of binary particle systems offers many new opportunities for materials science [190–193]. Moreover, shape-anisotropic particles may self-assemble into liquid crystalline phases which display various degrees of positional and orientational order [194], enabling e.g., displays. Nevertheless, shape-anisotropic particles in binary liquid-crystalline phases have hardly been investigated [72, 195]. Here, we present a quantitative 3D real-space analysis of a binary smectic liquid-crystalline phase (Sm_2) formed by colloidal silica rods and spheres. This Sm_2-phase combines long-range order of both short-range repulsive rods and spheres with the ability to align with external electric fields relevant for applications. Using a real-space analysis of sedimentation equilibria, we determine not only pressure, density and order parameter profiles, but also the experimental phase diagram exhibiting a stable Sm_2-phase. Using computer simulations we confirm that the Sm_2-phase can be stabilized by entropy alone, which opens up the possibility of combining new materials properties at a wide array of length scales.

3.1 Introduction

Three-dimensional structuring of matter on multiple length scales is key to the design of materials with new properties such as a photonic band gap [196] or a negative refractive index [197]. Self-assembly holds great promise of arriving at such materials in an affordable and sustainable way [190, 196, 197]. Self-assembly of multiple components such as in colloidal binary crystals increases the complexity of the structures and hence, the ability to tune the properties. Binary mixtures of colloidal rods and spheres have hardly been investigated experimentally [72, 195, 198], despite the existence of a significantly larger number of theoretical and simulation studies [199–212].

Here, we study through experiments and simulations a binary mixture of rod-like and spherical colloids as shown in Figs. 3.2a-b. We consider mixtures of fluorescent silica rods and silica spheres, which enables us to determine the positions and orientations of individual particles in 3D. Real-space imaging has been done before on a similar system, but not a quantitative 3D analysis [72, 195]. Using real-space analysis, we determine for the first time in experiment thermodynamic quantities such as pressure, local and global order parameters, and the experimental phase diagram of the binary silica rod-sphere mixture. We find the spontaneous formation of a binary smectic liquid-crystalline (Sm_2) phase in which smectic layers of rods alternate with layers of spheres (see Figs. 3.2c and 3.3). The first experimental Sm_2-phase was observed by Adams *et al.* in a mixture of *fd*-viruses (of end-to-end length to diameter ratio $L/D \sim 100$) and polymer spheres [72]. The stabilization mechanism was explained in terms of excluded-volume interactions, despite the fact that under particular conditions the chirality and flexibility of the *fd*-viruses play an important role in determining the phase behaviour [213]. We believe that the present system is simpler. We consider the rods as rigid and achiral, and also the interactions are short-range repulsive.

3.2 Methods

Particles Fluorescein isothiocyanate (FITC) fluorescently labeled silica rods were prepared according to the method of Kuijk *et al.* [44, 45], see Chapter 2 for more details. Rhodamine isothiocyanate (RITC) fluorescently labeled silica spheres were prepared via a modified Stöber synthesis [25, 26]. The mean dimension of the particles were determined from transmission electron microscopy (TEM) images made with a Philips Tecnai 10 or 12 microscope (Fei Company). Typically, 80 particles were measured by hand using the program iTem (Soft Imaging System GmbH, version 5). Both the end-to-end length (L) and the diameter (D) of the rods were measured, after which the aspect ratio (L/D) and the polydispersity (δ) were calculated. For self-assembly using an electric field, colloidal silica rods with the following dimensions were used: R1 rods; $L = 2860\,\mathrm{nm}$ and $D = 510\,\mathrm{nm}$ ($L/D = 5.6$ $\delta_L = 9\%$, $\delta_D = 9\%$). For single particle tracking the following colloidal silica rods were used; R2 rods with $L = 3591\,\mathrm{nm}$ and $D = 587\,\mathrm{nm}$ ($L/D = 6.1$ $\delta_L = 18\%$, $\delta_D = 10\%$). For all experiments, colloidal silica spheres with $\sigma = 385\,\mathrm{nm}$ ($\delta = 9\%$) were used. See Table 3.1 for details on particle properties.

Table 3.1 Properties of particles used in this chapter.
Here L is the end-to-end length of the rods, D is the diameter of the particles, δ is the polydispersity of the particles and l_g is the gravitational length of the particle based upon a 85 wt% glycerol-water mixture and the particle dimensions measured by TEM. The aspect ratio for simulations is defined as $L_{cyl}/D = (L/D)_{eff} - 1$.

	Particle dimensions from TEM						Effective particle dimensions		
	L nm	δ_L %	D nm	δ_D %	L/D	l_g µm	L_{eff} nm	D_{eff} nm	$(L/D)_{eff}$
Rods									
R2	3591	18	587	10	6.1	0.64	3711	707	5.25
R1	2860	9	510	9	5.6	1.06	2980	630	4.75
Spheres									
D385			385	9		17.65		465	

Dispersions For self-assembly using an ac electric field, silica spheres and R1 silica rods were dispersed in a refractive index-matched solvent mixture, $n_D^{21} = 1.46$, of 78 wt% dimethylsulfoxide (DMSO, $\geq$ 99.9%, Sigma-Aldrich) and 22 wt% ultrapure water.

For samples that were in sedimentation-diffusion equilibrium (SDE) of which single particle fitting was needed, particles were dispersed in an index-matched solvent mixture, $n_D^{21} = 1.45$, of 85 wt% glycerol ($\geq$ 99.0%, Sigma-Aldrich) and 15 wt% ultrapure water. This mixture has a relatively high viscosity (81 mPa s, 25 °C) [156]. This high viscosity causes the dynamics in the samples to slow down, this is especially important for imaging in the dilute top region, where the dynamics are fastest. In order to control the thickness of the double layer around the particles, lithium chloride salt (LiCl, Merck) was added to a concentration of 0.55 mM to the glycerol-water mixture. Taking a dielectric constant of $\epsilon_r = 49.6\epsilon_0$ for the solvent mixture, based on a linear interpolation of literature values [155], the typical Debye screening length (κ^{-1}) in this solution is estimated to be 10 nm.

The Debye screening length can be calculated from

$$\kappa^{-1} = \sqrt{\frac{\epsilon_m \epsilon_0 k_B T}{2 N_A c e^2}}, \tag{3.1}$$

with N_A Avogadro constant, c the concentration of dissociated monovalent salt in the solvent in mol m^{-3}, ϵ_r the dielectric constant of the solvent, ϵ_0 the permittivity of vacuum, e the elementary charge, k_B Boltzmann's constant and T the absolute temperature.

Confocal Microscopy Samples were studied with a confocal laser scanning microscope (Leica TCS SP8, equipped with a 12 kHz resonant scanner). All images were taken in fluorescence mode. The excitation wavelength was 488 nm for the FITC-labeled rods and 543 nm for the RITC-labeled spheres. To optimize image quality, a 100×, 1.35 NA glycerol confocal-objective (Leica) was used for single particle tracking, in combination with a quartz coverslip ($n_D = 1.46$, 0.15–0.18 mm, Laser Optex). For other purposes, oil objectives were used: either a 100× 1.3 NA oil confocal-objective (Leica) or a 63×, 1.4 NA oil confocal-objective (Leica). A typical image volume had the following dimensions in xyz : $\sim 25\,\mu\text{m} \times 12.5\,\mu\text{m} \times 120\,\mu\text{m}$. We imaged with a voxel size of $\sim 50\,\text{nm} \times 50\,\text{nm} \times 100\,\text{nm}$. Data shown here are averaged for at least 4 different confocal xyz-stacks, which were recorded consecutively or at different places in the sample.

Sample Cells For self-assembly using an ac electric field the sample cell was prepared using two 50 µm diameter nickel alloy wires (Goodfellow) running on opposite sides through a 0.1 mm × 1 mm rectangular glass capillary (Vitrocom, UK) and glued to a standard microscopy slide (Menzel Gläzer). The distance between the wires was around 0.7 mm. The cell was filled with particles dispersed in an index-matched solvent mixture of 78 wt% DMSO-water and sealed with UV-glue (Norland, No. 68). The samples were left to sediment with the long axis perpendicular to gravity. See Fig. 3.1a for a schematic.

For SDE samples of which single particle fitting was needed, the following sample cell was made. First, the back-end of a glass Pasteur pipette (WU Mainz) was cut off using a diamond pen. Afterwards, the resulting glass cylinder (⌀ 5 mm) was glued on top of a quartz coverslip using UV-glue. Next, the glass cylinder was slid through a circular hole of 7 mm that was drilled in the middle of a standard microscopy slide. Then, the cylinder was attached permanently by gluing the coverslip to the microscopy slide. The sample cells were filled with 150 µL dispersion containing ∼ 0.5 vol% particles, total height of the dispersion was ∼ 6 mm. The cells were closed with cotton wool wrapped in laboratory film (Parafilm) and sealed with candle wax. See Fig. 3.1b for a schematic.

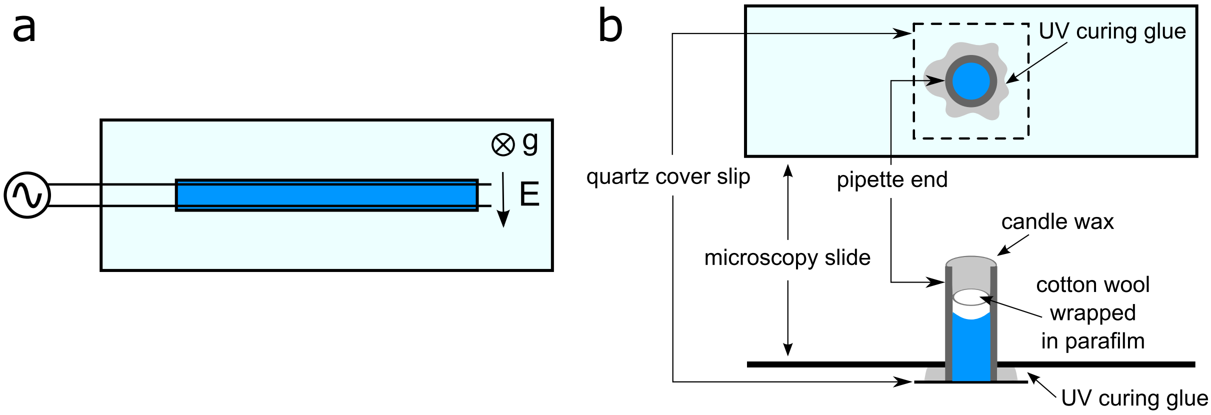

Figure 3.1 **(a)** Schematic representation of the electric sample cell used for the alignment with an ac electric field. Field direction was perpendicular to gravity. **(b)** Schematic representation of the sample cell used to study the sedimentation profile of mixtures of colloidal rods and spheres with 3D confocal microscopy.

Electric field A sinusoidal signal of 1 MHz and an amplitude of 3.0 V was generated using a function generator (Agilent, 33120A). This signal was then sent to the sample via a wide band amplifier (Krohn-Hite, 7602M), that was used to control the electric field strength in the sample cell. An electric field of $15\,\mathrm{V\,mm^{-1}}$ was applied for 48 hours while the sample was left to sediment, then the electric field was switched off. Four days after the electric field was switched off, the sample was imaged with the confocal microscope.

Six confocal images were made over an area of 0.5 mm × 0.7 mm, using the 'tile scan' option in the Leica LASAF 4.1 software. Of each of the images and each of the two separate channels of the confocal images a fast Fourier transform (FFT) image was made. This was done using the algorithm in ImageJ software (1.49m, NIH). The FFT images of one channel were combined by adding up the intensities from the six separate FFT images. This resulted in one combined FFT image from the rod channel and one image from the sphere channel. One overview image was created from the six confocal images by using the stitch procedure in the Leica LASAF software.

Measuring the Translational Diffusion Constant We followed the diffusion of spherical particles inside the Sm_2-phase, in a sediment of R1 rods and spheres at SDE. We measured inside the Sm_2-phase at a height close to the transition between the isotropic and Sm_2-phase. We recorded with the confocal microscope xyt-series, with a length of 1200 frames and an interval $\Delta t = 90\,\mathrm{ms}$. The xy-plane was chosen such that the y-axis corresponded to the nematic director $\hat{n}$ of the Sm_2-phase. We obtained 2D trajectories of the particles from the recorded images using particle fitting and tracking algorithms [169]. Next, we calculated the mean square displacement (MSD) as a function of time. To obtain values for the translational diffusion constant D_t inside the Sm_2-phase we fitted

$$\langle \Delta r^2(t) \rangle = 2dD_t t + 4\varepsilon_t^2 \tag{3.2}$$

to the plot of the MSD versus time t. Here $\langle \Delta r^2(t) \rangle$ is the MSD, d the dimensionality of the track and ε_t is the error of the measurement [214].

Single Particle Fitting Confocal data was deconvolved using commercially available Huygens SVI software (Version 14.10), using a theoretical point spread function (PSF). This theoretical PSF was close to the measured PSF [215]. The rod fitting algorithm of Besseling *et al.* was used to identify the positions and orientations of the rods [168]. The positions of the spheres were obtained using an algorithm similar to the method of Crocker and Grier [169] but extended to 3D [77]. For analysis, the experimental coordinate data were first divided into equally spaced slabs of $0.5\,D$ along the gravity direction, with D the average bare rod diameter, followed by calculation of the number density (ρ), composition (x), and pressure (P) for each slab. The local nematic order parameter S_i and the local smectic order parameter τ_i were calculated for each particle i. Successively, the averaged values $\langle S_i \rangle$ and $\langle \tau_i \rangle$ were calculated for each slabs by considering only the particles in the given slab. For details on the nematic S_i and smectic τ_i local order parameter, see Appendix 3.B.

3.3 Simulations

The colloidal silica spheres and rods are modeled as hard spheres of diameter σ and hard spherocylinders of (cylinder) length L_{cyl} and diameter D, respectively. Where the experimental end-to-end length L is defined as $L = L_{cyl} + D$. Particles interact via a purely excluded-volume pair potential: $U = \infty$ if two particles overlap, $U = 0$ otherwise. We first perform Monte Carlo (MC) simulations in the NPT ensemble of 1600 hard spherocylinders to map the behaviour of the experimental (single-component) system of silica rods onto hard particle behaviour, i.e., identify the effective dimensions of the silica rods (see Fig. A.3.1 and discussion in Appendix 3.A). After this analysis, we simulate $N_{tot} = N_{sph} + N_{rod} = 3125$ hard spheres and hard spherocylinders ($L_{cyl} = 6.46\,\sigma$, $D = 1.52\,\sigma$, $L_{cyl}/D \sim 4.25$) in the NPT ensemble with various composition $x_{sph} = N_{sph}/N_{tot}$. Each simulation consists of several million of MC steps, where one step is defined as N_{tot} moves randomly chosen from sphere translation, rod translation, rod rotation, and either isotropic or anisotropic change of the simulation box volume. Initial configurations at a given composition x are obtained from an equilibrated configuration at lower x by replacing an appropriate number of rods with spheres. Each state point has been characterized by several order parameters, some of which have been introduced before and used for the experimental data as well.

3.4 Results & Discussion

We synthesized silica spheres with an average bare diameter of $\sigma = 385\,\text{nm}$ (polydispersity $\delta_\sigma \simeq 9\%$) and two batches of silica rods; R1 rods with bare length $L = 2.9\,\mu\text{m}$ ($\delta_L \simeq 9\%$) and bare diameter $D = 0.51\,\mu\text{m}$ ($\delta_D \simeq 9\%$) and R2 rods with bare length $L = 3.6\,\mu\text{m}$ ($\delta_L \simeq 18\%$) and bare diameter $D = 0.59\,\mu\text{m}$ ($\delta_D \simeq 10\%$) [44, 45], see Figs. 3.2a-b. Colloidal rods and spheres were mixed and dispersed in a refractive index ($\text{n}_D^{21} = 1.45$) matched 85 wt% glycerol-water solvent mixture and left to sediment. In order to provide charge screening around the particles, 0.55 mM LiCl was added to the medium, thereby yielding a Debye screening length $\kappa^{-1} = 10\,\text{nm}$. Hence, the particles act as nearly hard particles with slightly larger effective dimensions.

The silica rods and spheres ($\rho \sim 2\,\text{g}\,\text{mL}^{-1}$) are not density-matched with the solvent mixture ($\rho \sim 2\,\text{g}\,\text{mL}^{-1}$). Hence, at sedimentation-diffusion equilibrium (SDE) most of the rods (R2, $l_g = 0.64\,\mu\text{m}$) reside at the bottom of the sediment and most of the spheres ($l_g = 17.65\,\mu\text{m}$) at the top, due to difference in gravitational height l_g between the particles. At intermediate heights, (for example $h \sim 17\,\mu\text{m}$, see Figs. 3.2d-g), both species were present and over time a Sm_2-phase was formed.

In most of the samples, the Sm_2-phase was not present as one single, large domain. Rather, we observed Sm_2-domains with different orientations throughout the sample, Fig. 3.3f. In order to show that the observed Sm_2-phase is stable, we aligned the Sm_2-phase by applying an ac electric field to the sample, which induced a dipole moment in each rod due to the dielectric constant mismatch between the rods and the solvent [70]. Our binary colloidal system responded by aligning its director to the electric field, over macroscopically large areas, whereas the spheres remained in between the smectic layers of

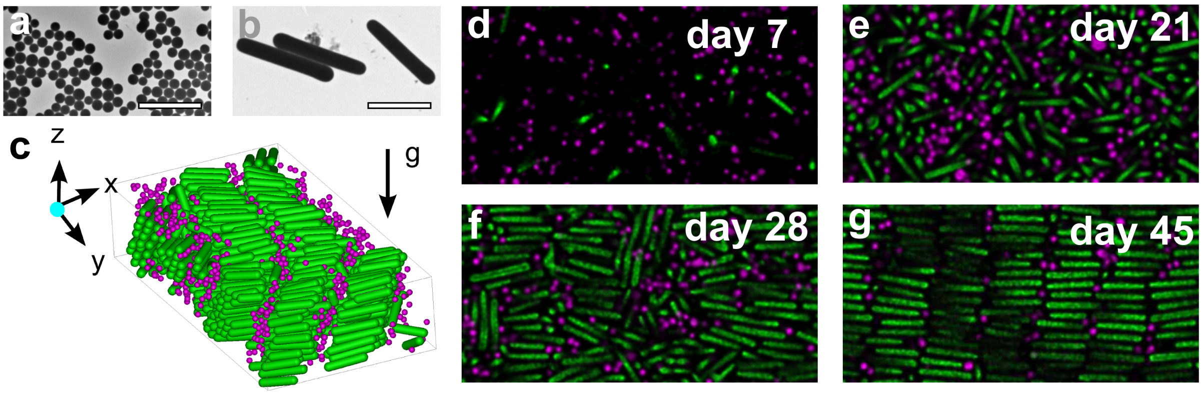

Figure 3.2 3D single particle analysis of a Sm$_2$-phase. **(a-b)** TEM images of **(a)** 385 nm silica spheres (polydispersity $\delta_\sigma \simeq 9\%$) and **(b)** silica rods with end-to-end length $L = 3.6\,\mu\text{m}$ ($\delta_L \simeq 18\%$) and diameter $D = 0.59\,\mu\text{mm}$ ($\delta_D \simeq 10\%$), scale bars 2.5 µm. **(c)** 3D reconstruction from fitted particles of a part of a confocal data stack showing a Sm$_2$-phase. **(d-g)** Formation of the Sm$_2$-phase in a rod-sphere mixture over time, images taken at height $\sim 17\,\mu\text{m}$.

rods, Figs. 3.3a-b. An ac electric field (15 V mm^{-1}, 1 MHz) was applied for 48 hours, during sedimentation of a dispersion of silica rods (R1, $L/D = 5.6$) and spheres ($\sigma = 385\,\text{nm}$) in DMSO-water. A zoom-out confocal image, over an area of 0.5 mm × 0.7 mm, is shown in Fig. A.3.7. Figs. 3.3a-b show that the alignment of the rods with the electric field was still preserved 4 days after turning off the field, although minor undulations in the smectic layers were observed. The effect of the electric field is clear when comparing the aligned Sm$_2$-phase, Fig. 3.3b, with a Sm$_2$-phase that assembled without the presence of an ac electric field, Fig. 3.3f. From these observations we conclude that the Sm$_2$-phase is a stable phase. To further characterize the order in the aligned Sm$_2$-phase, fast Fourier transform (FFT) images were made from the tiles of Fig. A.3.7. The FFT image of the rod channel (Fig. 3.3c) shows that the rods are organized in a smectic phase, in one single domain. Moreover, one characteristic length scale can be observed corresponding to the transverse distance between the rods in the smectic layers and one characteristic length scale associated to the spacing between the smectic layers. The FFT image of the sphere channel (Fig. 3.3d) shows only one characteristic length scale corresponding to the spacing between sheets of spheres. No long-range order of spheres was observed within the sheet of spheres. In Fig. 3.3e the FFT images of both the rod and the sphere channel are merged into one single image. This image shows that the spacing between sheets of spheres equals that of smectic layers of rods. Moreover, the ease of alignment and formation of the Sm$_2$-phase during sedimentation is important for use in applications. It is expected that such alignment with relatively small fields will work equally well for Sm$_2$-phases of particles of nanometer size and molecular dimensions as well.

In order to show that the Sm$_2$-phase was still dynamic and not kinetically arrested we measured the mean square of displacement (MSD) of spheres inside a sediment of the Sm$_2$-phase, see Fig. 3.4. The black symbols depict the MSD measured along the nematic director and the red symbols depict the MSD measured perpendicular to the nematic director. In Fig. 3.4d a confocal snapshot is shown from the recorded *xyt*-series of the spheres inside the Sm$_2$-phase, the double arrow denotes the nematic director $\hat{n}$.

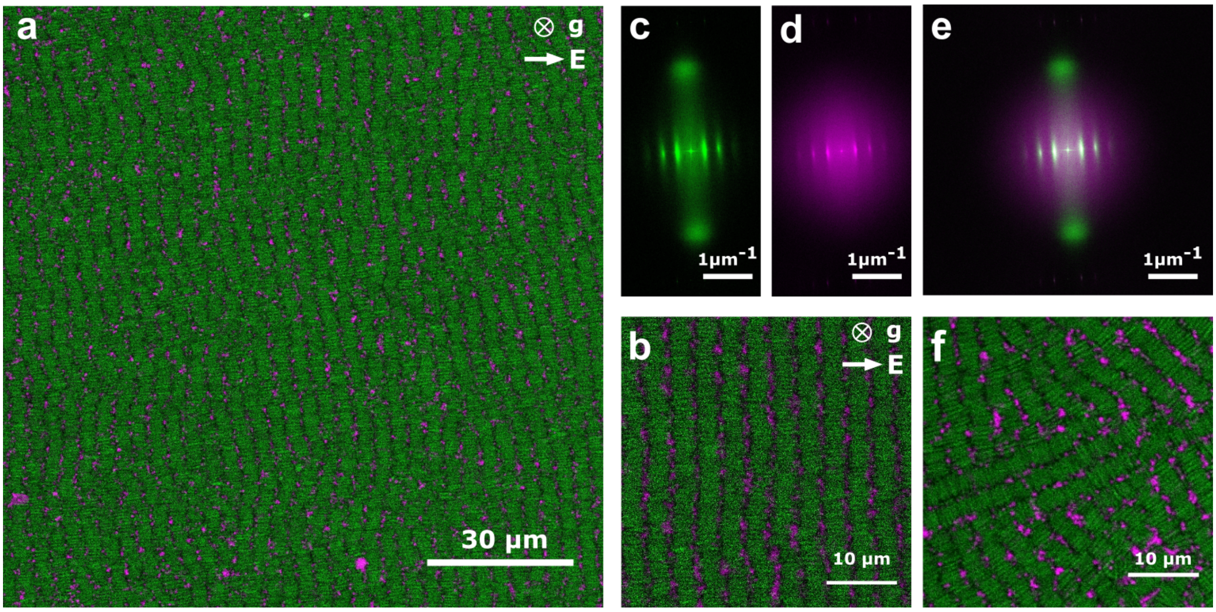

Figure 3.3 Longe-range ordering of the Sm$_2$-phase using an electric field. **(a)** Confocal image of a part of the sample four days after the electric field had been turned off. A zoom-out confocal image, over an area of 0.5 mm × 0.7 mm is provided in Fig. A.3.7. An ac electric field ($15\,\mathrm{V\,mm^{-1}}$, 1 MHz) was applied for 48 hours during sedimentation of a sample with rods (R1) and small spheres ($\phi \approx 1.5$ vol% particles). **(b)** Zoom-in of the same sample. **(c-e)** FFT-images of the aligned binary smectic Sm$_2$-phase (0.5 mm × 0.7 mm), FFT-images are displayed on a logarithmic intensity scale. **(c)** FFT-image of the rod channel **(d)** FFT-image of the sphere channel **(e)** overlay of the FFT-images of both the green (**(c)** rod) and magenta (**(d)** sphere) channel. **(f)** Binary smectic phase assembled without alignment by a field.

Fig. 3.4b shows that at $t < 1\,\mathrm{s}$, the short time self-diffusion was on average the same in both directions. The spheres were not hindered by the smectic layers of rods at $t < 1\,\mathrm{s}$. We fitted $\langle \Delta r^2 \rangle = \langle \Delta x^2 \rangle + \langle \Delta y^2 \rangle$ for $t < 1\,\mathrm{s}$ to equation 3.2 with $d = 2$, to obtain the short time self-diffusion coefficient. We found a short time self-diffusion coefficient $D_{t<1} = (4.00 \pm 0.21) \times 10^{-3}\,\mathrm{\mu m^2\,s^{-1}}$, with $\varepsilon_t = 45\,\mathrm{nm}$. We compared short time self-diffusion coefficient with the diffusion coefficient of spheres measured in a dilute suspension. For a dilute suspension of spheres we obtained $D_t = (1.300 \pm 0.016) \times 10^{-2}\,\mathrm{\mu m^2\,s^{-1}}$, with $\varepsilon_t = 38\,\mathrm{nm}$, see Fig. A.4.1 on page 51. The measured $D_{t<1}$ inside the Sm$_2$-phase was 1/3 of the D_t in a dilute suspension of spheres. This is reasonable as the hydrodynamic coupling close to neighboring particles tends to slow down self-diffusion [216]. It is known for only hard spheres that the short time self-diffusion coefficient at $\phi = 0.4$ is reduced to $\sim 1/3\,D_t$.

When $t > 1\,\mathrm{s}$, the diffusion in both directions slowed down. We observed that at longer time scales ($t > 10\,\mathrm{s}$) the MSD parallel to the nematic director reached a plateau. This is expected, because the diffusion of spheres along the nematic director is hindered due to the presence of smectic layers of rods. In contrast, the diffusion perpendicular to the nematic director was not hindered. Still, the self-diffusion at longer time scales ($t > 6\,\mathrm{s}$) became slower due to the presence of other spheres. By fitting equation 3.2 through the MSD perpendicular to the nematic director for $t > 6\,\mathrm{s}$, a long-time self diffusion

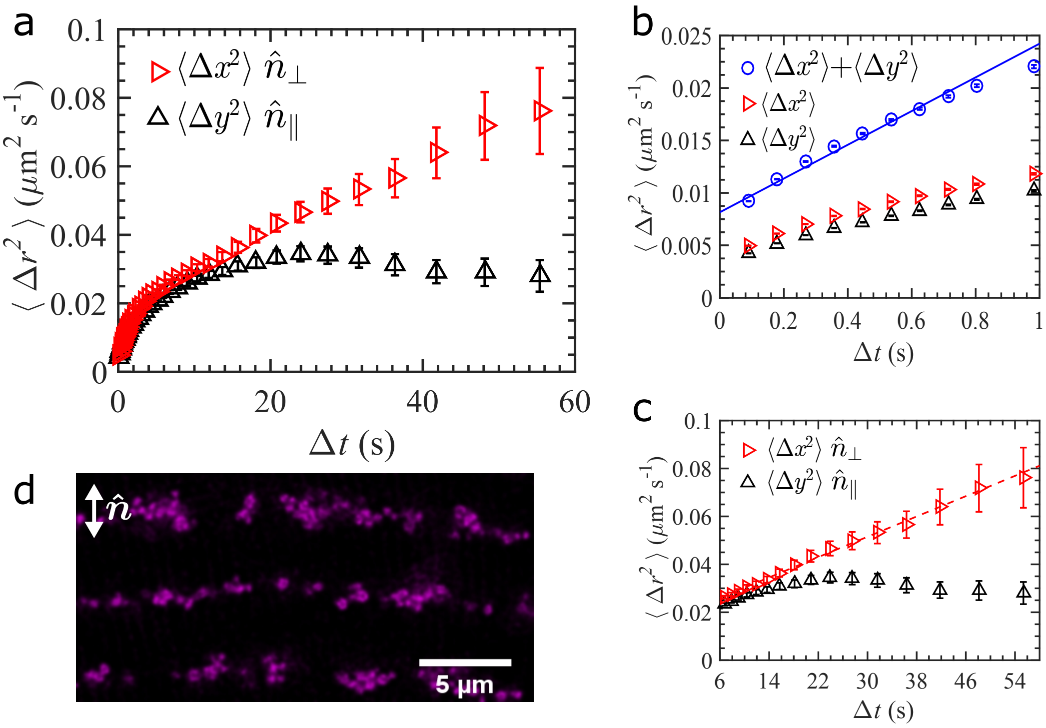

Figure 3.4 Mean square displacement inside the Sm$_2$-phase. **(a)** Measured MSD parallel to the nematic director (△) and perpendicular to the nematic director (▷). **(b)** Same as **(a)** but for $\Delta t < 1$ s. The solid line is a linear fit through $\langle \Delta r^2 \rangle$ for $t < 1$ s using equation 3.2. **(c)** Same as **(a)** but for $\Delta t > 6$ s. The dashed line is a linear fit through the MSD perpendicular to the nematic director for $t > 6$ s using equation 3.2. **(d)** Confocal snapshot of the recorded xyt-series. The double arrow denoted $\hat{n}$ is the nematic director, showing the average orientation of the rods. Only the spheres were imaged for this measurement.

coefficient was obtained of $D_{t>6} = (0.50 \pm 0.09) \times 10^{-3}\,\mu\text{m}^2\,\text{s}^{-1}$, see Fig. 3.4c. After 55 seconds the spheres had diffused on average 275 nm in the direction perpendicular to the nematic director. This distance is greater than the sphere's own radius, which further confirms that the Sm$_2$-phase observed is in equilibrium. Earlier, in simulations a liquid like diffusion for spheres was found inside the Sm$_2$-phase, showing that the spheres were not hindered by the smectic layers of rods [217]. These simulations investigated the diffusion at much longer time scales, such that liquid behavior of the liquid crystalline phase and the hopping of spheres between smectic layers could be retrieved. We investigated the diffusion of spheres inside the Sm$_2$-phase at much shorter time scales, such that only the diffusion of spheres in between the smectic layers was captured.

In order to determine the thermodynamic properties of the Sm$_2$-phase, we performed a real-space analysis of binary rod-sphere mixtures in SDE. Sedimentation enables us to probe the phase behaviour and thermodynamics of the system over a wide range of system parameters in just a single experiment. We let our samples sediment for at least four weeks. The equilibrated samples had a final sediment height of around 100 µm. We optimized our system for single-particle tracking, using a fast scanning confocal microscope, see Section 3.2 for details. We were able to image quantitatively in the sample up to a height of 130 µm. The original confocal images were deconvolved with a theoretical point spread function (PSF) using commercially available software. After deconvolution of the images we used single particle identification algorithms [168] to obtain the positions and orientations of all particles individually. Using these coordinates, we determined the number density of the rods $\rho_{rod}(z)$ and of the spheres $\rho_{sph}(z)$ as a function of height z in the sediment. Using not only the positions but also the orientations of the rods allowed us to determine the average local nematic $\langle S_i \rangle(z)$ and smectic $\langle \tau_i \rangle(z)$ order parameter profiles as a function of z, where the brackets denote an average over all particles in the slab at z, see Appendix 3.B for details on the local order parameters. In Fig. 3.5a, we plot both the composition ($x_{sph} = N_{sph}/N_{tot}$), with N_{sph} and N_{tot} the number of spheres and total number of particles, respectively, as well as the order parameters as function of z. For comparison, the deconvolved confocal xyz-stack is presented in Fig. 3.5b. We clearly observe a smectic phase with high nematic order $\langle S_i \rangle > 0.9$ and a high smectic order $\langle \tau_i \rangle > 0.6$, which is rich in rods, i.e., $x_{sph} \simeq 0.4$, at the bottom of the samples, whereas an isotropic sphere-rich phase with $x_{sph} \sim 1$ and low nematic and smectic order is observed at the top. The transition between the isotropic and Sm$_2$-phase occured at a height of ~ 14 µm, see Fig. 3.5f.

In order to distinguish the different phases, we did not use the positions of the spheres in the order parameter analysis, as the order of the spheres is dictated by that of the rods and is less pronounced, see Fig. A.3.8.

Finally, we mapped out the experimental phase diagram in the pressure P - composition x_{sph} representation by preparing and investigating many samples with different initial volume fractions and compositions, and by analyzing these using the same procedures as described above. Here $\beta = 1/k_BT$ denotes the inverse temperature with k_B Boltzmann's constant. To this end, we also determined the pressure P at height z by integrating the density profiles of both species to obtain the weight of all particles above it. The pressure changes as a function of height z in the sediment and depends solely on the local densities of the spheres $\rho_{sph}(z)$ and rods $\rho_{rod}(z)$, yielding the equation of state P, in ρ_{sph} and ρ_{rod} parameter space. In Fig. 3.6, we project the sedimentation path onto a two-dimensional P - x_{sph} plane.

From the top of the sediment down, each path shows an initial increase in pressure at large x_{sph}, followed by a nearly horizontal portion in the $P(x_{sph})$ curve suggestive of a broad coexistence between a low density phase and a Sm$_2$-phase. Finally, in the Sm$_2$-phase the pressure rises, while x_{sph} decreases only slowly. Each path presents the expected sequence isotropic I - (nematic N) - binary smectic Sm$_2$ that was identified by employing the average nematic and smectic local order parameters. We used the following threshold values to determine the different phases; isotropic if $\langle S_i \rangle < 0.5$ and $\langle \tau_i \rangle < 0.35$, nematic if $\langle S_i \rangle > 0.5$ and $\langle \tau_i \rangle < 0.35$, Sm$_2$ if $\langle S_i \rangle > 0.5$ and $\langle \tau_i \rangle > 0.35$ (see Fig. A.3.3). We thus find a stable Sm$_2$-phase in our experimental phase diagram for sufficiently high pressures $\beta P D_{eff}^3 > 3$ and compositions $0 \leq x_{sph} \leq 0.8$ in binary silica rod-sphere mixtures. In order to explore the possibility that the Sm$_2$-phase coexists with a low-density phase and to investigate if the Sm$_2$-phase can be stabilized by entropy alone, we determined the phase diagram using Monte Carlo (MC) simulations of hard spherocylinders and hard spheres with the effective dimensions of the experimental particles. We estimated the effective diameter of the spheres σ_{eff} by mapping the equation of state of the spheres as

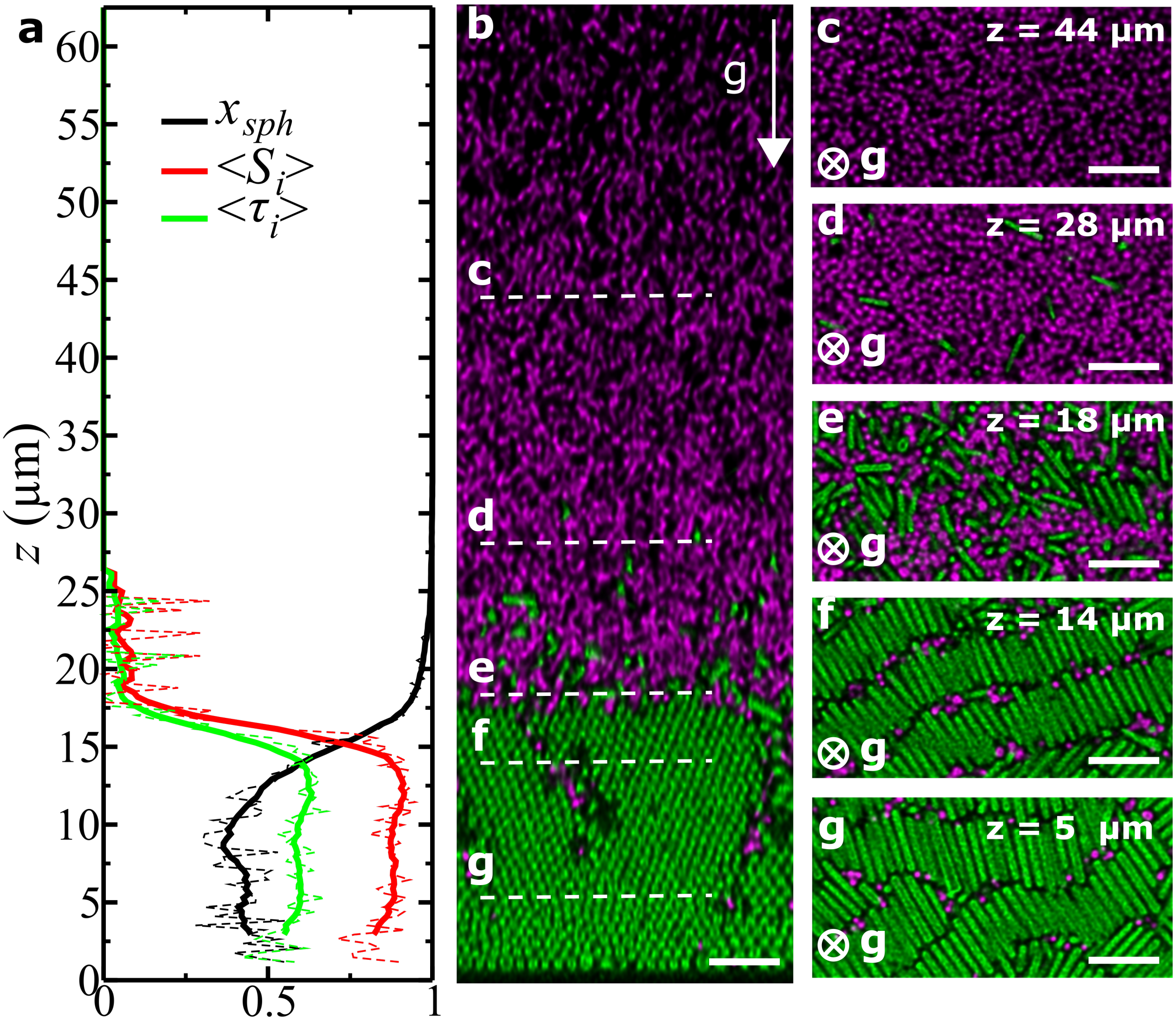

Figure 3.5 **(a)** Quantitative analysis of local structure after determination of particle positions and orientations of an equilibrated sample. Plot of averaged local nematic $\langle S_i \rangle$ order parameter (red), averaged local smectic $\langle \tau_i \rangle$ order parameter (green) and composition $\langle x_{sph} \rangle$ as a function of height z (black). Thin dashed lines are raw data divided in equally spaced slabs of $0.5\,D$, along the gravity direction. Thick lines are data smoothed by convolution using a top-hat function of $5\,D$ width. **(b-g)** Deconvolved confocal microscopy images of a sediment of rods (R2) and spheres. Images are shown **(b)** parallel to gravity and **(c-g)** perpendicular to gravity. The dashed horizontal lines in **(b)** indicate the height at which the images **(c-g)** were acquired. All scale bars are 5 µm. The height of the total sediment was 120 µm, height shown here is 62.5 µm.

obtained from the top part, which contained only spheres, of an equilibrated sediment to the Carnahan-Starling equation of state [20]. In addition, the effective dimensions of the rods, L_{eff} and D_{eff} were obtained by mapping the I-N transition as identified by the jump in the global nematic order parameter S in experimental data on a rods-only system to the transition as obtained from simulations (Fig. A.3.1). We performed simulations in the NPT ensemble at many different state points and analyzed the phase behaviour by employing local and global nematic and smectic order parameters (see Fig. A.3.4).

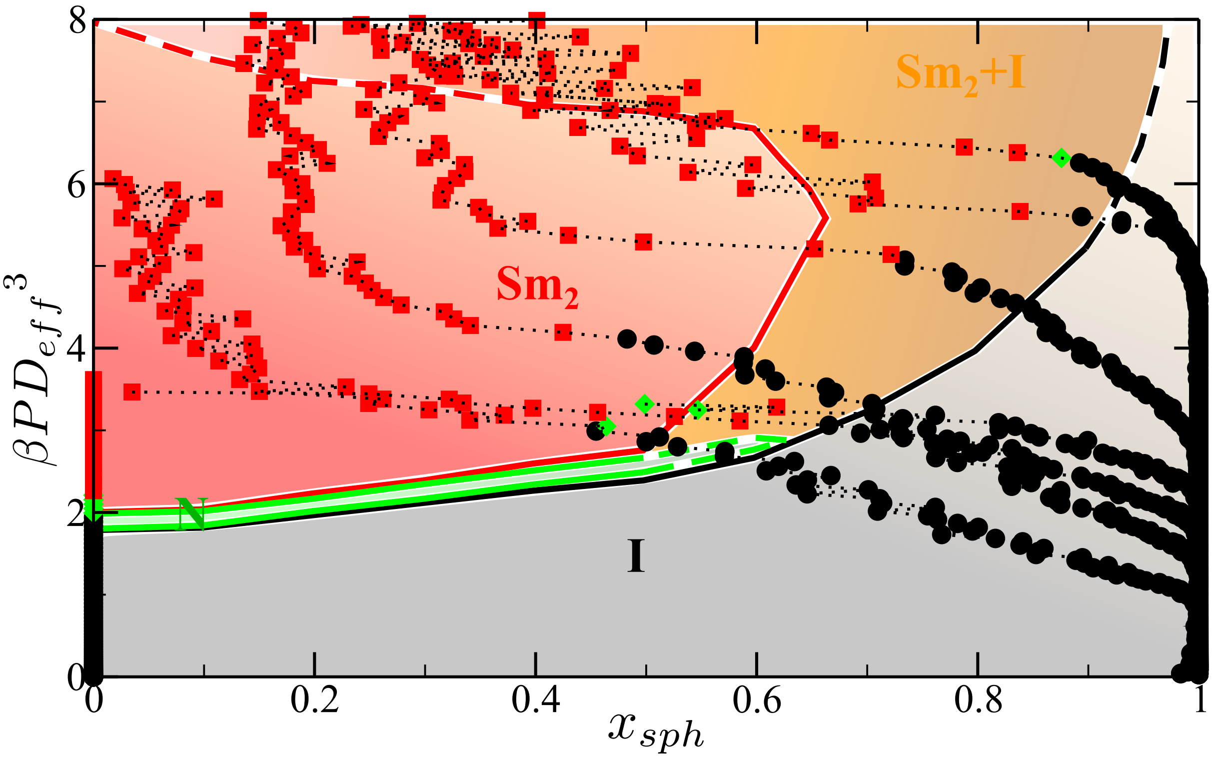

Figure 3.6 Mapping of the experimental sedimentation paths (symbols) on the bulk phase diagram obtained from Monte Carlo simulations. The phase diagram as obtained from MC simulations of bulk mixtures of hard spherocylinders and hard spheres displays a stable isotropic I (grey), nematic N (green), binary smectic Sm$_2$ (red), and a I-Sm$_2$ coexistence region (orange). The symbols denote the experimental sedimentation paths in the pressure $\beta P D_{eff}^3$ - composition x_{sph} plane as obtained from different sediments of rods and spheres (symbols) and a sediment of only rods at $x_{sph} = 0$. We used the following thresholds to determine in the experimental system the different liquid-crystal phases; I if $\langle S_i \rangle < 0.5$ and $\langle \tau_i \rangle < 0.35$ (black spheres), N if $\langle S_i \rangle > 0.5$ and $\langle \tau_i \rangle < 0.35$ (green diamonds), Sm$_2$ if $\langle S_i > 0.5 \rangle$ and $\langle \tau_i \rangle > 0.35$ (red squares).

In Fig. 3.6, we superimpose the experimental sedimentation paths on the phase diagram obtained by simulations. The topology of the phase diagram is consistent with previous theoretical studies [199] and shows a wide isotropic-binary smectic (I-Sm$_2$) coexistence region. We indeed confirm that the nearly horizontal parts of the experimental sedimentation paths agree qualitatively with the broad I-Sm$_2$ coexistence region as obtained from simulations. However, we note that $P(x_{sph})$ should actually be horizontal due to the condition of equal pressure for the two coexisting phases, but are slightly slanted due to the finite interfacial width. We thus conclude that the observed experimental phase behaviour of silica rods and spheres is predominantly driven by entropy, and thus by the particle shape alone, which was to be expected as the van der Waals interactions can be neglected due to the refractive index-matching and the Coulombic interactions were screened by the addition of salt.

In addition, we note that the theoretical phase diagram as obtained from MC simulations shows that the number of spheres in between the smectic layers of rods can be tuned in the Sm$_2$-phase as the composition ranges from $0 \leq x_{sph} \leq 0.6$, which is relevant for future application of these Sm$_2$-phases. We also mention that we did not observe any crystalline order in our samples likely due to the relatively high polydispersity in the length of the rods ($\delta_L = 18\%$) and in the diameter of the spheres ($\delta_\sigma = 9\%$). We expect to find stable crystal phases for systems with a lower polydispersity, see e.g. [195].

3.5 Conclusion

In conclusion, our results obtained from both experiments and simulations show that colloidal rods and spheres can spontaneously co-assemble in a single binary liquid crystal phase, i.e., a Sm$_2$-phase. Previous experimental work already showed the formation of the Sm$_2$-phase, but these studies did not reveal the detailed structure on the single-particle level and did not study the phase diagram as function of pressure and composition [72, 195]. Here, we used fluorescently labeled silica particles to determine for the first time the structure and composition of the Sm$_2$-phase on the single-particle level using a combination of confocal microscopy and particle fitting algorithms [168]. In addition, we showed that the Sm$_2$-phase can be aligned with an ac electric field. We also showed that inside the Sm$_2$-phase spheres still diffused freely. We investigated the system in SDE, which allowed us to determine the osmotic pressure at height z of the system, a quantity that is usually not accessible in experiments. Finally, we mapped out the experimental phase diagram in the pressure-composition representation, and find qualitative agreement with the phase diagram as obtained from simulations on mixtures of hard spherocylinders and hard spheres. The phase diagram exhibits a large stable region, where rods and spheres co-assemble in a single Sm$_2$-phase, which is surrounded by a huge demixing region at higher pressures and compositions x_{sph}. As the Sm$_2$-phase can be stabilized by entropy alone we expect that this intriguing phase can be realized for a broad class of systems at many different length scales. Hence, the co-assembly of two particle shapes in a single phase allows us to take advantage of multiple species in a single material and the tunability of the positional and orientational order in liquid-crystalline phases. For instance, realizing an aligned Sm$_2$-phase of gold nanorods and spherical semiconductor particles using a small electric field is of great interest. The spherical semiconductor particles at the gold nanorod tips will experience strong plasmon enhanced electromagnetic fields that will enhance the luminescence of the semiconductor particles.

3.6 Acknowledgments

I gratefully thank Simone Dussi for performing the simulations and for collaborating on the order parameters analysis. I would like to thank Thijs Besseling with the help on the single particle fitting analysis. Chris Kennedy for introducing me to the measurement on the sedimentation-diffusion equilibria. I would like to thank Barbera Droste who worked on this project at the early stage. I would also like to thank Evert Wiegant and Bing Liu who performed preliminary experiments. This chapter is based on the following publication [218]: Phase diagram of binary colloidal rod-sphere mixtures from a 3D real-space analysis of sedimentation-diffusion equilibria, *Soft Matter* **2016**, *12* , 9238-9245.

Appendix 3

3.A Determining Effective Particle Dimensions

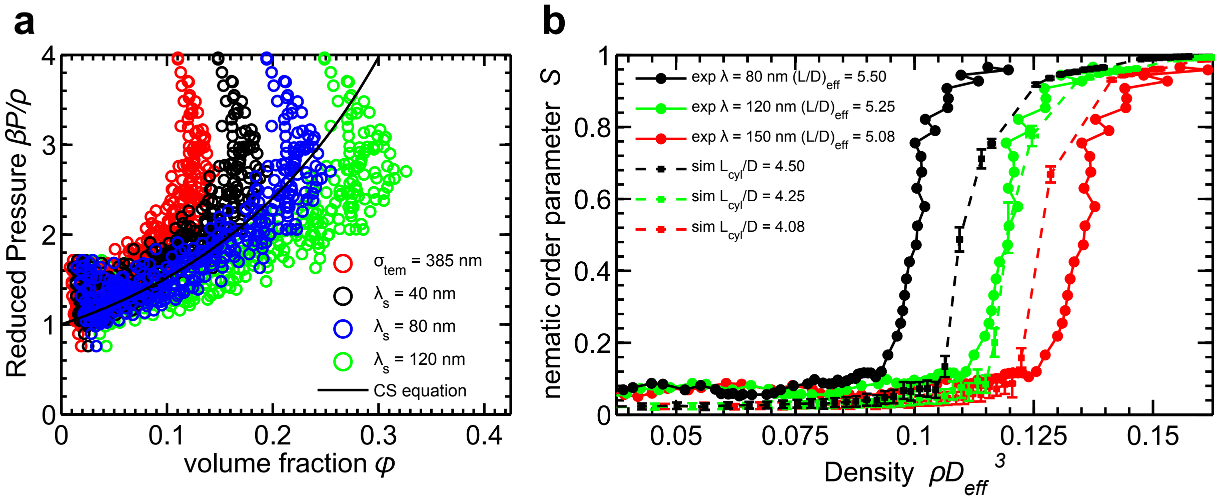

Figure A.3.1 Determination of the effective particle dimensions. **(a)** Fit to the Carnahan-Starling equation of state. The pressure (open symbols), as obtained by integrating the density profile of the spheres for the top part of a sediment of rods and spheres, was mapped to the CS equation of state (solid line), in order to obtain the effective diameter of the particles. Spheres with $\sigma_{eff} = \sigma_{tem} + \lambda_s$ and $\lambda_s = 80\,\text{nm}$ could be mapped as hard particles to the CS equation of state. This resulted in an effective diameter of the spheres: $\sigma_{eff} = 465\,\text{nm}$. **(b)** Plot of the global nematic order parameter S as a function of density, at the I-N transition. Experimental data points are shown as the solid lines with circles. Simulations are shown as dashed lines and squares. Experimental data with rods $D_{eff} = D_{tem} + \lambda_r$, with $\lambda = 120\,\text{nm}$ match best with data from simulations. This resulted in the following effective dimensions for the R2 rods: $D_{eff} = 707\,\text{nm}$, $L_{eff} = 3711\,\text{nm}$, $(L/D)_{eff} = 5.25$, $D_{eff} = 1.52\,\sigma_{eff}$.

In order to compare experimental data with simulations, we determine first the effective dimensions of the particles that account for the thin electric double layer. The colloidal particles used act as nearly hard particles, with a dimension slightly larger than that derived from TEM images. First, to determine the effective diameter of the spheres, $\sigma_{eff} = \sigma_{tem} + \lambda_s$, we mapped the equation of state as obtained by integrating the density profile of the top part of the sediment (that contained only spheres) to the Carnahan-Starling (CS) equation of state (see Fig. A.3.1a)

$$\beta P/\rho_{sph} = \frac{1+\phi+\phi^2-\phi^3}{(1-\phi)^3}, \tag{3.3}$$

where ρ_{sph} is the number density of the spheres, $\beta = 1/k_BT$, and $\phi = \rho v_{sph}$, with $v_{sph} = \frac{1}{6}\pi\sigma_{eff}^3$ the effective volume of one spherical particle. The pressure at height z in the sample was calculated using $P(z) = m_{sph} g \int_z^h \rho_{sph}(z)dz$. with m_{sph} the buoyant mass of the particles (calculated from TEM dimensions), g gravity, z the height in the sediment and h height of the sampled volume, where we made sure that the particle density vanished at h. The best fit with the CS equation of state was obtained by taking $\lambda_s = 80$ nm for the volume fractions $\phi < 0.2$ or pressures $\beta P/\rho_{sph} < 2.5$. The equation of state as obtained from experiments becomes unphysical at higher pressures (i.e., lower height z in the sediment) as the density of rods cannot be neglected at lower z. Next, in order to determine the effective dimensions of the rods, $D_{eff} = D_{tem} + \lambda_r$ and $L_{eff} = L_{tem} + \lambda_r$, we mapped the jump in the global nematic order parameter S at the isotropic nematic transition of an equilibrated sample containing pure hard rods to results obtained from NPT simulations of only rods (see Fig. A.3.1b and discussion below). Experimental data with $\lambda_r = 120\,\text{nm}$ matched best with data obtained from simulations. This resulted in the following effective dimensions for the R2 rods: $D_{eff} = 707\,\text{nm}$, $L_{eff} = 3711\,\text{nm}$, $(L/D)_{eff} = 5.25$, $D_{eff} = 1.52\,\sigma_{eff}$. We did not use the equation of state of rods to determine the effective dimensions of the rods as the equation of state is more sensitive to polydispersity.

For both procedures to find the effective dimensions, one should realize that discrepancies can arise due to polydispersity, which also can cause size segregation of particles with height.

3.B Order Parameters For Colloidal Rods

To distinguish between the isotropic and the different liquid crystalline phases we rely on global and local order parameters. The global nematic order parameter is obtained by diagonalizing the nematic order parameter tensor

$$\mathcal{Q}_{\alpha\beta} = \frac{1}{N}\sum_{i=1}^{N}\left[\frac{3}{2}\mathbf{u}_{i\alpha}\mathbf{u}_{i\beta} - \frac{1}{2}\delta_{\alpha\beta}\right], \tag{3.4}$$

where $\mathbf{u}_{i\alpha}$ is the α-component of the unit vector describing the orientation of the long axis of the rod i, N is the number of rods in the slab, and $\delta_{\alpha\beta}$ the Kronecker delta. The global nematic order parameter S is defined as the largest eigenvalue of $\mathcal{Q}$ and the corresponding eigenvector is the nematic director $\mathbf{n}$. S ranges from -0.5 to 1. In addition, we define as introduced in [200] the local nematic order parameter S_i of particle i as

$$S_i = \frac{1}{n_i}\sum_{j=1}^{n_i}\left[\frac{3}{2}(\mathbf{u}_i\cdot\mathbf{u}_j)^2 - \frac{1}{2}\right], \tag{3.5}$$

with n_i the number of neighbors of particle i and where two particles are considered neighbors if $\rho_{ij} < 1.0D$, with ρ_{ij} the minimum surface-to-surface distance. We take $D = D_{eff}$ in case of the experiments, whereas D equals the hard-core diameter of the spherocylinders in case of the simulations. S_i also ranges from -0.5 (particle transverse to its the neighbors) to 1 (perfect alignment).

The global smectic order can be probed by calculating the following order parameter [48, 219–221]

$$\tau = \max_{l}\left|\sum_{j=1}^{N} e^{2\pi i \mathbf{r}_j\cdot\mathbf{n}/l}\right|, \tag{3.6}$$

where the value of l that maximizes the above expression is identified as the layer spacing d. However, due to the limited statistics (small number of layers within confocal snapshot) and fluctuations in their positions, we obtained values of τ, smaller than what one would expect after visual inspection of the sample, and a rather noisy trend of τ as a function of height. We therefore introduce a novel order parameter to quantify the *local* tendency of the particles to form (single) smectic or crystalline layers and we use it as a local smectic order parameter. We first calculate the shift h_{ij} of the center of mass of particle i with respect to its neighbors j projected on a common axis (we pick the main orientation $\mathbf{u}_i$ of particle i but another direction such as the local nematic director would give similar results). We then normalize it and define

$$\Delta_i = 1 - \frac{1}{m_i}\sum_{j=1}^{m_i}\frac{h_{ij}}{r_{cut}} = 1 - \left(\frac{1}{m_i}\sum_{j=1}^{m_i}\frac{\mathbf{r}_{ij}}{r_{cut}}\cdot\mathbf{u}_i\right), \tag{3.7}$$

where $r_{cut} = (L_i + D)/2$ and m_i is the number of neighbors of particle i satisfying $r_{ij} < r_{cut}$, with r_{ij} the center-to-center distance between the rods. $\Delta_i = 1$ corresponds to the orthogonality condition between r_{ij} and the common axis (in this case $\mathbf{u}_i$). However, such a condition can be obtained both for perfectly aligned rods and in the case of transverse order (Fig. A.3.2). Notice that transverse rods are anyway expected in the smectic phase due to thermal fluctuations but we want to consider them as defects in a perfectly layered structure. In order to discriminate between these two configurations Δ_i is then multiplied by S_i. In conclusion, we define the local smectic order parameter as

$$\tau_i \equiv S_i\Delta_i. \tag{3.8}$$

Using τ_i we are able to distinguish (locally) the smectic order (high values of τ_i) from the isotropic, nematic, as well as columnar order for which we expect low values of τ_i. Note that the neighbor definition in Δ_i and τ_i is different and that the precise threshold value of the cut-off distance yields some degree of arbitrariness in the use of these order parameters to define the different phases. Furthermore, other approaches to define a local smectic order parameter are in principle possible, for example by considering

$$\max_l \left|\sum_{j=1}^{n_i} e^{2\pi i \mathbf{r}_{ij}\cdot\mathbf{u}_i/l}\right|, \tag{3.9}$$

with r_{ij} the center-to-center distance between particle i and its neighbors j, defined as particles that have a minimum surface-to-surface distance $\rho_{ij} < 1.0D$ (as for S_i). However, to avoid misidentifications a large number of neighbors n_i are needed, otherwise even particles in the isotropic phase could have a large value of such an order parameter. When imposing this kind of threshold on the number of neighbors, we found similar results as using $\tau_i \equiv S_i\Delta_i$.

We expect that future work on order parameters for anisotropic particles based on the local environment will refine the family of quantities needed to discriminate between the different liquid crystal phases, in analogy with what happened to the bond orientational order parameter for crystal symmetries of spherical particles [222, 223]. Such order parameters will be central in experimental studies on e.g. nucleation, glass transition and defects re-arrangement. Nevertheless, the order parameter $\tau_i \equiv S_i\Delta_i$ introduced here is suitable for the current purpose, i.e., the identification of the smectic order in absence of a large number of smectic layers.

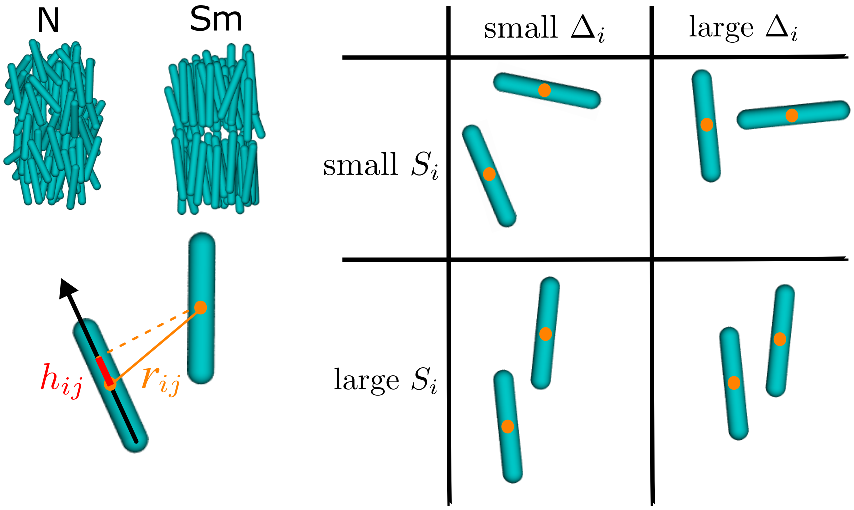

Figure A.3.2 Schematic of the smectic local order parameter $\tau_i = S_i \cdot \Delta_i$

3.C Determining Different Phases in the Bulk Phase Diagram from Experimental Data

In order to distinguish between the different phases in experimental data, we rely on the local order parameters S_i and τ_i for each particle i, as described above. Notice that the analysis of the local order parameters was based on the lengths L_i of the rods obtained by the particle tracking procedure, where the end-to-end length is defined as $L = L_i + D$, therefore are based on fluorescent shells present inside the rods. Subsequently, we determine the averaged values $\langle S_i \rangle$ and $\langle \tau_i \rangle$ by averaging over all particles in a certain slab in the sediment. The choice of the threshold values of the local order parameters at which we define the transition is admittedly somewhat arbitrary and can influence the identification of the different phases. Therefore, we chose values close to points of inflection observed in the trend of the averaged local order parameters (see Fig. A.3.3). We used the following threshold values to determine in the experimental system the different phases; isotropic (I) if $\langle S_i \rangle < 0.5$ and $\langle \tau_i \rangle < 0.35$, nematic (N) if $\langle S_i \rangle > 0.5$ and $\langle \tau_i \rangle < 0.35$, Sm_2 if $\langle S_i \rangle > 0.5$ and $\langle \tau_i \rangle > 0.35$. Analysis based on global order parameters is also in principle possible but usually more noisy due to the need to collect a larger amount of data. In particular the traditional global smectic order parameter, τ is sensitive to fluctuations of the layers and defects in and between layers.

3.D Estimating the Bulk Phase Diagram from Computer Simulations

According to theoretical predictions based on a second-virial density functional theory applied to a rod-sphere mixture with similar sizes ($L_{cyl}/\sigma = 7$, $D = \sigma$), we expect stable isotropic (I), nematic (N) and binary-smectic (Sm_2) liquid crystal phases [199]. In our study, we do not take into account the possible crystalline (hexagonal) order, neither within a single layer nor between different layers, and therefore we do not distinguish between (binary) Smectic-A and (binary) Smectic-B and possible (binary) crystal phases,

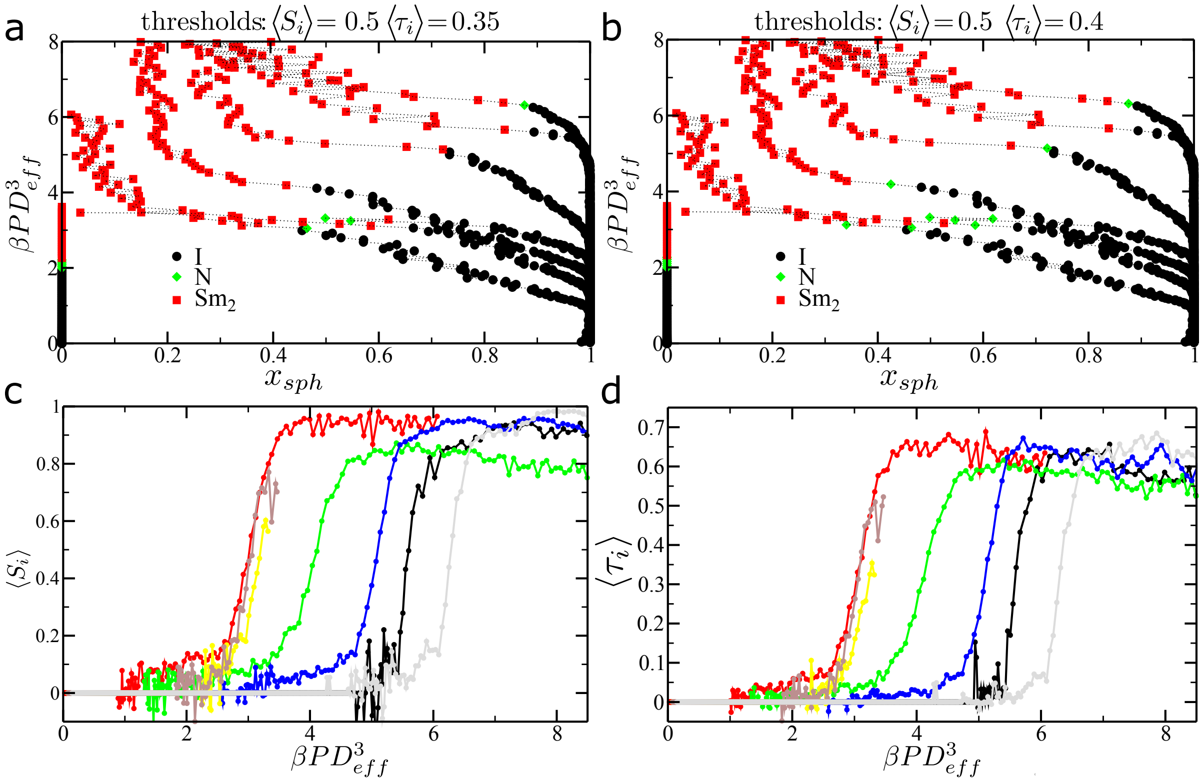

Figure A.3.3 Experimental State Diagram and Order Parameters. **(a)** Experimental state diagram (as Fig. 3.6 in Section 3.4), using the following thresholds: isotropic (I) if $\langle S_i \rangle < 0.5$ and $\langle \tau_i \rangle < 0.35$ (black circles), nematic (N) if $\langle S_i \rangle > 0.5$ and $\langle \tau_i \rangle < 0.35$ (green diamonds), Sm_2 if $\langle S_i \rangle > 0.5$ and $\langle \tau_i \rangle > 0.35$ (red squares). **(b)** Different choice of the threshold values for the local smectic order parameter τ_i, isotropic (I) if $\langle S_i \rangle < 0.4$ and $\langle \tau_i \rangle < 0.4$, nematic (N) if $\langle S_i \rangle > 0.5$ and $\tau_i < 0.4$, Sm_2 if $\langle S_i \rangle > 0.5$ and $\langle \tau_i \rangle > 0.4$. **(c)** Averaged local nematic order parameter $\langle S_i \rangle$ as a function of reduced pressure $\beta P D^3_{eff}$ for different equilibrated sediments. **(d)** Averaged local smectic order parameter $\langle \tau_i \rangle$ for different equilibrated sediments.

even though we (often) observe hexagonal arrangements of rods, both in experiments and in simulations. Since for the short rods considered here both the I-N and the N-Sm transitions are weakly first order [37], and a particularly broad I-Sm_2 coexistence region is expected when such rods are mixed with hard spheres [199], an accurate identification of the phase boundaries is clearly challenging. Nevertheless, we use both global and local order parameters to discriminate between the different liquid crystalline structures for a large number of state points (for which x_{sph} and P are imposed) and trace the state diagram of rod-sphere mixtures for which experiments have been performed, see Fig. A.3.4a. In particular, in the isotropic phase (see Fig. A.3.4b) all the order parameters vanish. The nematic phase (see Fig. A.3.4c) is characterized by a high value of the nematic order parameter (both the global S and the local S_i as can be seen from the color coding of the rods) but not of the smectic ones, since neither the rods nor the spheres form layers. We observe that the I-N shifts towards higher pressure upon increasing composition x_{sph} until a critical point (around $x_{sph} \simeq 0.6$) beyond which the nematic phase is no longer stable. In the Sm_2 phase (see Fig. A.3.4d) the rods locally form layers resulting in a

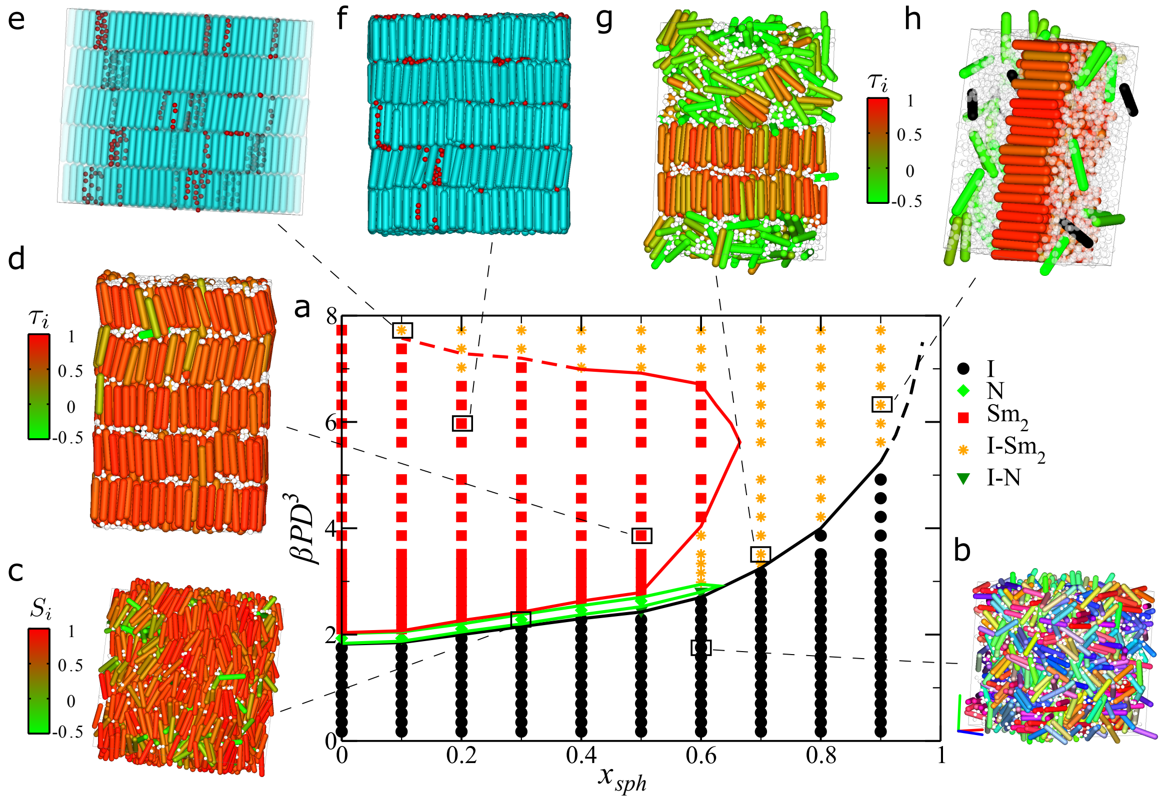

Figure A.3.4 State diagram from bulk MC-NPT simulations. **(a)** State diagram from bulk MC-NPT simulations. Representative snapshots for **(b)** isotropic phase (I) with $x_{sph} = 0.6$ $\beta PD^3 = 1.93$, rods are colored according to their orientation (axis colors indicated in the snapshot); **(c)** nematic phase (N) $x_{sph} = 0.3$ $\beta PD^3 = 2.28$ with rods colored according to the local nematic order parameter S_i; **(d)** binary smectic phase (Sm_2) $x_{sph} = 0.5$ $\beta PD^3 = 3.86$ with rods colored according to the local smectic order parameter τ_i; **(e)** Formation of columnar aggregates of hard spheres as indication of demixing between a smectic (or crystal) phase rich in rods and an isotropic phase rich in spheres. $x_{sph} = 0.1$ $\beta PD^3 = 7.73$; **(f)** Columns of spheres start to appear in a Sm_2 phases (most of the spheres are still arranged in layers) $x_{sph} = 0.2$ $\beta PD^3 = 5.97$; **(g)** Coexistence between I and Sm_2 phase, $x_{sph} = 0.7$ $\beta PD^3 = 3.86$, rods colored according to τ_i ; **(h)** Single layer of rods in coexistence with a sphere-rich isotropic phase, $x_{sph} = 0.9$ $\beta PD^3 = 6.32$, rods are colored according to τ_i.

large value of the local smectic order parameter τ_i as shown by the color coding. The structure is clearly long-range which is also confirmed by the (ordinary) global smectic order parameter τ. The binary character of the smectic phase is confirmed by the fact that the spheres are also arranged in layers, as clearly evident from the snapshot in Fig. A.3.4d. Such layering can also be quantified by a global smectic order parameter for the spheres, calculated along the nematic director of the rods $\mathbf{n}$ (that coincides with the layer normal), in full analogy with the one for the rods (see Appendix 3.B)

$$\tau_{sph} = \max_{l} \left| \sum_{j=1}^{N} e^{2\pi i \mathbf{r}_j \cdot \mathbf{n}/l} \right| . \tag{3.10}$$

Both the values of τ_{sph} and the associated spacing between layers of spheres are consistent with the values of τ (for only rods) and the spacing between the smectic layers of the rods, as expected for the Sm_2 phase. However, for small compositions x_{sph} and large pressures P (see Figs. A.3.4e-f), the spheres do not form layers anymore but rather are expelled from the layers of rods and organize themselves into linear aggregates. This structure is likely not a novel thermodynamically stable phase but rather should be considered as an indication of the underlying phase separation into a sphere-rich isotropic phase and rod-rich (binary) smectic phase (or probably a crystal phase of rods at sufficiently high pressures, as evident from Fig. A.3.4e). Indeed, since the system cannot really demix because of the finite size nature of the simulations, the spheres have to act as substitutes of rods to minimize the overall system free volume. It is important to remark that this columnar arrangement of spheres is not related to the columnar phase observed in the mixture of colloidal spheres and *fd*-viruses [72], since in that case the columns of spheres are perpendicular to the direction of the layers of the rods. The possibility of forming that structure with only hard-core interactions and its thermodynamic stability are still open questions.

The transition from a stable Sm_2 phase to this kinetically trapped structure, that is evidence of I-Sm_2 demixing, is often associated with a drop in τ_{sph} as reported in the Fig. A.3.5f. As can be seen from the Fig. A.3.4f, the formation of columns of spheres occurs also when most of the spheres are still arranged in layers, therefore yielding to a somehow arbitrary definition of the upper bound of the Sm_2 stability region.

For larger values of x_{sph}, the I-Sm_2 demixing is more evident as can be appreciated from Figs. A.3.4g-h in which a number of smectic layers (depending on x_{sph}) is in coexistence with an isotropic phase rich in spheres. This behaviour is also captured by the probability distribution of rods having a certain value of the local smectic order parameter τ_i (some examples are reported in the Fig. A.3.5a). Indeed, for state points inside the I-Sm_2 regions two populations of particles (one with $|\tau_i| \sim 0$ and one with τ_i bigger than a given threshold) are often evident. However, extracting the equilibrium composition of the two coexisting phases based on the amount of particles in the two populations seemed to be not an easy task due to the limited system size of our simulations and the sensitivity on the choice of the threshold value. By examining the state diagram obtained, we notice that compositions around $x_{sph} = 0.6$ show a peculiar *re-entrant* sequence upon increasing the pressure, going from an isotropic to I-Sm_2 region to a pure Sm_2 to a demixed region again. Representative snapshots at this composition, along with a quantitative analysis, are reported in the Fig. A.3.5. Finally, we notice that the topology of the phase diagram here reported is consistent with theoretical predictions [199], including the re-entrant behaviour of the Sm_2 region.

We wish to remark here that simulations in the NPT ensemble, in which the overall composition x_{sph} and pressure P are kept fixed, is not always the most convenient statistical ensemble to study broad demixing transitions as huge system sizes and long simulation times are need to obtain phase coexistence between different thermodynamic states. Indeed, a standard procedure to trace the phase diagram of a mixture would require simulations in the grand-canonical ensemble that are, however, not feasible for short rods (only the insertion/removal of the small spheres would be possible). Recently, the use of hard walls in computer simulations of rod-sphere systems composed of similar

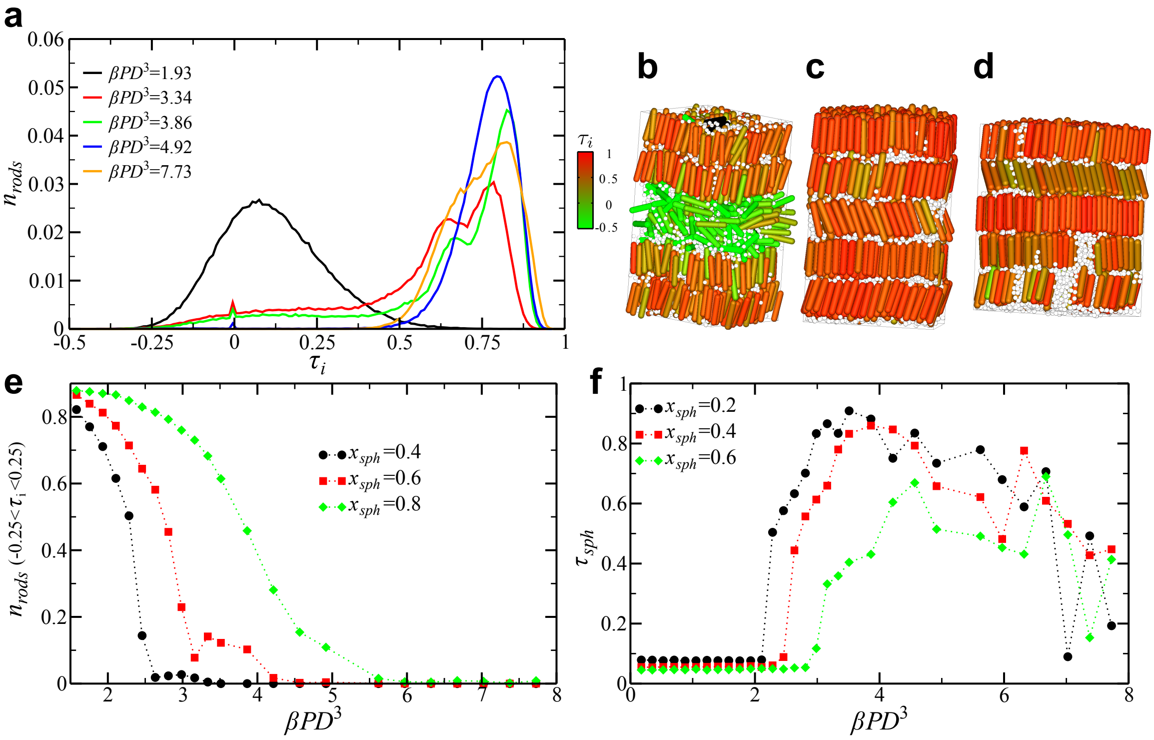

Figure A.3.5 Identifying coexistence between isotropic and binary smectic phase. **(a)** Fraction of rods n_{rod} with a given value of the local smectic order parameter τ_i for state points with $x_{sph} = 0.6$ and reduced pressures βPD^3 as indicated in the legend. $\beta PD^3 = 1.93$ corresponds to an isotropic state (representative snapshot in Fig. A.3.4b). $\beta PD^3 = 3.34$ corresponds to a two-phase I-Sm$_2$ coexistence state (typical snapshot in panel **(b)**), a small peak at $\tau_i \sim 0$ is evident. $\beta PD^3 = 4.92$ corresponds to a Sm$_2$ state (snapshot in panel **(c)**). $\beta PD^3 = 7.73$ corresponds to a I-Sm$_2$ state (snapshot in panel **(d)**). In this case the probability distribution of τ_i is not useful to identify the state point but the low value of τ_{sph} (see panel **(f)**) indicates that the spheres are not arranged in layers. In all the snapshots the rods are colored from green (low) to red (high) according to the value of τ_i. Rods that are colored black do not have neighbors and therefore have $\tau_i = 0$. Peaks around zero (panel **(a)**) are evidences of demixing between I and Sm$_2$. Tracking the number of rods with small values of τ_i could help in identifying the state point. In panel **(e)** the fraction of rods n_{rod} with a small τ_i (arbitrarily chosen such that $|\tau_i| < 0.25$) are plotted as a function of the reduced pressure βPD^3 for different composition x_{sph}. For $x_{sph} = 0.6$ the non-monotic behaviour of n_{rod} could be used to identify the re-entrant behaviour of the Sm$_2$ region, even if it is admittedly somehow arbitrary. In panel **(f)** the smectic order parameter associated to layers of spheres τ_{sph} (see text for the definition) is plotted against the pressure for different composition. The different arrangement of spheres, either in layers or in columns/random aggregates (these are indications of I-Sm$_2$ demixing) is associated to a large or small value of τ_{sph}, respectively.

number of particles as used here and similar particle dimensions, have been employed as an alternative to determine slightly more accurately the variation in composition of the isotropic-nematic transition but limiting the study to a small region in the $x_{sph} - P$ plane [224]. However, at the densities where the binary smectic phase is observed, the effect of walls would be still quite pronounced for ordinary system sizes. Ultimately, an accurate study of the equilibrium phase behaviour should be based on (computationally expensive) free-energy calculations, but this is beyond the scope of the present work.

3.E Figures

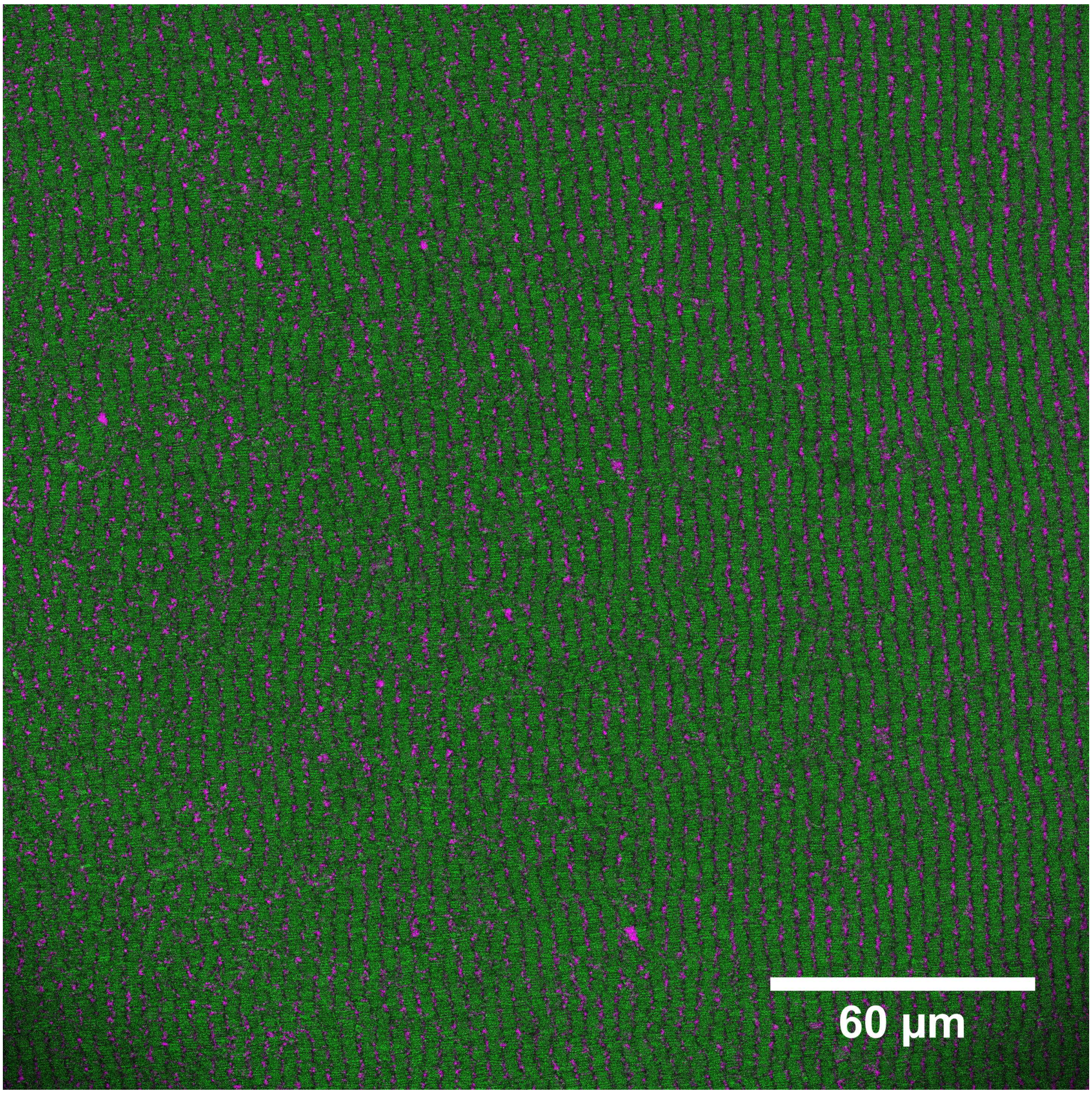

Figure A.3.6 Confocal image of an aligned Sm$_2$-phase using an ac electric field. Top right confocal image (246 µm × 246 µm) in Fig. A.3.7.

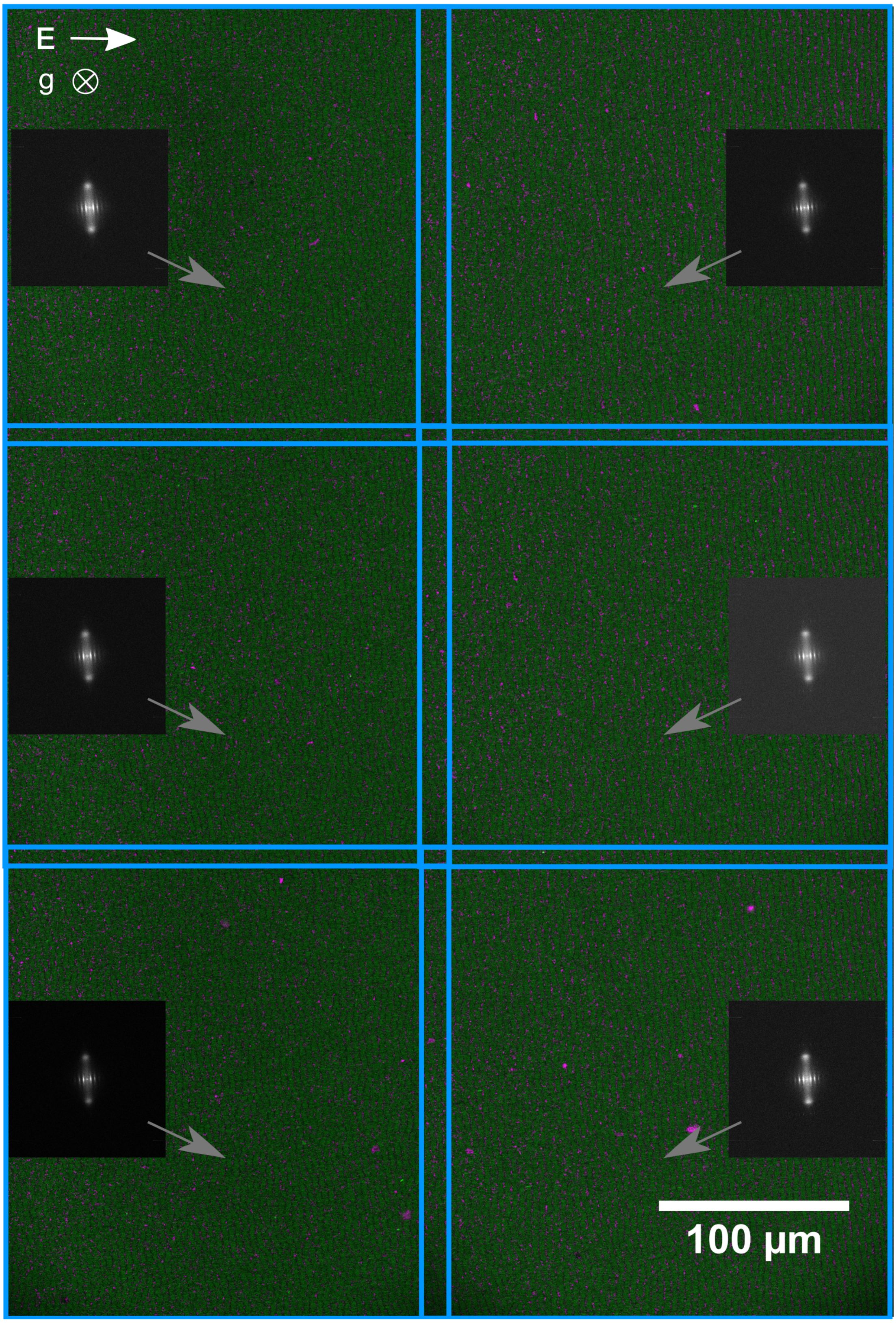

Figure A.3.7 Confocal image of an aligned Sm$_2$-phase using an ac electric field switched on during sedimentation ($15\,\mathrm{V\,mm^{-1}}$). Image size: $738\,\mu\mathrm{m} \times 492\,\mu\mathrm{m}$. The image consists of 6 images stitched together to form 1 image.

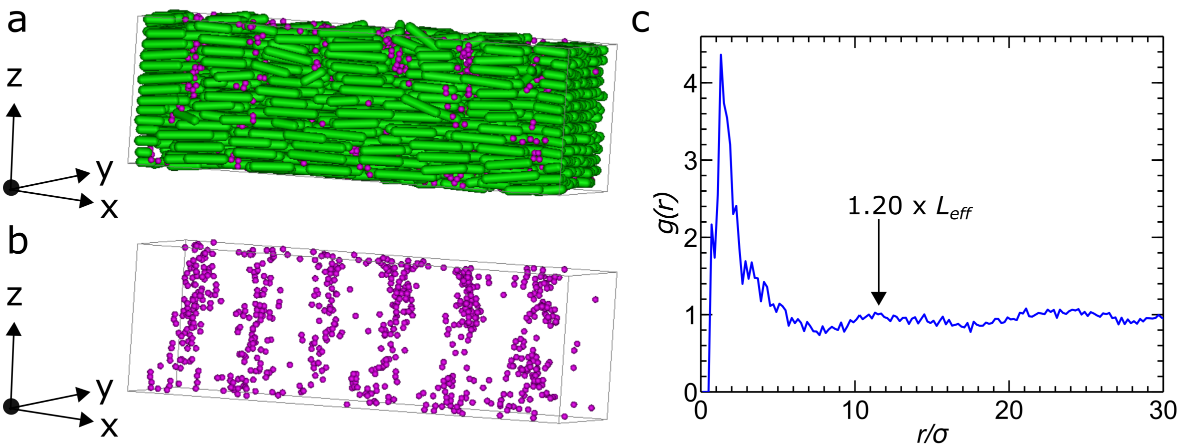

Figure A.3.8 $g(r)$ of spheres inside Sm_2-phase. **(a-b)** Computer drawn images from the coordinate data of a sediment of rods and spheres, showing the Sm_2-phase **(a)** depicted both rods and spheres **(b)** depicted only spheres. **(c)** $g(r)$ of spheres inside the Sm_2-phase, data taken from **(b)**. We observe a peak at $11.6\,\sigma$, with σ being the bare diameter of the spheres. This corresponds to a smectic layer spacing of $1.20\,L_{eff}$, with L_{eff} being the average effective length of the rods. From simulation [225] of only rods with $L_{cyl}/D = 5$ ($L/D = 6$) a spacing of 1.048 is expected. Kuijk *et al.* experimentally found a spacing between 1.1 and $1.2\,L_{eff}$ for silica rods [226]. The effective sphere diameter σ_{eff} is $0.13\,L_{eff}$.

4

Dynamics of Sedimentation of Binary Colloidal Rod-Sphere Mixtures

This chapter discusses the sedimentation dynamics of binary mixtures of silica rods and spheres. The first part of the chapter discusses the formation of a binary smectic phase over time, from a mixture of colloidal silica rods and spheres dispersed in a mixture of glycerol-water under the influence of gravity. It shows that the binary smectic phase nucleated from a nematic layer of rods at the bottom of the sample, once the pressure and volume fraction of rods were high enough. Moreover, we found that there is an interplay between the sedimentation of rods and sedimentation of spheres. As the concentration of spheres increased at the bottom of the sample, the sedimentation of rods slowed down. The bottom rod-rich sediment then pushed the spheres upwards. The second part of the chapter discusses sedimentation of a binary mixture of colloidal silica rods and silica spheres, where the silica spheres had a diameter larger than the diameter of the rods. Rods and spheres settled with on average the same speed. While the sediment became denser, bundles of aligned rods appeared inside the dense sediment. Over time the overall structure of the sediment did not change much. This indicated that perhaps the system was kinetically trapped. Although the rods aligned within bundles, the overall bundles orientation was random.

4.1 Introduction

Colloidal sedimentation is both of interest in industry and on the fundamental level. In industry it is important in food products, paints, water waste treatments, the mining industry and the settling of atmospheric particulates. Theoretical, Einstein was the first to derive a fluctuation-dissipation relationship between the thermal fluctuations, diffusion coefficient and the friction factor of a colloidal using sedimentation-diffusion equilibrium [9]. In the laboratory, Perrin was able to determine Avogadro's number by studying the sedimentation profile of a gamboge suspension [8]. These findings were important for the development of statistical mechanics. Using gravity as an external field, the whole equation of state can be obtained, by measuring the sedimentation profile of colloidal hard spheres [20–22] in sedimentation-diffusion equilibrium (SDE). Thus, gravity can be used to obtain in one go the equilibrium phase diagram for a one component system. To do so, the local density approximation must be valid. This beholds that one is able to define the necessary thermodynamical variables like density and osmotic pressure locally, and such the gravitational height cannot be too small. Gravity acting on colloids in a closed system couples settling, diffusion and nucleation together. Therefore, studying the dynamics of colloidal systems subjected to gravity is highly complex [227, 228]. Considering nucleation alone, there are two types of nucleation: homogeneous and heterogeneous nucleation. During homogeneous nucleation clusters spontaneously nucleate and grow from the supersaturated liquid. In the case of heterogeneous nucleation, clusters nucleate at surfaces or impurities in the sample [229, 230]. However, the dynamics of crystallization can be strongly affected by additional fields, like the gravitational field [231–233] or by a templated bottom wall [234]. Depending on the initial concentration of the dispersion, below or above the freezing concentration, either heterogeneous nucleation starting at the bottom container wall or homogeneous nucleation will be observed.

Nucleation of ordered phases of rod-like particles are often studied for relatively short aspect ratios (end-to-end length to diameter ratio L/D), for which the ordered phase forms directly out of the isotropic phase (I-Solid or I-Sm transition) [58, 226, 235–237]. Only a few experimental papers show nucleation, for rods with high enough aspect ratios, where the smectic phase nucleates from the nematic phase and an I-(N)-Sm transition is observed [58, 226]. Little is known about the nucleation of smectic layers inside a binary system under the influence of gravity.

For multicomponent systems, Spruijt and Biesheuvel [238] gave a theoretical frame work on the sedimentation profiles of multicomponent systems. Also, de las Heras and Schmidt developed a theory to relate the bulk phase diagram of binary colloidal mixtures to the stacking of different phases under the influence of gravity [239]. Simulation studies done on binary colloid mixtures show that the initial configuration is an important factor that influences the sedimentation dynamics and the final sedimentation profile [240–242]. Experimental papers on the sedimentation of binary colloidal mixtures are mostly focused on sedimentation profiles that have reached SDE [243–247] or on the final profiles after centrifugation of a mixture of particles [248, 249]. Most of these experimental papers did not investigate the change of the sedimentation profile over time, before SDE was reached. However, much could be learned from the nucleation and growth of the final equilibrium phases. Furthermore, most experimental papers use ensemble methods like scattering techniques such as x-ray or polarized light scattering, to investigate the structure. These techniques do not capture what happens on the single particle level.

This chapter describes the dynamics of sedimentation and nucleation and growth of binary mixtures of fluorescently labeled colloidal rods and spheres over time before SDE was reached and on the single particle level using confocal microscopy.

In the first part of the chapter we describe the sedimentation and nucleation and growth of a binary smectic (Sm_2) phase. When colloidal rods and spheres were mixed with the right size ratio, they were observed to form a binary smectic phase [72, 195], see Chapter 3 and ref. [218]. In the second part we describe the sedimentation and nucleation and growth of bundles of rods that form in a binary rod-sphere mixture where the average diameter of the spheres σ is larger than the average diameter of the rods D ($\sigma > D$). As both systems were not density matched, the colloids were subjected to a gravitational field. As the solvent viscosity (η) in our system is high, the dynamics were slow and we were able to follow the formation of the sediment over time on the single particle level. In order to do so, the samples were imaged using confocal microscopy at different times over a period of five weeks after the samples were prepared. Using particle identification algorithms [77, 168, 169], we were able to determine the local architecture of the samples during sedimentation on the single particle level. Moreover, using local nematic and smectic order parameters (S_i and τ_i) in combination with a cluster criterion [235, 236], we were able to follow the nucleation and growth of the smectic layers over time.

4.2 Sedimentation of Rods and Spheres

Perrin and Einstein showed that in sedimentation-diffusion equilibrium (SDE) at the top of a sediment a barometric sedimentation profile is found, given by: $n(z) = n_0 \exp(-z/l_g)$, where n is the number of particles per unit volume. The decay constant is the gravitational length

$$l_g = k_B T/\Delta\rho v_p g, \tag{4.1}$$

where k_BT is the thermal energy, $\Delta\rho = \rho_p - \rho_{solvent}$ the apparent density of the particle, g the gravitational constant and v_p is the volume of the particle. The time scale of the sedimentation process depends on the buoyant mass of the particles $v_p\Delta\rho$ and the translational diffusion coefficient of the particles $D_t = \frac{k_BT}{\gamma}$, where γ is the friction factor of the particle. For single spheres the translational diffusion coefficient is given by

$$D_t = \frac{k_B T}{6\pi\eta a}, \tag{4.2}$$

with η the viscosity of the solvent and a the radius of the sphere. The translational diffusion coefficient of finite rods in dilute solution can be expressed as [250]

$$D_t = \frac{k_B T\left(\ln\left(\frac{L}{D}\right) + v\right)}{3\pi\eta L}, \tag{4.3}$$

in this expression L is the length of the rod, D is the diameter of the rod. The factor δ_t is used to correct for end-effects

$$\delta_t = 0.312 + 0.565\frac{D}{L} - 0.100\left(\frac{D}{L}\right)^2. \tag{4.4}$$

The sedimentation velocity of an isolated particle can then be obtained using the Svedberg equation [251]

$$v_{sed} = \frac{v_p D_t g \Delta\rho}{k_B T}. \tag{4.5}$$

To compare the relative importance of Brownian motion and gravitational forces, we use a dimensionless Péclet number, which is defined as the ratio of the time t_b it takes for a particle to diffuse over its own radius a and the time t_s it takes for a particle to settle over its own radius [22]

$$Pe = \frac{t_b}{t_{sed}} = \frac{a v_{sed}}{D_t}, \tag{4.6}$$

where a is the radius of the particle. If $Pe \ll 1$, particle motion may still be described as Brownian. Whereas for $Pe \gg 1$, we are in the non-Brownian regime with respect to the process of sedimentation. Pressures at height z were calculated the same way as in Chapter 3 by integrating the density profiles of both species to obtain the weight of all particles above

$$P(z) = \Delta\rho v_{sph} g \int_z^h \rho_{sph}(z) dz + \Delta\rho v_{rod} g \int_z^h \rho_{rod}(z) dz, \tag{4.7}$$

with h height of the sampled volume, where we made sure that at SDE the particle density vanished at h.

4.3 Methods

Particles Fluorescein isothiocyanate (FITC) fluorescently labeled silica rods were prepared according to the method of Kuijk *et al.* [44, 45], see Chapter 2 for more details. Rhodamine isothiocyanate (RITC) fluorescently labeled silica spheres were prepared via a modified Stöber synthesis [25, 26]. The mean dimension of the particles were determined from transmission electron microscopy (TEM) images made with a Philips Tecnai 10 or 12 microscope (Fei Company). Typically, 80 particles were measured by hand using the program iTem (Soft Imaging System GmbH, version 5). Both the end-to-end length (L) and the diameter (D) of the rods were measured, after which the aspect ratio (L/D) and the polydispersity (δ) were calculated. For single particle tracking we used rods labeled R2 with $L = 3591$ nm and $D = 587$ nm ($L/D = 6.1$ $\delta_L = 18\%$, $\delta_D = 10\%$). Colloidal silica spheres with $\sigma = 385$ nm ($\delta = 9\%$) and $\sigma = 930$ nm ($\delta = 4\%$) were used. More details on particle properties can be found in Table 4.1.

Sample Cells To allow for single particle tracking, the same sample cell was used as described in Chapter 3, Section 3.2. A glass cylinder, made from the end of a glass Pasteur pipette (WU mains), was attached on top of a quartz coverslip ($n_D = 1.46$, 0.15–0.18 mm, Laser Optex). Next, the resulting sample cell was attached to a standard microscope slide, by sliding the cylinder through a circular hole that was drilled in the middle of the microscope slide. The sample cells were filled with 150 µL dispersion containing $\sim$ 0.3–0.5 vol% of particles, the total height of the dispersion was $\sim$ 6 mm. The cell was closed

Table 4.1 Properties of particles used during this study.
Particle dimensions were derived from TEM images. The values of l_g, v_{sed}, D_t, Pe are calculated for particles dispersed in 85 wt% glycerol-water (η = 81 mPa s [156]) at infinite dilution.

	L nm	δ_L %	D nm	δ_D %	L/D	l_g µm	v_{sed} nm s^{-1}	D_t µm^2 s^{-1}	Pe	D_t experimental µm^2 s^{-1}
Rods										
R2	3591	18	587	10	6.1	0.64	5.2	3.3×10^{-3}	0.46	2.9×10^{-3}
Spheres										
D930			930	4		1.25	4.6	5.7×10^{-3}	0.37	5.1×10^{-3}
D385			385	9		17.65	0.8	1.4×10^{-2}	0.011	1.3×10^{-2}

with cotton wool wrapped in laboratory film (Parafilm) and sealed with candle wax. The as prepared samples were left to sediment over time, to reach a sedimentation-diffusion equilibrium (SDE). During sedimentation the samples were imaged regularly at 1, 3, 7, 9, 11, 14, 15, 18, 21, 23, 26, 28, 30, 46 and 110 day(s) after the sample was prepared.

Dispersions Particles were dispersed in an index-matched solvent mixture, $n_D^{21} = 1.45$, of 85 wt% glycerol ($\geq$ 99.0%, Sigma-Aldrich) and 15 wt% ultrapure water (Milipore), η = 81 mPa s [156]. Lithium chloride salt (LiCl, Merck) was added to a concentration of 0.55 mM to the dispersion; this resulted in an estimated double layer thickness κ^{-1} of 10 nm. In the case of the small spheres and rods that formed a Sm$_2$-phase the sample contained 0.3 vol% particles, of which 0.1 vol% spheres and 0.2 vol% rods. For every rod, about 13 spheres were present. In the case of the large spheres and rods the dispersion contained 0.5 vol% particles, of which 0.2 vol% rods and 0.3 vol% spheres. For every two rods 7 spheres were present.

Confocal Microscopy Samples were studied with a confocal laser scanning microscope (Leica TCS SP8, equipped with a 12 kHz resonant scanner). All images were taken in fluorescence mode. The excitation wavelength was 488 nm for the FITC-labeled rods and 543 nm for the RITC-labeled spheres. To optimize image quality, a 100×, 1.35 NA glycerol confocal-objective (Leica) was used to allow for single particle tracking in combination with a quartz coverslip (n_D = 1.46, 0.15–0.18 mm, Laser Optex). An image volume had the following dimensions in xyz : $\sim$ 25 µm × 12.5 µm × 100–150 µm. We imaged with a voxel size of $\sim$ 50 nm × 50 nm × 100 nm. Data shown here were averaged over at least 5 confocal xyz-scans, which were recorded consecutively.

Single Particle Fitting Confocal data were deconvolved using commercially available Huygens SVI software (Version 14.10), using a theoretical point spread function (PSF). The rod fitting algorithm of Besseling *et al.* was used to identify the positions and orientations of the rods [168]. The positions of the spheres were obtained using an algorithm similar to the method of Crocker and Grier [169] but extended to 3D [16, 77]. For analysis, the obtained coordinate data were first divided into slabs of 0.5 D parallel to gravity, with D the rod diameter obtained from TEM images, followed by calculation of the volume fraction (ϕ), composition (x_{sph}) and pressure (P) for each slab. The local nematic order parameter S_i and the local smectic order parameter τ_i were determined for each rod i. Successively, the averaged values $\langle S_i \rangle$ and $\langle \tau_i \rangle$ were calculated for each slab by considering only the particles in the given slab. Data, on particle volume fractions and order parameters, shown here were smoothed by convolution of the data using a top-hat function of 5 rod diameters, D, in width. For details on the nematic S_i and smectic τ_i local order parameter, see Appendix 3.B on page 40.

Effective Dimensions Our silica particles were charge stabilized and have effective dimensions slightly larger than that derived from TEM images, which is due to a thin electric double layer around the particles, in addition to the shrinkage of the particles by the electron beam in TEM. The effective dimensions for spheres and rods were determined in Appendix 3.A. For the 385 nm spheres we used $\sigma_{eff} = \sigma_{TEM} + \lambda_s = 385 + 80 = 465\,\text{nm}$. For the 930 nm spheres we used $\sigma_{eff} = \sigma_{TEM} + \lambda_s = 930 + 80 = 1010\,\text{nm}$. For the R2 rods we used $D_{eff} = D_{TEM} + \lambda_r = 587 + 120 = 707\,\text{nm}$, $L_{eff} = L_{TEM} + \lambda_r = 3591 + 120 = 3711\,\text{nm}$ and $(L/D)_{eff} = 5.25$. Data shown below reflects the effective dimensions of the particles. In the case of rods and small spheres that form a Sm$_2$-phase the particles had the following relative dimensions: $D_{eff} = 1.52\,\sigma_{eff}$ and $L_{eff} = 7.98\,\sigma_{eff}$. In the case of rods and large spheres $D_{eff} = 0.7\,\sigma_{eff}$ and $L_{eff} = 3.67\,\sigma_{eff}$.

Measuring the Translational Diffusion Constant In order to have an idea about the dynamics in the system, we measured the diffusion coefficients of the particles dispersed in 85 wt% glycerol-water. We followed a dilute suspension of particles ($\phi < 0.1$ vol%) over time with a Leica TCS SP8 confocal microscope. We measured in the sample cell as described above at a height 20 µm above the surface, to avoid wall effects. Sedimentation still took place during measurement as $\rho_{colloid} > \rho_{solvent}$, but we assumed a decoupling between translational diffusion and sedimentation [252]. We recorded xyt-series with 1000–4800 frames, a typical pixel size of 50–100 nm and a typical time between frames of $\Delta t = 90$–$180\,\text{ms}$. We obtained 2D trajectories of the particles from the recorded images using particle fitting and tracking algorithms [168, 169]. Next, we calculated the mean square displacement (MSD) as a function of time. To obtain the translational diffusion constant D_t we fitted

$$\langle \Delta r^2(t) \rangle = 4D_t t + 4\varepsilon_t^2 \tag{4.8}$$

to the plot of the MSD versus time t. Here $\langle \Delta r^2(t) \rangle$ is the MSD and ε_t is the error of the measurement [214]. Results on the experimentally measured translational diffusion constant can be found in Appendix 4.A and Table 4.1.

4.4 Results & Discussion

4.4.1 Sedimentation of Colloidal Rod-Sphere Mixtures that form a Sm$_2$-phase

We quantitatively followed in time the sedimentation dynamics and the nucleation and growth of a binary smectic phase (Sm$_2$) in a mixture of silica rods (R2 rods, $L = 3.6\,\mu\text{m}$, $D = 0.6\,\mu\text{m}$, $L/D = 6.1$) and spheres (D385, $\sigma = 0.4\,\mu\text{m}$), using 3D confocal microscopy in combination with single particle tracking, see Table 4.1. These particles have Péclet numbers $Pe < 1$ ($Pe_{R2} = 0.46$, $Pe_{D385} = 0.011$), which makes them still behave Brownian. Fig. 4.1a shows deconvolved confocal images of the sediment over time at days 1, 7, 14, 28 and 46. The images show side views of the sample, the xz-plane, with z parallel to gravity of the lower 98 µm of the sample. The final sediment height was $\sim 120\,\mu\text{m}$ and the total height of the dispersion in the sample cell was 6 mm. Fig. 4.1b shows computer drawn images of the sample after particle fitting of the confocal data. For clarity only the lower 40 µm of the sediment is shown. After day 46 the sediment morphology no longer changed much, so we deem it to be at equilibrium. A Sm$_2$-phase had formed on the bottom and a less ordered mixed phase lies on top. On days 1 and 7 the binary smectic phase had not formed yet, but a thin sediment of mainly rods was already present at the bottom of the sample. Due to the differences in gravitational length l_g and sedimentation velocity v_{sed} between the particles (see Table 4.1), the rods and spheres partly segregated upon sedimentation. Over time the Sm$_2$-phase formed and the height of the rod sediment grew.

To get a better view of the morphology change of the sediment, we plotted some of the characteristic properties of the system in 2D color-map plots, Figs. 4.2-4.5. The 2D color-map plot shows the sediment height as a function of time (in days). The color depicted in the 2D color-map plot indicates the value of the characteristic property of the system, e.g. total volume fraction ϕ_{tot}, volume fraction spheres ϕ_{sph}, volume fraction rods ϕ_{rod}, composition of spheres x_{sph}, the averaged local nematic order parameter $\langle S_i \rangle$, or the averaged local smectic order parameter $\langle \tau_i \rangle$. To obtain these properties, the experimental coordinate data were first binned into equally spaced slabs of $0.5\,D$ parallel to gravity, followed by the determination of the characteristic properties. Data shown in the 2D color-map plots were smoothed by convolution of the data using a top-hat function of $5\,D$ in width.

Fig. 4.2 depicts a 2D color-map plot of the change in total volume fraction, of both rods and spheres, over time in the sample. The total sediment height grew linearly until day 11, and after day 11 the growth in sediment height leveled off.

If one looks at the change in volume fraction of rods and spheres separately, Fig. 4.3, one can see that the rods were the first to end up at the bottom. Until day 7 mainly rods had settled down, from day 9 onwards also the settling of spheres became significant. Between days 3 and 11 the spheres were ‘pushed’ upwards by the still settling rods. However, around day 14 the pressure of the accumulating spheres became large enough to push the interface between the Sm$_2$-phase and isotropic phase down and the rod settling rate was slowed down. Rods that ended up on top of the other rods, first had to diffuse through the layer of spheres and push the spheres upwards. The layer of spheres became thicker and more concentrated over time, slowing down the sedimentation of rods. An

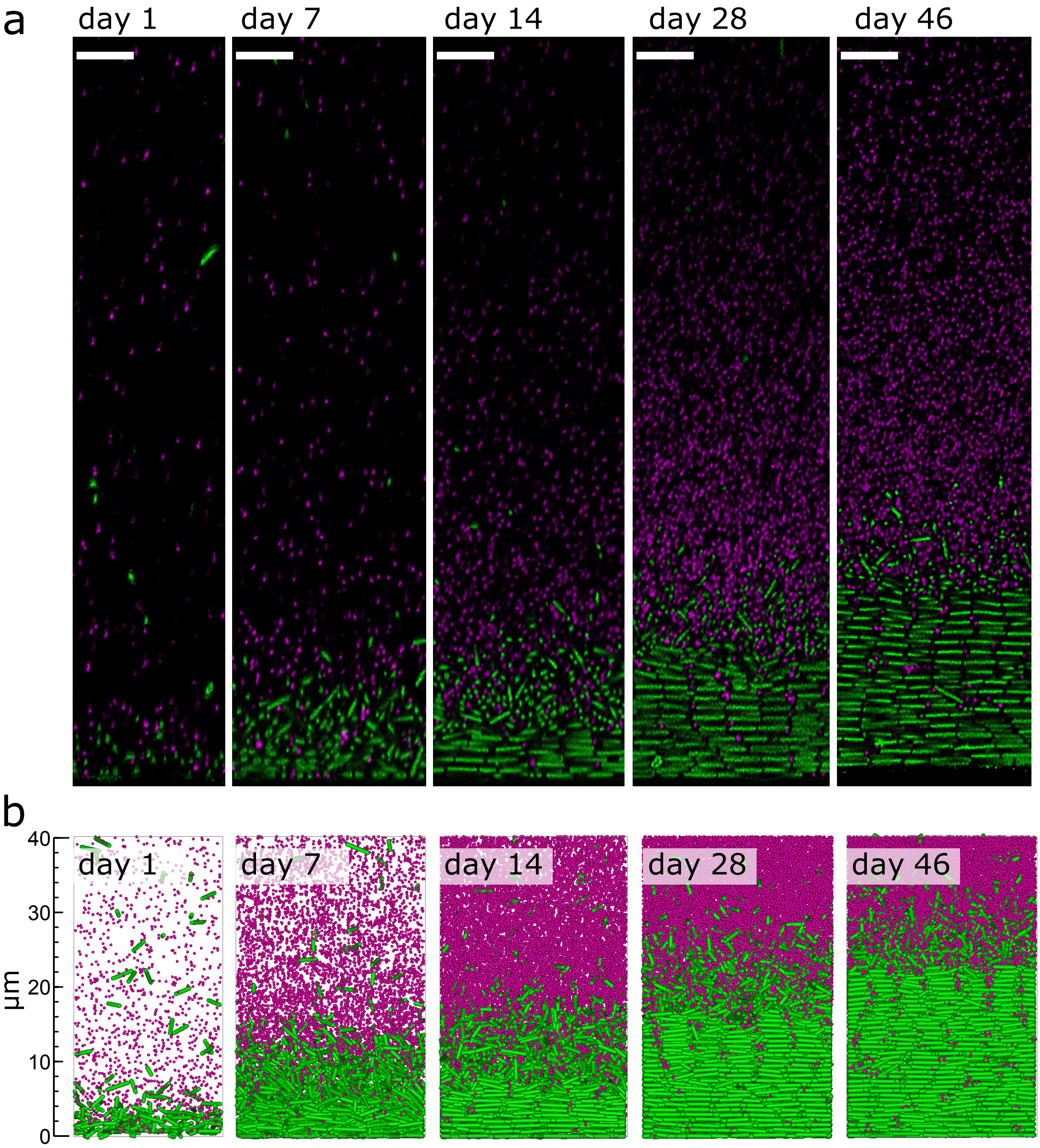

Figure 4.1 **(a)** Deconvolved confocal images of the sediment after 1, 7, 14, 28 and 46 days. The images show a 98 µm high side view of the sample, the xz-plane. The shown height is only part of the total sediment height (total sediment height $\sim$ 120 µm, total sample height $\sim$ 6 mm). The initial dispersion was homogeneously mixed and contained 0.3 vol% particles of which 0.1 vol% spheres and 0.2 vol% rods, scale bars 7.5 µm. **(b)** Computer drawn images after particle fitting of the sample sediment, after 1, 7, 14, 28 and 46 days. The images show a side view of the sample, the xz-plane. The height of all shown computer reconstructions is 40 µm.

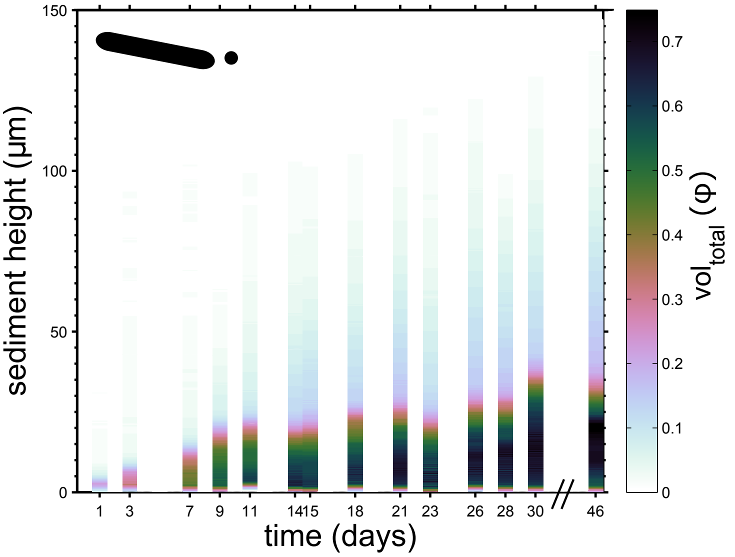

Figure 4.2 2D color-map plot of the change in total volume fraction, of both rods and spheres, in sediment height as function of time. The graph shows that there was a slow increase of the sediment height over time and that the sediment also became more compact over time.

increased particle concentration in a closed container is known to slow down the sedimentation velocity [227, 232, 253]. Although the sediment did not continue to grow in height after 30 days, the sediment morphology still changed between days 30 and 46: The top layer of mainly spheres became more concentrated, the Sm$_2$-phase became more compact and more spheres diffused into the Sm$_2$-phase. This was seen in Fig. 4.4, which shows the composition $x_{sph} = N_{sph}/N_{tot}$, with N_{sph} being the number of spheres and N_{tot} the number of spheres and rods. Moreover, together with Figs. 4.1 and 4.5b, the graph shows that there were always spheres present inside the Sm$_2$-phase, but less nearer the bottom where the pressure is higher.

Not only the sedimentation profile changed over time, also the local structure of the sample changed over time. The sample morphology changed from a completely isotropic phase towards a Sm$_2$-phase on the bottom of the sample cell. These structural changes were quantified by the determination of the local nematic order parameter (S_i) and a local smectic order parameter (τ_i). More background and rationale for the local order parameters S_i and τ_i can be found in Appendix 3.B. The change of the averaged local nematic order parameter $\langle S_i \rangle$ and the averaged local smectic order parameter $\langle \tau_i \rangle$ over time inside the sample is depicted in Fig. 4.5. Previously, In Appendix 3.C we argued that we chose to designate the system as isotropic (I) if $\langle S_i \rangle < 0.5$ and $\langle \tau_i \rangle < 0.35$, nematic (N) if $\langle S_i \rangle > 0.5$ and $\langle \tau_i \rangle < 0.35$ and Sm$_2$ if $\langle S_i \rangle > 0.5$ and $\langle \tau_i \rangle > 0.35$. These values are close to the inflection point when the averaged local order parameters, $\langle S_i \rangle$ and $\langle \tau_i \rangle$, are plotted as a function of reduced pressure (βPD^3), see Fig. 4.6. The horizontal dashed and solid lines in Figs. 4.5a-b show the interface between I-N and N-Sm$_2$ respectively, where $\langle S_i \rangle = 0.5$ and $\langle \tau_i \rangle = 0.35$. These graphs show that when the rods settled down, and became more compact, first alignment occurred and a nematic phase formed at day 7. On day 9 it had transformed into a Sm$_2$ phase, that grew in height and carried a thin

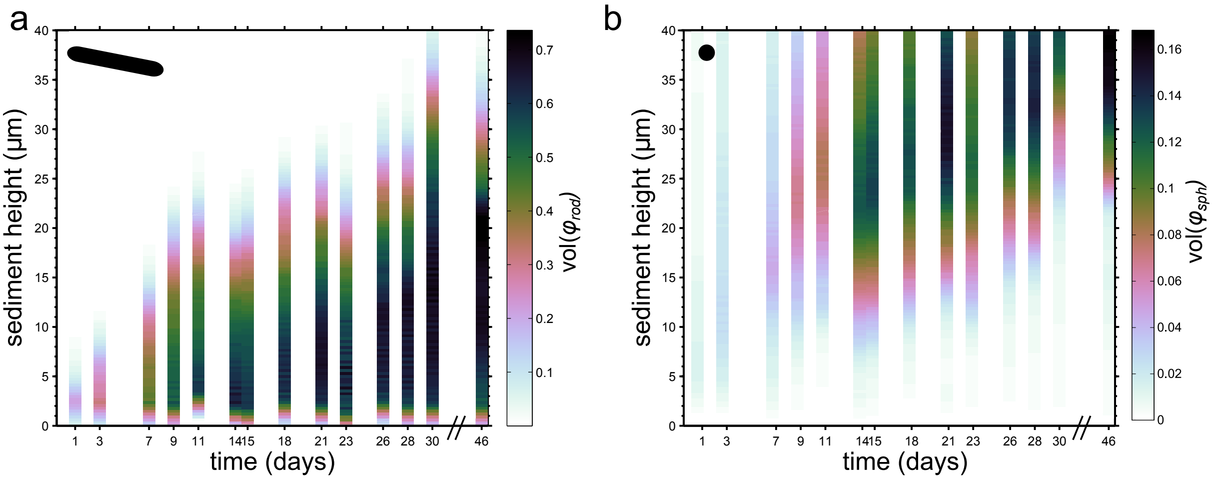

Figure 4.3 2D color-map plots of the change in volume fraction of rods **(a)** or spheres **(b)** in sediment height as function of sedimentation time. The graph depicts that first a sediment of mainly rods formed at the bottom. Only later, a sediment of spheres forms on top of the rods. The height of the rod sediment still grew over time, albeit slower. Because, the rods have to diffuse through a higher volume fraction of spheres.

nematic layer on top. After day 9, the average value of $\langle \tau_i \rangle$ in the sediment still increased, indicating that the sediment became more ordered.

At day 46 the equilibrated height of the nematic phase was $\Delta z = 0.29\,\mu\text{m}$. This is the same height as the bin size used in analysis ($\Delta z = 0.29\,\mu\text{m} = 0.5\,D$), and therefore not significant. In contrast, for a sediment of only R2 rods in SDE we found a nematic height of $\Delta z = 1.5\,\mu\text{m}$. This value is significantly higher and in agreement with literature [37, 57]. We calculated the height of the expected nematic phase of a sediment of only rods, using pressures and densities at the I-N and N-Sm transitions from literature for rods with end-to-end $(L/D)_{eff} = 5.2$ and $l_g = 0.64\,\mu\text{m}$ (with L/D close to the L/D of R2 rods), and we obtained an expected height of $\Delta z = 1.3\,\mu\text{m}$ [37, 57]. The fact that in the equilibrated mixture no nematic phase was observed is also in line with the phase diagram obtained from Monte Carlo simulations of a binary mixture of rods and spheres with the same size, see ref. [218] and Chapter 3. In this sediment the I-(N)-Sm transition took place at $x_{sph} = 0.67$ and therefore a nematic phase in the equilibrated sediment was not expected. Interestingly, however, before the sediment reached SDE a thin nematic layer was always present on top of the Sm_2-phase ($\Delta z = 0.59$–$1.2\,\mu\text{m}$) between days 14–30. This indicates that the formation of the Sm_2-phase went via a nematic phase.

To get an idea about the local change in structure over time, and follow nucleation and growth processes, we applied a cluster criterion similar to that in refs. [235, 236]. The cluster criterion tells whether a rod is part of the same nematic or smectic domain.

Three criteria were used to determine whether a rod is part of the same cluster. First, for a nematic phase the rods should have $S_i > 0.5$. Second, rods in the same domain should be within a certain cut-off surface-to-surface distance $\rho_{ij} < 1D$. Third, the relative orientation between rods within the same domain should be such that $\hat{u}_i \cdot \hat{u}_j > 0.66$ ($S_{ij} > 0.5$). For rods to be in a smectic domain, the threshold values were $\tau_i > 0.35$, surface-to-surface distance $\rho_{ij} < 0.25\,D$ and orientation between rods in the same domain

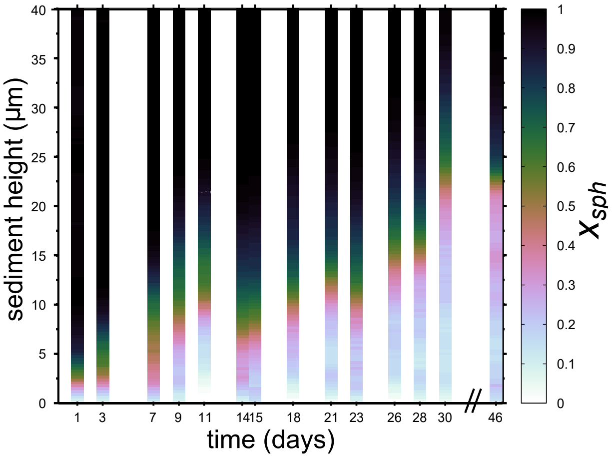

Figure 4.4 2D color-map plot of the change of the composition of spheres in sediment height, as function of sediment time. Comparing this graph with Figs. 4.3a-b, it is clear that inside the smectic rod phase still quite some spheres are present. Over time more spheres diffused inside the binary smectic phase coming from the top layer.

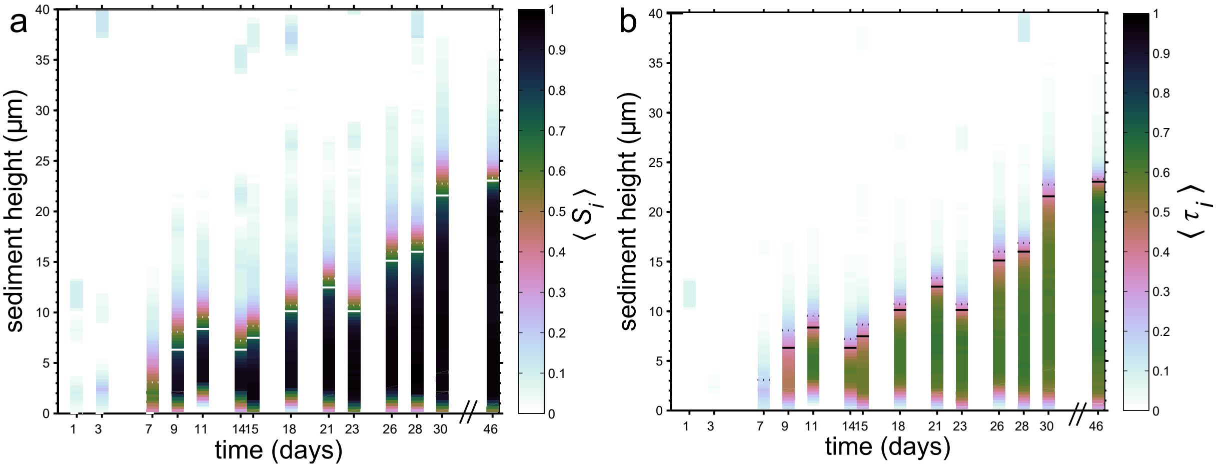

Figure 4.5 2D color-map plots **(a)** of the averaged local nematic order parameter $\langle S_i \rangle$ and **(b)** the averaged local smectic order parameter $\langle \tau_i \rangle$ over time as function of sediment height. It shows that before a binary smectic phase can form, rods align into a nematic phase and alignment starts from the bottom wall. The dashed lines indicate the height below which $\langle S_i \rangle > 0.5$, the solid lines indicates the height below which $\langle \tau_i \rangle > 0.35$.

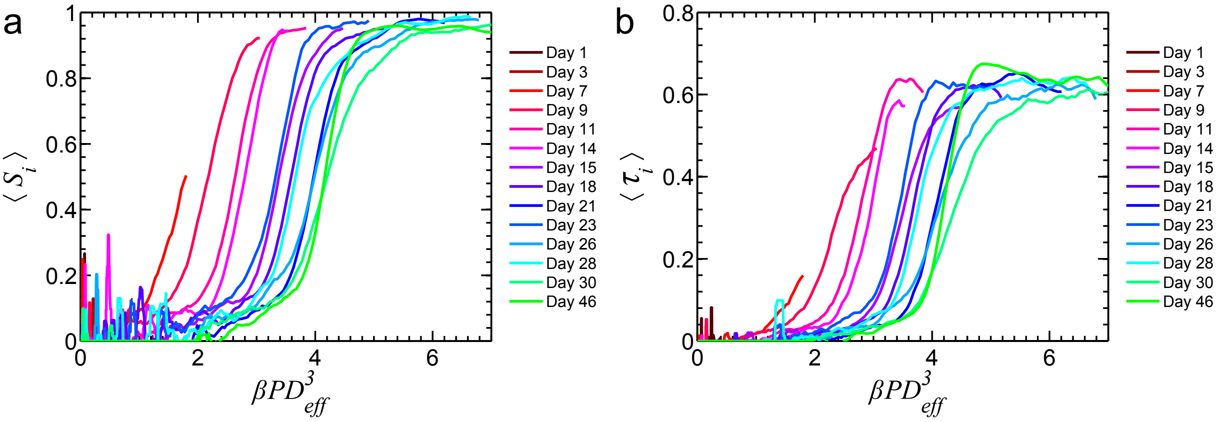

Figure 4.6 Line plots of **(a)** the averaged local nematic order parameter $\langle S_i \rangle$ and **(b)** the averaged local smectic order parameter $\langle \tau_i \rangle$ as function of reduced pressure $\beta P D^3_{eff}$.

$\hat{u}_i \cdot \hat{u}_j > 0.98$. This last value was chosen such to better distinguish smectic domains with different orientations. Note, that orientation values and the surface-to-surface threshold values are somewhat arbitrary. Moreover, in the definition of the nematic domain, the fact that rods can also be smectic if $S_i > 0.5$ was ignored (smectic: $S_i > 0.5$ and $\tau_i > 0.35$; nematic: $S_i > 0.5$ and $\tau_i < 0.35$). This was done because not all particles that were smectic, were also part of a smectic domain. However, these particles could be part of an aligned domain. Ignoring these particles and only considering purely nematic particles for a nematic domain gave a skewed impression, as then only small nematic domains were observed.

Fig. 4.7 shows computer drawn images from the first 15 µm of the sediment over time. In the first column, the images show the fitted rods and spheres colored respectively green and red. The second column shows in dark shades the rods that are part of a nematic domain, including the smectic rods. Rods are colored according to their domain. Particles, rods and spheres, that are not part of a nematic domain are shown in light shaded transparent blue. In the fourth column smectic domains are depicted in the same manner. In between the nematic domains and smectic domains, the third column shows the rods that are part of an aligned domain, but not of a smectic domain.

From Fig. 4.7 it can clearly be observed that alignment started at the bottom of the sediment and we observed heterogeneous nucleation of the nematic phase close to the wall. This is expected as the initial particle concentration was below the particle concentration needed for a nematic or smectic phase to form [231–233].

Some small nematic pairs were observed inside the isotropic phase, above the large nematic domain at the bottom, but these nematic pairs did not grow larger over time. This seems to be an artifact of the cluster criterion and was also observed earlier [235–237]. By day 7 a single domain nematic layer had formed. Next, we observed that the Sm_2-phase nucleated homogeneously from the aligned phase. The formation of the Sm_2-phase did not start at the wall, but in several places inside the aligned nematic phase around day 7. These relatively small domains grew in size and slowly ‘ate’ away the nematic phase. Over time the smectic domains annealed into one larger domain. On top of the

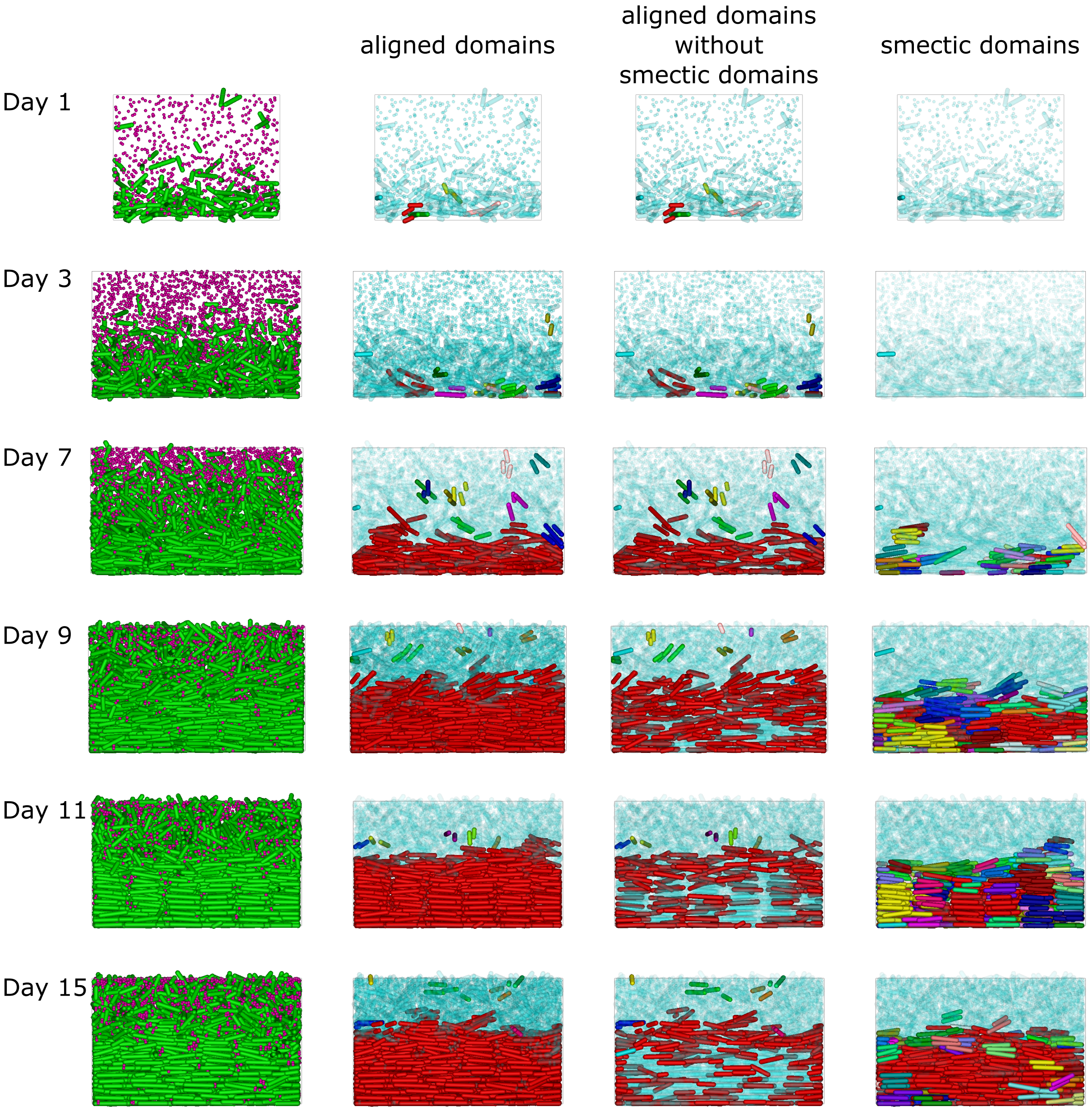

Figure 4.7 Computer drawn images after particle fitting of the bottom part of the sediment, xz-view, the first 15 µm of the sediment are shown. In the first column the rods and spheres are colored green and red, respectively. The second column shows in solid the rods that are part of a nematic domain, including the smectic rods. For a rod to be part of a nematic domain $S_i > 0.5$, $\hat{u}_i \cdot \hat{u}_j > 0.66$ and $\rho_{ij} < 1D$. The different colors indicate the different domains; rods with the same color are part of the same domain. Particles, rods and spheres, that are not part of a nematic domain are shown transparent blue. In the fourth column the smectic domains are depicted in the same manner. For a rod to be part of a smectic domain $S_i > 0.5$, $\tau_i > 0.35$, $\hat{u}_i \cdot \hat{u}_j > 0.98$ and $\rho_{ij} < 0.25D$. In between the nematic domains and smectic domains, the third column shows the rods that are part of an aligned domain, but not of a smectic domain.

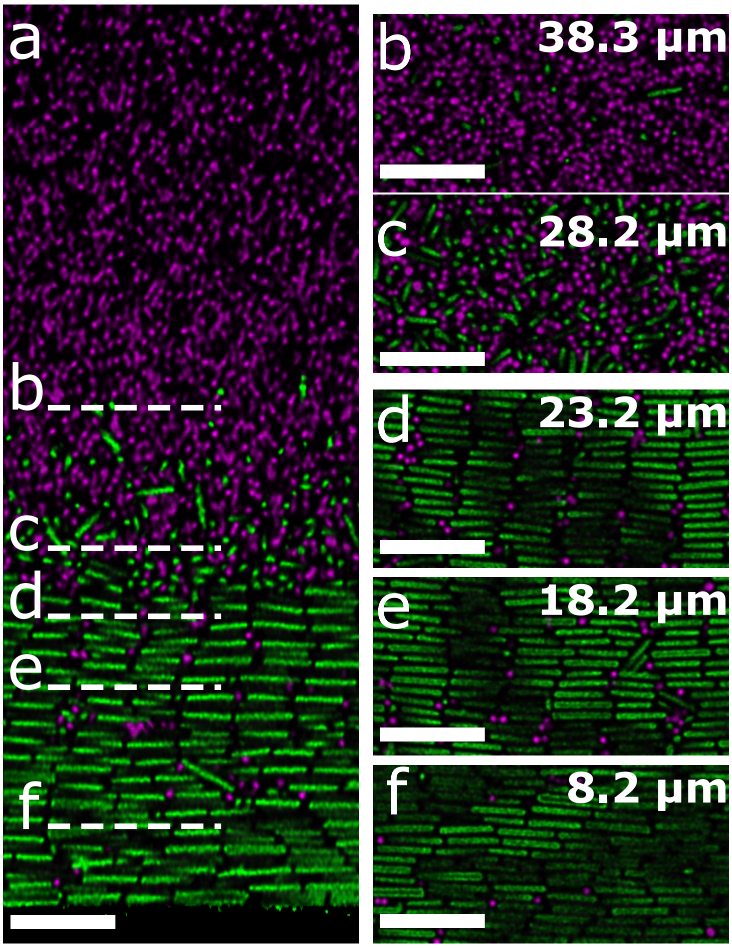

Figure 4.8 Deconvolved image of the sediment after 46 days, with **(a)** the side xz-view and **(b-f)** xy-images at different heights in the sediment. Scale bars 7.5 µm and height **(a)** 67.5 µm. The corresponding movies shown on page 77 were taken at these heights.

smectic phase a thin nematic domain remained present over time, as also became clear from the analysis of $\langle S_i \rangle$ and $\langle \tau_i \rangle$, see Fig. 4.5.

To check whether the phases observed were still dynamic and not kinetically arrested, we made xyt-movies at different heights in the sediment on day 46 (see Supporting Movies on page 77, for the heights at which the movies were recorded see Fig. 4.8). The time between subsequent frames was $\Delta t = 84\,\mathrm{s}$, over a total of 20 frames. The total sediment height was 148.2 µm, the height shown here is 67.5 µm. The movies show that at heights where mainly spheres were present ($z = 38.3\,\mu\mathrm{m}$ and $z = 28.2\,\mu\mathrm{m}$) the system was very dynamic. Lower in the sample at $z = 23.2\,\mu\mathrm{m}$ diffusion in the Sm$_2$-phase was less apparent, but the rods and spheres were still dynamic. Going deeper into the sediment the movement of the rods slowed down ($z = 8.2\,\mu\mathrm{m}$ and 18.2 µm, Figs. 4.8e-f), but the small spheres were still quite mobile. The dynamics in the sediment indicate that the Sm$_2$-phase in the sediment is sufficiently dynamic to reach equilibrium and there is no kinetic arrest even at this last stage of compaction.

4.4.2 Sedimentation of Colloidal Rod-Sphere Mixtures, with Sphere Diameter Larger than the Rod Diameter

For comparison, we also studied the sedimentation of a binary rod-sphere mixture, with sphere diameter $\sigma > D$ and $\sigma < L$, that did not form a Sm_2-phase in experiment. In this case small bundles of rods were formed over time inside the sediment instead, see Fig. 4.9. The bundles consisted of parallel rods as in a single smectic layer. They did not stack, however, into a smectic phase. The rods appear to be ordered hexagonally within the bundles. We investigated the formation and dynamics of these bundles over time. To do so, the sample was imaged at different times over a period of five weeks after the sample had been prepared. Within this time the sample reached sedimentation-diffusion equilibrium (SDE). Figs. 4.9a-b show the sediment after 1, 7, 14, 21 and 110 days after the sample was prepared. It shows that the rods and spheres settled down with on average the same speed, and no segregation was visible between rods and spheres, as was the case with the smaller spheres. This is also expected, as the sedimentation velocities v_{sed} of the rods, $v_{sed} = 6.7\,\mathrm{nm\,s^{-1}}$, and spheres, $v_{sed} = 5.2\,\mathrm{nm\,s^{-1}}$, were very similar in magnitude, as were the gravitational heights l_g for the rods ($l_g = 0.64\,\mu\mathrm{m}$) and the large spheres ($l_g = 1.25\,\mu\mathrm{m}$) and their Péclet numbers ($Pe_{R2} = 0.46$, $Pe_{D930} = 0.37$).

Moreover, it can be seen that at day 1, all the particles were mixed homogeneously and a sediment began to form at the bottom. After a week, a denser sediment had formed on the bottom of the sample. Inside the denser sediment the particles were no longer homogeneously distributed, but the rods had clustered together into bundles, especially near the bottom, with a dense fluid of spheres and rods in between.

After 21 days the sediment did not grow further in height, see Fig. 4.9. Thus, most particles had settled down and the sample reached SDE. On top of the dense part of the sediment containing the bundles, $60\,\mu\mathrm{m} < z < 80\,\mu\mathrm{m}$, an isotropic region was present, where no bundles were formed. The height of this isotropic region did not change over time, indicating that this height is needed to obtain enough pressure for the dense bundle phase to form underneath.

To get a more detailed view on the sample, we plotted some of the characteristic properties of the system in color-maps, Figs. 4.10-4.12, as described in the previous Section 4.4.1. Fig. 4.10 depicts a color-map of the total volume fraction (ϕ) as function of sediment height and time. The color-maps show that there was a steady increase of the sediment height from day 1 until day 21. The total volume fraction of the dense part of the system was $\phi \sim 0.6$.

From the striped patterns of the color-maps of the volume fraction of rods (ϕ_{rod}), Fig. 4.11a, and spheres (ϕ_{sph}), Fig. 4.11b, it can be seen that the rods and spheres were distributed heterogeneously throughout the dense sediment. The stripy pattern in these color-maps is caused by the bundles of rods, which had a cross section similar in size to the xy-cross section of the sampled volume. On a larger scale the composition was nearly uniform throughout the sediment. In total 60% of the total particle volume in the dense sediment were spheres, which comes down to the same ratio of rods and spheres as in the initial dispersion. Thus, not much segregation in height between rods and spheres occurred in the sample, in contrast to the sample with small spheres and rods.

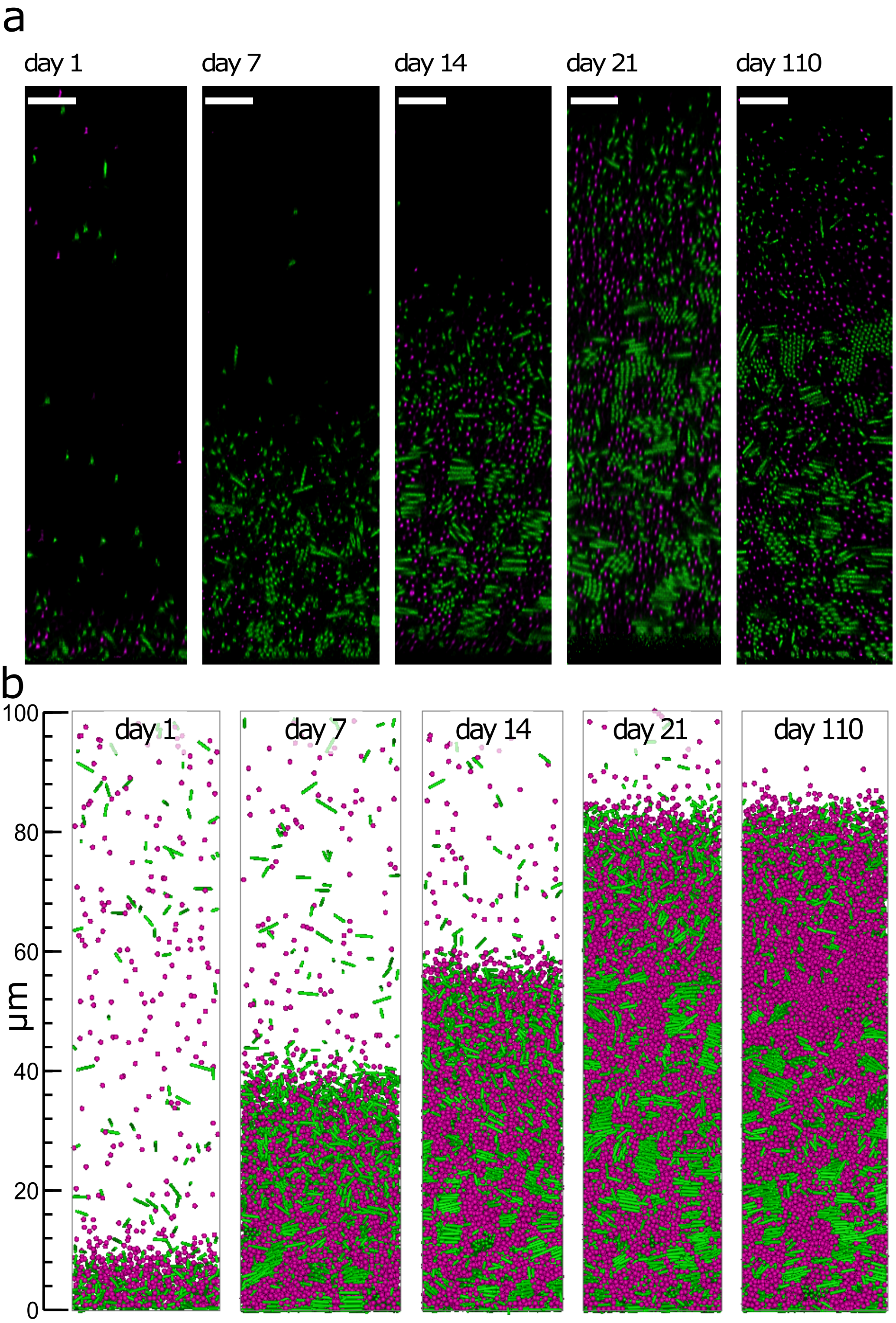

Figure 4.9 Side view of the sediment after 1, 7, 14, 21 and 110 days. The initial dispersion was homogeneously mixed and contained 0.5 vol% particles: 0.3 vol% spheres and 0.2 vol% rods. The initial dispersion height in the sample cell was 6 mm. **(a)** Deconvolved confocal xz-images, height of all confocal images shown is 92 µm. **(b)** Computer drawn images after particle fitting of the sample sediment. The height of all shown computer reconstructions is 100 µm.

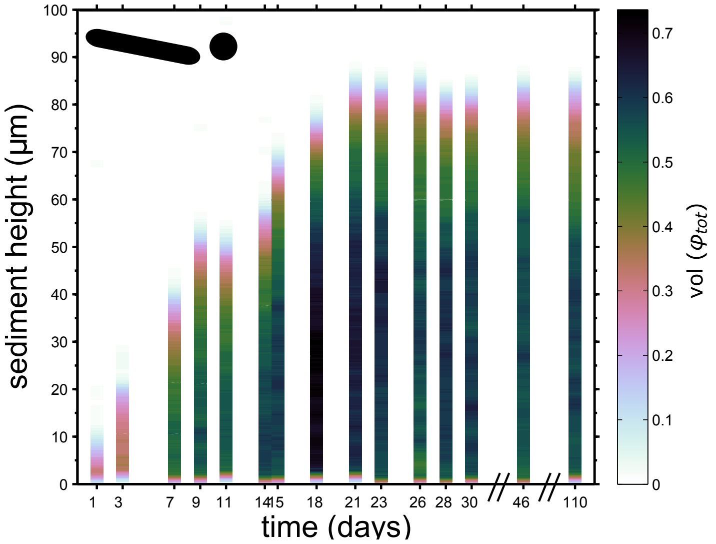

Figure 4.10 2D color-map plot of the change in total volume fraction, of both rods and spheres, in sediment height as function of time.

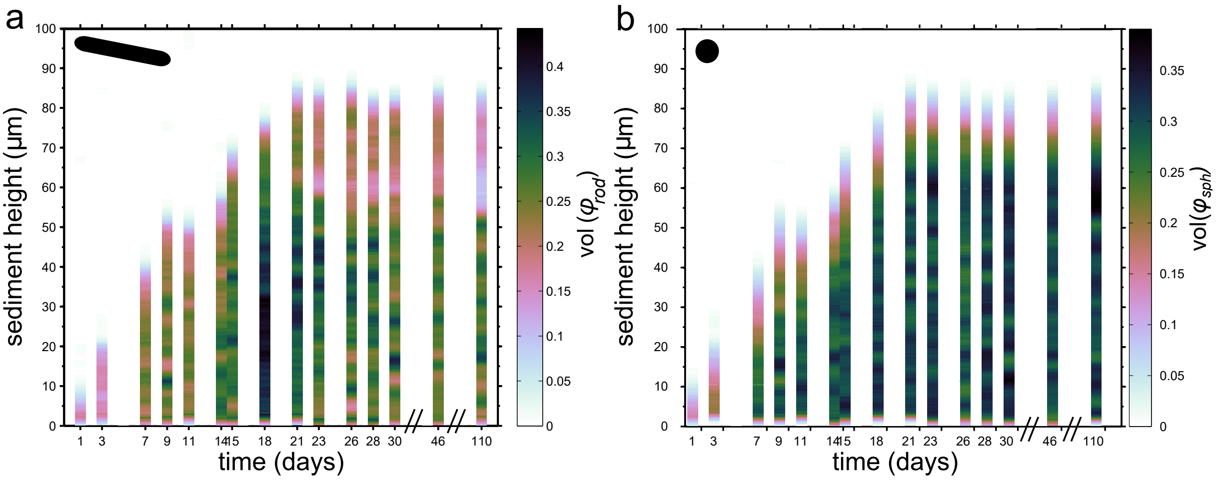

Figure 4.11 2D color-map plot of the change in volume fraction of **(a)** rods or **(b)** spheres in sediment height as function of time.

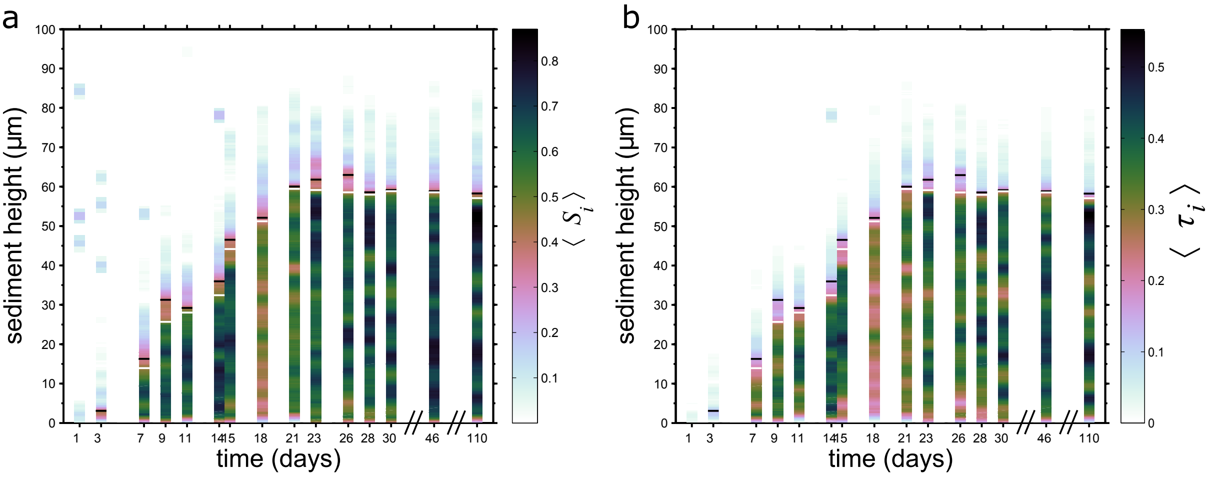

Figure 4.12 2D color-map plots of **(a)** the averaged local nematic order parameter $\langle S_i \rangle$ and **(b)** the averaged local smectic order parameter $\langle \tau_i \rangle$ versus height as function of time. The horizontal black lines indicate the height below which $\langle S_i \rangle > 0.35$, the horizontal white lines indicate the height below which $\langle \tau_i \rangle > 0.2$.

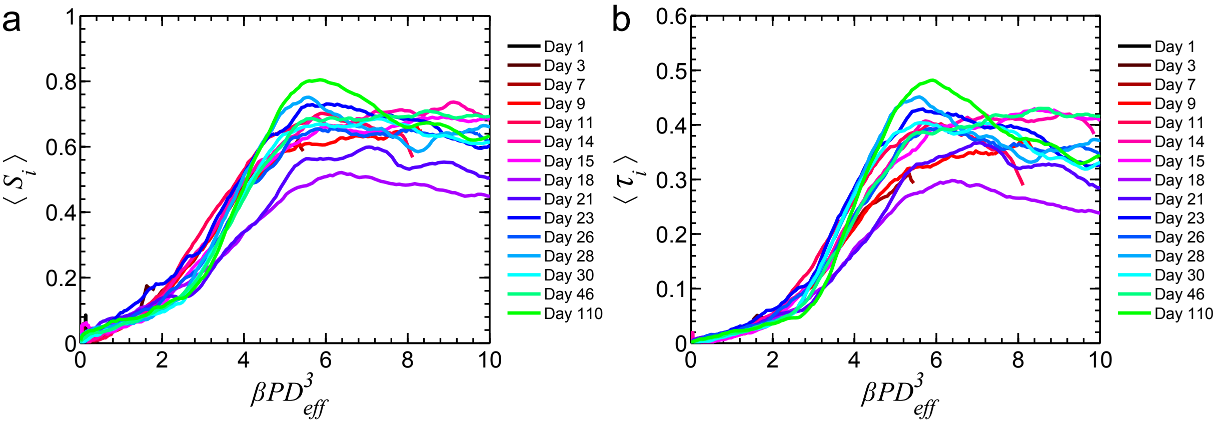

Figure 4.13 Line plots of **(a)** the averaged local nematic order parameter $\langle S_i \rangle$ and **(b)** the averaged local smectic order parameter $\langle \tau_i \rangle$ as function of reduced pressure $\beta P D^3_{eff}$. Data shown here, was smoothed with a top-hat function of 20 D width, because averaging with a top-hat function of 5 D width shows large fluctuation due to the granularity of the bundles formed. Figure A.4.2 in Appendix 4.A shows the data smoothed with the usual top-hat function of 5 D width.

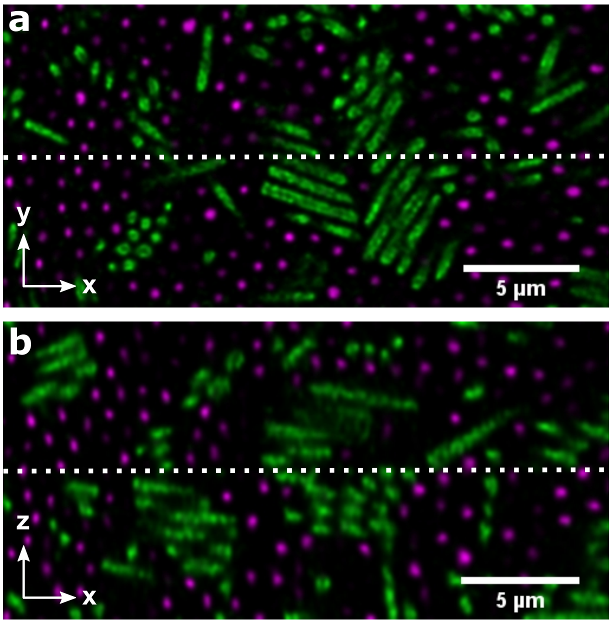

Figure 4.14 Deconvolved confocal microscopy images of the sediment on day 110 **(a)** at $z = 29.4\,\mu\mathrm{m}$ showing some hexagonally ordered spheres on the left side of the images. The dotted line in **(a)** indicates were the xz-view of **(b)** was taken, showing that the ordered patches of spheres only persisted for a few layers.

To measure the degree of structural organization inside the sediment, we calculated the local nematic and smectic order parameters for every rod detected inside the sample volume. The averaged local nematic order parameter $\langle S_i \rangle$ as a function of time is depicted in Fig. 4.12a. Inside the dense sediment $\langle S_i \rangle \sim 0.7$. Alignment was already visible from day 3 onwards. The average local smectic order parameter $\langle \tau_i \rangle$ is depicted in Fig. 4.12b. Inside the sediment $\langle \tau_i \rangle \sim 0.4$, and smectic ordering started from day 7 onwards. To determine the transition between the isotropic mixed phase and the dense bundle phase we again used the points of inflection as observed in the graphs of $\langle S_i \rangle$ and $\langle \tau_i \rangle$ as function of reduced pressure $\beta P D^3_{eff}$, see Fig. 4.13. Therefore, threshold values of $\langle S_i \rangle > 0.35$ and $\langle \tau_i \rangle > 0.2$ were used. These threshold values were lower compared to the Sm$_2$-phase, because, apart from the bundles of rods also isotropic loose rods were present in the bundled phase, lowering $\langle S_i \rangle$ and $\langle \tau_i \rangle$ significantly. The horizontal black and white solid lines in Fig. 4.12 show the interface below which $\langle S_i \rangle > 0.35$ and $\langle \tau_i \rangle > 0.2$, respectively. On day 3 already some alignment was visible, and thereafter the dense bundle phase had formed. On day 110 the height between the transitions $\langle S_i \rangle > 0.35$ and $\langle \tau_i \rangle > 0.2$ is $\Delta z = 1.18\,\mu\mathrm{m}$. Before day 110 this value fluctuated between $\Delta z = 0.29\,\mu\mathrm{m}$ and $\Delta z = 5.58\,\mu\mathrm{m}$. The pressure needed for the dense bundle phase to form according to the criterion $\langle \tau_i \rangle > 0.2$ is $\beta P D^3 = 3.9 \pm 0.3$. Next to bundles of rods, we also found small patches of hexagonally ordered spheres in the sediment, see Fig. 4.14. The space between the bundles was small, therefore the ordered patches remained rather small and they often were only a few layers in height. Also, single rods, in between the bundles of rods, prevented the spheres from becoming more crystalline.

To get a better idea about the change of the local structure of the sample over time, we used a cluster criterion [235, 236] to identify aligned domains and smectic clusters, as also described in Section 4.4.1, see Fig. 4.15. Rods within the same nematic domain should have $S_i > 0.35$, within a certain cut-off surface-to-surface distance $\rho_{ij} < 1D$ to rods in the same domain, and the orientation of neighboring rods should be $\hat{u}_i \cdot \hat{u}_j > 0.66$. For smectic domains we used $\tau_i > 0.2$, $\rho_{ij} < 0.25D$ and $\hat{u}_i \cdot \hat{u}_j > 0.98$.

In Fig. 4.15a rods are colored based upon their orientation, in Figs. 4.15b-c rods that are part of a nematic or smectic domain are colored in dark shades, while rods and spheres that are not part of a nematic or smectic domain are shown light shaded transparent blue.

If one looks at Fig. 4.15a, it is clear that rods, inside the dilute phase, can exhibit all orientations possible. Inside the dense phase bundles of rods, with more or less the same orientation inside the bundle, were visible. Bundles tended to orient with the rod axis parallel with the bottom of the sample cell. However, within this plane all orientations were equally possible. Also, orientations of rods were not always uniform within a bundle. Orientations of rods were seen to be slightly shifted from one end to the other end of the bundle. The planar orientation of bundles of rods indicated that the bundles nucleated heterogeneously starting from the bottom wall. Next, it can be seen that between the bundles of rods, quite some loose rods were visible that are mixed with the spheres. These rods did not end up in bundles over time. In total 20–28% of all the rods present in the dense sediment had a low value of S_i and therefore were not part of a bundle. An exception were day 18 and 21, at these days the percentage of rods with a low value of S_i was considerably higher 40% and 31%, respectively. The reason for this is unknown. However, it also affected the observed value of $\langle S_i \rangle$ and $\langle \tau_i \rangle$ inside the dense sediment, see Fig. 4.12.

From Fig. 4.15b it can be observed that bundles of particles with similar orientation only form when the sediment is thick enough, from day 3 onwards. After the bundles had formed and the sediment grew in height, not much structural change can be observed over time. Some of the nematic domains became quite large and contained many bundles. Comparison with Fig. 4.15c shows that these bundles show smectic character, and are connected together by similarly oriented rods that are not part of a smectic domain.

We calculated the number and size of the average nematic and smectic domain over time inside the sediment, see Fig. 4.16. The average nematic domain size, which also included the smectic domains, grew only in size until day 9 and remained roughly constant thereafter. The average smectic domain size grew from around 3 to around 8 rods until day 46, while the height of the sediment remained constant after day 21. This indicates, although it was a small increase and it was not clearly visible by eye, that rods inside the bundles got more aligned over time. That the average domain size grew can also be observed from the fact that the number of smectic domains decreased after day 21, while at the same time we observed that the number of aligned rods inside the dense sediment remained the same. Thus, small structural changes still occurred in the sample after day 21, albeit slowly.

To see how dynamic these phases still were, we made *xyt*-movies at different heights inside the sediment at day 110 (see Supporting Movies on page 77, for heights at which the movies were recorded, see Fig. 4.17); the time between subsequent frames was $\Delta t = 53\,\mathrm{s}$. The movies show that in the more dilute region at a height of 76.7 µm (Fig. 4.17b), the

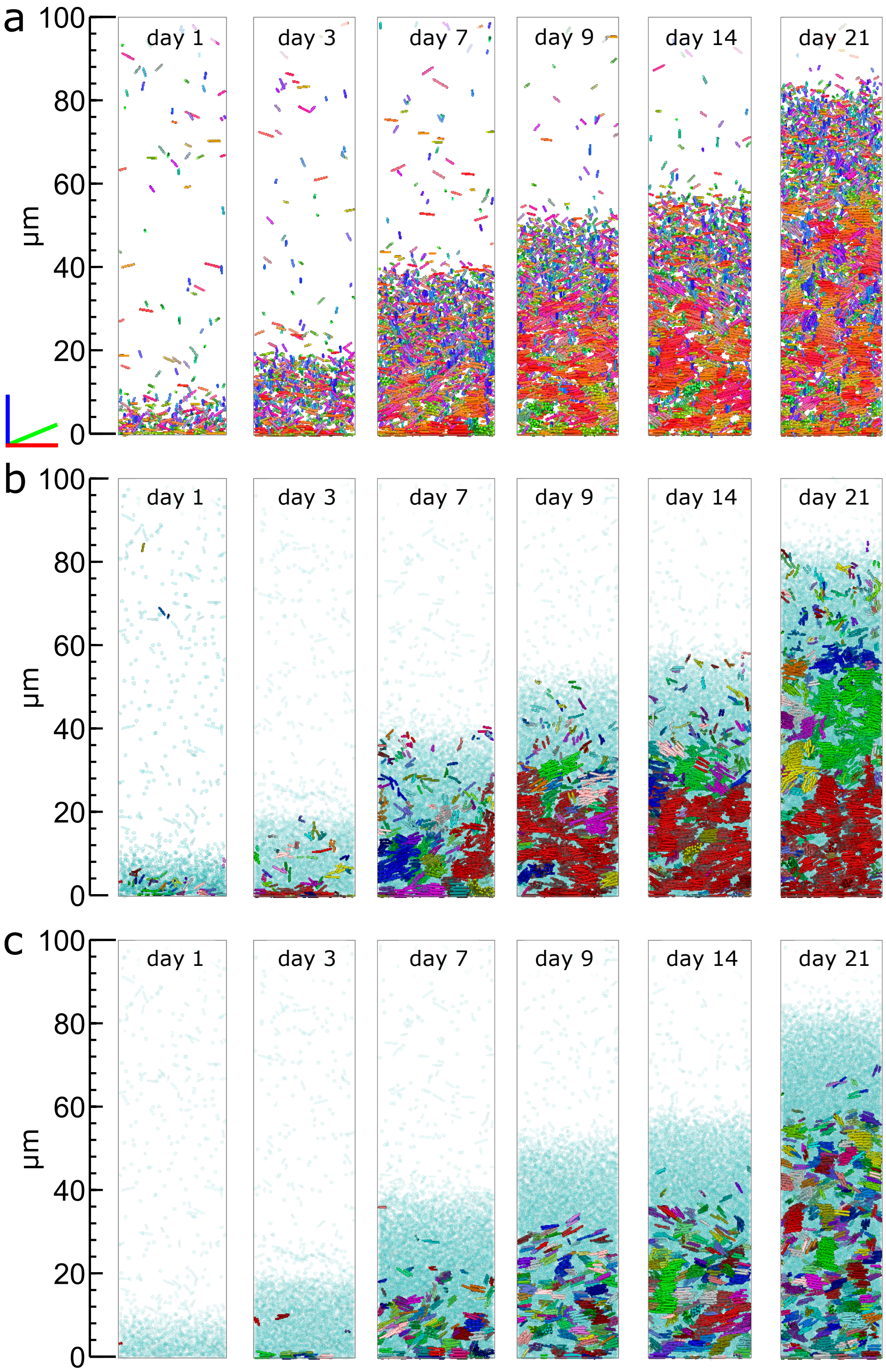

Figure 4.15 Computer drawn images after particle fitting of part of the sample sediment, showing a side view of the sample. **(a)** Only rods are shown, with a color based on their orientation. **(b)** Rods which are part of an aligned domain are shown in solid. Rods that are in an aligned domain have $S_i > 0.35$, $\hat{u}_i \cdot \hat{u}_j > 0.66$ and $\rho_{ij} < 1D$. **(c)** Rods that are part of a smectic domain are shown in solid and have $\tau_i > 0.2$, $\hat{u}_i \cdot \hat{u}_j > 0.98$ and $\rho_{ij} < 0.25\,D$. In **(b-c)** spheres and rods that are not part of a domain are shown transparent. The different colors of the rods indicate the different domains.

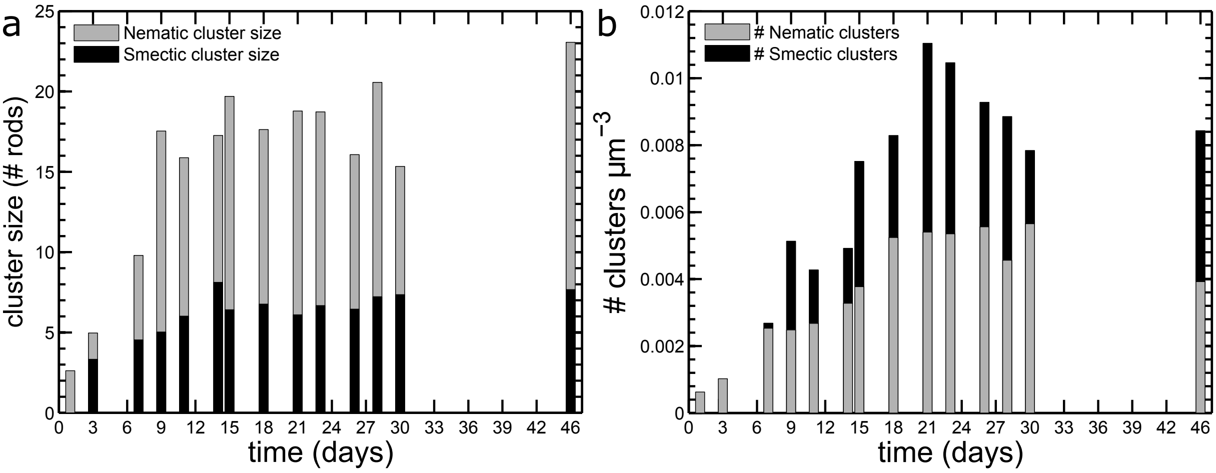

Figure 4.16 **(a)** Bar plot of the average nematic and smectic domain size over time. **(b)** Bar plot of the number of nematic and smectic domains over time.

particles were able to diffuse freely. At the interface between the region with bundles of rods and without bundles of rods, height 56.7 µm (Fig. 4.17c), there was still some movement and diffusion, but a lot less. At heights 6.7 µm, 26.7 µm and 46.7 µm the particles could not diffuse freely anymore. However, the particles still wiggle around on their positions. Going down in the sediment where the pressure is higher this wiggling movement became less. Probably, this little movement is still enough for the system to make small structural changes.

As part of the sediment was still mobile, we expected that equilibrium can be obtained. However, we still do not know what the equilibrium phase will look like. From trends in theoretical predictions [201], we speculated that we did not expect the Sm_2-phase to form for this size-ratio and composition. Rather, we expected phase phase coexistence, between a normal smectic phase and a miscible liquid. Unfortunately, at this moment in time, the full phase diagram for mixtures of spheres and rods with this size ratio is not known. Therefore, we can only speculate what the expected equilibrium phases are for a SDE with this particular size ratio and composition of rods and spheres. And perhaps, the equilibrium structure is as seen: a strongly structured but not fully phase separated liquid mixture.

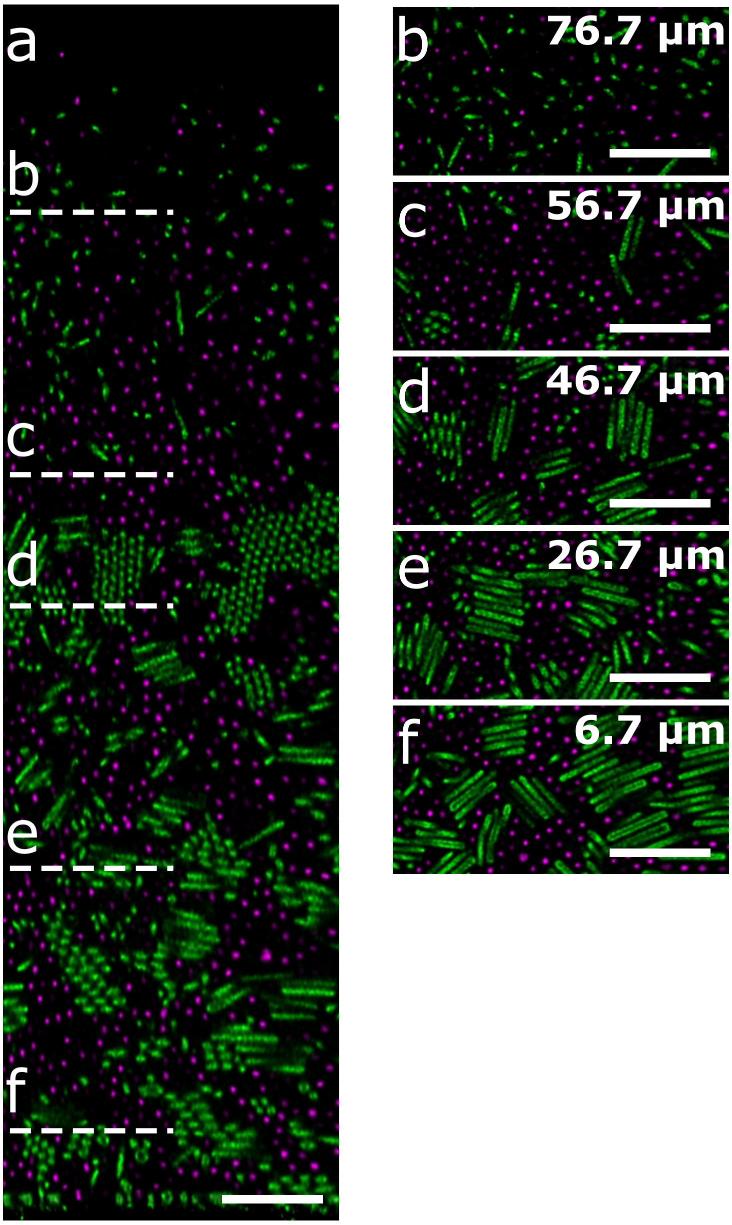

Figure 4.17 Deconvolved image of the sediment after 110 days, with **(a)** the side *xz*-view and **(b-f)** *xy*-images at different heights in the sediment. Scale bar 7.5 µm and height **(a)** 92.5 µm. The corresponding movies shown on page 77 were taken at these heights.

4.5 Conclusion

By using fluorescently labeled colloids in combination with confocal microscopy and slowing down the dynamics using a high viscosity dispersion medium of a 85 wt% glycerol-water solvent mixture ($\eta = 81\,\mathrm{mPa\,s}$ [156]), we were able to follow the sedimentation dynamics of binary rod-sphere mixtures. In addition, by using single particle identification algorithms we determined the local architecture of the samples during sedimentation on the single particle level. Next, by using local nematic and smectic order parameters and employing a cluster criterion [235, 236], we were able to follow the nucleation and growth of both the Sm_2-phase, in the case of $\sigma < D$, and the dense bundle phase, in the case of $\sigma > D$. In the case of rods and small spheres ($\sigma = 0.66\,D$), due to differences in l_g and v_{sed}, we observed an interesting interplay between the sedimentation of rods and sedimentation of spheres. We showed that first a nematic phase nucleated heterogeneously from the bottom wall. At different places inside the nematic phase a smectic phase nucleated homogeneously, of which the smectic nuclei were already aligned by the nematic phase. Then these domains grew into a single-domain binary smectic (Sm_2) phase. The formation of the smectic nuclei inside a nematic phase is similar to what was observed earlier for nickel dimethylglyoxime rods with L/D in the range 10–35 [58]. However, it is different from the random orientation of smectic nuclei observed in experiments and simulations for spherocylinders with relatively low L/D [58, 226, 235–237], where there is an I-Sm transition, as in our case the smectic nuclei already get aligned by the nematic phase. As more spheres accumulated on top of the Sm_2-phase, the Sm_2-phase became more compact and more spheres diffused into the interlayer space. We found that inside the Sm_2-phase, spheres were still mobile. Therefore, the phase was quite dynamic, showing every character of an equilibrium phase. We compared the sedimentation dynamics with a binary mixture of rods and spheres, with $\sigma = 1.58\,D$, that did not form a Sm_2-phase nor a nematic phase. With the initial conditions used here, this binary-rod sphere mixture did not form a Sm_2-phase in experiment. From trends in theoretical predictions found in literature [201], we did not expect to observe a Sm_2-phase for this size-ratio and composition. However, it is still not certain as the full phase diagram for this size-ratio is not known. Also, in this case v_{sed} and l_g of the rods and spheres were similar and segregation by sedimentation did not occur. Inside the dense isotropic sediment we found many bundles of rods arranged as in a smectic layer in combination with small crystalline patches of spheres and ‘loose’ rods and spheres. Although, at first sight, the system was kinetically trapped, the bundles of rods slowly became more aligned and still grew in size with passing time. The dynamics were rather slow and it is possible that this prevented the formation of a more ordered smectic phase. This in agreement with simulations of mixtures of polymer and rods of similar aspect ratio which have shown that only single crystalline layers nucleate from an isotropic phase and these grow only laterally [237]. Formation of the smectic phase took place by top-bottom coalescence. Such a scenario has also been observed in experiments on one-component colloidal rods [58]. Since we do see much larger clusters of nematic-like order it is also possible that the formation of the smectic is hampered by an I-N transition, as has been suggested by simulations of shorter hard spherocylinders [235]. However, the presence of spheres in our system complicates a direct comparison and may well lead to a different equilibrium state. Not much is known about the influence of the diameter ratio σ/D on the phase behavior of rod-sphere mixtures, apart from a few papers [72, 201]. It would be interesting to further study this influence and the phase separation kinetics in these mixed systems.

4.6 Acknowledgements

I would like to thank Gülşen Heessels-Gürboğa for the synthesis of 385 nm and 930 nm RITC-labeled silica spheres. I also would like to thank Simone Dussi for helping to define a cluster criterion and providing me with the code to determine the nematic and smectic domains inside the sample.

Appendix 4

4.A Figures

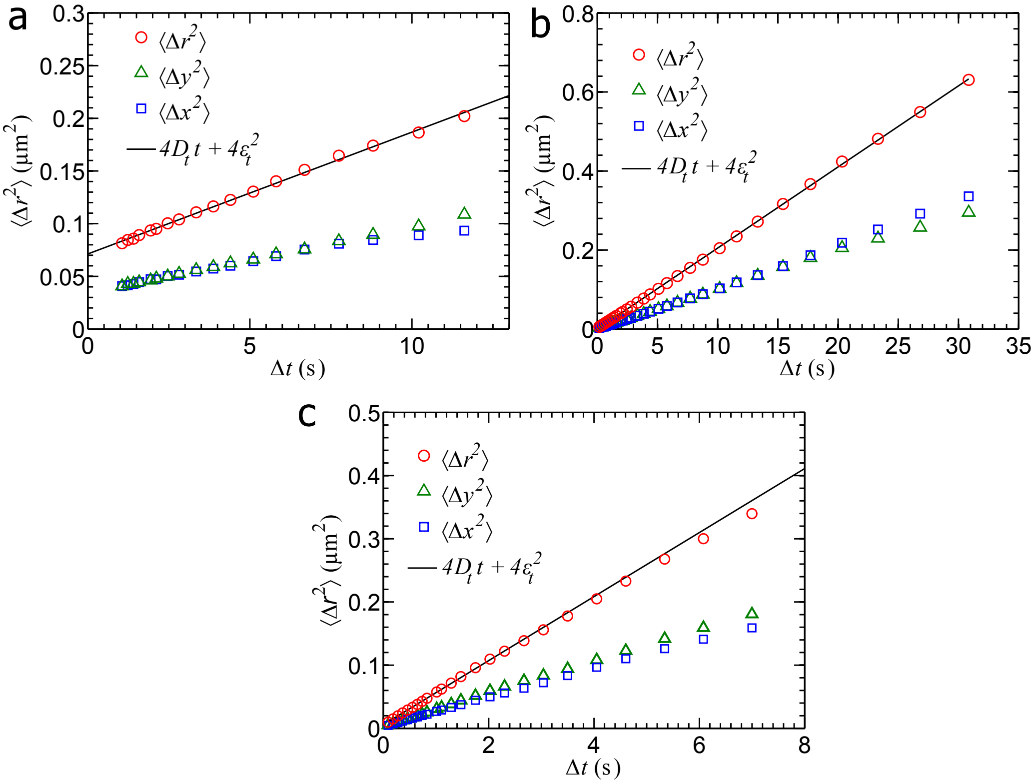

Figure A.4.1 Experimental measurements of the mean square displacement on a dilute suspension of particles. **(a)** R2 rods, $D_t = 2.9 \times 10^{-3}\,\mu\mathrm{m}^2\,\mathrm{s}^{-1}$ and $\varepsilon_t = 133\,\mathrm{nm}$. **(b)** 930 nm RITC-labeled silica spheres , $D_t = 5.1 \times 10^{-3}\,\mu\mathrm{m}^2\,\mathrm{s}^{-1}$ and $\varepsilon_t = 9\,\mathrm{nm}$. **(c)** 385 nm RITC-labeled silica spheres , $D_t = 1.3 \times 10^{-2}\,\mu\mathrm{m}^2\,\mathrm{s}^{-1}$ and $\varepsilon_t = 38\,\mathrm{nm}$.

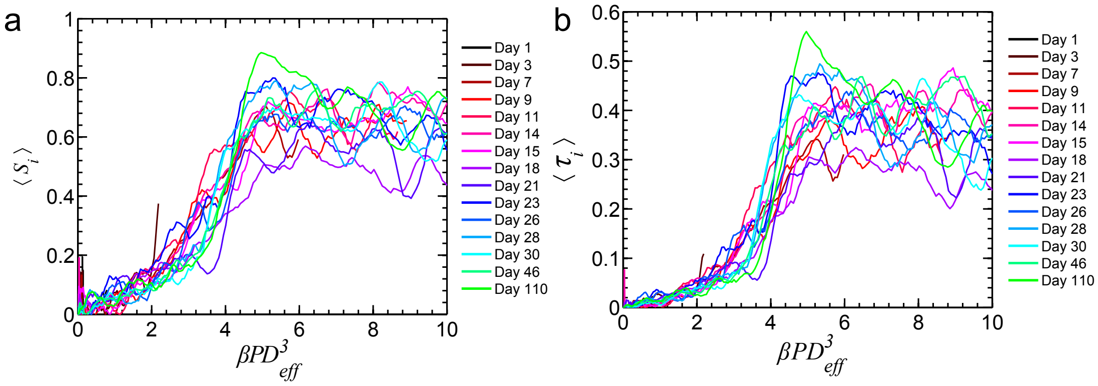

Figure A.4.2 Line plots of **(a)** the averaged local nematic order parameter $\langle S_i \rangle$ and **(b)** the averaged local smectic order parameter $\langle \tau_i \rangle$ as function of reduced pressure $\beta P D^3_{eff}$. Data, shown here, was smoothed with the usual top-hat function of 5 D width.

4.B Supporting Movies

Digital version Please click on the movie titles to get directed to the movie.

Printed version Please scan the QR code on the right to get directed to the supporting movies.

Binary smectic phase Movies of confocal microscopy time-series are shown at different heights inside the sediment on day 46, see Fig. 4.8.

Movie 4.1 Shows a *xyt*-series at height 8.2 µm in the sediment. Time between frames $\Delta t = 84\,\mathrm{s}$. Movie shown at 168× real time.

Movie 4.2 Shows a *xyt*-series at height 18.2 µm in the sediment. Time between frames $\Delta t = 84\,\mathrm{s}$. Movie shown at 168× real time.

Movie 4.3 Shows a *xyt*-series at height 23.2 µm in the sediment. Time between frames $\Delta t = 84\,\mathrm{s}$. Movie shown at 168× real time.

Movie 4.4 Shows a *xyt*-series at height 28.2 µm in the sediment. Time between frames $\Delta t = 84\,\mathrm{s}$. Movie shown at 168× real time.

Movie 4.5 Shows a *xyt*-series at height 38.2 µm in the sediment. Time between frames $\Delta t = 84\,\mathrm{s}$. Movie shown at 168× real time.

Sphere diameter larger than rod diameter Movies of confocal microscopy time-series are shown at different heights inside the sediment on day 110, see Fig. 4.17.

Movie 4.6 Shows a *xyt*-series at height 6.7 µm in the sediment. Time between frames $\Delta t = 53\,\mathrm{s}$. Movie shown at 53× real time.

Movie 4.7 Shows a *xyt*-series at height 26.7 µm in the sediment. Time between frames $\Delta t = 53\,\mathrm{s}$. Movie shown at 53× real time.

Movie 4.8 Shows a *xyt*-series at height 46.7 um in the sediment. Time between frames $\Delta t = 53\,\mathrm{s}$. Movie shown at 53× real time.

Movie 4.9 Shows a *xyt*-series at height 56.7 µm in the sediment. Time between frames $\Delta t = 53\,\mathrm{s}$. Movie shown at 53× real time.

Movie 4.10 Shows a *xyt*-series at height 76.7 µm in the sediment. Time between frames $\Delta t = 53\,\mathrm{s}$. Movie shown at 53× real time.

5

Micro-electrophoresis of Silica Rods and Spheres using Confocal Microscopy

We performed micro-electrophoresis measurements on fluorescently labeled colloidal silica spheres and silica rods, using confocal microscopy. We determined the electrophoretic mobility, which for rods can be anisotropic, and the zeta-potential (ζ) of these particles. We show that, in the case where colloidal particles move uniformly in and parallel to the direction of the electric field, the measurement time can be decreased by recording an xyz-stack over the whole depth of the capillary, instead of taking xyt-series at different depths inside the capillary to obtain the parabolic flow profile, as was done in previous work from our group. The rod-like particles do not always move uniformly in the electric field, but can exhibit a velocity that depends on the angle between the long axis of the rod and the electric field. We measured the orientation dependent velocity of individual silica rods during electrophoresis as function of κa, where κ^{-1} is the double layer thickness and a the radius of the rod associated with the diameter, to determine the anisotropic electrophoretic mobility of the silica rods with different sized double layers. We measured electrophoresis of silica rods suspended in different solvents and salt concentrations and we compared these results with theoretical predictions. We show that even at relatively high κa when the Smoluchowski limiting law is assumed to be valid ($\kappa a > 10$), an orientation dependent velocity was found. Furthermore, we observed that at decreasing values of κa the anisotropy in the electrophoretic mobility of the rods increases. However, in low polar solvents with $\kappa a < 1$ this trend was reversed: the anisotropy in the electrophoretic mobility of the rods decreased. We argue that this decrease is due to the fact that end effects start to play a role, which was already predicted theoretically [254]. If end effects are not taken into account, this will lead to strong underestimation of the experimentally determined zeta-potential.

5.1 Introduction

Charged particle dispersions, with particles ranging from the nano- to micrometer range, are present in every day life. One could think of small DNA strands, proteins, *fd*-virus, micelles or charged colloids, such as present in e-ink and printer toners. Their surface potential is an important parameter to characterize their stability and interactions. The always present van der Waals forces are attractive if the particles are identical [227]. In case there are no polymers present on the particle surface that can provide so-called steric stabilization [255], most colloidal particles rely on stabilizing repulsive forces that are caused by repulsions caused by excess charges present on/in the particles. Therefore, measuring electrophoretic mobilities of charged particles is of importance for fundamental studies in a broad range of fields [256–263], in biophysics [264–267], but also in more applied work in industry [73, 268–271].

There are much less papers in which the electrophoretic motion of rod-like particles are evaluated experimentally in solution than for spheres, and most of the published work is from the field of biophysics using anisotropic biomolecules or particles. At relatively thin double layers, $\kappa a \gg 10$, where κ^{-1} is the double layer thickness and a is the radius of the rods diameter, it is well-known that the electrophoretic mobility of a particle does not depend on its shape and it does not rotate [272]. For moderate double layer thickness, Henry predicted in 1931 that the electrophoretic mobility of infinitely long spherocylinders is dependent on the orientation of the cylinder with respect to the applied electric field [273]. In general a rod moves at an angle with respect to the field. However, Henry neglected the relaxation effect of the double layer, so that the result is only valid for zeta-potentials (ζ) that are smaller than 25 mV ($\zeta < k_BT/e$). A theory for infinitely long cylinders, where the relaxation effect was included, was developed by Stigter [274, 275]. However, in practice, rod-like particles like DNA strands, *fd*-virus, microtubules, f-actin or silica rods are finite and need a more accurate description. Using numerical calculations to described the mobility of finite cylinders, both Allison *et al.* and Buitenhuis found that with smaller aspect ratio the mobility of spherocylinders decreases at small κa as end effects become more pronounced [276, 277].

Experimentally, most measurements to determine the zeta-potential are done using capillairy zone electrophoresis [266] or electrophoretic light scattering [277, 278]. Using these techniques only orientationally averaged electrophoretic mobilities of the rod-like particles can be obtained. On the other hand, using optical microscopy, one can measure the electrophoretic mobility of single rod-like particles and its dependence on the orientation of the spherocylinder with respect to the applied electric field. In this way the electrophoretic mobility, which in general can be decomposed into two values: a mobility in the direction parallel and a mobility perpendicular to the rod, can be measured [264, 265]. In addition, if one uses confocal microscopy for the micro-electrophoresis [256–258] measurements with its strong sectioning capabilities and increased resolution, one can even investigate the electrophoresis of concentrated dispersions on the single particle level. Here use of the fact that both coordinates and orientations of rod-like model colloids can be obtained from microscopy images [168]. As far as we know, no experiments have been done that measure the anisotropic electrophoretic motion of silica rods as function of κa. Silica rods are well approximated by short and rigid spherocylinders, in contrast to the long and semi-flexible microtubules and *fd*-virus earlier used. This makes them ideal, for use as model particles.

In this chapter, we first describe a method to faster measure electrophoretic mobility profiles of silica spheres and rods, as compared to methods used by our group previously [256–258]. This method uses crosscorrelation between subsequent confocal images in a xyz-stack and can be used in the case were the particles move uniformly in and solely parallel to the electric field. Measuring electrophoretic mobility profiles, using optical microscopy in closed capillaries, was previously done by measuring xyt-series at 10 different depths in the capillary, which is time consuming [256–258]. Using crosscorrelation between subsequent frames in a xyz-stack, over the whole depth of the capillary, we were able to significantly decrease the measurement time needed for micro-electrophoresis of spherical particles and for rod-like particles in the Smoluchowski limit of high κa. Secondly, we describe our findings on the anisotropic electrophoretic mobility of colloidal silica rods as a function of the double layer thickness κa, by recording xyt-series at the stationary plane z_{stat}. Using confocal microscopy and particle fitting algorithms [168, 169], we were able to measure the anistropic electrophoretic motion on the single particle level. We dispersed the silica rods in different (mixtures of) solvents of different dielectic constants (ϵ_m), which both changes the surface potential of the particles and the double layer thickness, κ^{-1}. In order to have additional control over the double layer thickness in that particular solvent we also added salt containing a large cation to screen interactions.

We show that even at already relatively high κa, where the Smoluchowski limiting law is often assumed to be valid, an orientation dependent velocity was found. Furthermore, at decreasing values of κa the anisotropy in mobility increases. However, in low polar solvents with lower values of κa the opposite trend was observed. The anisotropy in mobility again decreases. We argue that is due to the fact that end effects start to play a role, which was already predicted theoretically [254].

5.2 Theoretical Framework

Electrophoresis measurements are commonly done to determine the surface potential of a colloid. From the velocity of a particle driven by a direct current (dc) electric field, the electrophoretic mobility can be determined. The electrophoretic mobility of the particles is related to the velocity of the particles, and given by

$$\mu(z) = v(z)/E, \tag{5.1}$$

where v is the mean particle velocity ($\mathrm{m\,s^{-1}}$) and E is the electric field strength ($\mathrm{V\,m^{-1}}$).

When a dc electric field is applied to a dispersion of particles, several forces act on the particles, the driving electrostatic force (F_e), the frictional force (F_γ), the retardation force (F_{ret}) and the relaxation force (F_{rel}). These forces are dependent on each other and are therefore not simply additive. The driving electrostatic force is simply

$$F_e = QE, \tag{5.2}$$

with $Q = Ze$ the electrokinetic charge on the particle (C), Z the charge number and e the elementary charge. The frictional force is opposite to F_e and arises from the drag the fluid exerts on a moving particles. For an uncharged particle the drag force is

$$F_\gamma = -\gamma v, \tag{5.3}$$

with γ the friction factor of the particle, for a sphere $\gamma = 6\pi\eta a$, with η the viscosity of the fluid (Pa s) and v the velocity of the particle ($\mathrm{m\,s^{-1}}$). However, the particles are not uncharged, but surrounded by a counterion cloud and also F_{ret} and F_{rel} act on the particle [279]. F_{ret} is the friction force that the moving counter charge exerts on the particle. Counterions move in the opposite direction of the particle and slow the particle down. Co-ions move ahead of the particle and speed up the particle. At high zeta-potentials, $\zeta > k_BT/e$, also F_{rel} becomes important. F_{rel} is caused by the fact that the center of the particle charge and the center of the counter charge do not coincide. A certain time is needed to build up this asymmetric distribution of counter charge, during which a dipole arises that slows down the particle.

At low ζ the relaxation force can be neglected. In the limit of $\kappa a \gg 1$ the following relationship is valid

$$\mu = \frac{\epsilon_0 \epsilon_m \zeta}{\eta}, \tag{5.4}$$

with ϵ_m the dielectric constant of the solvent, ϵ_0 the permittivity of vacuum. This is the Smoluchowski limiting law, and is valid for particles with any shape [272]. Henry showed that for intermediate κa the deformation of the local electric field around the particle should be taken into account, and that the external field can be superimposed on the particle's electric field [273]. The electrophoretic mobility for a sphere is given by

$$\mu = f(\kappa a) \cdot \frac{2\epsilon_m \epsilon_0 \zeta}{3\eta}, \tag{5.5}$$

where $f(\kappa a)$ goes to 3/2 at for sufficiently large κa in the Smoluchowski limit and to 1 at sufficiently low κa in the Debye-Hückel limit. $f(\kappa a)$ is only valid at low zeta-potentials, $\zeta < k_BT/e$, where the relaxation effect can be neglected.

In the case of infinitely long colloidal rods, Henry [273] predicted in 1931 that the electrophoretic mobility of rods aligned with the long axis perpendicular to the electric field ($\mu_\perp$) is given by a similar relation. Again neglecting the relaxation effect, he showed that $\mu_\perp$ can be written as function of κa, where a is now the cylinder radius, similar to the electrophoresis of spheres at lower κa

$$\mu_\perp = f_\perp(\kappa a) \cdot \frac{\epsilon_m \epsilon_0 \zeta}{\eta}. \tag{5.6}$$

A close approximation of $f_\perp(\kappa a)$ is depicted as the solid black line in Fig. 5.7 [280]: $f_\perp(\kappa a)$ goes to 1 at sufficiently high κa and to 1/2 at low κa. For (infinitely) long rods with the long axis orientated parallel to the applied electric field, $\kappa L/2 \gg 1$. Therefore, the Smoluchowski limiting law holds for this orientation

$$\mu_\parallel = \frac{\epsilon_m \epsilon_0 \zeta}{\eta}. \tag{5.7}$$

Thus, at intermediate κa, the resulting velocity of a colloidal rod subjected to an electric field is expected to be orientation dependent. Moreover, it should move at an angle with respect to the field. We define the experimental anisotropy in electrophoretic mobility as

$$f_{\perp}(\kappa a) = \mu_{\perp}/\mu_{\parallel}. \tag{5.8}$$

Measuring the electrophoretic mobility using scattering techniques, one obtains the orientationally averaged mobility [275, 281]

$$\mu_{eff} = \frac{1}{3}\mu_{\parallel} + \frac{2}{3}\mu_{\perp}. \tag{5.9}$$

By recording the trajectories and corresponding orientations of rods in an electric field using confocal microscopy, we can obtain $\mu_{\parallel}$ and $\mu_{\perp}$, separately. We determine the particle velocity parallel v_x and perpendicular v_y to the applied electric field. Figure 5.1a shows the frame of reference, here the subscripts $\parallel$ and $\perp$ are taken with respect to the rod's long axis. The orientation dependent velocities of the rods in the x and y direction are related to $\mu_{\parallel}$ and $\mu_{\perp}$ [264] and are given by

$$v_x = \left[\left(\mu_{\parallel} - \mu_{\perp}\right)\sin^2\theta + \left(\mu_{\perp} + \mu_{EOF}\left(z\right)\right)\right]\cdot E, \tag{5.10}$$

$$v_y = \left[\frac{1}{2}\left(\mu_{\parallel} - \mu_{\perp}\right)\sin 2\theta\right]\cdot E, \tag{5.11}$$

where $\mu_{EOF}(z)$ is the mobility of the particles due to the electro-osmotic flow (EOF) inside the sample. During electrophoresis measurements inside a closed capillary, a parabolic Poiseuille flow sets up in the sample cell, due to electro-osmosis of the fluid [279], see Fig. 5.1c. Thus, the motion of the particles in the sample cell is a result of the superposition of the electrophoretic velocity and the flow profile set-up by electro-osmotic flow. At the stationary planes, $z = z_{stat}$, the net flow of the fluid is zero, and the particles solely translate because of their electrophoretic mobility $\mu_E = \mu(z_{stat})$ and the superimposed Brownian motion of the particles. In a rectangular cell the stationary planes (z_{stat}) are located at [279]

$$\frac{z_{stat}}{h} = \pm\sqrt{\frac{1}{3} + 4\left(\frac{2}{\pi}\right)^5 \frac{1}{k}}, \tag{5.12}$$

where k is the ratio of the minor and major cross section of the capillary, h is the distance from the center of the cell ($z = 0$) and either of the walls.

To determine $\mu_{\perp}$ and $\mu_{\parallel}$ from experimental data, equation 5.10 was used. As $\mu_{\perp}$ can only be derived from a fit of the data to equation 5.10, it was decided to derive both $\mu_{\parallel} - \mu_{\perp}$ and $\mu_{\perp}$ from equation 5.10. Using the effective mobility (equation 5.9), we are able to determine the zeta-potential (ζ) of a rod using

$$\mu_{eff} = \frac{\epsilon_m \epsilon_0 \zeta}{\eta}\left[\frac{1}{3} + \frac{2}{3}f_{\perp}(\kappa a)\right]. \tag{5.13}$$

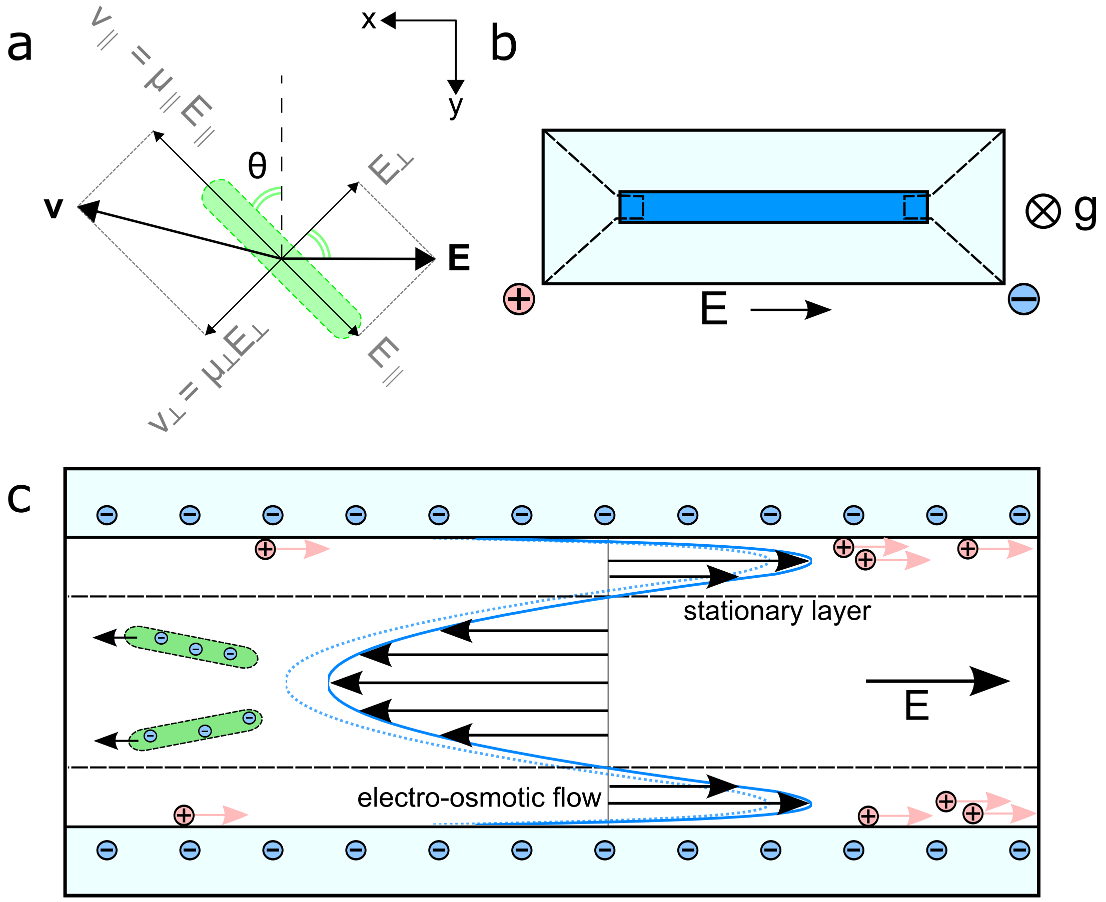

Figure 5.1 **(a)** Schematic showing the orientation dependent velocity of a negatively charged spherocylinder subjected to a dc electric field adapted from [264]. **(b)** Sample cell used during micro-electrophoresis. **(c)** Flow inside capillary during micro-electrophoresis.

5.3 Methods

We used fluorescently labeled silica spheres (SiO_2, density $\rho_{SiO_2} = 1.9\,\mathrm{g\,cm^{-3}}$; dielectric constant $\epsilon_r = 4.5$, refractive index $n_D^{21} = 1.45$), synthesized via a modified Stöber synthesis [25, 26]. The particles were labeled either with the fluorescent dye rhodamine isothiocyanate (RITC) or fluorescein isothyocyanate (FITC). We also used FITC labeled silica rods ($\epsilon_r \sim 4.5$, $n_D^{21} = 1.45$) that were prepared according to the method of Kuijk *et al.* [44, 45]. Details on the particles used in this chapter can be found in Table 5.1. Additionally, SR29 rods that were stable in cyclohexylchloride (CHC, $> 98\%$, Merck), were modified with octadecyltrimethoxylsilane (OTMOS, 90%, Sigma-Aldrich) [148]. In short, silica rods were dried under a flow of nitrogen. Next, 10 wt% of silica rods were added to a mixture of OTMOS, butylamine (99.5%, Sigma-Aldrich) and dried toluene (1:1:10 v/v/v). The dispersion was sonicated at 30–55 °C for 4 hours (Branson 2250). Afterwards, the silica rods were washed successively with toluene ($\geq$99.5%, Sigma Aldrich), cyclohexane ($\geq$99.8%, Sigma Aldrich) and CHC. The as prepared coated rods were dispersed in deionized CHC until further use. The mean dimensions of the particles and their standard deviations were determined from transmission electron microscopy (TEM) images made with a Philips Tecnai 10 or 12 microscope (Fei Company). Typically, 80 particles were measured by hand using the program iTem (Soft Imaging System GmbH, version 5).

Table 5.1 Particle properties used in this study.
With L being the end-to-end length of the rod, D the diameter of the particle, L/D the aspect ratio of the particle, $D_\perp$ and $D_\parallel$ the estimated translational diffusion coefficient perpendicular and parallel to the rod long axis [250], respectively, calculated from their TEM dimensions.

	L nm	δ_L %	D nm	δ_D %	L/D	$D_\perp/D_\parallel$
Rods						
R2	3591	18	587	10	6.1	0.76
SR29	2290	6	600	6.5	3.8	0.81
Spheres						
D385			385	9		
D970			970	3		
D930			930	4		

When measuring zeta-potentials using crosscorrelation, the particles were suspended in a refractive index-matched solvent mixture, $n_D^{21} = 1.45$, of 85 wt% glycerol ($\geq$99%, Sigma Aldrich) and 15 wt% ultrapure water (Milipore system), with 0.55 mM lithium chloride (LiCl). When measuring $\mu_\perp$ and $\mu_\parallel$ of silica rods, the R2 silica rods were dispersed in polar solvents: either 85 wt% glycerol in ultrapure water or 78 wt% dimethylsulfoxide (DMSO, $\geq$99.9%, Sigma-Aldrich) in ultrapure water. LiCl was added to the polar solvents to change the thickness of the double layer. SR29 silica rods were dispersed in the non-polar solvent cyclohexylchloride (CHC, 98% Alfa Aesar GmbH & Co KG). Tetrabutylammonium chloride (TBAC, $\geq$97% Sigma-Aldrich) was added to CHC as a salt to change the double layer thickness. Properties of solvents used in this study can be found in Table 2.3 on page 18.

For electrophoresis measurements, a sample cell was constructed in the following way. A borosilicate rectangular capillary (Vitrocom, UK), with dimensions ($x \times y \times z$) of either 40 mm × 1 mm × 0.1 mm or 40 mm × 2 mm × 0.1 mm was attached to a standard microscope glass slide (Menzel Gläzer) using adhesive tape (Scotch). Two 50 µm diameter nickel alloy wires (Good Fellow) were shaped in rectangular U-shaped electrodes and inserted in opposite ends of the glass capillary, see Fig. 5.1b. The typical spacing of the electrodes was $\sim$ 2 cm. The wires were attached to the glass slide using adhesive tape. The as prepared electrophoresis cell could only be filled with dispersion once.

The electrophoresis cells were filled with dispersions of silica particles, using a glass Pasteur pipette (Wu Mainz). The dispersions prepared had a volume fraction $\phi \sim 0.01$. It was checked that no air bubbles were present between the electrodes, before sealing the cell with UV-curable glue (Norland Optical Adhesive no 68.). The filled electrophoresis cells were homogenized in a slowly rotating stage (rotation about the long axis) for 10–

60 min before measuring. The measurements were carried out as follows; a dc electric field of 1.0–6.3 $\mathrm{V\,mm^{-1}}$ was applied between the electrodes, using a wide band amplifier (Krohn-Hite, model 7602M). To record the velocity of colloids during electrophoresis, we used a laser scanning confocal microscope (Leica TCS SP8) equipped with a 63× 1.4 NA oil confocal-objective (Leica). The sample cell was placed with the long axis perpendicular to gravity. In some cases (Fig. 5.3), we used a Nikon C1 confocal microscope equipped with a 40× 1.25 NA oil confocal-objective (Leica) mounted on a microscope body that was tilted 90°. Here, the sample cell was placed with the long axis parallel to gravity, which prevents a density gradient across depth (z) of the capillary due to sedimentation of particles that disturbs the recording of mobility profiles.

We recorded series of confocal images in two ways. We either recorded time series of xy-images ($\sim$ 50–100 images; typical images size 56 µm × 56 µm; typical pixel size $\sim$ 0.1–0.3 µm, time between frames Δt = 0.4–1.2 s) at fixed depths; typically $\sim$ 10 depths over the total height 0.1 mm of the electrophoresis cell [256–258]. Or we recorded an xyz-stack over the whole depth of the capillary (the average step size was $\Delta z \sim 1\,\mu\mathrm{m}$ and time between frames $\Delta t = 0.75\,\mathrm{s}$). The positions in z of the top and bottom walls were determined using the reflection mode of the confocal microscope.

To derive average particle velocities from confocal xyt-series recorded at 10 different depth we took two approaches. The first approach was that we obtained 2D trajectories of particles using particle fitting and tracking algorithms [168, 169] to find the average displacement between frames at height z (xyt particle tracking). Sometimes, the average displacement of particles between two consecutive images was larger than the average distance between colloids, which does not allow for reliable single particle tracking. If this happened, we first used crosscorrelation between subsequent frames [282] to estimate the average displacement, in integer number of pixels, parallel to the electric field (x-direction). After that, the average displacement in x was subtracted from the found particle coordinates. In this 'co-moving' frame of reference the particles could then be tracked. To obtain the true particle trajectories, the average displacement was added back to the x-coordinate after particle tracking. From the particle trajectories and electric field strength we derived the electrophoretic mobilities of the particles parallel to the electric field as a function of depth z (equation 5.1). The second approach was to use crosscorrelation between two consecutive frames to find the average particle displacement with subpixel accuracy at height z [283] (xyt crosscorrelation). A different and third approach was to record a single xyz-stack across the whole depth of the capillary. Because of the finite time it takes to record one image, particles will appear at shifted positions in subsequent frames. The crosscorrelation of subsequent frames at height z provides the average particle displacement (xyz crosscorrelation).

We fitted the obtained mobility profiles as a parabolic function, and set $z = 0$ at the maximum of the parabolic profile and assumed this to be the center of the capillary. From the value of the fit at z_{stat} we derived the true electrophoretic mobility. For our capillaries we measured a depth of $2h \approx 110\,\mu\mathrm{m}$ and z_{stat} is located at (equation 5.12) $z_{stat} \approx \pm\, 32.7\,\mu\mathrm{m}$ ($k \approx 20$) $\vee \pm\, 33.7\,\mu\mathrm{m}$ ($k \approx 10$).

In order to determine the anisotropy in mobility ($\mu_{\perp}/\mu_{\parallel}$) of silica rods, we generally recorded only at z_{stat} image series of typically $\sim$ 50–100 frames. An exception were the samples of R2 silica rods dispersed in 85 wt% glycerol in water; in this case we took xyt-

series at ten different depths of the sample. The typical images size was 95 µm × 95 µm; pixel size 0.37 µm; the time interval between subsequent frames $\Delta t = 0.2$–$0.9\,\mathrm{s}$.

An estimate for the Debye screening length, κ^{-1} was obtained from the measured conductivities of the used solvents. The conductivities of the polar solvents were measured with a CDM 230 conductivity meter (Radiometer Analytical). The conductivity of CHC, an apolar solvent, was measured using a Scientifica 627 conductivity meter. We assumed that ions contributing to the conductivity in CHC were H^+ and Cl^-. And we assumed independent migrations of ions. The conductivity is related to the concentration of dissociated salt, given by

$$\sigma = c\Lambda_0 \tag{5.14}$$

with σ the measured conductivity ($\mathrm{S\,m^{-1}}$), Λ_0 the limiting molar conductance of the salt at infinite solution ($\mathrm{S\,m^2\,mol^{-1}}$) in the given solvent and c is the concentration of dissociated salt.

Using Walden's rule, one can calculate Λ_0 for different solvents, using literature values of known species. Walden's rule state that the product of the limiting conductance and the viscosity is a constant for the same species in different solvents

$$\Lambda_0^A \eta^A = \Lambda_0^B \eta^B, \tag{5.15}$$

the superscript denotes the particular solvent and η is the viscosity (Pa s) of the solvent. In order to calculate Λ_0 for CHC, we used known literature values for HCl in ethanol, $\Lambda_0^{EtOH} = 84.3\,\mathrm{S\,cm^2\,mol^{-1}}$ [284], $\eta^{EtOH} = 1.08\,\mathrm{mPa\,s}$ [284]. For polar solvents we assumed that ions contributing to the conductivity were Li^+ and Cl^-. In order to estimate Λ_0 in polar solvents, we used literature values for LiCl in glycerol; $\Lambda_0^{glycerol} = 27.1 \times 10^{-2}\,\mathrm{S\,cm^2\,mol^{-1}}$ [285], $\eta^{glycerol} = 910\,\mathrm{mPa\,s}$ (25 °C) [156]. Literature values for viscosity's of the different solvent(-mixtures) used can be found in Table 2.3 on page 18. Using the relation between the ionic strength and conductivity we can calculate κ^{-1} using the following relation, valid for monovalent ions

$$\kappa^{-1} = \sqrt{\frac{\epsilon_m \epsilon_0 k_B T}{2 N_A c e^2}}, \tag{5.16}$$

with N_A Avogadro constant, c the concentration of dissociated monovalent salt in the solvent.

For the polar solvents we sometimes added LiCl to change the thickness of the double layer. In the 85 wt% glycerol-water mixture, without any salt added, the ionic strength was controlled by the trace ions present. For this mixture we measured a conductivity of $0.168\,\mathrm{\mu S\,cm^{-1}}$. Although we do not know the composition of the trace-ions, we used the limiting conductivity for LiCl in glycerol to estimate the screening length, which we estimated to be $\kappa^{-1} \sim 32\,\mathrm{nm}$. When 0.55 mM LiCl was added to the 85 wt% glycerol-water mixture, all the trace ions in the solution were masked by this salt. For this mixture we measured a conductivity of $1.13\,\mathrm{\mu S\,cm^{-1}}$, with a corresponding screening length of $\kappa^{-1} \sim 12\,\mathrm{nm}$. For the 78 wt% DMSO-water mixture, without any salt added, we measured a conductivity of $0.260\,\mathrm{\mu S\,cm^{-1}}$, with a corresponding screening length $\kappa^{-1} \sim 132\,\mathrm{nm}$. When 0.067 mM LiCL was added to the solvent, we measured a conductivity of $1.6\,\mathrm{\mu S\,cm^{-1}}$, with a corresponding screening length of $\kappa^{-1} \sim 53\,\mathrm{nm}$. For silica rods dispersed in CHC, we aimed for large screening lengths. Therefore, as much trace-ions as possible were removed from the solution [286]. Activated alumina was added to a vial of CHC that was left on a roller-bench overnight. The cleaned CHC was then separated from the alumina by centrifugation. Molecular sieves, with a pore size of 4 Å, were added to the cleaned CHC. The measured conductivity of the cleaned CHC was 10 pS cm^{-1}, which corresponds to a screening length of $\kappa^{-1} \sim 7\,\mu\mathrm{m}$. Moreover, to decrease the double layer in CHC, a saturated solution of TBAC in CHC was made. This was done by adding TBAC to cleaned CHC (up to a concentration of 260 mM) [287], and left to equilibrate for one week. We then diluted the solvents to 0.26 µM and 0.026 µM. The measured conductivity of $\sim 0.026\,\mu\mathrm{M}$ TBAC in CHC was 108 pS cm^{-1}, which corresponds to a screening length $\kappa^{-1} \sim 2.2\,\mu\mathrm{m}$. The measured conductivity of $\sim 0.26\,\mu\mathrm{M}$ TBAC in CHC was 4800 pS cm^{-1}, which corresponds to a screening length $\kappa^{-1} \sim 0.33\,\mu\mathrm{m}$.

5.4 Results & Discussion

5.4.1 Measuring Electrophoretic Mobility Using Crosscorrelation

Figure 5.2 shows the electrophoretic mobility profiles obtained for particles dispersed in a 85 wt% glycerol-water mixture with 0.55 mM LiCl. We measured R2 rods (Fig. 5.2a), 970 nm FITC-labeled silica spheres (Fig. 5.2b) and 930 nm RITC-labeled silica spheres (Fig. 5.2c). Results on the obtained electrophoretic mobilities from these graphs can be found in Table 5.2. In this solvent $\kappa a \gg 10$ and we assume the Smoluchowski limiting law is valid. Hence, the rods move uniformly through and parallel to the electric field. We measured the electrophoretic mobility profiles perpendicular to gravity and compared the three different methods. First, the electrophoretic velocity of the particles was recorded at 10 different depths inside the capillary by recording confocal *xyt*-series. The mean particle mobility at height z was determined either by determining particle trajectories (*xyt* particle tracking) or by measuring the mean displacement using crosscorrelation between subsequent frames (*xyt* crosscorrelation). Next, a confocal *xyz*-stack was recorded over the whole depth of the capillary. The mean displacement of particles between subsequent frames in z was determined by using crosscorrelation between subsequent images in the *xyz*-stack. Hence a velocity profile of the particles as a function of z inside the sample cell could be obtained (*xyz* crosscorrelation). From Fig. 5.2 and Table 5.2 it can be concluded that for both rods and spheres, the three different methods gave similar results. Also, it is seen that the mobilities did not depend on the field strength used.

When the viscosity η is low and the density of the particles does not match the density of the solvent ($\rho_{colloid} \neq \rho_{solvent}$), sedimentation (or creaming for particles with a density lighter than that of the solvent, which is not the case here) can occur during the time of the measurement. For silica particles > 300 nm that is a concern. Although the sedimentation velocity is small compared to the electrophoretic velocity, accumulation of particles near the bottom can disturb the measured mobility profiles. To prevent significant sedimentation during measurements, the sample cell can be placed with the long axis parallel to gravity and the electrophoretic mobility profile is then measured

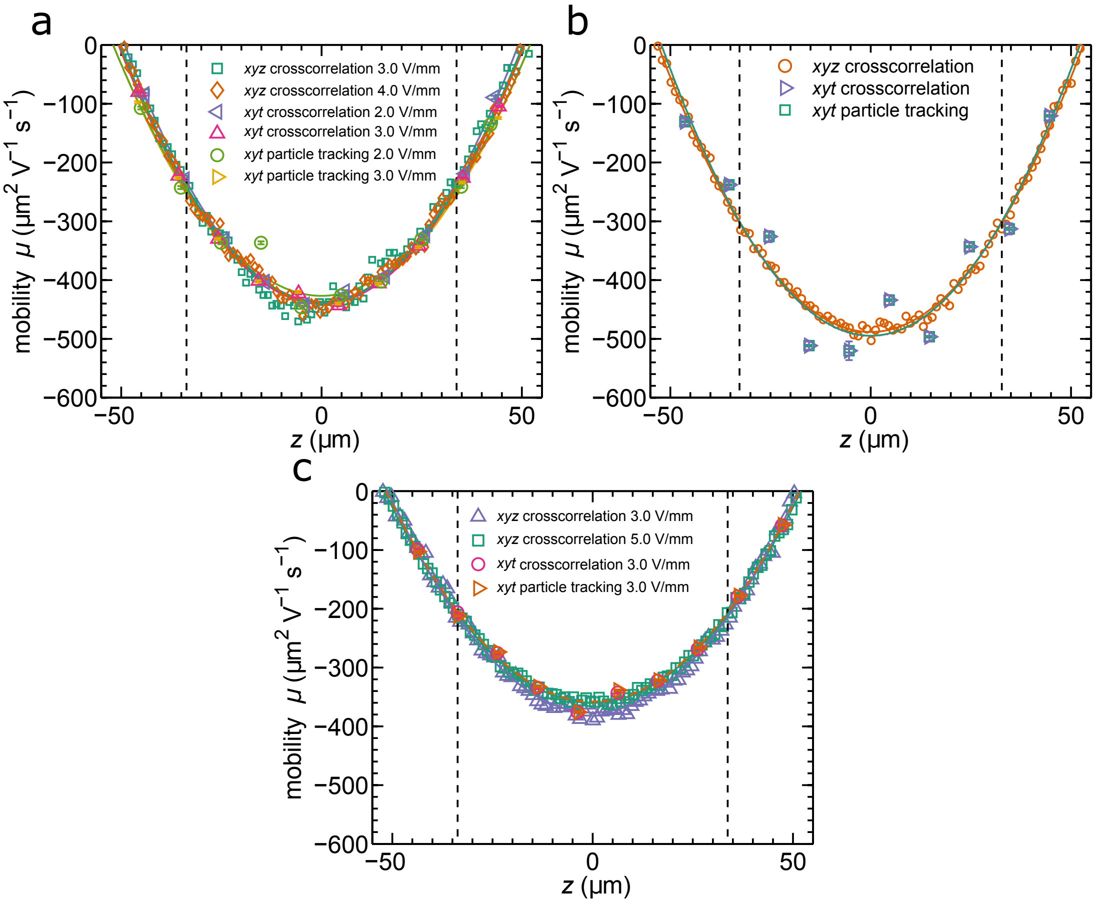

Figure 5.2 Electrophoretic mobility profiles measured perpendicular to gravity in three different ways: Crosscorrelation on a recorded xyz-stack, crosscorrelation on xyt-series recorded at 10 different depths in the capillary and particle tracking on xyt-series recorded at 10 different depths in the capillary. Particles were dispersed in 0.55 mM LiCl 85 wt% glycerol-water. **(a)** R2 rods, $\kappa a \approx 24.5$, $\zeta = -47.0 \pm 0.5\,\mathrm{mV}$. **(b)** 970 nm FITC-labeled silica spheres measured at a field strength of $3.0\,\mathrm{V\,mm^{-1}}$, $\kappa a \approx 40.4$, $\zeta = -55.53 \pm 0.14\,\mathrm{mV}$. **(c)** 930 nm RITC-labeled silica spheres, $\kappa a \approx 38.8$, $\zeta = -40.1 \pm 0.4\,\mathrm{mV}$. The three different methods to measure electrophoretic mobility profiles gave similar results.The dashed vertical lines indicate the stationary planes. We set $z = 0\,\mu\mathrm{m}$ at the maximum of the parabolic profile. The lines are parabolic fits through the data. Error bars, for xyt crosscorrelation and xyt particle tracking, indicate the standard error of the measurement, which is typically smaller than the size of a symbol. The given standard deviation on ζ is the standard deviation on the different estimates of ζ obtained from the parabolic fits through the data.

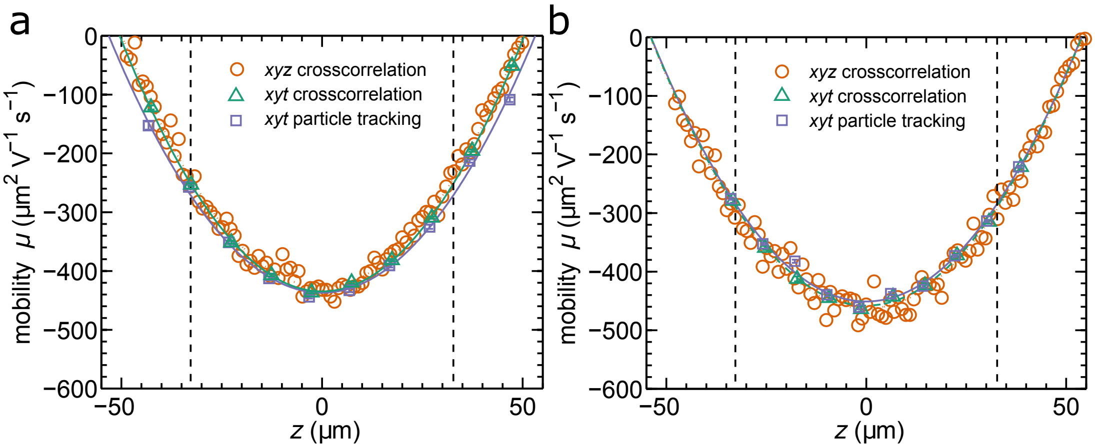

Figure 5.3 Electrophoresis mobility profiles measured parallel to gravity in three different ways: Crosscorrelation on a recorded xyz-stack, crosscorrelation on xyt-series recorded at 10 different depths in the capillary and particle tracking on xyt-series recorded at 10 different depths in the capillary. Mobility profiles were corrected for the effect of gravity on the apparent mobility of the particles. Particles were dispersed in 0.55 mM LiCl 85 wt% glycerol-water. **(a)** R2 rods measured at a field strength of $3.0\,\mathrm{V\,mm^{-1}}$, $\kappa a \approx 24.5$, $\zeta = -47.0 \pm 1.6\,\mathrm{mV}$. **(b)** 970 nm FITC-labeled silica spheres measured at a field strength of $3\,\mathrm{V\,mm^{-1}}$, $\kappa a \approx 40.4$, $\zeta = -53.3 \pm 0.5\,\mathrm{mV}$. The dashed vertical lines indicate the stationary planes. We set $z = 0\,\mu\mathrm{m}$ at the maximum of the parabolic profile. The lines indicate a parabolic fit through the data. Error bars, for xyt crosscorrelation and xyt particle tracking, indicate the standard error of the measurement, which is typically smaller than the size of a symbol. The given standard deviation on ζ is the standard deviation on the different estimates of ζ obtained from the parabolic fits through the data.

parallel to gravity [256]. Figure 5.3 shows the electrophoretic mobility profiles, measured parallel to gravity, obtained by the same methods as described above, for the R2 rods (Fig. 5.3a) and 970 nm FITC-spheres (Fig. 5.3b). Particles were dispersed in 85 wt% glycerol-water with 0.55 mM LiCl. We corrected for the effect of gravity on the apparent mobility of the particles, by taking the average of the two mobility profiles with different field direction, canceling out any effect of gravity. For R2 rods using equation 5.4 we found a zeta-potential of $\zeta = -47.0 \pm 1.6\,\mathrm{mV}$, which is the same within error as was found when the electrophoretic mobility was measured perpendicular to gravity: $\zeta = -47.0 \pm 0.5\,\mathrm{mV}$ (Fig. 5.2a). For the 970 nm FITC-spheres we found $\zeta = -53.3 \pm 0.5\,\mathrm{mV}$, which is close to the value as was found when the measurements were done perpendicular to gravity (Fig. 5.2b, $\zeta = -55.53 \pm 0.14\,\mathrm{mV}$). We thus found similar results for electrophoretic mobility profiles measured parallel to gravity and mobility profiles measured perpendicular to gravity.

Fig. 5.4 presents the electrophoretic mobility profiles measured using xyz crosscorrelation at different field strengths, for the 970 nm FITC-spheres (Fig. 5.4a), the R2 rods (Fig. 5.4b), the 385 nm RITC-spheres (Fig. 5.4c) and the 930 nm RITC-spheres (Fig. 5.4d). It shows that at the field strengths used, the electrophoretic mobilty was not dependent on the applied electric field strength. For the 970 nm FITC-spheres and the 930 nm RITC-spheres we found similar values for the zeta-potential as in Figs. 5.2-5.3.

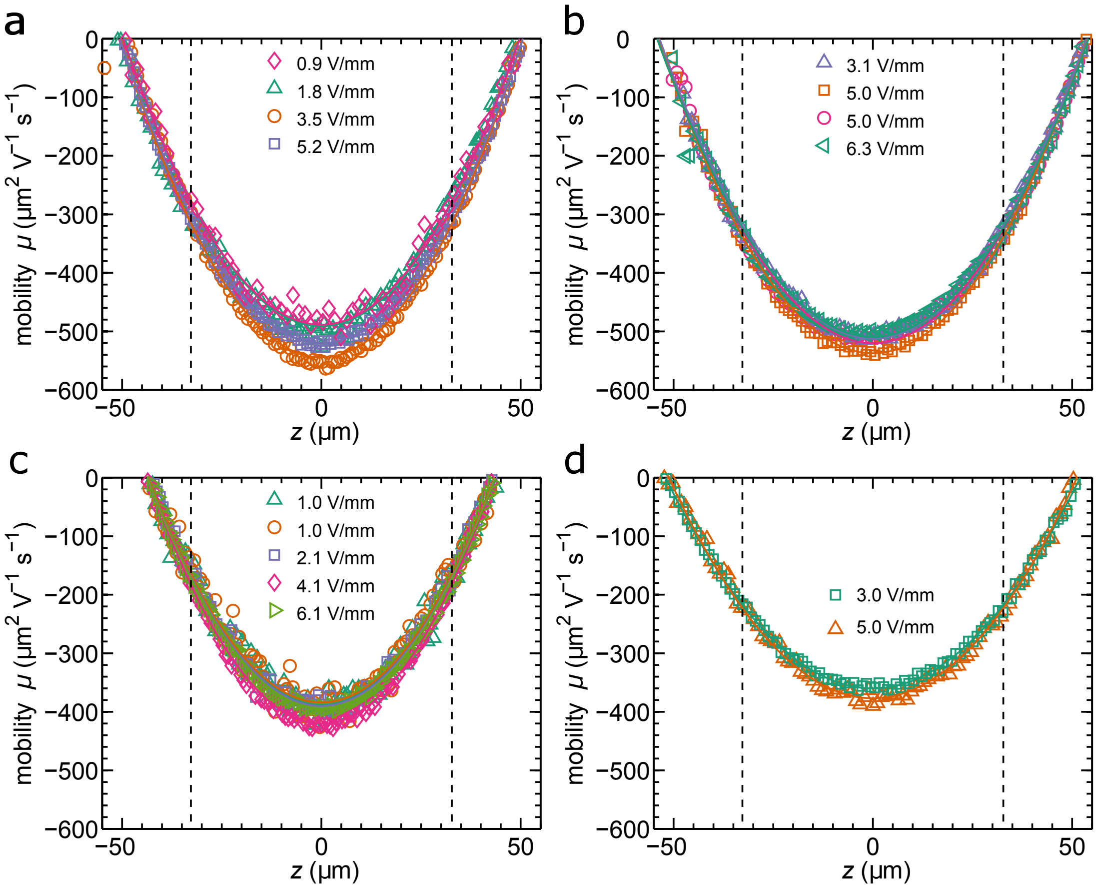

Figure 5.4 Electrophoresis mobility profiles measured perpendicular to gravity using cross-correlation on a recorded *xyz*-stack. **(a)** 970 nm FITC-labeled silica spheres, $\kappa a \approx 40.4$, $\zeta = -54.1 \pm 1.7\,\mathrm{mV}$. **(b)** R2 rods, $\kappa a \approx 24.5$, $\zeta = -60.4 \pm 0.7\,\mathrm{mV}$. **(c)** 385 nm RITC-labeled silica spheres, $\kappa a \approx 16$, $\zeta = -31.7 \pm 0.5\,\mathrm{mV}$. **(d)** 930 nm RITC-labeled silica spheres, $\kappa a \approx 38.8$, $\zeta = -40.6 \pm 0.5\,\mathrm{mV}$. All particles were dispersed in 0.55 mM LiCl 85 wt% glycerol-water. The measurements are done at different field strengths and show that the electrophoretic mobility μ, at these field strengths, is not dependent on the applied electric field. The dashed vertical lines indicate the stationary planes. We set $z = 0\,\mu\mathrm{m}$ at the maximum of the parabolic profile. The lines indicate a parabolic fit through the data. The given standard deviation on ζ is the standard deviation on the different estimates of ζ obtained from the parabolic fits through the data.

Table 5.2 Results on the accuracy of the estimated mobility μ for the particles. Three different methods compared. Showing δ, the half-width of the 95% confidence interval for μ. The 95% confidence interval is defined as $(\mu - \delta, \mu + \delta)$. E is the electric field strength used in experiment. The lowest section depicts the average δ for the three different methods and the corresponding calculated estimated standard deviation s.

Fig. 5.2a	E $\mathrm{V\,mm^{-1}}$	μ $\mathrm{\mu m^2\,V^{-1}\,s^{-1}}$	$\pm\ \delta$ $\mathrm{\mu m^2\,V^{-1}\,s^{-1}}$
xyz crosscorrelation	3.0	−241.0	4.4
xyz crosscorrelation	4.0	−242.7	2.4
xyt crosscorrelation	3.0	−245.9	4.4
xyt crosscorrelation	2.0	−232.6	7.6
xyt particle tracking	3.0	−253.7	4.7
xyt particle tracking	2.0	−248.0	19.8

Fig. 5.2b	E $\mathrm{V\,mm^{-1}}$	μ $\mathrm{\mu m^2\,V^{-1}\,s^{-1}}$	$\pm\ \delta$ $\mathrm{\mu m^2\,V^{-1}\,s^{-1}}$
xyz crosscorrelation	3.0	−291.6	1.9
xyt crosscorrelation	3.0	−288.8	39.6
xyt particle tracking	3.0	−288.8	39.2

Fig. 5.2c	E $\mathrm{V\,mm^{-1}}$	μ $\mathrm{\mu m^2\,V^{-1}\,s^{-1}}$	$\pm\ \delta$ $\mathrm{\mu m^2\,V^{-1}\,s^{-1}}$
xyz crosscorrelation	3.0	−213.8	2.0
xyz crosscorrelation	5.0	−209.0	1.1
xyt crosscorrelation	3.0	−205.4	7.1
xyt particle tracking	3.0	−205.8	8.1

Fig. 5.3a	E $\mathrm{V\,mm^{-1}}$	μ $\mathrm{\mu m^2\,V^{-1}\,s^{-1}}$	$\pm\ \delta$ $\mathrm{\mu m^2\,V^{-1}\,s^{-1}}$
xyz crosscorrelation	3.0	-242.6	5.7
xyt crosscorrelation	3.0	-255.4	2.6
xyt particle tracking	3.0	-271.1	6.9

Fig. 5.3b	E $\mathrm{V\,mm^{-1}}$	μ $\mathrm{\mu m^2\,V^{-1}\,s^{-1}}$	$\pm\ \delta$ $\mathrm{\mu m^2\,V^{-1}\,s^{-1}}$
xyz crosscorrelation	3.0	−293.0	3.7
xyt crosscorrelation	3.0	−289.0	5.9
xyt particle tracking	3.0	−284.2	11.0

Measurement method	average δ $\mathrm{\mu m^2\,V^{-1}\,s^{-1}}$	s $\mathrm{\mu m^2\,V^{-1}\,s^{-1}}$
xyz crosscorrelation	3.0	0.8
xyt crosscorrelation	11.2	4.9
xyt particle tracking	14.9	4.6

For the 970 nm FITC-spheres in Fig. 5.4 we found $\zeta = -54.1 \pm 1.7\,\mathrm{mV}$. Likewise, in Figs. 5.2-5.3 we found $\zeta = -55.53 \pm 0.14\,\mathrm{mV}$ and $\zeta = -53.3 \pm 0.5\,\mathrm{mV}$, respectively. For 930 nm RITC-spheres in Fig. 5.4 we found $\zeta = -40.6 \pm 0.5\,\mathrm{mV}$. Similarly, in Fig. 5.2 we found $\zeta = -40.1 \pm 0.4\,\mathrm{mV}$. However, for R2 rods we found a much higher value of $\zeta = -60.5 \pm 0.7\,\mathrm{mV}$ compared to $\zeta = -47.0 \pm 1.6\,\mathrm{mV}$. Although the measurements were done in separately prepared sample cells, the exact reason for this difference is not known.

In order to compare the robustness of the different measurement methods in Figs. 5.2-5.3, we calculated the 95% confidence intervals for the estimated electric mobility from the fit of the different measurement methods using Matlab (version R2016a), the results can be found in Table 5.2. The table shows that the confidence interval of the predicted mobility from the fit is on average smaller for the xyz crosscorrelation method, compared to the xyt particle tracking and xyt crosscorrelation method. Thus, the determination of the mobility profile using the xyz crosscorrelation method is the most robust.

In summary, the three different methods to measure electrophoretic mobilities gave similar results. We also found similar results for electrophoretic mobility profiles measured parallel to gravity and mobility profiles measured perpendicular to gravity. The fit of the mobility profile for xyz crosscorrelation is more robust, compared to the two other measurement methods. Moreover, it should be noted that xyz crosscorrelation is much faster ($\sim 75\,\mathrm{s}$) than our earlier measurement technique (xyt particle tracking), where times series are measured at different heights, which takes much longer to complete ($\gtrsim 10 \times 40\,\mathrm{s}$). Not only sedimentation is less of a problem with xyz crosscorrelation during the time scale of the measurement, also the Segre and Silberberg effect or flow focusing [288] will be less of a problem. The Segre and Silberberg effect describes that during laminar Poiseuille flow in a capillary, particles tend to position themselves at $0.6R$ from the center of the capillary. We observed this unfavorable flow focusing effect during electrophoresis experiments after measuring for $\gtrsim 3$ minutes. Hence, if one can measure faster, one can measure the electrophoretic mobility profile over the whole depth of the capillary, before this effect sets in.

The xyz crosscorrelation method of measuring electrophoretic mobility profiles was applied to both colloidal silica spheres and rods. However, the method measures only the mobility component parallel to the field (μ_x). Thus, for colloidal rods this technique is most accurate in the case of high $\kappa a \gg 10$. At lower κa the rods were found to have an anisotropic mobility that depended on the angle it has with respect to the applied electric field (as described above in Section 5.2). Using equation 5.13 and assuming infinitely long rods, one can still obtain ζ from the measured μ_{eff} [274, 289]. However, measuring both $\mu_\perp$ and $\mu_\parallel$ to obtain ζ will probably be more accurate. Hence, crosscorrelation works best if the particles move uniformly through the electric field. At $\kappa a \approx 24.5$ the anisotropy in mobility of the rods $\mu_\perp/\mu_\parallel = 0.98$ (see Section 5.4.2). Thus, the particles moved almost parallel to the electric field, and we assumed that the small anisotropy in mobility did not significantly affected the measured zeta-potential. Moreover, the crosscorrelation method works best if (long-range) order in the sample is absent, otherwise one will find several peaks in the crosscorrelation matrix, making it difficult to determine the real displacement of the sample.

5.4.2 Anisotropic Electrophoretic Mobilities of Silica Rods

Electrophoretic Motion of Silica Rods

As observed earlier for microtubules [264], we observed that the electrophoretic velocity and direction of electrophoretic motion of colloidal silica rods can be dependent on the orientation of the rods with respect to the electric field, see Fig. 5.1a. This is in line with equations 5.10 and 5.11. A diagram of the electric field components acting on a silica rod that is oriented with an angle θ with respect to the y-axis is shown in Fig. 5.1a. The electric field is directed along the x-axis to the right. The resulting velocity is not parallel with the electric field, but points towards the long axis of the rod, i.e. $\mu_\perp < \mu_\parallel$.

Fig. 5.5a shows a sequence of cut outs of confocal images of the electrophoretic motion of R2 silica rods dispersed in a 78 wt% DMSO in water mixture, without any salt added, $\kappa a = 2.2$, taken at height $z = z_{stat}$. In these frames, the rods that are highlighted have different orientations with respect to the electric field. The movement of the rods is not exactly parallel to the electric field, but is slightly directed in the direction of the long axis of the silica rod. Fig. 5.5b shows an overlay of subsequent confocal images taken of the electrophoretic motion of SR29 silica rods in CHC, $\kappa a = 0.04$, taken at height $z = z_{stat}$. The time interval between the images was $\Delta t = 0.37$ s. In total 30 frames were used to make the overlay. At $t = 0$ s the color of the rod is blue. The rod moved in a more or less straight line in the direction opposite to the electric field direction, and due to the rotational Brownian motion its orientation fluctuated. The orientation dependent velocity of silica rods, dispersed in 78 wt% DMSO in water, during electrophoresis can be clearly observed by eye. However, for rods dispersed in pure CHC it is harder to observe the orientation dependent velocity by eye, because the anisotropy in mobility is smaller.

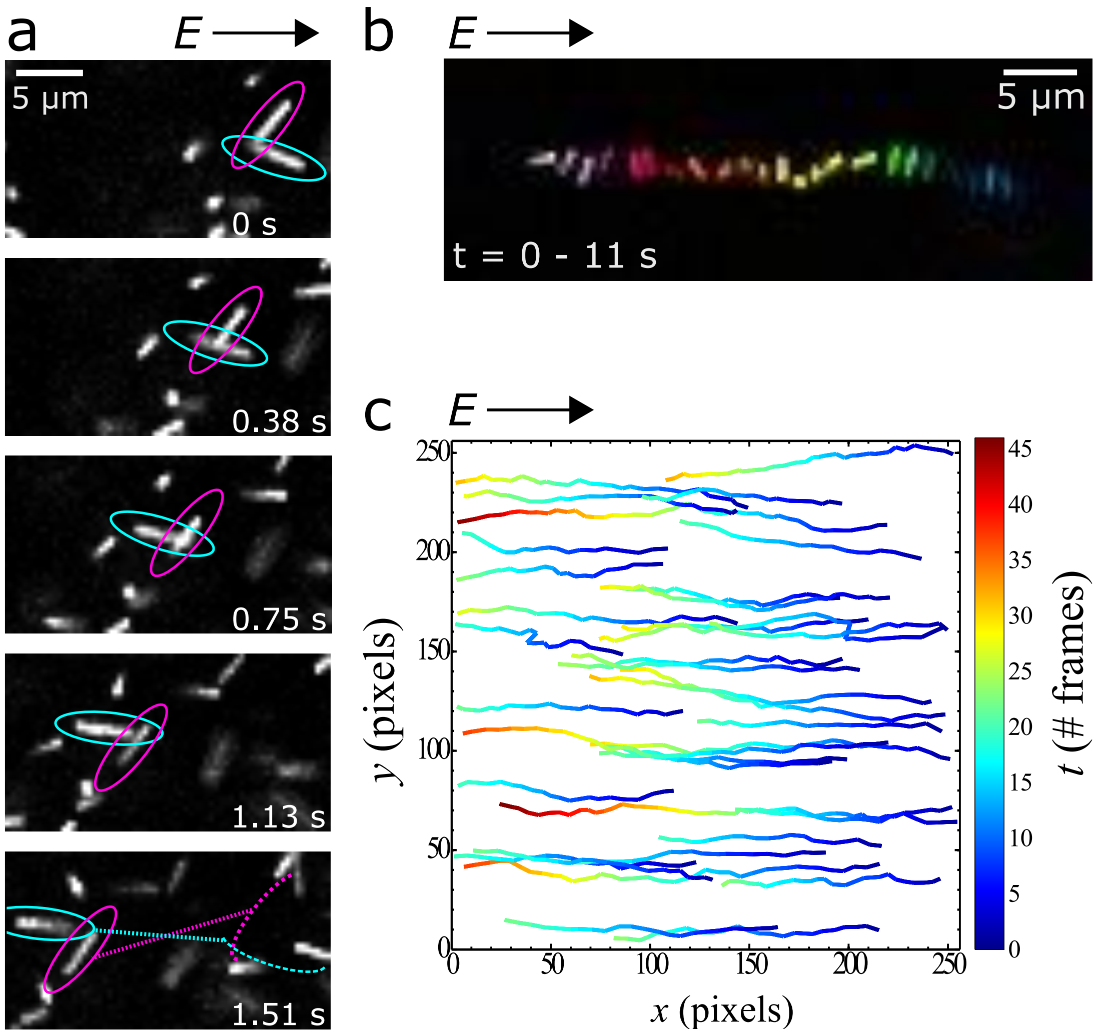

Figure 5.5 **(a)** Confocal images of xyt-series of the electrophoresis of R2 silica rods in DMSO-water $\kappa a = 2.2$. Silica rods show an orientation dependent velocity and motion with respect to the applied electric field. **(b)** Overlay of xyt-series of the electrophoresis of silica rods dispersed in CHC, $\kappa a = 0.04$, 30 frames, $\Delta t = 0.37\,\mathrm{s}$. It clearly shows that the rods still exhibit rotational diffusion, due to Brownian motion. Electric field strength $2.0\,\mathrm{V\,mm^{-1}}$. At $t = 0$ the color of the rod is blue. **(c)** Several trajectories of SR29 rods dispersed in CHC, $\kappa a = 0.04$, during electrophoresis, the position of the center of mass is plotted. Minimum length of trajectory displayed here is 20 frames.

Quantifying the Anisotropy in Mobility of Silica Rods

In order to quantify the exact electrophoretic mobilities of rods orientated parallel and perpendicular to the electric field, we used particle tracking. In each frame we determined the orientations of the rods and recorded their displacements since the previous frame. The displacements were converted to mobilities parallel and perpendicular to the electric field, and were averaged in bins of 4° in θ. Fig. 5.6a shows the result for the measured orientation dependent mobility of the R2 silica rods dispersed in 78 wt% DMSO-water, $\kappa a = 2.2$, at $\mathrm{E} = 1.14\,\mathrm{V\,mm^{-1}}$. Note that the mean square angular displacement, due to the rotational Brownian motion, of the rods in the interval between frames (0.374 s) is about 12°. The electric field was pointing in the positive x-direction. The green symbols indicate the mobility of the rods in the y-direction μ_y, which is perpendicular to the applied electric field. The red symbols indicate the mobility of the rods in the x-direction parallel to the electric field. When the rod was oriented perpendicular or parallel to the electric field ($\theta = 0° \vee 180°$ or $\theta = 90°$) only a mobility component parallel μ_x to the electric field was observed. For rods that were not completely oriented parallel or perpendicular to the electric field ($0° < \theta < 90°$ or $90° < \theta < 180°$) a mobility component perpendicular to the electric field μ_y was found, which was either positive or negative. In other words the rods dispersed in a 78 wt% DMSO-water mixture showed an orientation dependent velocity, and depending on the orientation they also had a velocity component in the positive or negative y-direction. The solid lines in Fig. 5.6a are a fit of equations 5.10 and 5.11 through the unbinned data. From the fitted amplitude $(\mu_{\parallel} - \mu_{\perp})$ and offset

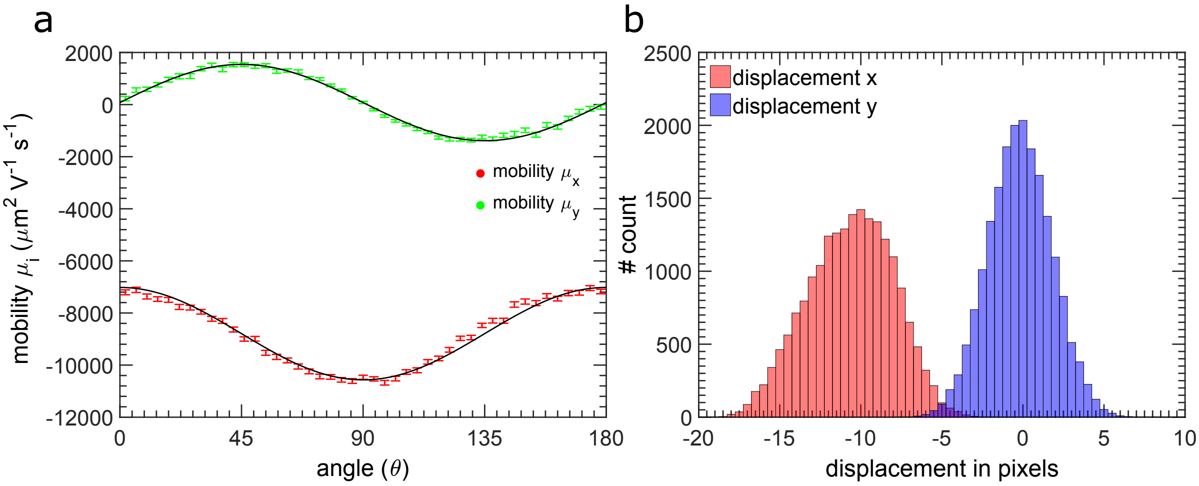

Figure 5.6 Electrophoresis measurement of R2 silica rods dispersed in DMSO-water, without salt added, $\kappa a = 2.2$. **(a)** Orientation dependent mobility in x-direction (red symbols), parallel to electric field, and y-direction (green symbols), perpendicular to applied electric field. For clarity raw data is binned in 4° wide bins. The error bars indicate the standard error on the binned data points. The solid lines are a fit through the raw data using equation 5.10 (μ_x) and equation 5.11 (μ_y). **(b)** Histogram of displacement of rods in x and y direction. An anisotropy of $\mu_{\perp}/\mu_{\parallel} = 0.664 \pm 0.006$ was found and $\zeta = -75\,\mathrm{mV}$. The direction of the electric field was in the positive x-direction, $E = 1.14\,\mathrm{V\,mm^{-1}}$, $\Delta t = 0.374\,\mathrm{s}$. The error on $\mu_{\perp}/\mu_{\parallel}$ is the estimated standard error obtained from the covariance matrix of the fitted parameters.

($\mu_\perp$) of equation 5.10 we determine $\mu_\perp$, $\mu_\parallel$ and the anisotropy in mobility $\mu_\perp/\mu_\parallel$. In this case the measured anisotropy was $\mu_\perp/\mu_\parallel = 0.664 \pm 0.006$. The zeta-potential was determined using equations 5.8, 5.9 and 5.13. In all cases, we used equation 5.10 to obtain $\mu_\parallel - \mu_\perp$. Values obtained from equation 5.11 were 0–20% off from the value found by equation 5.10. The difference may arise because the the fitted values for $\mu_\parallel - \mu_\perp$ and $\mu_\perp$ in equation 5.10 are dependent on each other, whereas $\mu_\perp$ is not of any influence in equation 5.11 to determine $\mu_\parallel - \mu_\perp$. Fig. 5.6b shows the corresponding histogram of displacements of R2 rods in the x and y direction, respectively parallel or perpendicular to the applied electric field. We find a distribution of displacements, because the rods behave Brownian and their orientation fluctuates (see equations 5.10 and 5.11). Moreover, the main displacement due to the electrophoresis is parallel to electric field, and hence the histogram of displacement in the x-direction is centered around a negative displacement.

We measured the orientation dependent electrophoretic mobilities for silica rods over a range of κa. We tuned κa by dispersing the rods in solvents with different dielectric constants, and by the addition of salt to change the concentration of free ions in solutions. Although using different solvents affects ζ, the value of $\mu_\perp/\mu_\parallel$ is much less affected. The results on the measured orientation dependent mobilities at different κa can be found in Appendix 5.A (Figs. A.5.1-A.5.6). An overview on these results is presented in Fig. 5.7. The graph shows the anisotropy in mobility of the two types of silica rods $\mu_\perp/\mu_\parallel$ as a function of κa. The symbols in the graph are experimental data points of the measured $\mu_\perp/\mu_\parallel$ for the SR29 rods in CHC (green squares) and for the R2 rods in polar solvents (purple circles). Table 5.1 shows data of the particle properties of the rods used. The solid black line depicts Ohshima's analytical expression, for Henry's solution of infinitely long rods and low zeta-potential $\zeta < k_B T/e$ [280]. The dashed, dotted and dashed-dotted lines depict Ohshima's approximate analytical expression for infinitely long rods and at moderate zeta-potentials [289], taking the relaxation effect into account, for $|\zeta| \approx 25\,\text{mV}$, $|\zeta| \approx 50\,\text{mV}$ and $|\zeta| \approx 75\,\text{mV}$, respectively.

For relatively small double layers (R2 rods, purple circles), when $\kappa a > 2$, our experimental data show a similar trend as theoretical predictions for infinitely long rods [273, 289]. For SR29 silica rods in a polar solvents with relatively large double layers (green squares), the experimental data do not agree with theoretical predictions for infinitely long cylinders. Rather, $\mu_\perp/\mu_\parallel$ increases as κa decreases, and the orientation dependent velocity during electrophoresis becomes less pronounced. The difference arises because end effects start to play a role [254, 276]. In this case, the Smoluchowski equation does not hold anymore for rods orientated parallel to an electric field. Calculations on short DNA strands ($\kappa a \sim 1$) and orientated parallel to the electric field, showed that the mobility is significantly slowed down during electrophoresis compared to longer DNA strands [276], whilst the mobility of rods perpendicular to the electric field remains roughly the same (compared to infinitely long rods). For theoretical calculations on *fd*-virus a similar trend was observed when the aspect ratio decreased at values of $\kappa a = 3.56 \times 10^{-4}$ [277].

Because at $\kappa a < 1$ the Smoluchowski approximation (equation 5.4) is not valid anymore for short rods that are oriented parallel to the electric field, this would lead to an underestimation of ζ using equation 5.13. For $\mu_\parallel$ one would expect a dependence on $\kappa L/2$, hence $f_\parallel(\kappa L/2)$. A simple improvement for $\mu_\perp/\mu_\parallel(\kappa a)$, for aspect ratios of rods $L/D = 6.1$ and $L/D = 3.8$, can be found in Fig. 5.8. This relation is found by calculating

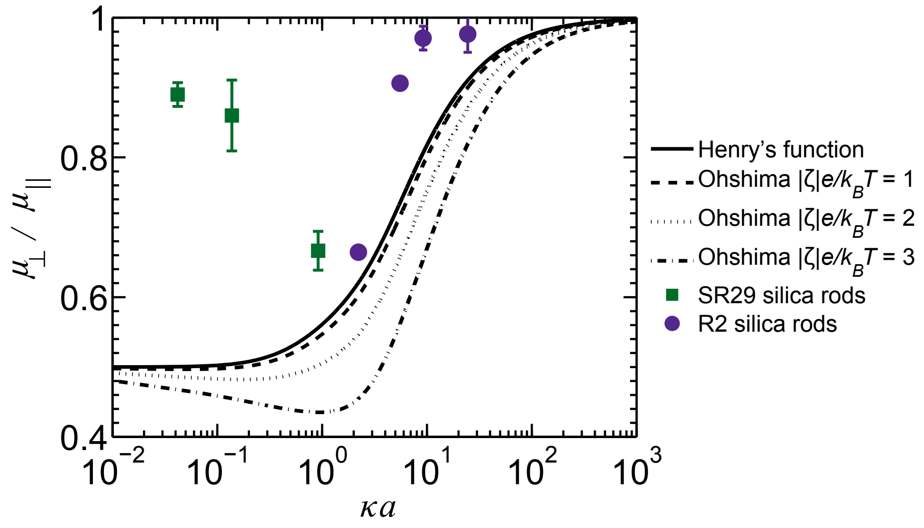

Figure 5.7 Anisotropy in mobility of silica rods perpendicular and parallel to the electric field ($\mu_\perp/\mu_\|$) plotted as a function of κa. The black solid line depicts Ohshima's analytical expression of Henry's solution, for infinitely long rods and low zeta-potential $\zeta < k_BT/e$ [280]. The dashed, dotted and dashed-dotted lines depicts Ohshima's approximate analytical expression for infinitely long rods and moderate zeta-potentials [289], taking the relaxation effect into account, for $|\zeta| \approx 25$ mV, $|\zeta| \approx 50$ mV and $|\zeta| \approx 75$ mV respectively. The symbols are experimental data points of the measured anisotropy in mobility. Squares (green) are SR29 rods in CHC, from left to right: without TBAC added; with ~ 0.026 µM; with ~ 0.26 µM TBAC. Circles (purple) are R2 rods in polar solvents (DMSO-water and glycerol-water), from left to right 78 wt% DMSO-water, 78 wt% DMSO-water with LiCl, 85 wt% glycerol-water and 85 wt% glycerol-water with LiCl. The error bars indicate the estimated standard deviations.

$f_\perp(\kappa a)/f_\|(\kappa L/2)$ using Ohshima's approximate analytical expression for infinitely long rods and moderate zeta-potentials [289]. It shows indeed an expected increase of $\mu_\perp/\mu_\|$ at $\kappa a \lesssim 3$. This captures the trend in the experimental data for SR29 rods dispersed in CHC reasonably.

The anisotropy in mobility in this study was mostly determined by recording confocal xyt-series at a height $z = z_{stat}$, because the rods sediment to the bottom during the electrophoresis measurements before the whole parabolic electro-osmotic flow profile can be measured. SR29 rods dispersed in CHC sediment in 7 minutes 100 µm, which is the depth of the capillary. R2 rods dispersed in DMSO-water sediment 100 µm in 10 minutes. The drawback, of measuring only at z_{stat}, is that z_{stat} is located in a steep part of the parabolic electro-osmotic flow profile. A small error in the position of z_{stat}, already causes a relatively large error in the determination of $\mu_\perp$. Only when the rods were dispersed in a viscous 85 wt% glycerol-water mixture, the rods did not sediment appreciably during the time scale of the measurements. These rods need 6 hours to sediment over 100 µm. In this case, we recorded confocal xyt-series at ten different depths inside the capillary. Through the determination of the electro-osmotic flow profile, we could more accurately determine $\mu_\perp$. To overcome the problem of sedimentation in less viscous solvents, a confocal microscope with a tilted frame can be used [256], so that the electric field is parallel with gravity. However, using this set-up we encountered new problems. When a

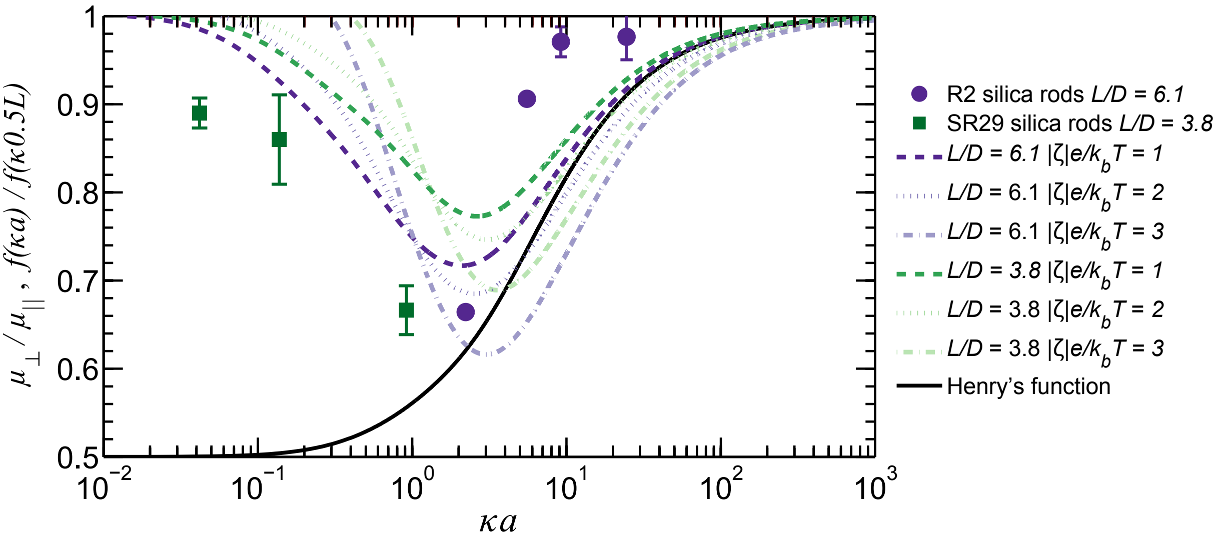

Figure 5.8 Anisotropy in electrophoretic mobility $\mu_\perp/\mu_{||}$ plotted as a function of κa. The black line depicts Ohshima analytical expression, an approximation of Henry's solution, for infinitely long rods and low zeta-potential $\zeta < k_BT/e$ [280]. In the case of low zeta-potential, the relaxation effect can be neglected. Data from Fig. 5.7 are plotted together with Ohshima's approximate analytical expression for 'finite' rods and moderate zeta-potentials. This was done by naively assuming that rods oriented parallel to the electric field are subjected to the same retardation function as rods orientated perpendicular to the electric field. Thus, $f(\kappa a)$ is $f(\kappa L/2)$. To obtain the anisotropy in mobility for finite rods $f(\kappa a)$ is divided by the function $f(\kappa L/2)$. This naive assumption predicts that $\mu_\perp/\mu_{||}$ increases as the size of the double layer increases ($\kappa a \ll 1$), for finite rod sizes as observed experimentally.

relatively high volume fraction ($\phi \approx 0.04$) of rods was used to measure the anisotropic electrophoretic mobility, swirls occurred in the sample, and non-uniform settling was observed [290]. However, decreasing the vol% of rods did not solve the problem. Instead, flow focusing [288] occurred in the sample within the time scale of the measurement, as described above in Section 5.4.1. Therefore, not enough statistics for the orientation dependent displacements of the rods at each height could be obtained before flow focusing sets in. Because, measurements that determine the orientation dependent mobility take longer, compared to measurements that only determine the mobility component parallel to the applied electric field.

Balance between Brownian Motion and Anisotropy in Mobility

The visual appearance of the motion of silica rods during electrophoresis was dependent on the solvent the silica rods were dispersed in. For instance, in a pure 78 wt% DMSO-water mixture ($\kappa a = 2.2$) an anisotropy in mobility $\mu_\perp/\mu_{||} \sim 0.664$ was measured for the R2 rods. Hence, the rods showed a clear orientation dependent velocity during electrophoresis. When we look at Movie 5.1 on page 107, which shows the electrophoretic motion of these silica rods in 78 wt% DMSO-water, we observed that the silica rods created the impression of 'swimming'. The direction of motion of the silica rods was approximately in the direction of their long axis. Because the silica rods still behaved Brownian, the angle of each rod with respect to the applied electric field fluctuated, so that the mobility direction changed on a time scale of seconds. The relatively low viscosity (3.54 mPa s) of the solvent mixture used in this case results in a calculated $D_r = 0.032\,\mathrm{rad}^2\,\mathrm{s}^{-1}$ of the silica rods. During 1 second the rods are expected to rotate $\sqrt{4D_r\tau} = 0.35\,\mathrm{rad}$ (20°). The combination of Brownian motion and an orientation dependent electrophoretic motion led to an apparent ‘swimming’ behavior of these silica rods dispersed in DMSO when a dc electric field was applied to the sample. On the contrary, a sample of silica rods in 85 wt% glycerol-water showed a completely different behavior (Movie 5.2 on page 107). The silica rods were pulled in a more of less straight line towards the positive electrode, without much rotational diffusion of the rods. This is partly due to the relatively high viscosity of the medium (81 mPa s) that makes the rotational diffusion of the rods rather slow $D_r = 0.0014\,\mathrm{rad}^2\,\mathrm{s}^{-1}$. Furthermore, the measured anisotropy in mobility $\mu_\perp/\mu_\parallel \sim 0.97$ did not give rise to a clear orientation dependent motion. Movie 5.3 on page 107 then again shows that silica rods in CHC were pulled to one side during electrophoresis, without too much ‘swimming’ motion observed. In CHC the SR29 silica rods had a measured anisotropy in mobility $\mu_\perp/\mu_\parallel \sim 0.89$. The much lower viscosity (1.57 mPa s) of CHC, and the slightly smaller dimension of the SR29 silica rods, compared to R2 rods, results in a higher $D_r = 0.195\,\mathrm{rad}^2\,\mathrm{s}^{-1}$ of the rods. Hence, rotational diffusion of the rods was clearly visible on top of the electrophoretic motion the silica rods.

In summary, differences in the observed motions of the silica rods during electrophoresis were due to differences in viscosity and the κ^{-1} of the particles due to the solvent the particles were dispersed in. These parameters make up for an intriguing changing interplay between rotational diffusion (Brownian motion) and the orientation dependent electrophoretic mobility.

5.5 Conclusion

To conclude, we showed that measuring the electrophoretic mobility as well as the electro-osmotic flow profile of colloidal particles, that move uniformly through ($\mu_\parallel/\mu_\perp \sim 1$) and parallel to an electric field, can be done by recording an *xyz*-stack over the whole depth of a capillary using confocal microscopy. Recording an *xyz*-stack is much faster compared to the method that was used previously in which *xyt*-series were recorded at 10 different depths inside the capillary. In the case of rods that did not move uniformly through an electric field, we were able to measure the orientation dependent velocity of silica rods during electrophoresis. From this we could determine the anisotropy in the mobility of rods, with $L/D \sim 5$, during electrophoresis and compare this with theoretical values from literature. We showed that even at relatively high values of κa, where the Smoluchowski limiting law was assumed to be valid, a small anisotropy in mobility was found. Furthermore, for the R2 rods dispersed in polar solvent our data agree qualitatively with the theoretical prediction for infinitely long cylinders and low zeta-potential ($\kappa a \gtrsim 2$). However, this theory starts to break down at small values of κa, where $\kappa a \lesssim 1$. At these values end effects start to play a role, and rods are significantly slowed down. Also, the value of the measured anisotropy in mobility was observed to decrease again at smaller values of κa. This was already predicted in theoretical calculations for finite cylinders [276, 277]. If this end effect is not taken into account while calculating zeta-potentials, this will lead to an underestimation of the experimental established zeta-potential by up to a factor two.

5.6 Acknowledgements

I would like to thank Judith Wijnhoven for the synthesis of the D970 spheres and for proofreading this chapter, Gülşen Heessels-Gürboğa for the synthesis of D385 and D930 spheres, Thijs Besseling for provinding the SR29 rods. Moreover I would like to thank Peter Helfferich and Thijs Besseling for the introduction into the experimental procedure of micro-electrophoresis. I would also like to thank Peter Helfferich for all his useful technical assistance.

Appendix 5

5.A Figures

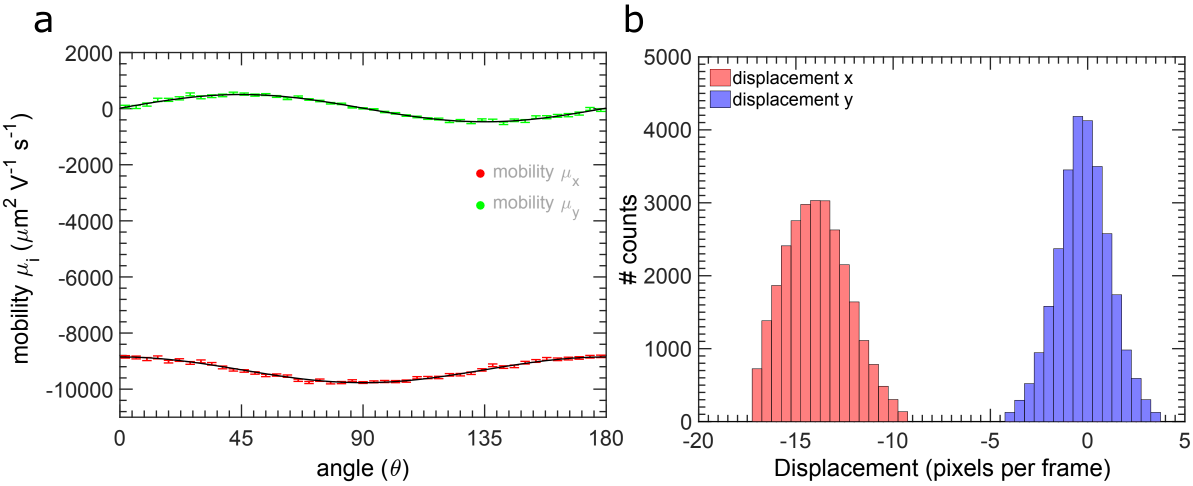

Figure A.5.1 Electrophoresis measurement of R2 silica rods dispersed in DMSO-water, with 0.067 mM LiCl added, $\kappa a = 5.5$. **(a)** Orientation dependent mobility in x-direction (red symbols), parallel to electric field, and y-direction (green symbols), perpendicular to applied electric field. For clarity raw data is binned in 4° wide bins, the error bars indicate the standard error on the binned data points. The solid lines are a fit through the raw data using equation 5.10 (μ_x) and equation 5.11 (μ_y). **(b)** Histogram of the displacements of the rods in x and y direction. An anisotropy of $\mu_\perp/\mu_\parallel = 0.906 \pm 0.004$ was found and $\zeta = -70\,\mathrm{mV}$, $E = 1.45\,\mathrm{V\,mm^{-1}}$, $\Delta t = 0.377\,\mathrm{s}$. The error in $\mu_\perp/\mu_\parallel$ is the estimated standard error obtained from the covariance matrix of the fitted parameters.

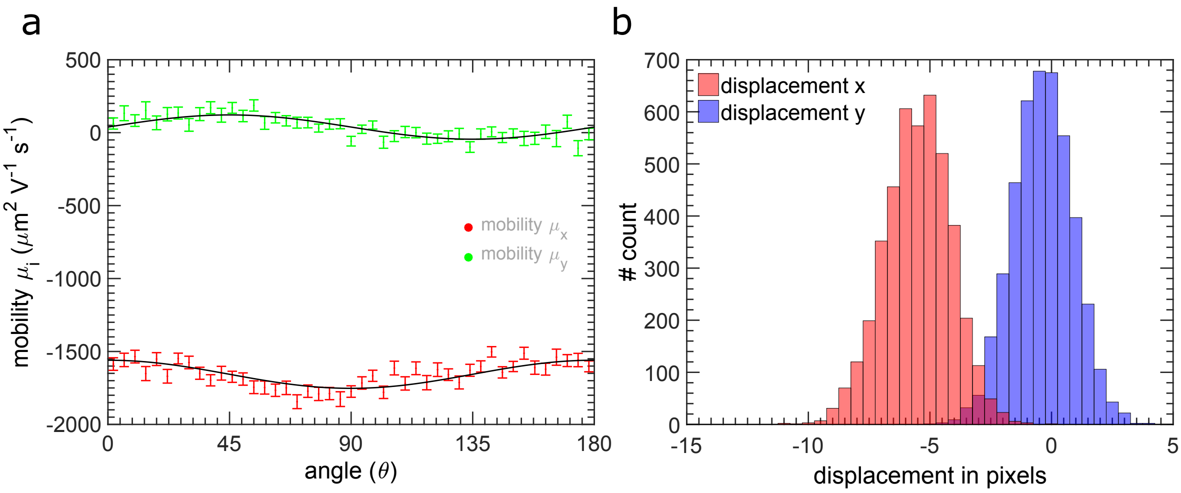

Figure A.5.2 Electrophoresis measurement of SR29 silica rods dispersed in CHC, without salt added, $\kappa a = 0.04$. **(a)** Orientation dependent mobility in x-direction (red symbols), parallel to electric field, and y-direction (green symbols), perpendicular to applied electric field. For clarity raw data is binned in 4° wide bins, the error bars indicate the standard error on the binned data points. The solid lines are a fit through the raw data using equation 5.10 (μ_x) and equation 5.11 (μ_y). **(b)** Histogram of the displacements of the rods in x and y direction. An anisotropy in mobility of $\mu_\perp/\mu_\parallel = 0.89 \pm 0.02$ was found and $\zeta = -41\,\mathrm{mV}$, $E = 3.1\,\mathrm{V\,mm^{-1}}$, $\Delta t = 0.374\,\mathrm{s}$. The error in $\mu_\perp/\mu_\parallel$ is the estimated standard error obtained from the covariance matrix of the fitted parameters.

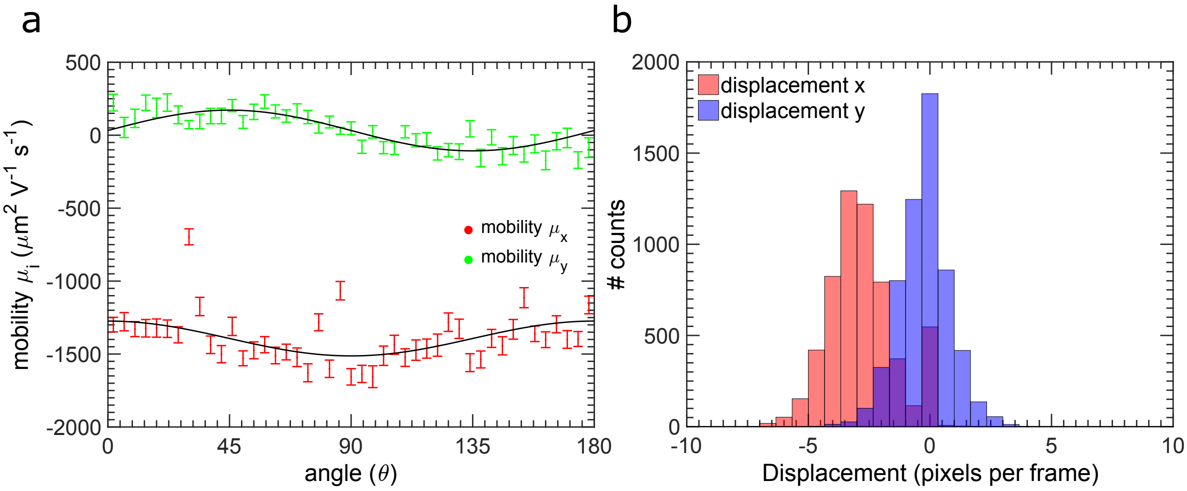

Figure A.5.3 Electrophoresis measurement of SR29 silica rods dispersed in CHC, with TBAC added ($\sim 0.026\,\mu\mathrm{M}$), $\kappa a = 0.14$. **(a)** Orientation dependent mobility in x-direction (red symbols), parallel to electric field, and y-direction (green symbols), perpendicular to applied electric field. For clarity raw data is binned in 4° wide bins, the error bars indicate the standard error on the binned data points. The solid lines are a fit through the raw data using equation 5.10 (μ_x) and equation 5.11 (μ_y). **(b)** Histogram of the displacements of the rods in x and y direction. An anisotropy in mobility of $\mu_\perp/\mu_\parallel = 0.86 \pm 0.05$ was found and $\zeta = -35\,\mathrm{mV}$, $E = 3.35\,\mathrm{V\,mm^{-1}}$, $\Delta t = 0.191\,\mathrm{s}$. The error in $\mu_\perp/\mu_\parallel$ is the estimated standard error obtained from the covariance matrix of the fitted parameters.

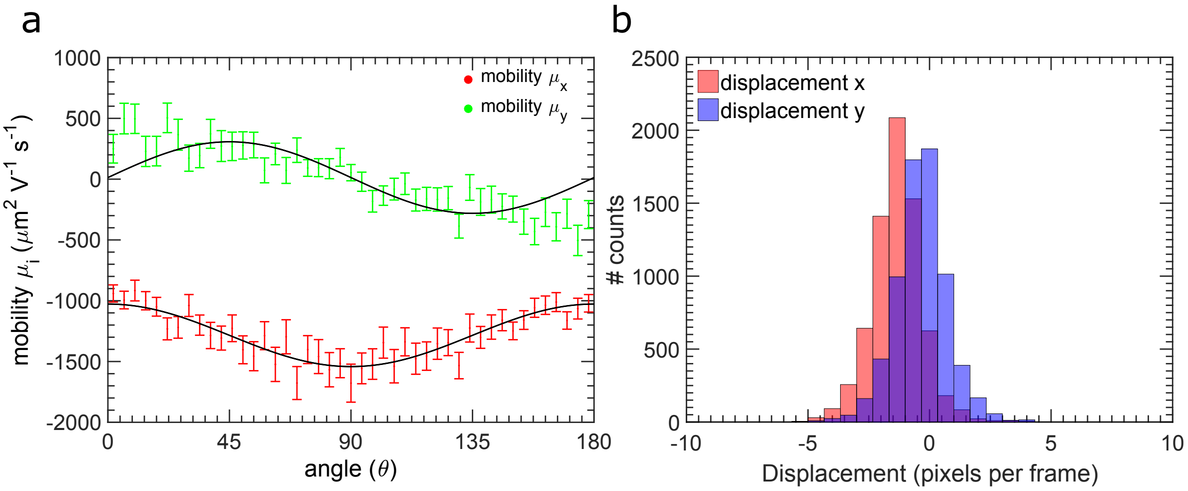

Figure A.5.4 Electrophoresis measurement of SR29 silica rods dispersed in CHC, with TBAC added ($\sim 0.26\,\mu$M), $\kappa a = 0.92$. **(a)** Orientation dependent mobility in x-direction (red symbols), parallel to electric field, and y-direction (green symbols), perpendicular to applied electric field. For clarity raw data is binned in 4° wide bins, the error bars indicate the standard error on the binned data points. The solid lines are a fit through the raw data using equation 5.10 (μ_x) and equation 5.11 (μ_y). **(b)** Histogram of the displacements of the rods in x and y direction. An anisotropy in mobility of $\mu_\perp/\mu_\parallel = 0.67 \pm 0.03$ was found and $\zeta = -36\,$mV, $E = 3.7\,$V mm^{-1}, $\Delta t = 0.069\,$s. The error in $\mu_\perp/\mu_\parallel$ is the estimated standard error obtained from the covariance matrix of the fitted parameters.

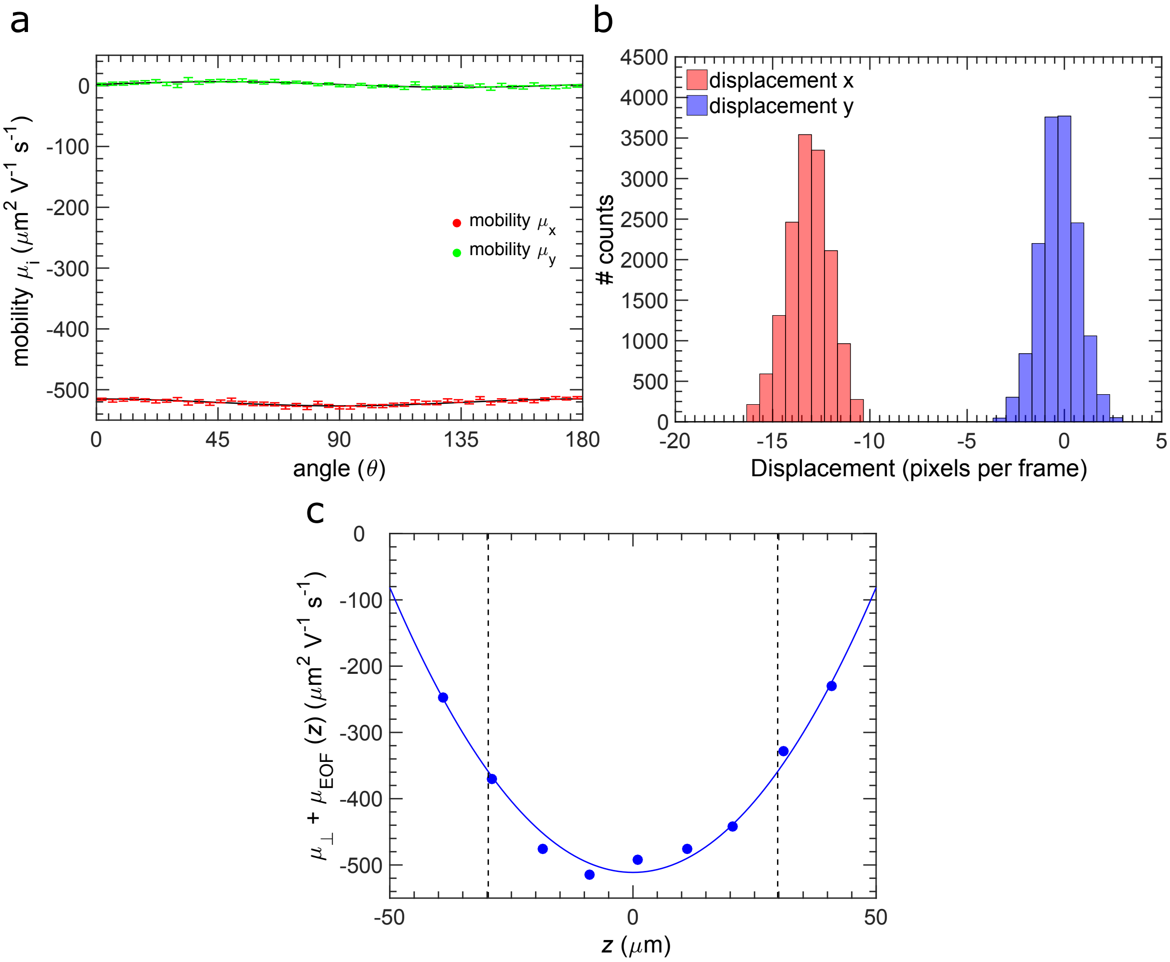

Figure A.5.5 Electrophoresis measurement of R2 silica rods dispersed in 85 wt% glycerol in water, with LiCl added, $\kappa a = 24.5$. **(a)** Orientation dependent mobility in x-direction (red symbols), parallel to electric field, and y-direction (green symbols), perpendicular to applied electric field. For clarity raw data is binned in 4° wide bins, the error bars indicate the standard error on the binned data points. The solid lines are a fit through the raw data using equation 5.10 (μ_x) and equation 5.11 (μ_y). **(b)** Histogram of the displacements of the rods in x and y direction. **(c)** Measured electrophoretic mobility profile of rods aligned with the long axis perpendicular to the electric field $\mu_\perp + \mu_{EOF}$ (blue circles), the dashed vertical lines indicate the stationary planes, where we determine $\mu_\perp$. We set $z = 0\,\mu\text{m}$ at the maximum of the parabolic profile. The solid blue line indicate a parabolic fit through the data. An anisotropy in mobility of $\mu_\perp/\mu_\parallel = 0.98 \pm 0.03$ was found and $\zeta = -68\,\text{mV}$, $E = 3.125\,\text{V}\,\text{mm}^{-1}$, $\Delta t = 0.863\,\text{s}$. The error in $\mu_\perp/\mu_\parallel$ is the estimated standard error obtained from the covariance matrix of the fitted parameters.

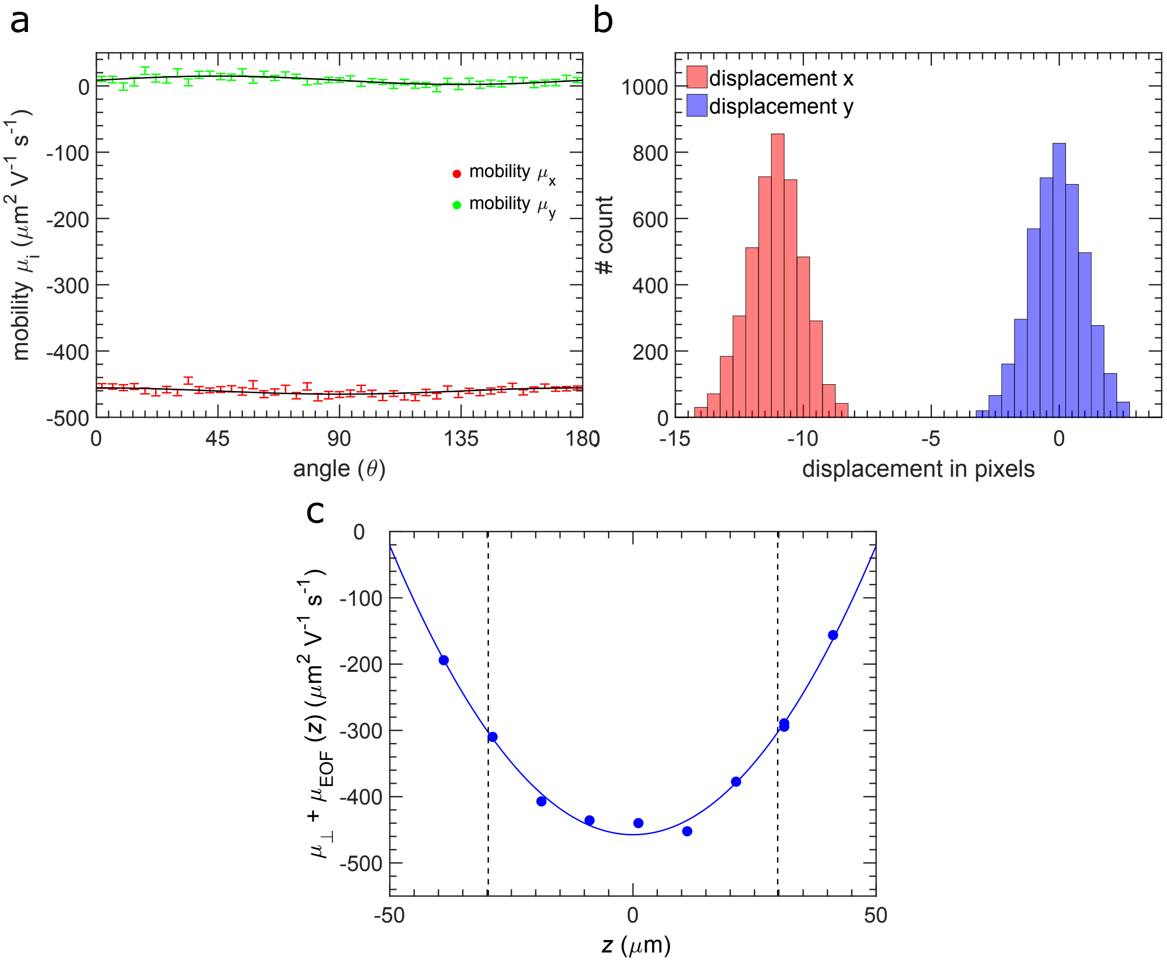

Figure A.5.6 Electrophoresis measurement of R2 silica rods dispersed in 85 wt% glycerol in water, without salt added, $\kappa a = 9.2$. **(a)** Orientation dependent mobility in x-direction (red symbols), parallel to electric field, and y-direction (green symbols), perpendicular to applied electric field. For clarity raw data is binned in 4° wide bins, the error bars indicate the standard error on the binned data points. The solid lines are a fit through the raw data using equation 5.10 (μ_x) and equation 5.11 (μ_y). **(b)** Histogram of the displacements of the rods in x and y direction. **(c)** Measured electrophoretic mobility profile of rods aligned with the long axis perpendicular to the electric field $\mu_\perp + \mu_{EOF}$ (blue circles), the dashed vertical lines indicate the stationary planes, where we determine $\mu_\perp$. We set $z = 0\,\mu\text{m}$ at the maximum of the parabolic profile. The solid blue line indicate a parabolic fit through the data. An anisotropy in mobility of $\mu_\perp/\mu_\parallel = 0.97 \pm 0.02$ was found and $\zeta = -57\,\text{mV}$, $E = 3.0\,\text{V}\,\text{mm}^{-1}$, $\Delta t = 0.863\,\text{s}$. The error in $\mu_\perp/\mu_\parallel$ is the estimated standard error obtained from the covariance matrix of the fitted parameters.

5.B Supporting Movies

Digital version Please click on the movie titles to get directed to the movie.

Printed version Please scan the QR code on the right to get directed to the supporting movies.

Orientation dependent mobility Confocal microscopy time series are shown during electrophoresis. The time series are shown at 2× real time. All movies are recorded at $z = z_{stat}$.

Movie 5.1 Shows the electrophoresis of R2 silica rods dispersed in pure 78 wt% DMSO-water, $\kappa a = 2.2$, $\eta = 3.542\,\mathrm{mPa\,s}$, $\epsilon_m = 56.1$. We measured an anisotropy of $\mu_\perp/\mu_\parallel = 0.664 \pm 0.006$.

Movie 5.2 Shows the electrophoresis of R2 silica rods dispersed in pure 85 wt% glycerol-water, $\kappa a = 9.2$, $\eta = 81\,\mathrm{mPa\,s}$, $\epsilon_m = 49.6$. We measured an anisotropy of $\mu_\perp/\mu_\parallel = 0.97 \pm 0.02$.

Movie 5.3 Shows the electrophoresis of SR29 silica rods dispersed in de-ionized CHC, $\kappa a = 0.04$, $\eta = 1.5675\,\mathrm{mPa\,s}$, $\epsilon_m = 7.6$. We measured an anisotropy of $\mu_\perp/\mu_\parallel = 0.89 \pm 0.02$.

6

Assembly of Thin Films of Silica Rods or Spheres

This chapter describes the preparation of thin colloidal films made of silica rods or spheres by spin coating or doctor blade coating (DBC), respectively. The first part of the chapter discusses spin coating of colloidal silica rods. By dispersing the silica rods in a mixture of a liquid acrylate monomer and 1-propanol, we obtained colloidal films with the rods radially aligned. The second part of the chapter investigates the process of DBC of colloidal silica spheres dispersed in a liquid monomer. The process of DBC was followed in real time and real-space using a DBC set-up mounted on an inverted confocal laser scanning microscope. We were able to determine the flow profile close to the blade. It was established that, in our case, capillary forces determined the properties of the obtained colloid crystalline film and we observed Landau-Levich flow. Moreover, we were able to make the colloidal crystalline film permanent by polymerizing the liquid monomer using UV light.

6.1 Introduction

Colloidal self-assembly into ordered crystalline arrays, with many interesting photonic properties, together with the use of these arrays as a template, have been of considerable interest in a wide range of applications including displays [107, 108], chemical [109, 110] and biological sensors [36, 111, 112], optical devices [291–293], antireflection coatings [113–115], spectrometers [294] and security data encryption [116, 117]. A variety of techniques, such as assembly by sedimentation [120, 121], convective self-assembly [122–125], Langmuir-Blodgett techniques [126], assembly using external electric or magnetic fields [68, 127, 128], shear alignment [87, 88], spin coating [83–85] and doctor blade coating (DBC) [66, 86, 129] are available to fabricate and direct the assembly of colloidal crystals. Often, these methods are not scalable to produce large quantities of colloidal crystals, but are only useful to produce small quantities in research laboratory set-up. Both spin coating and DBC are widely used in the coating, microelectronics, textile, paper, ceramics and printing industry [295–303] to produce uniform thin films over large areas. Therefore, both spin coating [83, 84] and DBC techniques [86] are suitable techniques to produce colloidal crystal on an industrial scale. More recently, a slightly different roll-to-roll process was developed using a bending-induced oscillatory shear technique, which can also be applied on an industrial scale. This process is related to both spin coating and DBC through the use of shear alignment and uses core-shell nanoparticles for which the elastomeric shell of the particles forms the continuous matrix of the colloidal crystal [89].

Whereas spin coating is still a batch process and needs relatively large amounts of dispersion, DBC is a continuous process and is more efficient. Also DBC can be employed as a roll-to-roll process [86]. Both spin coating and DBC techniques make use of shear alignment in order to obtain colloidal crystals [79–82]. In this chapter we investigate the potential of spin coating and DBC to form thin, ordered films of spherical and rod-like particles.

Colloidal spin coating is mostly done using spherical colloids [83, 84, 304] and to our knowledge spin coating has not been done with anisotropic particles. Anistropic colloids can be used as building blocks to obtain colloidal structures that are not accessible by using spherical colloids [34, 305]. For instance, an ordered phase of rods will diffract light preferentially along one axis. To be applicable on an industrial scale, anisotropic particles in an ordered phase need to be oriented in one direction over large areas. For the self-assembly into ordered structures additional fields are needed to control the orientation of anisotropic particles [64, 66, 70, 148, 306–308]. In spin coating the flow field can be used to align silica rods. In the first part of the chapter the spin coating of silica rods dispersed in a liquid monomer (ethoxylated trimethylolpropane triacrylate, ETPTA) is described. When 1-propanol was added to the dispersion, we were able to obtain a colloidal film with the silica rods radially aligned along the direction of flow.

In the second part of the chapter we describe DBC of silica spheres dispersed in ETPTA. Not many experimental papers are available were DBC is used to obtain crystalline colloidal films [86, 309–312]. Using silica spheres dispersed in ETPTA it was shown that the thickness of the obtained films was dependent on the substrate velocity used, but also on particle concentration and the particle sizes used [86]. Yang *et al.* argued that pressure driven flow determined the properties of the particle films. However, the exact mechanism for colloidal crystal formation during DBC is not known. In order to obtain more insight in the DBC process we developed a system to follow this process in real time and real-space using confocal microscopy. We studied DBC of fluorescently labeled silica spheres dispersed in ETPTA, such that the spheres could be resolved with confocal microscopy. We characterized the recorded flow profiles during DBC using a digital particle image velocimetry (DPIV) algorithm [313–315]. We obtained colloidal crystalline films and we observed Landau-Levich type flow [316], commonly seen in dip-coating of fluids, at the parameters used here. For a Landau-Levich film, the thickness of the resulting film is a balance between the viscosity of the solvent and capillary forces. Moreover, we were able to make the colloidal crystalline films permanent by polymerizing the ETPTA with UV light. Finally, we tested DBC for silica rods. DBC is a promising technique to obtain a uniform films of aligned anisotropic particles, when the flow is mainly shear-driven and a plane of zero-shear is absent [299]. In this way, shear induced ordering is facilitated troughtout the whole particle film.

6.2 Theoretical Framework

6.2.1 Spin Coating

Spin coating is widely used to produce uniform films on thin substrates [295–298]. The formation of films during spin coating can be described in three steps: first, the deposition of the fluid on a substrate; second, the spin-up cycle where the fluid covers the entire substrate; and the third step, the spin-off cycle where the film reaches the desired thickness and excess fluid is flung off the substrate by spinning at higher speeds. The resulting film thickness and uniformity can be tuned by changing the spin time and spin speed. This behavior is dependent on whether the spincoated fluid is a Newtonian fluid, a non-Newtonian fluid, a Bingham plastic-fluid, and/or evaporates (partly) during spin coating and is described in several models [295, 317–319].

In this section a simplified model for spin coating of Newtonian fluids [295] is discussed, that describes the spin-off cycle of spin coating during which particle ordering takes place. For this model the following assumptions are made: the fluid is Newtonian; the process is cylindrically symmetric; there is no evaporation and the density of the fluid stays constant during spin coating; the gravitational force normal to the surface can be neglected as the fluid layer is thin and there is only net flow in the radial direction: $v_z \approx 0$, $v_\theta \approx r\omega$, where v_z is the fluid velocity in vertical plane ($\mathrm{m\,s^{-1}}$), v_θ the tangential velocity ($\mathrm{m\,s^{-1}}$), r the radial position (m) and ω the angular velocity of the disk ($\mathrm{rad\,s^{-1}}$).

The force balance can be written as a balance between the viscous force of the fluid and the centrifugal force resulting from the rotating disk

$$-\eta\frac{\partial^2 v_r}{\partial z^2} = \rho\omega^2 r, \tag{6.1}$$

where η is the viscosity of the medium (Pa s), v_r the radial velocity of the fluid ($\mathrm{m\,s^{-1}}$), z the height in the fluid layer (m), ρ the density of the fluid ($\mathrm{kg\,m^{-3}}$). We can integrate this force balance to obtain the fluid velocity in the film, by using the following boundary

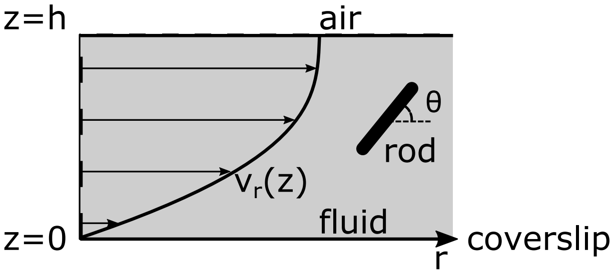

Figure 6.1 Schematic representation of the flow profile of a fluid on a rotating disk, which is half of a parabola. Image adapted from ref. 85.

conditions: it is assumed that that there is no slip at the substrate ($v_r|_{z=0} = 0$) and zero stress at the air-liquid interface ($\eta \frac{\partial v_r}{\partial z}|_{z=h} = 0$), where h is the local film thickness.

$$v_r(z,h) = \frac{\rho\omega^2 r}{\eta}(hz - \frac{1}{2}z^2) \tag{6.2}$$

From this equation it can be seen that the flow profile is half a parabola, see Fig. 6.1. The shear rate is defined as $\dot{\gamma} = \frac{\partial v_r}{\partial z}$. Hence, the shear rate during spin coating can be written as

$$\dot{\gamma} = \frac{\rho\omega^2 r}{\eta}\left(h - z\right). \tag{6.3}$$

In order to obtain the height of the film after spin coating, we need an expression for the volumetric flow. Integration of the radial flow velocity over the height of the film gives the volumetric flow per unit length of the circumference

$$q = \int_0^h v_r(z,h)dz = \frac{\rho\omega^2 r h^3}{3\eta}. \tag{6.4}$$

By applying the equation of continuity, we obtain a differential equation for the height of the liquid film h,

$$r\frac{\partial h}{\partial t} = -\frac{\partial(rq)}{\partial r}. \tag{6.5}$$

Hence, we can obtain

$$\frac{\partial h}{\partial t} = -\frac{\rho\omega^2}{3\eta r}\frac{\partial}{\partial r}\left(r^2h^3\right). \tag{6.6}$$

In the case that the fluid layer is uniformly spread over the substrate after the spin-up cycle, h does not depend on r

$$\frac{dh}{dt} = -\frac{2\rho\omega^2 h^3}{3\eta}, \tag{6.7}$$

after integration we obtain $h(t)$

$$h(t) = \frac{h_0}{\sqrt{\left(\frac{4\rho\omega^2 h_0^2 t}{3\eta} + 1\right)}}. \tag{6.8}$$

Note that, also for liquid films that are initially non-uniform in thickness, Emslie *et al.* showed that the liquid layer, in case of a Newtonian fluid, spreads out to a layer of more or less uniform thickness [295].

6.2.2 Flow Behavior of Rod-like Particles

Rod-like particles can exhibit different behavior when subjected to shear flow. Theoretically, the behavior of hard rods under shear flow can be described by the Doi-Edwards-Hess theory [90, 91]. The theory describes the time evolution of the orientation probability density function and predicts that the average orientation of the rods can dynamically change. Depending on the shear rate and concentration the rods can exhibit a flow aligning, tumbling, kayaking, wagging and log-rolling motion [320]. At low shear rates 'tumbling' is found where the average director of the rods rotates in the shear plane. At intermediate shear rates, the director oscillates in the shear plane between two limiting angles, this is called 'wagging'. If the initial director is out of the shear plane also a 'kayaking' motion is expected where the kayaking orbit is out of the shear plane. At low shear rates, with initial director out of the shear plane, a stable phase is found with the director perpendicular to the shear plane called the 'log-rolling' regime [321]. At higher shear rates the director aligns with the flow, and a shear aligned or para-nematic phase is expected. These states were also found with Brownian Dynamics simulations for rod with length of diameter ratio $20 < L/D < 60$ [94, 95]. Experimentally, the tumbling, wagging and flow aligned were observed using *fd*-viruses [92, 93]. Moreover, at again higher shear rates shear thickening behavior was found in experiments [65, 93], although this is not supported by theoretical predictions.

A dimensionless rotational Peclet number Pe_r can be determined that represents the interplay between the randomizing rotational Brownian motion and the alignment due to flow

$$Pe_r = \frac{\dot{\gamma}}{2D_r}, \tag{6.9}$$

where the time scale associated with flow is $1/\dot{\gamma}$ and $2D_r$ the rotational relaxation time of the rod. If $Pe_r \gg 1$ flow is dominant and shear-induced alignment can be expected. If $Pe_r \ll 1$, Brownian motion is dominant and not much influence from shear flow is expected.

In order to obtain alignment over large areas laminar flow is needed. Therefore, the Reynolds number Re, which indicates the ratio of the inertial forces over the viscous forces, needs to be small. The Reynolds number is given by [322]

$$Re = \rho v h/\eta, \tag{6.10}$$

with v the velocity of the solvent.

6.3 Methods

Dispersions Properties of particles used for spin coating and DBC can be found in Table 6.1. Particles were transferred from ethanol to the liquid monomer ethoxylated trimethylolpropane triacrylate (ETPTA, Mw. 428, Sigma-Aldrich) for both spin coating and DBC. First, a stock dispersion of particles in ethanol was centrifuged and the ethanol was carefully removed with a pipette. After, ETPTA was added such that desired particle volume fraction was obtained. The particles were redispersed by sonication or vortexing. The remaining ethanol was evaporated by heating the dispersion to 32 °C for about

Table 6.1 Properties of particles used in this chapter.
With L being the end-to-end length of the rod, D the diameter of the particle, L/D the aspect ratio of the particle, $D_\perp$ and $D_\|$ the translational diffusion coefficient perpendicular and parallel to the rod long axis, respectively, calculated from their TEM dimensions and D_r calculated for rods in pure ETPTA, with $\eta = 70\,\mathrm{mPa\,s}$ [250].

	L µm	δ_L %	D µm	δ_D %	L/D	$D_\perp/D_\|$	D_r $\mathrm{rad^2\,s^{-1}}$
Rods							
I02	1.42	14	0.24	21	5.9	0.77	0.0247
R10	2.56	9	0.38	12	6.8	0.75	0.0046
R10-2	2.40	11	0.36	15	6.6	0.76	0.0055
R12	2.72	11	0.40	12	6.9	0.75	0.0038
R2	3.59	18	0.59	10	6.1	0.76	0.0015
Spheres							
D970			0.97	3			

30 minutes, while gently stirring under a flow of nitrogen. The as prepared dispersions had a particle volume fraction between 7.5–52.5 vol%. Before spin coating we added in some cases technical grade ethanol (Interchema), 1-propanol (Merck) or 1-butanol (Acros Organics) to the dispersions to obtain a 1:1 v/v alcohol-solvent mixture.

Spin coating The substrates for spin coating were standard 22 mm diameter round coverslips (Thermo Scientific, no. 1, thickness 0.13–0.16 mm). Coverslips were cleaned with piranha acid before use, a 3:1 mixture of concentrated sulfuric acid (H_2SO_4, 98%, Acros Organics) and hydrogen peroxide (H_2O_2, 30 wt%, Sigma-Aldrich), in order to improve the wetting of the coverslips with ETPTA. After cleaning the coverslips with piranha acid, the coverslips were subsequently rinsed with ultrapure water (Milipore) and 100% ethanol and stored in 100% ethanol until use. A droplet of 20 µL dispersion was placed on a coverslip and then the spin-cycle was started. The spin coater (model P6700, Specialty Coating Systems, USA) first rotated slowly (200–1400 rpm) for 1–3 minutes during the spin-up cycle, uniformly spreading the dispersion on the coverslip, and then faster (600–3400 rpm) for 3–5 minutes during the spin-off cycle to obtain a thin film and spin off excess fluid.

Doctor blade coating We also prepared thin colloidal crystalline films using a DBC technique [86, 309–312]. For DBC we used a modified parallel plate shear cell on top of an inverted confocal scanning laser scanning microscope (Leica TCS SP2) [323], from which the top plate was replaced by a cassette which contained a perpendicular razor blade (Merkur, 908 100), which was made 0.4 cm in width. Figures 6.2a-b display images of the top cassette. The height of the perpendicular blade could be adjusted on the micrometer scale using a precision micrometer head. During DBC the blade remained stationary and

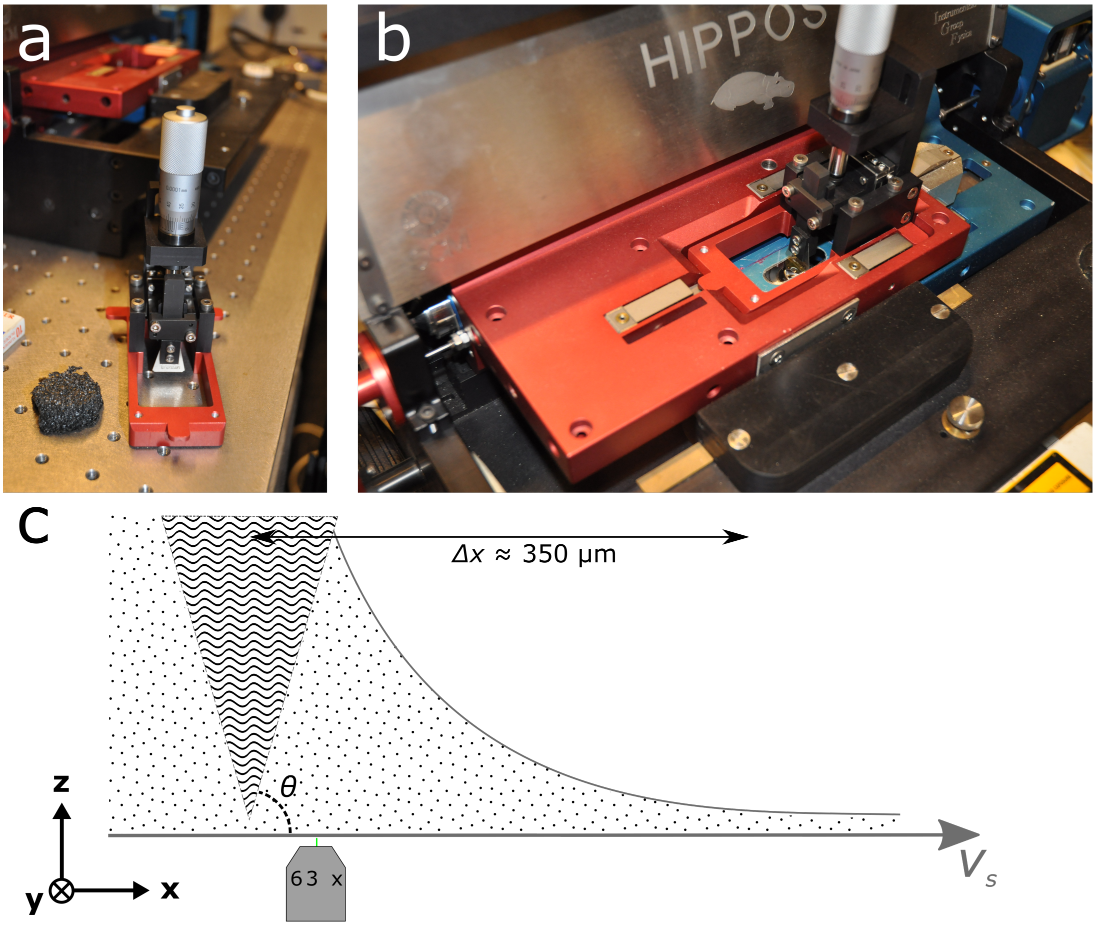

Figure 6.2 Doctor blade coating set-up. **(a)** Cassette containing perpendicular blade fitted for the parallel plate shear shell [323]. **(b)** Cassette as mounted on the parallel plate shear shell, the bottom plate (blue) moves with respect to the blade. **(c)** Schematic of DBC, upstream from the blade (left) the dispersion is loaded and the substrate moves with a velocity v_s to the right. Imaging is done from below the substrate. The blade had an angle $\theta \approx 75°$ with the substrate and a width $\Delta y = 0.4\,\mathrm{cm}$.

the substrate was moved, with a velocity v_s, to obtain a thin film. In our experiments the gap between the blade and the substrate was $\sim 2\,\mu\mathrm{m}$, and the substrate moved with $v_s = 1$–$1000\,\mu\mathrm{m\,s^{-1}}$. The substrate, a 24 mm × 50 mm glass coverslip (Menzel Gläzer, no. 1.5, thickness 0.15–0.17 mm) was mounted to the bottom cassette as described by Wu *et al.* [323]. In this way, using confocal microscopy, we were able to follow in real time and real-space the DBC process. In order to keep a constant gap between the blade and the substrate during coating, the cassettes were aligned one by one. The alignment was checked using the reflection mode of the confocal microscope by using an air confocal objective (Leica, 20× 0.7 NA). For quantitative particle imaging the objective was changed to an immersion-oil confocal objective (Leica, 63× 1.4 NA). The sample was loaded by placing a 0.4–2 μL drop of particle dispersion upstream from the blade (see Fig. 6.2c).

Confocal Microscopy and Image Analysis The obtained particle films of silica rods were imaged with confocal scanning laser microscopes (Leica TCS SP2 or SP8) using a 63× 1.4 NA oil-immersion confocal objective (Leica). We analyzed the alignment of the rods inside the films by using the OrientationJ plugin from the ImageJ (1.49m, NIH) software [324]. This was done as the particles did not had a large enough non-fluorescent outer shell that allowed for particle tracking. The OrientationJ routine computes the structure tensor J for each pixel in the image, given by the 2×2 symmetric matrix

$$J = \begin{pmatrix} \langle f_x, f_x \rangle_w & \langle f_x, f_y \rangle_w \\ \langle f_x, f_y \rangle_w & \langle f_y, f_y \rangle_w \end{pmatrix}, \tag{6.11}$$

with f_i the spatial derivatives of the images $f(x, y)$ calculated using a cubic B-spline interpolation [324–326]. The brackets indicates a weighted inner product

$$\langle a, b \rangle_w = \int\int_{R^2} w(x,y) a(x,y) b(x,y) dxdy, \tag{6.12}$$

with $w(x, y)$ a Gaussian window of the size of the region of interest. The local orientation in each pixel is then given by the eigenvector corresponding to the largest eigenvalue of the tensor. A Gaussian window with a width (standard deviation) of 3 pixels was used for the analysis. A pixel orientation distribution was then obtained and from this the projected 2D nematic order parameter $S_{2D'}$ was calculated, given by diagonalizing the 2×2 nematic order parameter tensor

$$\mathcal{Q}_{\alpha\beta}{}^{2D} = \frac{1}{N} \sum_{i=1}^{N} \left[2\mathbf{u}'_{i\alpha} \mathbf{u}'_{i\beta} - \delta_{\alpha\beta} \right], \tag{6.13}$$

with N the number of pixels in the image, $\mathbf{u}'_{i\alpha}$ the a-component of the unit vector describing the main orientation of pixel i, $\delta_{\alpha\beta}$ the Kronecker delta and $\alpha, \beta = x, y$. The 2D nematic order parameter $S_{2D'}$ is defined as the largest eigenvalue of $\mathcal{Q}$ and the corresponding eigenvector is the projected nematic director $\hat{\mathbf{n}}'$

$$S_{2D'} = 2\langle \cos^2 \theta \rangle - 1, \tag{6.14}$$

where $\cos\theta = \hat{\mathbf{u}}' \cdot \hat{\mathbf{n}}'$, with $\hat{\mathbf{u}}'$ the unit vector along the projected main orientation of the pixels.

Digital Particle Image Velocimetry In order to visualize the particle flow during DBC, xzt-series were recorded. Digital Particle Image Velocimetry (DPIV) was used to obtain the average flow field from these xzt-series. We used `PIVlab` a time-resolved digital particle image velocimetry tool for MATLAB (`PIVlab` 1.41, in Matlab R2016a) to process our confocal data into vector maps of the local flow fields [313–315]. Time-resolved digital particle image velocimetry needs and image pair at t_0 and $t_0 + \Delta t$. From the (average local) particle displacements between image t_0 an $t_0 + \Delta t$ the velocities of the particles can be determined. In DPIV the displacement of groups of particles, that are present in sub regions or interrogation areas in the image, are determined. Thus, DPIV does not not determine the displacements of single particles. DPIV evaluates the crosscorrelation matrix of these sub regions. The peak in the crosscorrelation matrix gives the most likely displacement for one sub region between image t_0 and $t_0+\Delta t$. A discrete fourier transform (DFT) with window deformation algorithm in `PIVlab` was used to calculate the vector maps of the flow field during DBC. We used three pass DFT with an interrogation area that decreased every pass. We used the following decreasing sizes for the interrogation area: 64 × 64 pixels, 48 × 48 pixels and 24 × 24 pixels. Data was preprocessed by applying contrast limited adaptive histogram equalization (CLAHE) to all the images of the time series [313–315], it spreads the most frequent intensities of the intensity histogram over the full 8-bit range from 0 to 255. CLAHE operates on subimages within the image to adjust the intensity. Sub-pixel accuracy on the average particle displacements in `PIVlab` is obtained by fitting a 3-point Gaussian fit through the integer crosscorrelation matrix in both the horizontal and vertical direction. After crosscorrelation, some erroneous vectors were obtained, which were the outliers in the data. In order to remove these outliers, we used a scatter plot of $v_x\hat{\mathbf{i}}$ and $v_y\hat{\mathbf{j}}$ component vectors to clip out these outliers, in our case less than 2% of the original data was removed. Missing vectors were then replaced by vectors obtained by interpolation of the surrounding data. To obtain the average flow profile, we averaged the vector plots of subsequent image pairs (1 + 2, 3 + 4, etc.).

6.4 Results & Discussion

6.4.1 Spin Coating

Spin Coating of Silica Spheres Before spin coating with colloidal silica rods, we tested that spin coating of monodispersed silica spheres resulted in uniform crystalline particle films as seen in ref. 85. Indeed, spin coating of 15 vol% 970 nm silica spheres dispersed in ETPTA, with a spin-up cycle of 60 s, 400 rpm and a spin-off cycle of 60 s, 2000 rpm, yielded a uniform crystalline film, see Fig. 6.3a for a confocal image. The as prepared film completely wetted the surface and it did not dewet in time. The corresponding fast Fourier transform (FFT) image in Fig. 6.3b was made by applying a 2D FFT algorithm from Matlab (R2016a) to the confocal image. Before applying the FFT algorithm, we used a 2D Hann window to avoid artefacts due to the finite size of the image. The FFT image shows a six-fold symmetry with distinct peaks, confirming the crystalline order.

Spin-up Cycle In order to obtain uniform particle films of silica rods, we first investigated which parameters led to the best substrate coverage during the spin-up cycle. For the spin-up cycle we varied the volume fraction of rods between 10–30 vol% and varied the spin-up speeds between 200–1400 rpm. For 19 vol% I02 rods best spreading was obtained at spin speeds between 600–1400 rpm. For 30 vol% R10 rods, best spreading was obtained at spin speeds between 800–1000 rpm and a spin time of 180 s. For 10, 20 and 30 vol% R10-2 rods, best spreading was obtained at a volume fraction of 10 vol% at 600 rpm. Although, large variations in substrate coverage could be found from sample to sample taken with the same spin-up cycle.

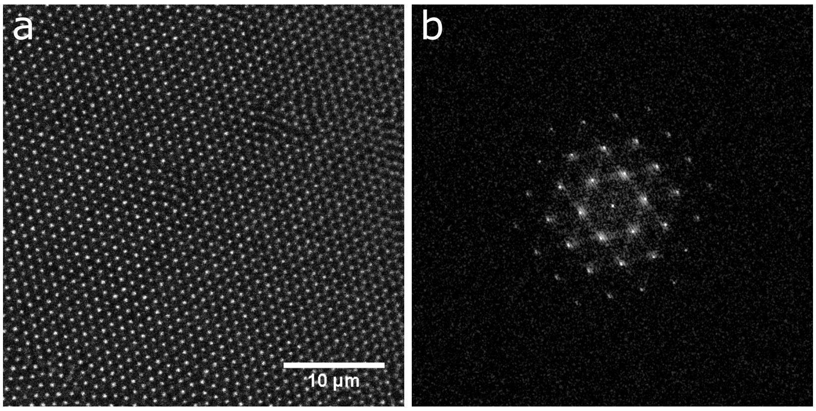

Figure 6.3 Part of the resulting particle film after spin coating, using 15 vol% 970 nm silica spheres in ETPTA with a spin-up cycle 60 s, 400 rpm and a spin-off cycle 60 s, 2000 rpm. **(a)** Confocal image. **(b)** Corresponding FFT image showing six-fold symmetry with distinct peaks.

In case of good substrate coverage, we obtained a thin film in the middle of the coverslip, while at the edges there was accumulation of sample, see Fig. 6.4a for a schematic. Often still some small gaps in the film were present. The accumulation of dispersion is caused by a discontinuity of the surface forces on the fluid film at the edge of the coverslip [295]. When substrate coverage was poor, only part of the coverslip was coated, see Figs. 6.4b-c. Poor coverage can have different reasons. When the sample was spun at low spin speeds the dispersion did not spread over the entire coverslip, see Fig. 6.4b for a schematic. However, often we found that the dispersion reached the edges of the coverslips, but large areas of the coverslip were still uncoated, Fig. 6.4c for a schematic. The reason for this is not known, although we hypothesize that the average orientation of rods in the droplet varied. As the viscosity of the dispersion is dependent on the orientation of the rods, this influenced the flow of the dispersion droplet over the substrate. Resulting in a spider-like circumference of the film on the coverslip.

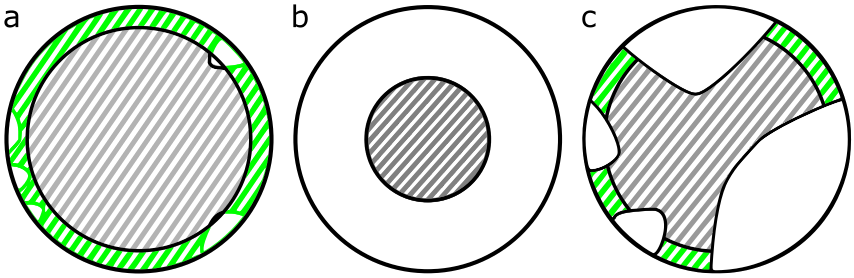

Figure 6.4 Schematic of coverslip coverage after spin coating. **(a)** Good coverage, with still some holes. **(b-c)** Poor coverage due to low spin speeds used, **(b)** or different reasons **(c)**. The hatched gray area is covered with a film; green area indicates an accumulation of sample.

During the spin-up cycle, the parameters needed to obtain proper substrate coverage turned out to be specific to the batch of rods used, for which the dimensions differed slightly from batch to batch. Only a narrow range of parameters values, led to proper substrate coverage. This spin-up cycle for rods differed to that of spheres, as for spheres a shorter spin time and a slower spin speed were needed to obtain proper coverslip coverage [85].

Spin-off Cycle After establishing the best spin-up cycle for the different batches of rods, we investigated the effect of different spin-off cycles on the structure of the film and the alignment of the rods inside the film. We varied the spin-off time between 180–540 s, the spin-off speed between 600–3400 rpm, but we were not able to obtain uniform particle films of silica rods for which the silica rods were radially aligned. When alignment of rods within the sample was found, also large variations in film thickness, density of silica rods and areas without alignment of rods were found in the same sample. For I02 rods, proper substrate coverage was obtained, however, no alignment was observed in the resulting particle films.

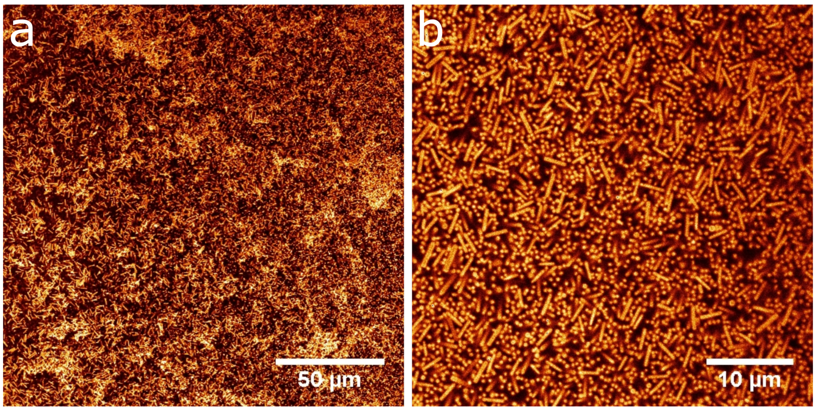

Figure 6.5 Result of spin coating using 10 vol% R10-2 rods in ETPTA with a spin-up cycle 180 s, 600 rpm and a spin-off cycle 180 s, 1400 rpm. **(a)** Confocal image showing inhomogeneous spreading of rods. **(b)** Confocal images showing the occurrence of a high area fraction of standing rods in the sample.

A few trends during the spin-off cycle of silica rods were observed. When large spin-off speeds (for R10 $>$ 2200 pm, for R10-2 rods $>$ 1000 rpm) were used, we found large variations in the rod density and clusters of rods inside the particle film, see Fig. 6.5a. Sometimes, rods were found to be oriented perpendicular to the direction of shear and the direction of flow during spin coating, see Fig. 6.5b. These non-uniformities in density and orientation may well lead to local differences in viscosity and therefore in a non-uniform flow, preventing the formation of a well-ordered film. Next, increasing the time of the spin-off cycle did not improve the alignment and structure of the resulting films. Actually, best alignment was found, when the speed of the spin-off cycle was the same as the spin-up cycle. Finally, in case no alignment was found in the center of the film, we did often found radial alignment at the edge of the coverslip, where an accumulation of dispersion was found, see Fig. 6.6. In this case, the shear needed to spread the dispersion was too large to obtain aligned silica rods in the center of the coverslip and led to non-uniformities in the particle film. In contrast, at the edge the flow and shear forces are less due to a discontinuity of surface forces [295] and the rods were found to radially align.

This indicated that a balance is needed between the shear that is needed to spread the dispersion and shear needed to align the rods.

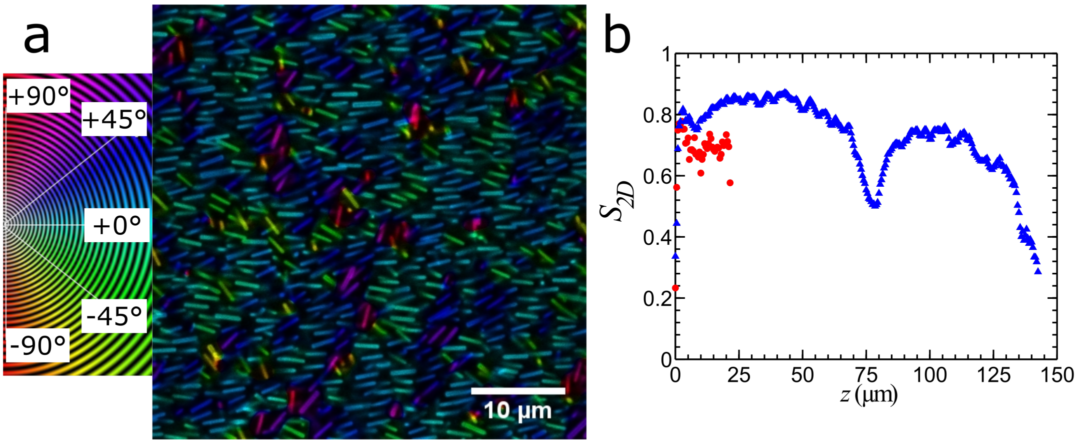

Figure 6.6 Result of spin coating using R10-2 10 vol% rods in ETPTA with a spin-up cycle 360 s, 600 rpm. **(a)** Confocal image taken at height 10 µm at the edge of the coverslip 180°, the color indicates the direction of the average pixel orientation. **(b)** The value of the projected 2D order parameter ($S_{2D'}$) as function of height at two different location in the sample; at the edge of the coverslip (▲) or halfway the coverslip (r = 6 mm, ●).

Spin coating of silica rods in pure ETPTA did not result in uniform particle films with the rods radially aligned. We did not expect that sedimentation affected the structure inside the particle film. A single R12 will sediment 3.25 µm over 15 min, the course of an experiment ($v_{sed} = 3.8\,\mathrm{nm\,s^{-1}}$). The variations in jamming and alignment of particles films indicated that the flow dynamics during spin coating of silica rods were far more dynamic that the simplified theory given in Section 6.2.1. Moreover, rods subject to shear flow are known to show collective motions which are different from shear alignment, as described in Section 6.2.1. For a typical shear rate of 600 rpm and film thickness of 20 µm, the maximum shear rate given by equation 6.3, at 6 mm from the center of the coverslip and at the bottom of the film ($h = 0\,\mu\mathrm{m}$), is $\dot{\gamma} = 10\,\mathrm{s^{-1}}$. For this we used the viscosity of pure ETPTA ($\eta = 70\,\mathrm{mPa\,s}$), and the average density of a dispersion with $\phi = 0.3$, $\rho_{average} = 1690\,\mathrm{kg\,m^{-3}}$. Due to the higher particle density, the viscosity is expected to be higher than the pure solvent, giving a slightly lower $\dot{\gamma}$. Nevertheless, $Pe_r \approx 10^3$ so that shear alignment of rods is expected under these circumstances. However, it still shows that using these parameters, we are likely in the regime where earlier non-collective rotation and turbulent motion of rods was observed [65]. At these high rod densities the tumbling and rotation of one rod can affect many other rods and hence could have given rise to jamming and standing rods as we observed during spin coating.

Spin Coating with 1-propanol In order to overcome the problem of poor spreading during the spin-up cycle and undesirable collective motions of the silica rods, we tested spin coating of 5, 10 and 15 vol% R12 silica rods dispersed in a 1:1 v/v 1-propanol:ETPTA solvent mixture. Adding 1-propanol to the system reduced the viscosity of the dispersion, and therefore improved the spreading of the dispersion during the spin-up cycle. Also, 1-propanol is volatile and will evaporate during spin coating. This increases the final volume fraction of the particles in the film and hence reducing most likely the randomization after film formation. Thus, we expected the following mechanism: first, we started with an isotropic state and the rods shear aligned in a para-nematic phase; As the 1-propanol evaporated the volume fraction of rods increased and a radially aligned nematic phase was obtained. Samples were spincoated with only a spin-up cycle, with spin-time 180 s and spin-up speed between 100–800 rpm. At spin speeds between 400–600 rpm and 15 vol% of rods, we found radial alignment of rods. Figure 6.7a shows an example of a radially aligned colloidal rod film after spin coating with a spin-up cycle of 180 s and 400 rpm. Figure 6.7b shows that in most spots on the sample a high values of $S_{2D'}$ also persisted higher up in the film away from the coverslip. Close to the air-fluid interface the alignment of the rods was seen to decrease. Probably, this happens because the shear rate goes to zero at the air-fluid interface, see Fig. 6.1. Moreover, during imaging still some flow and drift was present in the samples, probably because not all of the 1-propanol had evaporated after the spin-cycle was completed. Therefore, the radial alignment only persisted for ~ 30 minutes. Next, the height of the sample still varied from spot to spot, we obtained a thickness between 20 µm and 50 µm. We expect that due to the evaporation of 1-propanol from the substrate concentration gradients can occur and that the resulting Marangoni effect can interfere with a smooth particle layer [327, 328]. Due to a concentration gradient along the interface, also a surface tension gradient exist. This surface tension gradient causes flows along the interface and this is known as the Marangoni effect.

Spin coating with ethanol or 1-butanol instead of 1-propanol was also tested. Dispersions of rods prepared with ethanol did not spread properly during spin coating, as the ethanol evaporated before proper spreading of the dispersion and alignment of the rods was achieved. Some preliminary tests were done in which air inside the spincoater was saturated with ethanol, during spin coating with an ethanol-ETPTA mixture. However, this still led to improper spreading of the dispersion on the substrate. When using dispersions prepared with 1-butanol, the evaporation of the alcohol was too slow. Therefore the evaporation of 1-butanol still occurred after the spin cycle was completed, resulting in flows in the sample that destroyed the alignment obtained by spin coating.

In conclusion, spin coating of rods in order to obtain radially aligned particle films appeared to be less straight forward, compared to spin coating of spheres. By adding 1-propanol to a dispersion of silica rods in ETPTA, we were able to obtain thin films of silica rods with the rods radially aligned, for which the ordering persisted also higher up in the film. Many parameters, such as spin-time, spin-speed, particle concentration, viscosity of the dispersion, etc, influence the process of spin coating. Therefore, this huge parameter space still offers many possibilities to improve the protocol to obtain uniform films of silica rods with the rods radially aligned along the direction of flow. In future the ETPTA can be polymerized using UV light by adding a photo-sensitive initiator to the dispersion, as described in Section 6.4.2 below. In this way the obtained particle film can be made permanent and a free standing colloidal particle film can be obtained [83, 85].

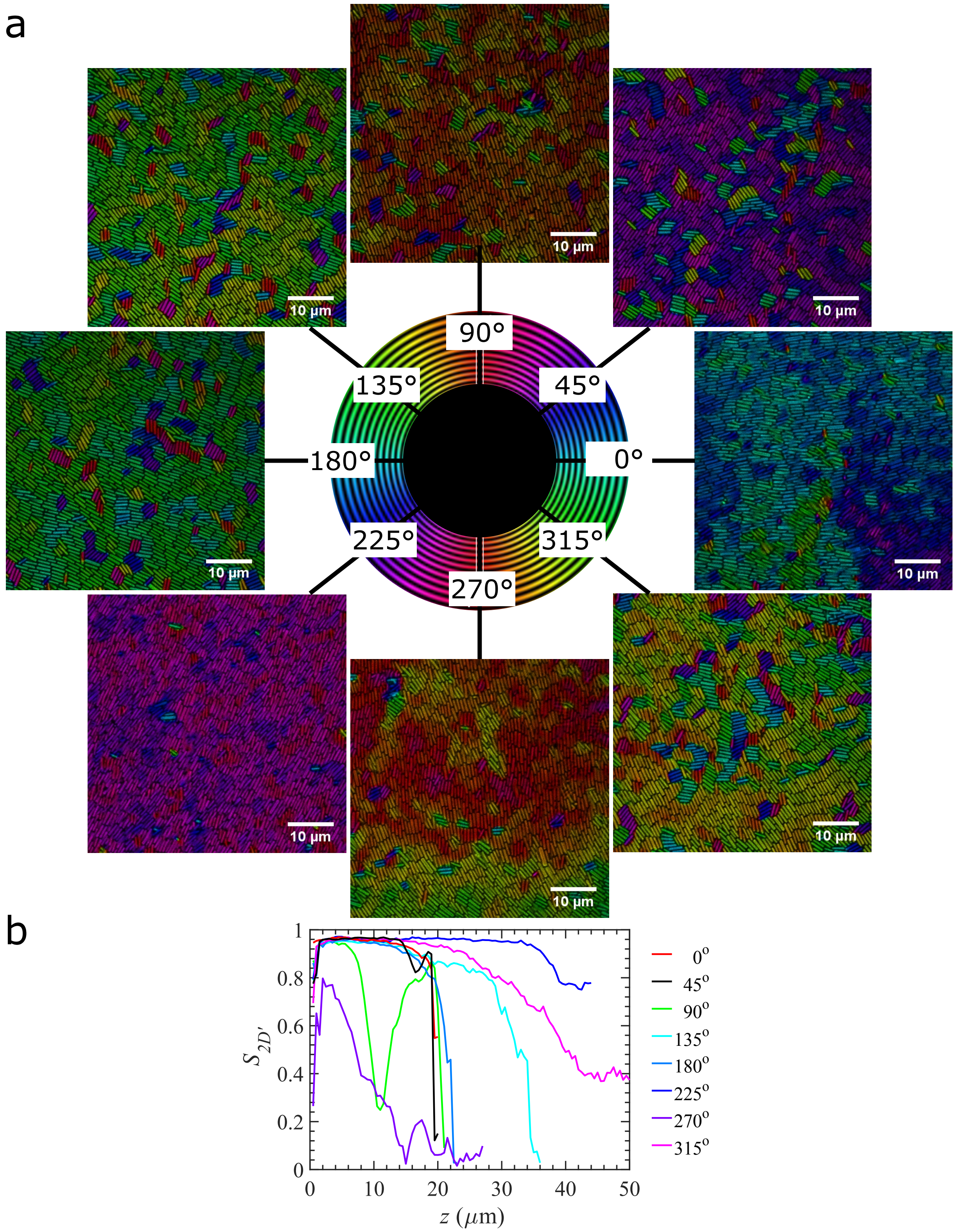

Figure 6.7 Radial alignment of spincoated sample of 15 vol% R12 silica rods in 1-propanol:ETPTA at 180 s, 400 rpm. **(a)** Confocal images taken in a circle around the center of rotation. The color indicates the (projected) orientation of the pixels in the 2D plane, as shown on the circular colormap in the middle. **(b)** Projected 2D nematic order parameter $S_{2D'}$ as function of height of spots shown in **(a)**.

6.4.2 Doctor Blade Coating

Resulting Particle Films With doctor blade coating (DBC) we prepared colloidal films made of 970 nm diameter FITC-labeled silica spheres dispersed in ETPTA. The silica spheres used here were larger compared to the silica spheres used earlier [86], which had a size of 290–560 nm. We used core-shell fluorescently labeled silica spheres, which consisted of a fluorescently labeled silica core with a thick non-fluorescent silica shell. In this way we were able to resolve individual silica particles during DBC. We used dispersions with different initial particle concentrations of 9–52.5 vol% and we used different substrate velocities between $v_s = 0.5\,\mu\mathrm{m\,s^{-1}}$ and $1000\,\mu\mathrm{m\,s^{-1}}$. At 43.8 vol% and 52.5 vol% the dispersions were crystalline without applied shear. The parameter range was chosen such that we could compare our results with ref. 86, where a particle concentration of 20–50 vol% and substrate velocities between $v_s = 0.1\,\mu\mathrm{m\,s^{-1}}$ and $16\,\mu\mathrm{m\,s^{-1}}$ were used.

After DBC we examined the resulting film on four different spots using confocal microscopy. Fig. 6.8 shows confocal images of the resulting particle films obtained after DBC. The fast Fourier transform (FFT) images in Fig. 6.8 were made by applying a 2D FFT algorithm from Matlab (R2016a) to the images. Before applying the FFT algorithm, we used a 2D Hann window to avoid artefacts due to the finite size of the images. For dispersions with 8.8 vol% silica spheres, we obtained films that were one particle layer thick for $v_s = 2.5\,\mu\mathrm{m\,s^{-1}}$–$30\,\mu\mathrm{m\,s^{-1}}$. At this vol% and these substrate velocities the films were not crystalline, see Figs. 6.8a-c. For $v_s = 100\,\mu\mathrm{m\,s^{-1}}$ a thin film with crystalline patches was obtained, see Figs. 6.8d-f. For dispersions with 17.5–52.5 vol% spheres in ETPTA we obtained crystalline films with $v_s = 30\,\mu\mathrm{m\,s^{-1}}$–$100\,\mu\mathrm{m\,s^{-1}}$, see Figs. 6.8g-i. At lower blade velocities we did not always obtain crystalline films, but mostly thin colloidal films with some crystalline patches. Fully crystalline films were obtained with 35.0 vol% particles, $v_s = 10\,\mu\mathrm{m\,s^{-1}}$; 43.8 vol% particles, $v_s = 1\,\mu\mathrm{m\,s^{-1}}$ and $v_s = 5\,\mu\mathrm{m\,s^{-1}}$; 52.5 vol% particles, $v_s = 2.5\,\mu\mathrm{m\,s^{-1}}$.

We also tested substrate velocities $v_s = 100\,\mu\mathrm{m\,s^{-1}}$ and $v_s = 500\,\mu\mathrm{m\,s^{-1}}$ for particle concentrations of 43.8 vol%. This resulted in thicker films between 8 and 16 µm thick that were crystalline in the lower part of the film, but at the top these films were not crystalline, see Fig. 6.9a for an example. However, by blading the particle film for a second time, with the blade $\sim 10\,\mu\mathrm{m}$ lifted, we obtained films that were crystalline over the full height of the film, although these films were less thick $\sim 8\,\mu\mathrm{m}$, see Fig. 6.9b. We also tested this double blading technique with higher substrate velocities $v_s = 600\,\mu\mathrm{m\,s^{-1}}$ and $v_s = 1000\,\mu\mathrm{m\,s^{-1}}$. Again, this resulted in films with the top of the film being less crystalline. All colloidal films that were crystalline showed clear Bragg reflections, see Fig. 6.10a for an example.

We also measured the resulting thickness of the films as function of substrate velocity, see Fig. 6.10b. The thickness of the resulting particle layer increased on average with increasing particle concentration. However, the resulting thickness was rather small: between 2.2 µm and 16 µm thick. Previously, using similar parameters, film thicknesses between 3 µm and 325 µm were obtained [86]. The gap height, between the blade and the substrate, in these experiments was set to be as small as possible ($\sim 2\,\mu\mathrm{m}$), similar as was done in ref. 86. Varying the gap height between 2–40 µm resulted in an equally thick film and this variation in gap height did not have any influence on the structure of the film.

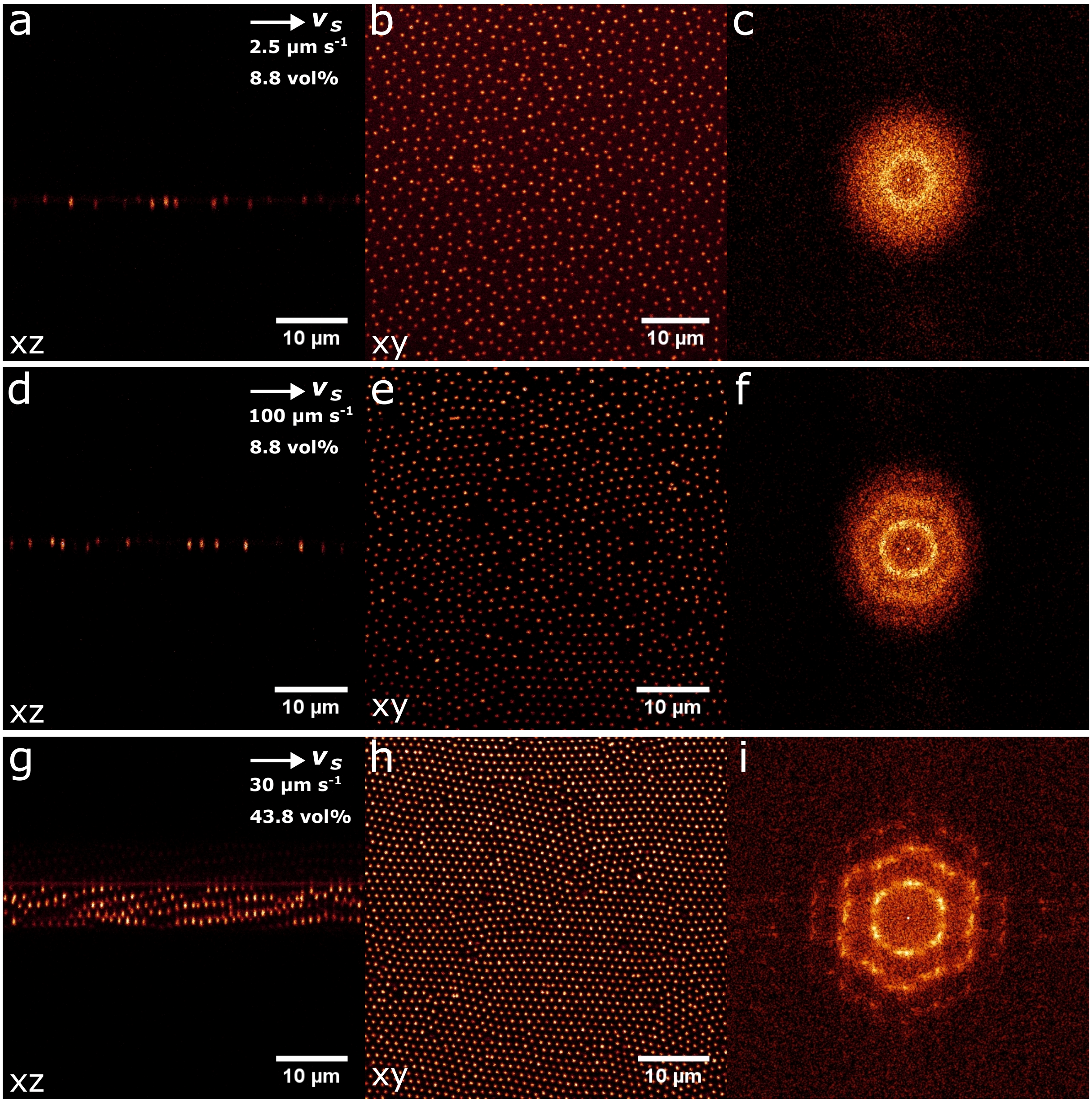

Figure 6.8 Confocal images of resulting film after doctor blade coating, with different blade velocities. **(a-c)** $v_s = 2.5\,\mu\mathrm{m\,s^{-1}}$ and 8.8 vol% 970 nm spheres. **(a)** Cross section of resulting film **(b)** xy-image of resulting particle film. **(c)** Corresponding FFT image. **(d-f)** $v_s = 100\,\mu\mathrm{m\,s^{-1}}$ and 8.8 vol% 970 nm spheres. **(d)** Cross section of resulting film **(e)** xy-image of resulting particle film. **(f)** Corresponding FFT image showing six-fold symmetry. **(g-i)** $v_s = 30\,\mu\mathrm{m\,s^{-1}}$ and 43.8 vol%. **(g)** Cross section of resulting film **(h)** xy-image of resulting particle film. **(i)** Corresponding FFT image showing six-fold symmetry with distinct peaks.

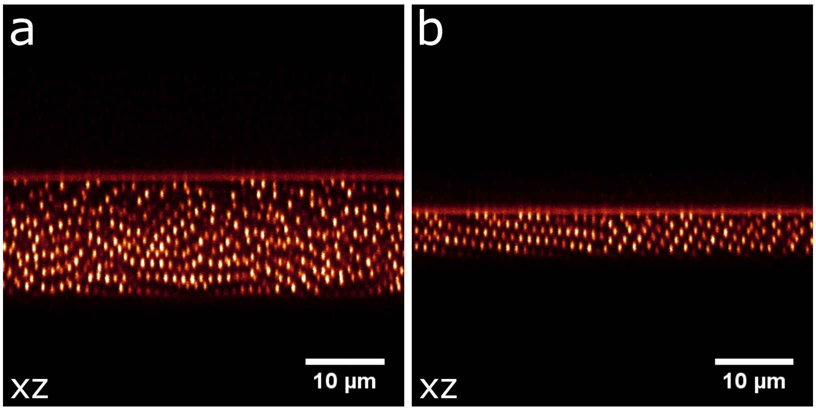

Figure 6.9 Confocal images of resulting film after doctor blade coating with 43.8 vol% particles and $v_s = 200\,\mu\mathrm{m\,s^{-1}}$. **(a)** Cross section of resulting film when bladed a single time. **(b)** Cross section of resulting film when bladed twice.

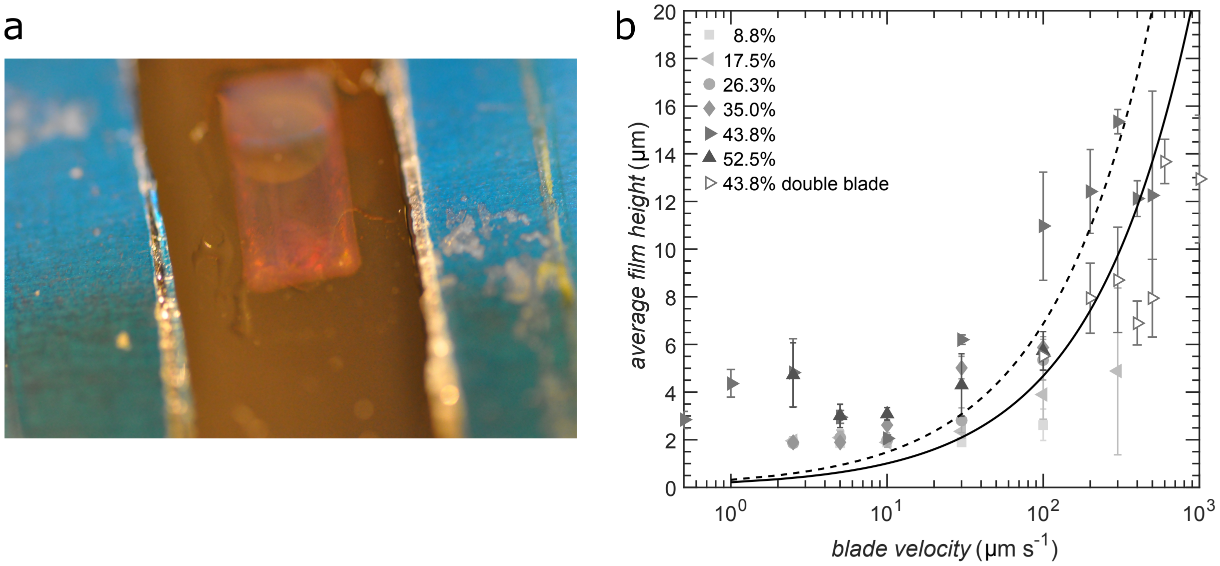

Figure 6.10 **(a)** Bragg reflection of resulting particle film after doctor blade coating. **(b)** Average film thickness as a function of substrate velocity at different vol% spheres in ETPTA. The film thickness was measured from recorded xz-confocal images at three different spots (film length 0.5–1 cm). The error bars indicate the measured standard deviation of the measured film thickness. The lines are a plot of equation 6.15 as a function of substrate velocity (dashed line $\sigma = 0.01\,\mathrm{N\,m^{-1}}$, solid line $\sigma = 0.1\,\mathrm{N\,m^{-1}}$).

Normally, in DBC the final thickness of the film is dependent on the gap height of the system [299, 300]. This indicates that in our case, the colloidal crystal formation during DBC is not caused by shear force in pressure driven flow, as was argued earlier [86].

Mechanism of Doctor Blade Coating In order to investigate the colloidal crystal formation during DBC, we used a DBC set-up that was mounted on a confocal microscope. The set-up used here, allowed us to follow in real time and real-space the formation of these thin colloidal films. After loading a sample on the DBC set-up, the dispersion wetted both sides of the blade due to capillary forces and a meniscus downstream from the blade was obtained, see Fig. 6.2c. As the substrate was moved from underneath the blade, the meniscus was pulled away from the blade and a steady state static meniscus was formed. The steady meniscus had a length of $\Delta x \approx 350\,\mu\text{m}$ and further downstream a thin film was formed. The blade had a width of $\Delta y = 0.4\,\text{cm}$ and angle θ 75° with the substrate. To analyze the flow inside the steady meniscus and in the film entrainment region, we recorded xzt-series of the particle flow near the blade and analyzed the flow pattern using Digital Particle Image Velocimetry (DPIV), see Figs. 6.11−6.16 and the movies shown on page 141. We used $v_s = 2.5\,\mu\text{m}\,\text{s}^{-1}$ and a particle concentration of 52.5 vol%. From these xzt-series it was concluded that the crystals were not formed near the blade, but rather away from the blade in the tail of the dispersion profile.

Movie 6.1 on page 141 and Fig. 6.11 show the flow upstream from the blade. We observed shear flow close and parallel to the substrate, with on top a circular flow. The movie shows that crystals were formed before the blade, but that the flow close to the blade destroyed these crystals. Movie 6.2 on page 141 and Fig. 6.12 depict the flow underneath the blade. The flow was highest near the substrate. Upstream from the blade and higher up away from the substrate, the flow of particles was directed upwards. On the right, downstream from the blade and higher up away from the substrate, the particle flow was directed downwards and towards the blade. This can also be clearly seen in Movie 6.3 on page 141 and Fig. 6.13. About $20\,\mu\text{m}$ downstream from the blade crystalline layers were formed near the substrate and seen to slide over each other. Close to the substrate, the flow direction and particle velocity were similar to the substrate velocity. About 4 particle layers away from the substrate, the direction of flow changed and the particle velocity decreased significantly. This gradient in velocity close to the substrate resulted in crystalline layers sliding over each other. Going further downstream, $\sim 100\,\mu\text{m}$ from the blade, we observed a similar flow pattern, see Movie 6.4 on page 141 and Fig. 6.14. Close to the substrate the particle velocity is highest and around 8 particle layers were sliding over each other. Higher-up the particle flow is directed upwards. Going $\sim 200\,\mu\text{m}$ downstream from the blade, the steady meniscus gets thinner and most particles in the tail of the meniscus are arranged in crystalline layers, see Movie 6.5 on page 141 and Fig. 6.15. Only the lowest four crystalline particle layers moved in the same direction as the substrate. Above these four particle layers the particle flow direction was opposite to the substrate velocity, and crystalline particle layers slid the other way. Film entrainment was observed $300\,\mu\text{m}$ downstream from the blade, see Movie 6.6 on page 141 and Fig. 6.16. Here, a particle film of around 2 particles thick was pulled out of the steady meniscus.

The transition between the steady meniscus downstream of the blade and the film entrainment region, was observed to be quite complex. Initially, more particles were

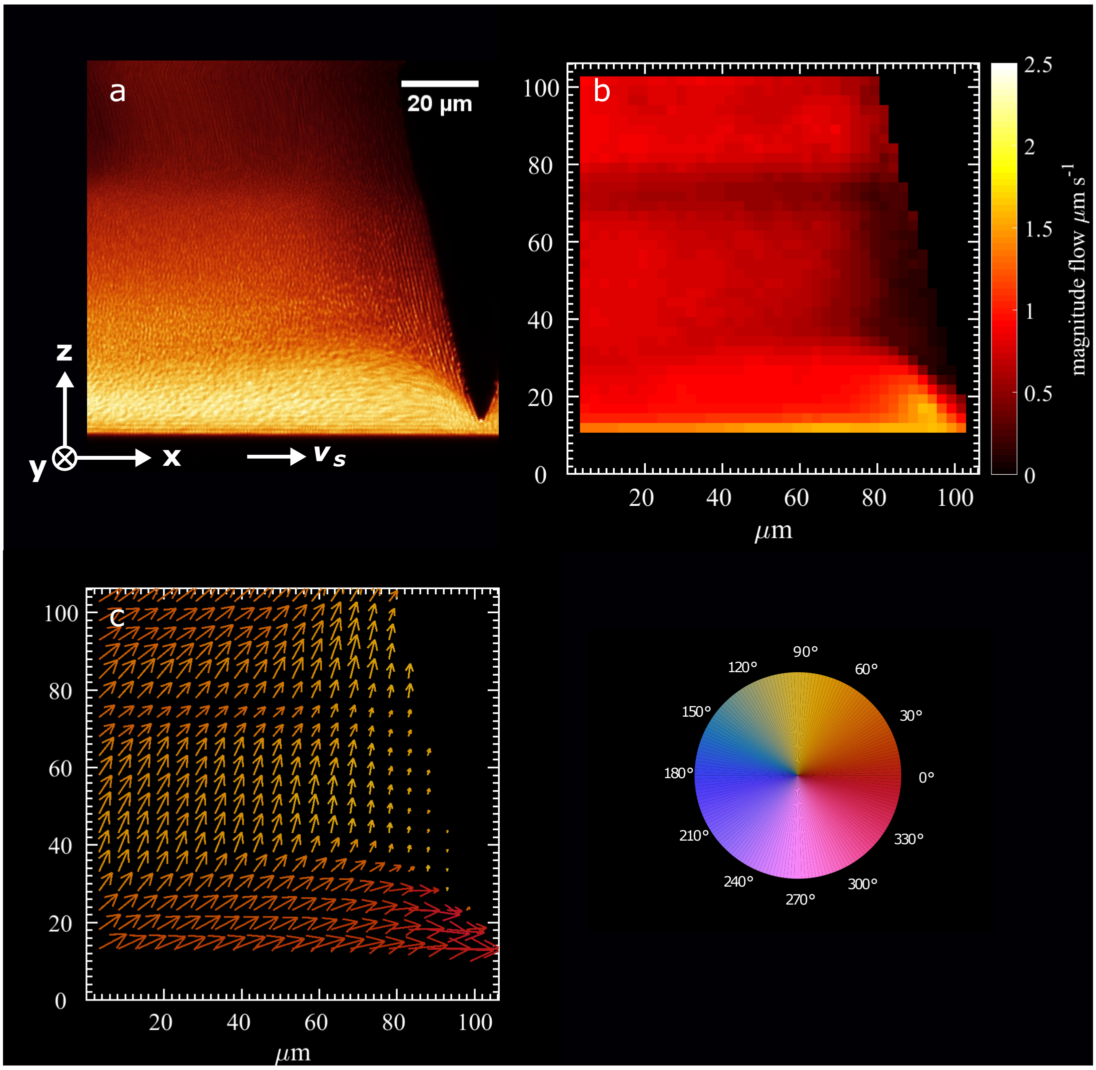

Figure 6.11 Flow profile during doctor blade coating upstream from the blade calculated using DPIV. **(a)** Average of 200 confocal images taken upstream from the blade during doctor blade coating of 52.5 vol% at $v_s = 2.5\,\mu\text{m}\,\text{s}^{-1}$. **(b-c)** Average flow profile showing **(b)** the magnitude of flow and **(c)** direction of flow. The color of the arrows depicts the orientation of the flow. The flow profile was average over 200 frames (time = 84.4 s and $\Delta t = 0.422$ s). Note, that due to a slight refractive index mismatch the scale in the z-direction is off by a few percent. See the corresponding Movie 6.1 on page 141.

pulled away from the blade than could be accommodated in the resulting particle film. Hence, in order to maintain a steady meniscus, fluid started to flow back at this transition point, resulting in a somewhat complex particle flow, that breaks up the already formed crystals, see Movie 6.7 on page 141 and Fig. 6.17. Although complex, the flow observed here occurs at relatively low Reynolds number ($Re \sim 10^{-5}$) and we still have laminar flow. The flow in DBC for Newtonian fluids is normally considered as a superposition of shear-driven flow and pressure-driven flow [299, 300]. In case when a pressure-driven flow is dominant, a parabolic flow profile is expected and the final film thickness is thicker than the blade gap. Moreover, a decrease in film thickness is expected with increasing substrate

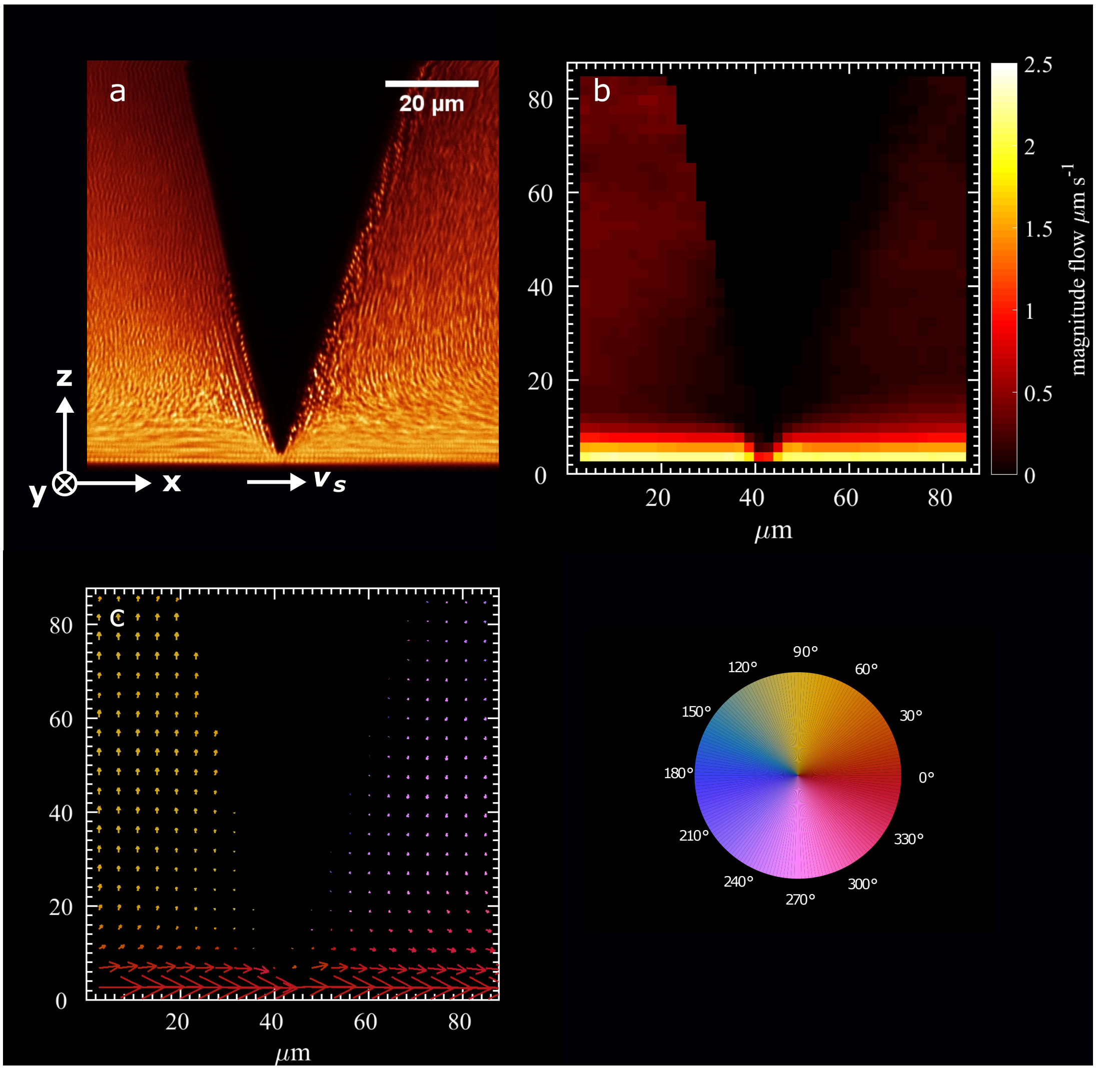

Figure 6.12 Same as in Fig. 6.11 but centered on the blade. See the corresponding Movie 6.2 on page 141.

velocity. When a shear-driven flow is dominant, a drag or Couette flow is observed and the final film thickness is thinner than the blade gap and not dependent on the substrate velocity. In both cases, the blade height influences the final thickness of the film. The flow we observed during our experiments was different from classical descriptions of flow during DBC [299, 300, 302]. In addition, the film thickness increased with increasing substrate velocity, but was not dependent on the height of the blade. Figure 6.18 depicts a schematic of the flow profile observed during our DBC experiments. Close to the substrate we found shear flow in the same direction as the substrate moves. On top of the shear flow we found on both sides a recirculation flow. The steady meniscus observed downstream from the blade indicates that capillary forces were important. From these observations, we conclude that the flow observed during our DBC experiments resembles that of Landau-Levich type flow [316], commonly seen in dip-coating of fluids. The flow profile in Landau-Levich consists of two parts. One part being a steady meniscus, which is

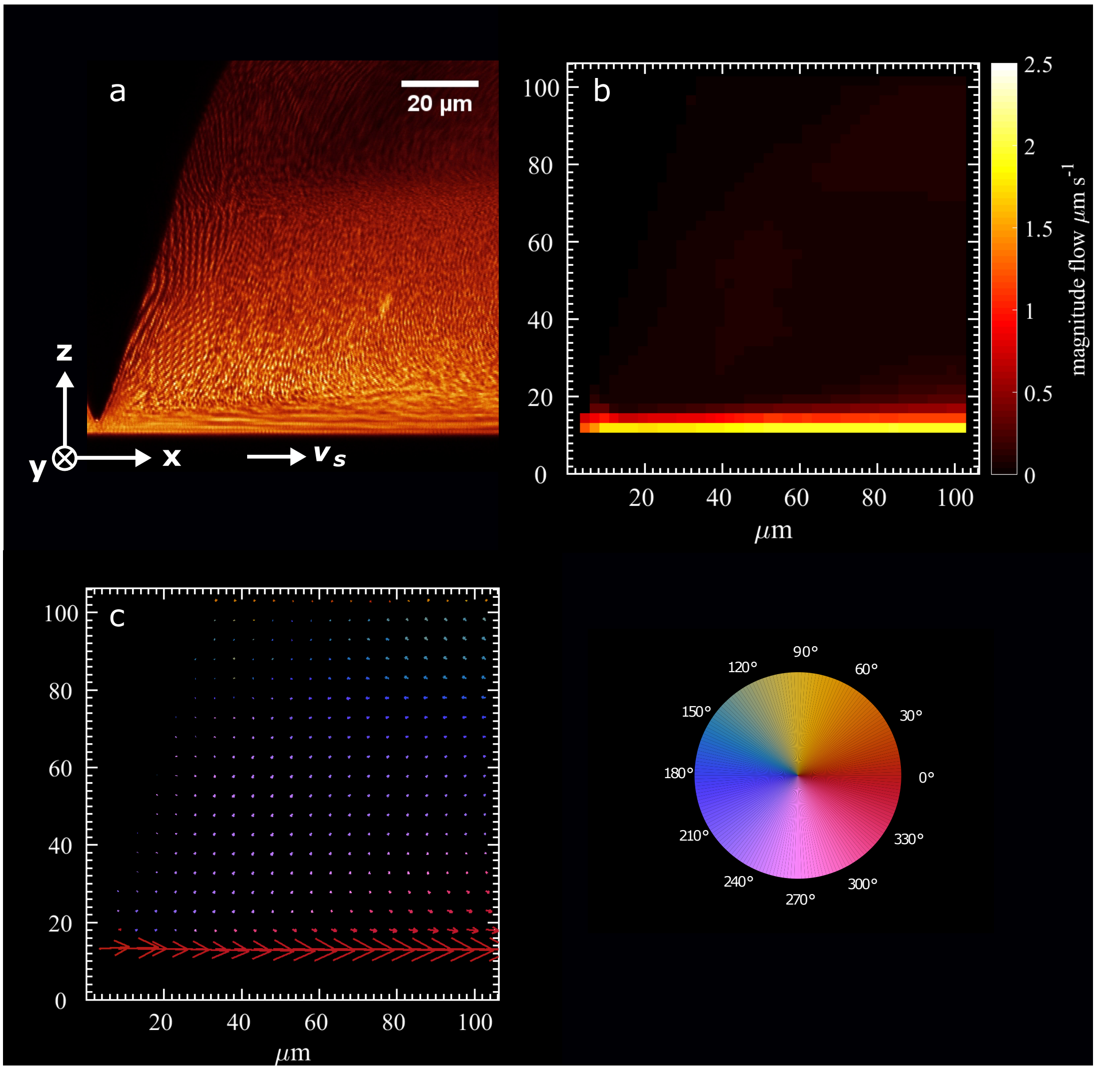

Figure 6.13 Same as in Fig. 6.11 but downstream from the blade. See the corresponding Movie 6.3 on page 141.

controlled by surface tension and a hydrostatic pressure field. The second part is the film entrainment region were the viscous forces are dominant. This results in a shear-driven flow region, near the bottom of the substrate, with on top a recirculation region. Thus, a balance exists between capillary forces and viscous forces and we can relate the film thickness to the capillary number in the following way [316]

$$h = 0.945 l_c Ca^{2/3}, \tag{6.15}$$

with h being the film thickness, the capillary length $l_c = \sqrt{\sigma/\rho g}$, with σ being the fluid-air surface tension and g the gravitational constant and the capillary number $Ca = \eta v_s/\sigma$. Here, it is assumed that the solvent is completely wetting the substrate. This relationship neglects gravitational and inertial effects and is only valid in the limit of small capillary number, which is the case in our experiments. Hence, the resulting film thickness is

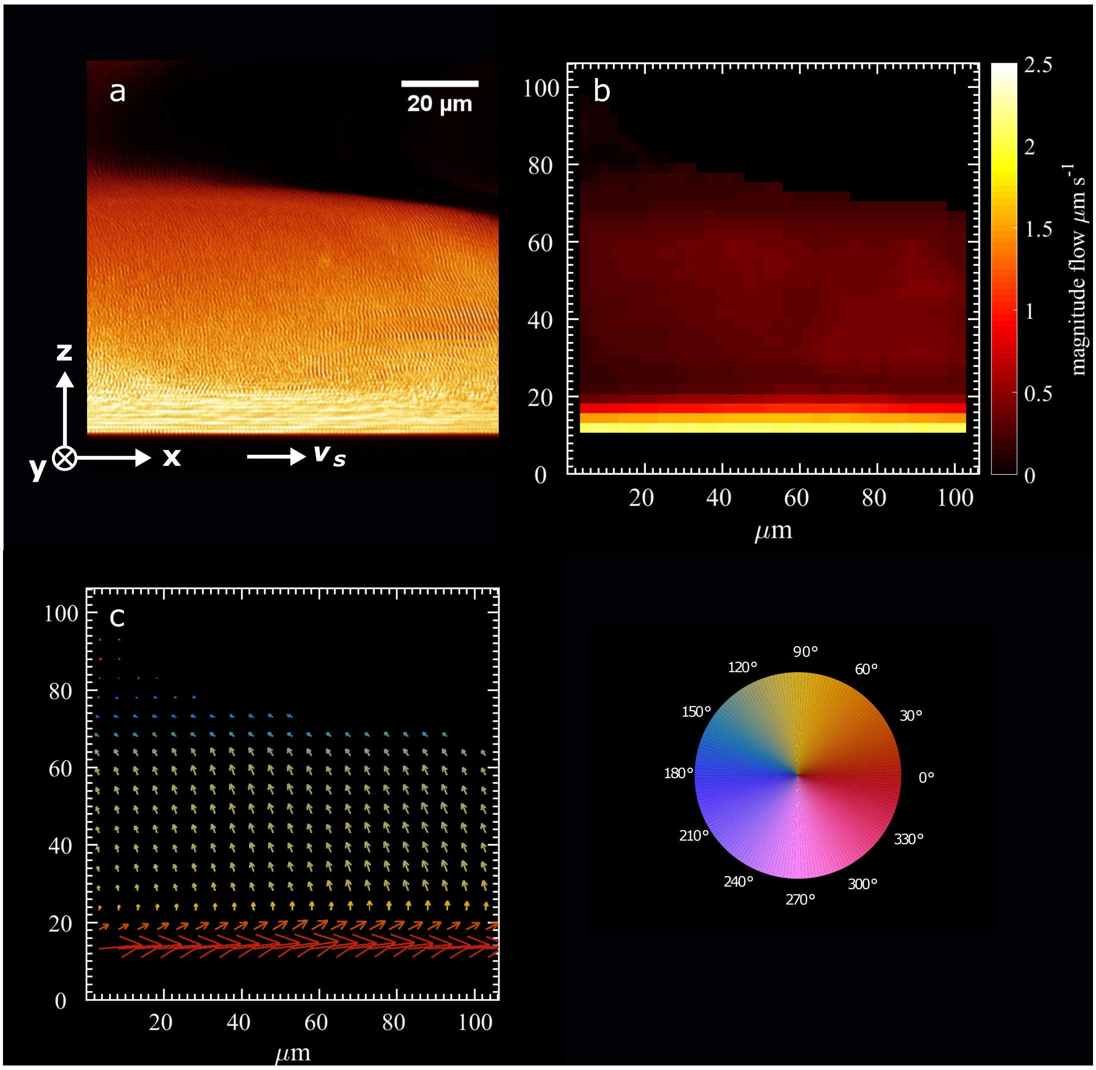

Figure 6.14 Same as in Fig. 6.11 but 100 µm downstream from the blade. See the corresponding Movie 6.4 on page 141.

dependent on the viscosity, substrate velocity and surface tension of the dispersion. This also explains why the resulting film thickness was not dependent on the blade height.

We plotted equation 6.15 as function of substrate velocity v and compared it with the film thicknesses we obtained in experiments, see Fig. 6.10. We took $\rho = 1200\,\mathrm{kg\,m^{-3}}$ and $\eta = 70\,\mathrm{mPa\,s}$, which are the density and viscosity of pure ETPTA, respectively. We assumed that the viscosity was Newtonian and not dependent on the particle volume fraction ϕ. As we do not know the surface tension of ETPTA, we plotted equation 6.15 for both a low surface tension $\sigma = 0.01\,\mathrm{N\,m^{-1}}$ (dashed line) and a high surface tension $\sigma = 0.1\,\mathrm{N\,m^{-1}}$ (solid line). Although the spread in experimental data is quite large, especially at faster blade velocities, equation 6.15 describes our experimental data reasonably well. In case of slower blade velocities, we found a larger film thickness than predicted. We argue that this happens because particles were accommodated inside the particle film, that were larger than the predicted final film thickness [329]. Next, also

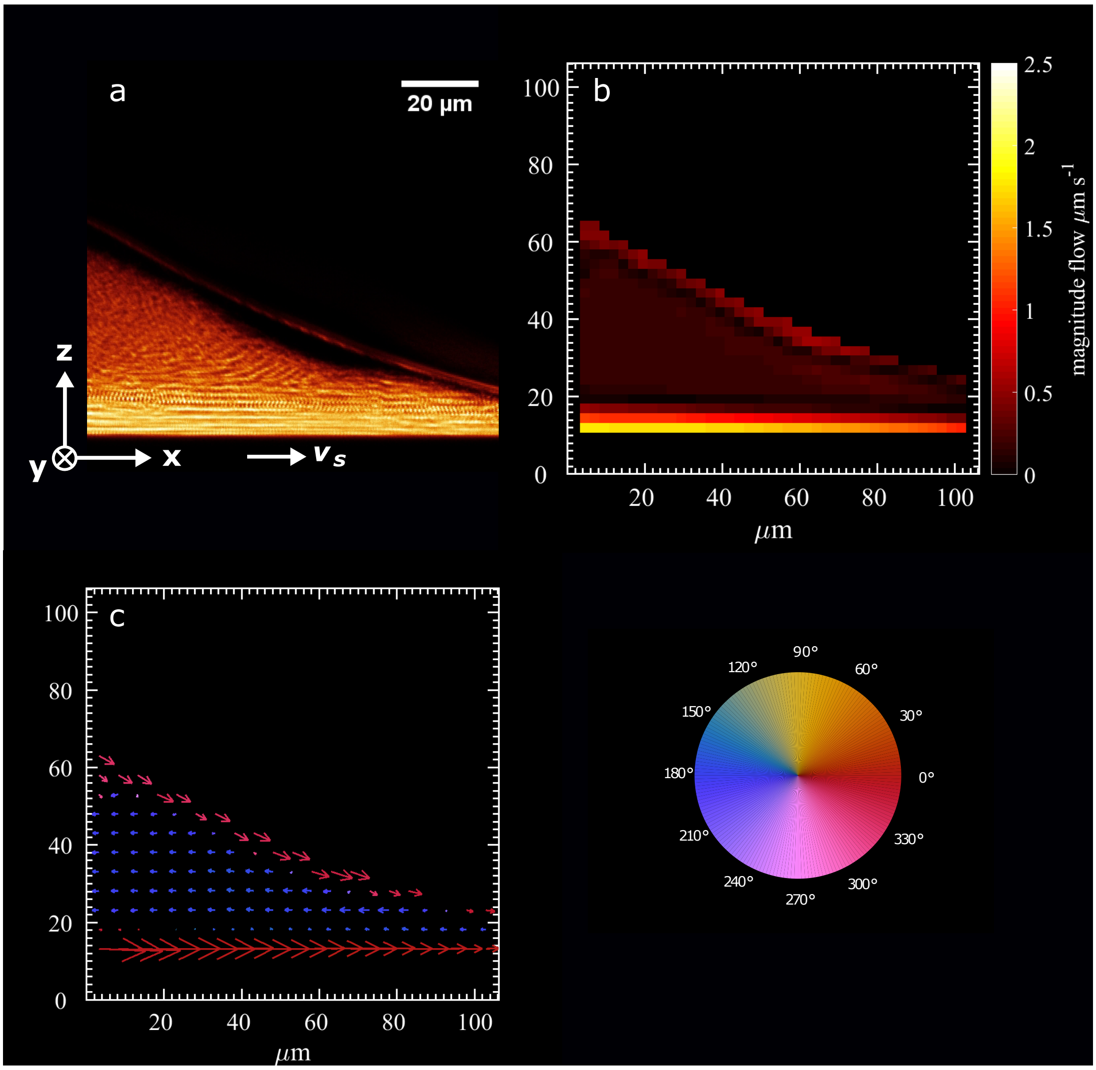

Figure 6.15 Same as in Fig. 6.11 but 200 µm downstream from the blade. See the corresponding Movie 6.5 on page 141.

surfactants (Marangoni flows), dust, and other impurities could have influenced both the resulting flow profile and the final film thickness [330–332]. In Fig. 6.15 particles at the air-liquid interface were observed to move downstream, instead of upstream. We expected that the flow pattern was influenced by heat or concentration gradients at the air-liquid interface [331]. Also, a region void of particles was observed below the air-liquid interface. The exact cause for this is not known, but this can also be due to a change in flow pattern. However, we did not expect that particle sedimentation caused this region void of particles, as we only observed this region void of particles 200 µm downstream from the blade. The sedimentation velocity of a single silica sphere in ETPTA is $5.12\,\mathrm{nm\,s^{-1}}$, over the course of the experiment, 1 hour, a single sphere was expected to sediment 18 µm.

In order to fit our data to equation 6.15, we took the viscosity of pure ETPTA. However, the viscosity of a colloidal dispersion is known to be dependent on the volume fraction and the applied shear [66, 79, 86, 333]. Earlier experimental work [66], found

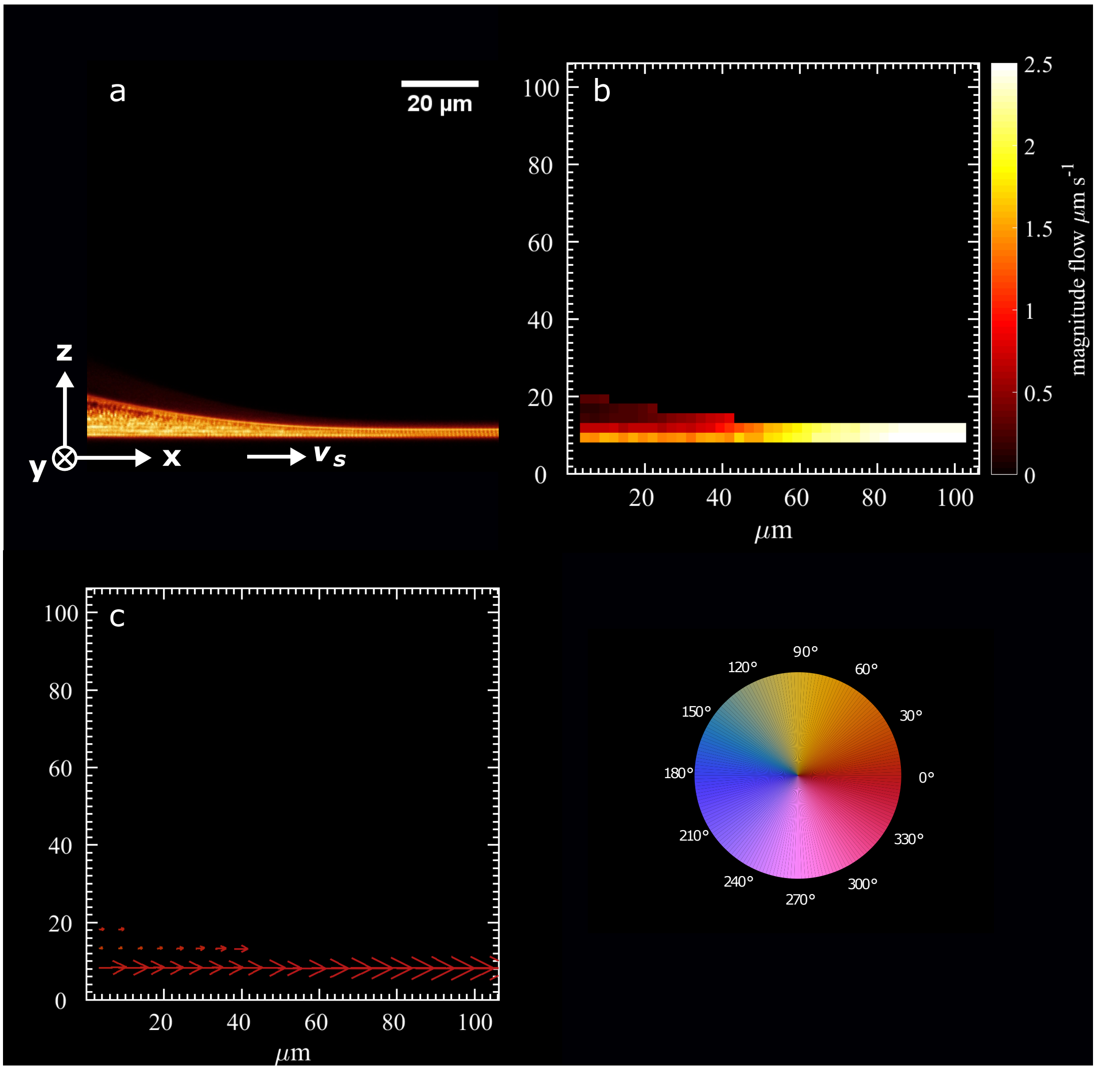

Figure 6.16 Same as in Fig. 6.11 but 300 μm downstream from the blade. See the corresponding Movie 6.6 on page 141.

that the volume fraction dependent viscosity of a dispersion of ellipsoids did not play a significant role in determining the resulting film thickness. In similar experiments of DBC, using smaller silica spheres, Yang *et al.* obtained much thicker particle films [86]. We did not find an acceptable explanation for this discrepancy with our results. They argue, but do not prove, that pressure driven flow determined the properties of the obtained particle film. Therefore, with faster blading velocities, a larger pressure difference is obtained as more dispersion accumulates upstream at the blade. This causes thicker films at faster blade velocities. However, we observed Landau-Levich type flow with DBC using similar conditions. In case of Landau-Levich type flow, thicker films might be explained by the partial wetting of the liquid with the substrate [334].

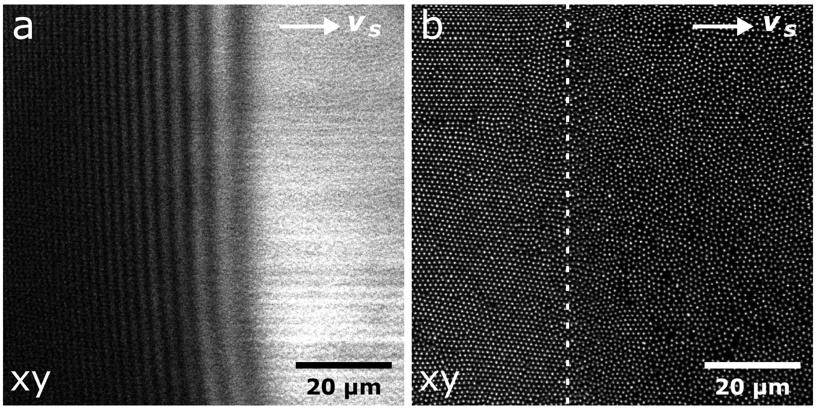

Figure 6.17 Confocal xy-images in the velocity vorticity plane at the boundary of the steady meniscus and the region of film entrainment, 300 µm downstream from the blade. **(a)** Confocal image taken in reflection mode, showing the interference pattern upstream at the left side indicative of a curved interface. **(b)** Confocal image taken in normal fluorescence mode. Downstream, right from the dashed line, the final particle film is formed, showing smaller crystalline domains compared to upstream. See the corresponding Movie 6.7 on page 141.

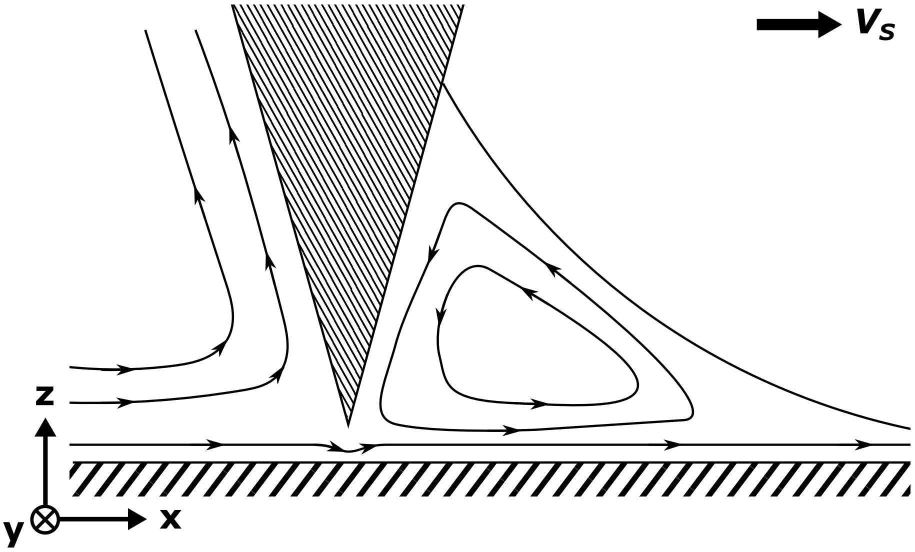

Figure 6.18 Schematic of the flow profile observed during DBC experiments. Substrate velocity v_s is to the right. Note, the drawing is not to scale.

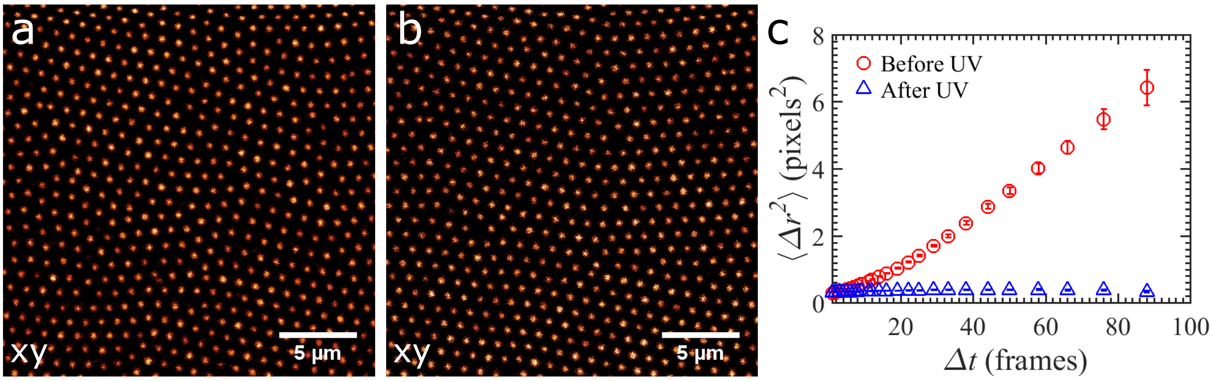

Figure 6.19 Polymerization of particle film after DBC. Confocal images of a particle film **(a)** before and **(b)** after 50 s of UV exposure. **(c)** Mean square displacement before and after UV exposure, time between frames $\Delta t = 0.422\,\mathrm{s}$, pixel size 47 nm × 47 nm. The finite displacement found after UV exposure is due to the error in particle tracking.

Free Standing Film of Silica Spheres To test whether we were able to obtain a free standing film of colloids after DBC, we prepared one sample of 43.8 vol% particle in ETPTA with 2 vol% of the photoiniator Irgacure 2100 (BASF) added to the dispersion. We prepared a particle film using a substrate velocity of $v_s = 100\,\mu\mathrm{m\,s}^{-1}$. After preparing the sample, we illuminated the sample with UV light (365 nm, Thorlabs M356LP1-C2) for 50 seconds to polymerize the ETPTA. The result is shown in Fig. 6.19. The UV light was focused on the sample with the same 63× 1.4 NA confocal objective as used for confocal imaging, such that the intensity of the UV light was high enough to allow for polymerization. We recorded a confocal movie of the particle film before and after UV exposure and subsequently tracked the particles in 2D [169]. Figure 6.19c shows the mean square displacement of the particles per frame before and after UV exposure. The average drift in the sample was removed before calculating the mean square displacement. Before UV exposure, we found a MSD that increased linear in time. As the particles were confined to their crystal lattice position, one would expect to observe sub-diffusive behavior at longer time scales ($\langle \Delta r^2(t) \rangle \sim D_t^b$ with $b < 1$). However, we also observed some rearrangements of colloids within in the particle film, which contributed to an increase in the MSD over time. This might explain why we still observed that the MSD depends linear on time. After UV exposure the particle movement halted and the measured MSD was not dependent on time. The finite mean square displacement found after UV exposure is probably due to the error in finding the position of the particles by the particle fitting code. After washing away the non-polymerized dispersion, a small free standing film consisting of silica colloids and polymerized ETPTA remained on the bottom cassette, see Fig. 6.20a. The steps at the sides of the colloidal film, shown in the bright field image, show the layering of the resulting particle film. Figure.6.20b depicts a zoomed-in fluorescence microscopy image. The hexagonal ordering of the spheres confirmed again that the crystalline structure was maintained on a large scale after UV exposure. We do not show it here, but it was shown in our group before [85] that the polymer could be burned away without leaving any cracks in crystalline colloidal film.

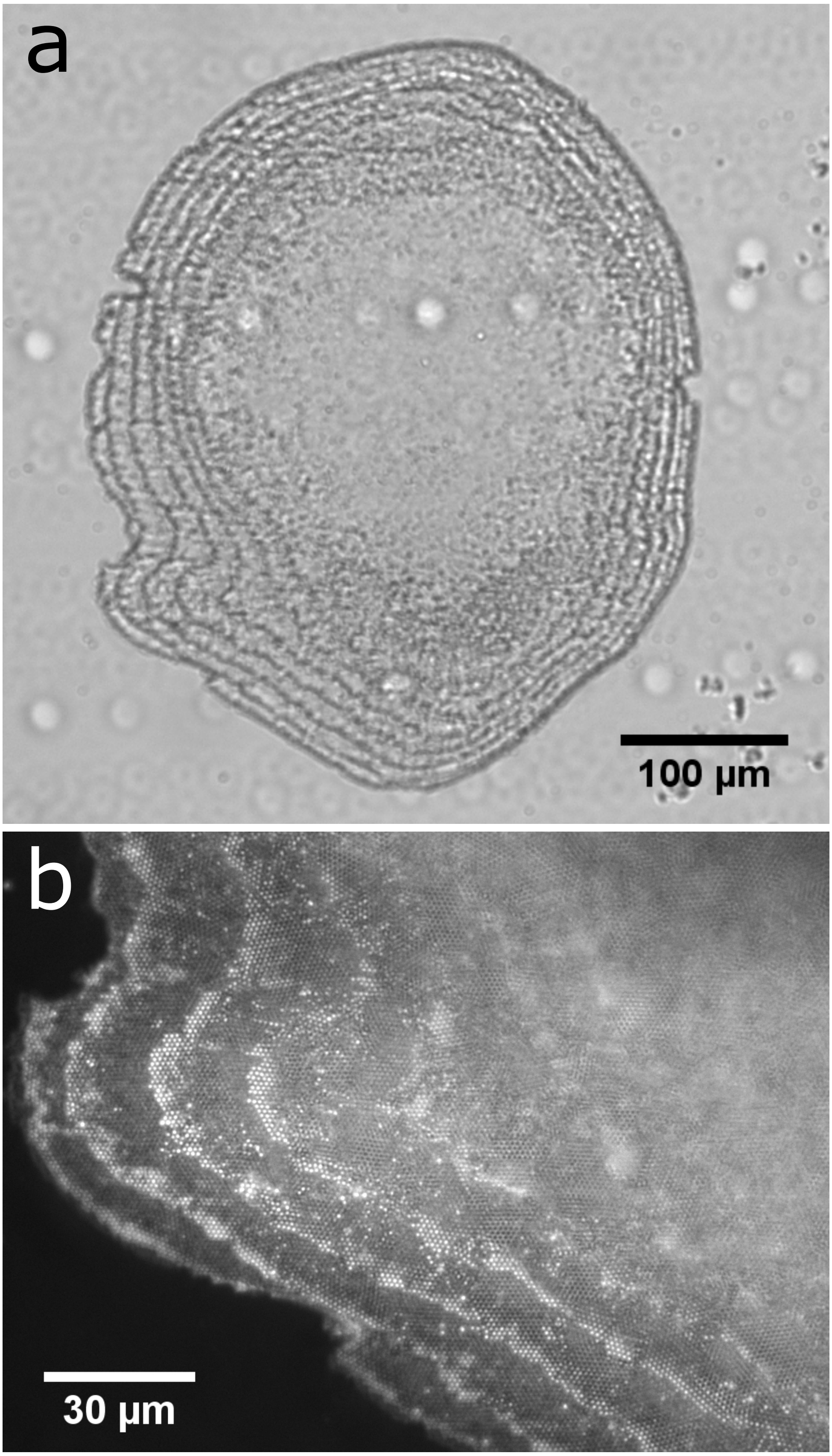

Figure 6.20 Resulting particle film after polymerization. **(a)** Bright field microscope image of the resulting particle film after UV exposure at one focused spot. **(b)** Fluorescence microscopy image, showing that the crystalline structure is maintained.

Doctor Blade Coating with Silica Rods We performed some preliminary experiments with doctor blade coating of silica rods (batch R2) dispersed in ETPTA with $\phi = 30\,\mathrm{vol\%}$ and $v_s = 2.5\,\mu\mathrm{m\,s^{-1}}$. In this way we aimed to use the shear flow to align the silica rods in the resulting particle film. The flow pattern observed in xz-view, 350 µm downstream from the blade, was similar to the flow pattern observed for silica spheres, see Fig. 6.21. Close to the substrate a shear flow was found in the same direction as the substrate velocity and on top a recirculation flow was found. The shear rate close to the substrate ($z = 0$–$20\,\mu\mathrm{m}$) was $\dot{\gamma} = 0.1\,\mathrm{s^{-1}}$, therefore, $Pe_r \approx 40$ which is enough to obtain alignment of the silica rods used. The alignment of silica rods inside the steady meniscus did not directly occur during DBC, initially we found no orientational order. Figure 6.22a shows a confocal snapshot taken $\sim 300\,\mu\mathrm{m}$ downstream from the blade inside the steady meniscus. The snapshot was taken 4 minutes after doctor blade coating was started and we found little alignment: $S_{2D'} = 0.36$. Figure 6.22b shows a snapshot taken at the same spot, but 3 minutes later, and we observed shear alignment of the rods close to the substrate $S_{2D'} = 0.89$. The observed alignment inside the steady meniscus was maintained during the whole coating process. Although we observed shear alignment of the rods during DBC, it did not result in alignment of the rods inside the particle film. Figure 6.23 shows the particle film after DBC and we obtain $S'_{2D} = 0.55$. The film thickness was $\sim 2.5\,\mu\mathrm{m}$.

We believe that at the boundary of the steady meniscus and the film entrainment region dispersion flows back. This is needed to maintain the steady meniscus, but distorts the alignment of rods that ended up inside the particle film. This back flow of dispersion, was already seen to affect the crystallinity of the spherical particle film, see Fig. 6.17.

Although we did not obtain alignment of silica rods inside the resulting particle film, we do believe that it should be possible to obtain aligned particle films using DBC. Using a similar procedure, aligned films of smaller size ellipsoidal titania particles ($\sim 100\,\mathrm{nm}$) were obtained [66]. One option would be to use faster blade velocities to aim for thicker films, see equation 6.15. With thicker film, the back flow of solvent needed to maintain a steady meniscus, is probably less of a problem. But care should be taken as faster substrate velocities can lead to tumbling of rods, although not much is known yet about tumbling at higher volume fractions. Another option could be to polymerize the aligned rods inside the steady meniscus during the process of DBC to obtain a $\sim 1\,\mathrm{cm}$ long particle film.

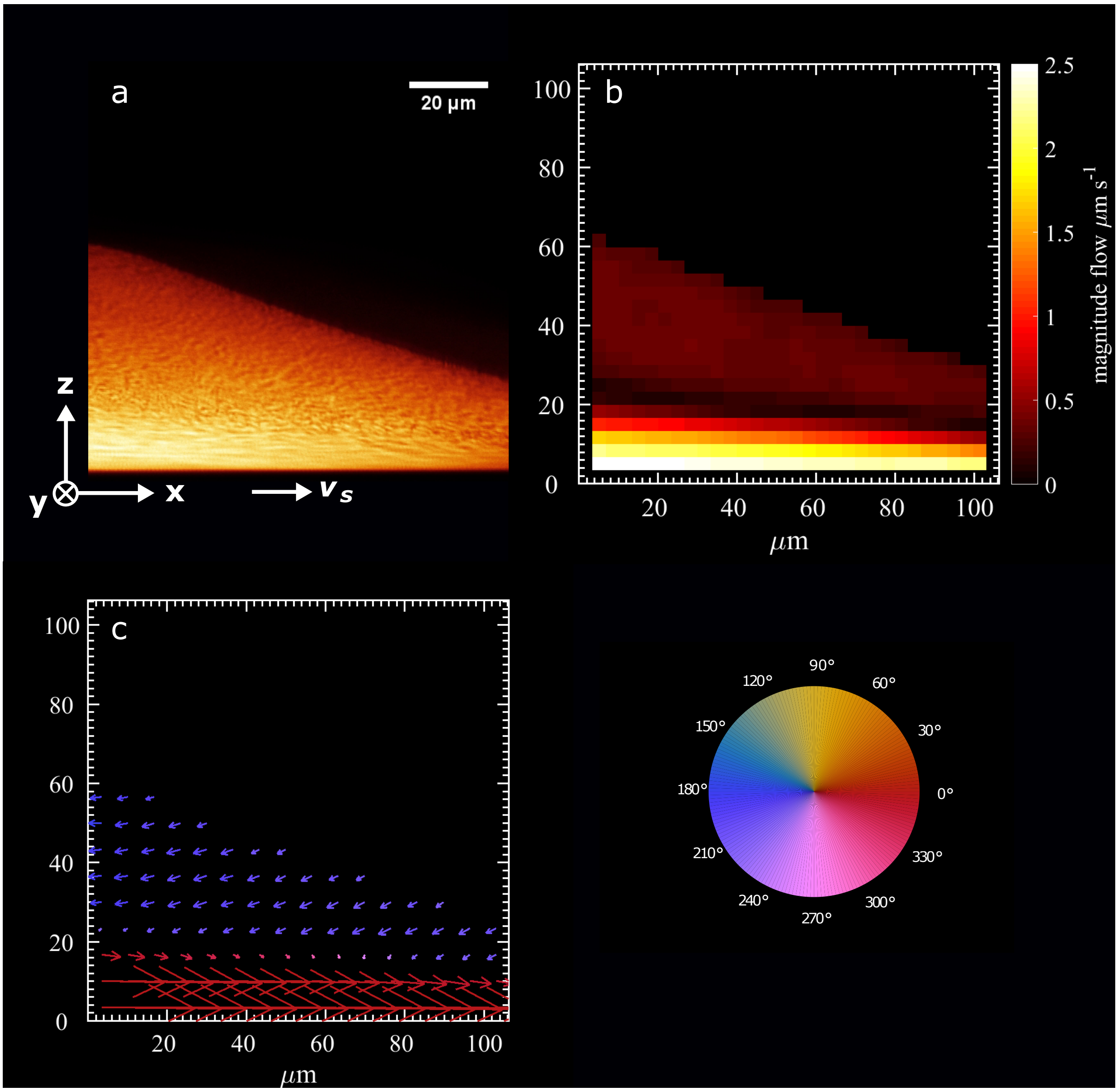

Figure 6.21 Flow profile during DBC with R2 silica rods observed 300 µm downstream from the blade as calculated using DPIV. **(a)** Average of 200 confocal images taken upstream from the blade during DBC of 30 vol% and $v_s = 2.5\,\mu\mathrm{m\,s^{-1}}$. **(b-c)** Average flow profile of **(b)** the magnitude of flow and **(c)** the direction of flow. The color of the arrows depict the orientation of the flow. The flow profile was averaged over 200 frames (time = 84.4 s and $\Delta t = 0.422$ s). Note, that due to a slight refractive index mismatch the scale in the z-direction is off by a few percent. See the corresponding Movie 6.8 on page 141.

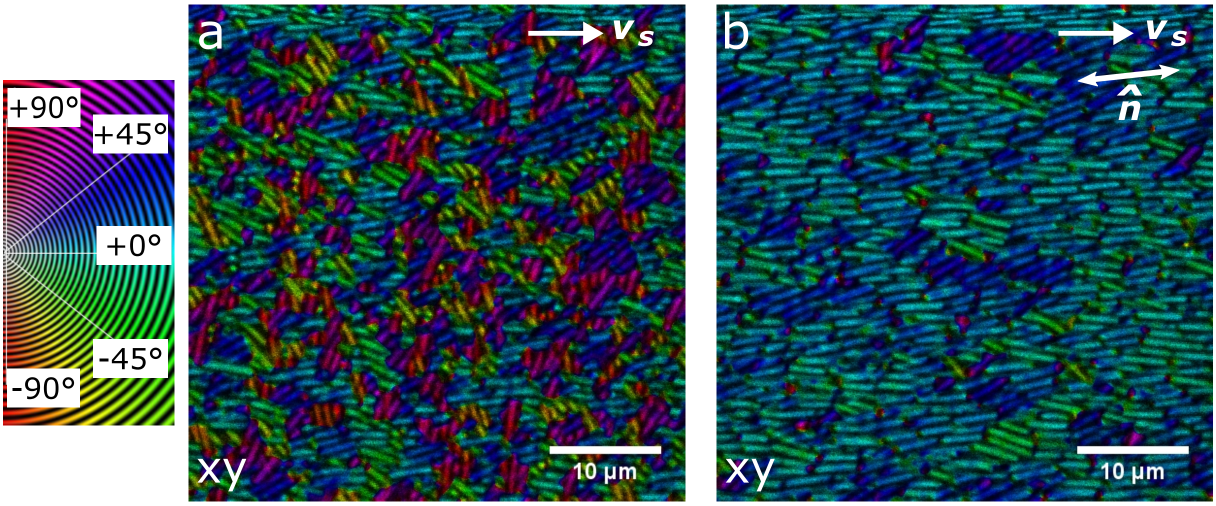

Figure 6.22 Confocal snapshots of the DBC of 30 vol% R2 silica rods, $v_s = 2.5\,\mu\mathrm{m\,s^{-1}}$, 300 µm downstream from the blade. **(a)** Confocal xy-image taken 4 minutes after start DBC, showing no orientational order, $S'_{2D} = 0.36$, $\theta = 8°$. **(b)** Confocal xy-image taken 7 minutes after start of DBC, showing shear alignment $S'_{2D} = 0.89$ and $\theta = 6°$. The color in the images indicates the average pixel orientation. The arrows denoted v_s indicate the movement of the substrate. The double arrow in **(b)** denotes the nematic director.

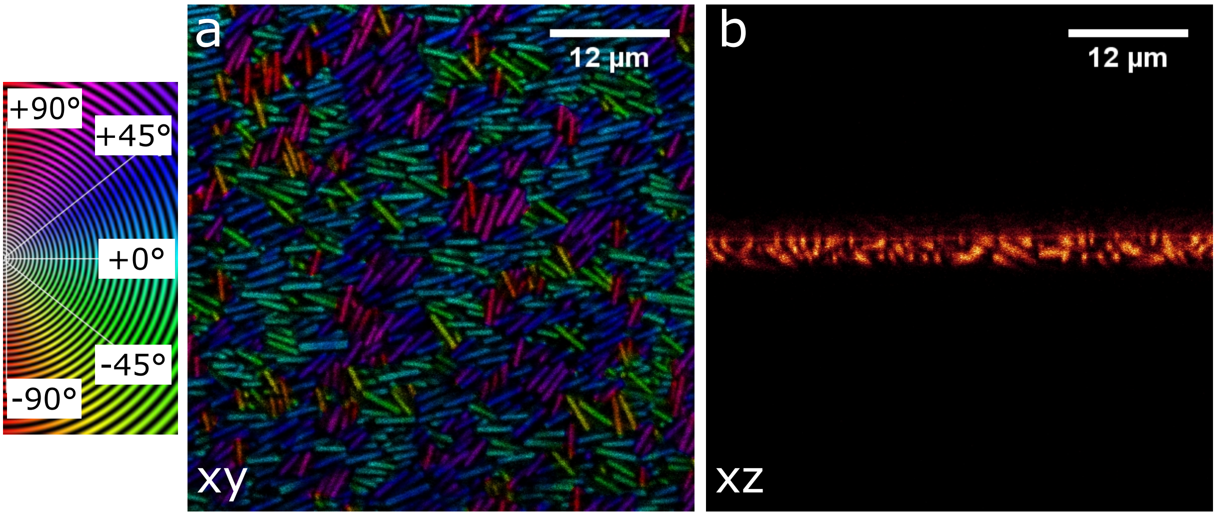

Figure 6.23 Confocal images of the resulting particle film after doctor blade coating with R2 silica rods. **(a)** Confocal xy-image, with projected $S'_{2D} = 0.56$ and $\theta = 17°$. **(b)** Cross section of resulting particle film.

6.5 Conclusion

To conclude, we showed that it is possible to obtain colloidal films with radially aligned silica rods using spin coating. To do so, silica rods were dispersed in a 1:1 v/v 1-propanol-ETPTA solvent mixture at a particle concentration of 15 vol%. During a spin coating cycle, we started with an isotropic state that flow aligned into a para-nematic state. As the 1-propanol evaporated the particle density in the film increased and a radially aligned nematic-like particle film was obtained. More research is needed to optimize the protocol to evaporate all of the 1-propanol in one spin cycle, in order to get rid of the flows that disrupt the structure of the film. Also, more research is need to obtain a free standing particle film by polymerization of the ETPTA, although we did show proof of principle.

Colloidal silica spheres ($D = 970\,\text{nm}$, $\delta_D = 3\%$) dispersed in ETPTA at various volume fractions at ($\phi = 9$–$52.5\,\text{vol}\%$) were used for DBC. We obtained crystalline particle films at particle concentrations $\phi > 17.5\,\text{vol}\%$ and substrate velocities between $v_s = 30\,\mu\text{m}\,\text{s}^{-1}$–$100\,\mu\text{m}\,\text{s}^{-1}$. For $\phi > 35.0\,\text{vol}\%$ we also obtained crystalline particle films at lower substrate velocities. Resulting particle films had a thickness between 2 µm and 16 µm.

Next, we were able to follow the process of DBC in real-space and real time by using a modified parallel shear plate mounted on top of an inverted confocal laser scanning microscope [323], from which the top plate was replaced by a cassette that contained a blade oriented perpendicular to the substrate. We analyzed the observed flow profiles during DBC using a DPIV algorithm [313].

The flow profile observed during DBC, with the parameters used here, closely resembled Landau-Levich flow [316], which is also often observed during dip-coating for a completely wetting liquid [303]. Crystalline domains were observed to form inside the steady meniscus before they were pulled out to form a film. At the region of film entrainment, the large crystalline domains were broken up in smaller crystalline domains reducing the order in the resulting film. This was probably due to back flow of solvent into the steady meniscus at the boundary of the steady meniscus and the film entrainment region.

We were able to obtain a free standing colloidal particle film of 300 µm × 300 µm by using UV light to polymerize the ETPTA after DBC. In future, the size of the free standing colloidal film could be enlarged by moving the substrate during polymerization and by using a confocal objective with a lower numerical aperture to enlarge the spot size.

DBC of silica rods resulted in shear alignment of the rods inside the steady meniscus. However, silica rods were not flow aligned inside the resulting particle film. We expect that back flow of dispersion at the boundary of the steady meniscus and film entrainment region, distorted the alignment of silica rods that ended up in the particle film. We argue that better aligned particle films could be obtained in two ways: either by faster blading to obtain thicker films or by local polymerization of the the aligned silica rods inside the steady meniscus during the process of DBC.

6.6 Acknowledgments

I would like to thank Judith Wijnhoven for the synthesis of 970 nm FITC-labeled silica spheres. Isabelle Palstra and Guy Frissen are thanked for their work on the spin coating of silica rods. I would like to thank Marcel van Asselen and Sander Deelen of the Scientific Instrumentation group (Utrecht University) for making the DBC inset in our parallel plate shear shell. Peter Helfferich is greatly acknowledged for his patience, knowledge and his assistance with using the doctor blade coating set-up. Finally, Ernest van der Wee is thanked for his collaboration on the polymerization of the ETPTA after doctor blade coating in order to obtain a free standing colloidal particle film.

Appendix 6

6.A Supporting Movies

Digital version Please click on the movie titles to get directed to the movie.

Printed version Please scan the QR code on the right to get directed to the supporting movies.

Doctor blade coating Movies of confocal microscopy time series during doctor blade coating are shown at different positions with respect to the blade position. Silica spheres had a diameter $D = 970\,\mathrm{nm}$ ($\delta_D = 3\%$) and were dispersed in ETPTA (viscosity $\eta = 70\,\mathrm{mPa\,s}$). The volume fraction of the dispersion was 52.5 vol%. The substrate moved with a velocity $v_s = 2.5\,\mathrm{\mu m\,s^{-1}}$ to the right. The field of view in movies 6.1 and 6.3–6.8 was 106.2 µm × 106.2 µm. The field of view in Movie 6.2 was 87.7 µm × 87.7 µm.

Movie 6.1 Shows a *xzt*-series at directly upstream from the blade. Movie is shown at 5× real time at 12 frames/s.

Movie 6.2 Shows a *xzt*-series underneath the blade. Movie is shown at 5× real time at 12 frames/s.

Movie 6.3 Shows a *xzt*-series directly downstream from the blade. Movie is shown at 5× real time at 12 frames/s.

Movie 6.4 Shows a *xzt*-series 100 µm downstream from the blade. Movie is shown at 5× real time at 12 frames/s.

Movie 6.5 Shows a *xzt*-series 200 µm downstream from the blade. Movie is shown at 5× real time at 12 frames/s.

Movie 6.6 Shows a *xzt*-series 300 µm downstream from the blade. Movie is shown at 5× real time at 12 frames/s. Here, the dynamics at the boundary between the steady meniscus and the film entrainment is captured.

Movie 6.7 Shows a *xyt*-series 300 µm downstream from the blade. Movie is shown at 4× real time. The movie shows how the larger crystal domains, formed inside the steady meniscus were broken up, once the crystal domains entered the film entrainment region.

Movie 6.8 Shows a *xzt*-series imaged 300 µm downstream from the blade of 30 vol% R2 rods. The movie shows the alignment of silica rods inside the steady meniscus. Movie is shown at 5× real time at 12 frames/s.

7

Shape-Dependent MultiExciton Emission and Whispering Gallery Modes in Supraparticles of CdSe/MultiShell Quantum Dots

Semiconductors are indispensable as the active light-emitting element in many optoelectronic devices. However, even the purest bulk semiconductors suffer from considerable non-radiative recombination leading to low photoluminescence efficiencies. Zero-dimensional quantum dots show a much better carrier-to-photon conversion caused by confinement of the excitons, but suffer from non-radiative recombination when assembled into a solid, due to exciton energy transfer. Here, we report on the shape-dependent optical properties of self-assembled supraparticles composed of CdSe/multishell nanocrystals. All supraparticles showed stable and bright photoluminescence in ambient up to high excitation intensities. When the supraparticles were deposited on a silicon surface their spherical shape was deformed due to drying. These deformed supraparticles showed the onset of whispering gallery modes in microscope images, while sharp Mie modes in the spectrum were absent. In addition to single-exciton emission, we observed bright emission from multiexciton states at high excitation powers. In contrast, supraparticles excited with two photon excitation did not show any bright emission from multiexciton states. Moreover, supraparticles that retained their perfectly spherical shape show a spectrum with sharp Mie whispering gallery modes, while multiexciton emission was absent.

7.1 Introduction

Semiconductors are indispensable as the active light-emitting element in many optoelectronic devices. However, even the purest bulk semiconductors, such as Si or GaAs [335, 336], suffer from considerable non-radiative recombination due to the long carrier or exciton diffusion length, which means that excitons can wander around and find a defect center, eventually. High photoluminescence quantum efficiencies are possible when charge carrier and exciton diffusion are confined, such as in well-prepared quantum wells [337]. Also zero-dimensional quantum dots (QDs) can show a very good carrier-to-photon conversion caused by confinement of the excitons in the volume of the QD. However, when nanocrystalline QDs are assembled into a QD solid, exciton energy transfer from QD to QD can occur, which again leads to a considerable reduction of the photoluminescence quantum yield [338–341]. The solution of the problem has been to grow a shell, or multiple shells, around the QD. A shell does not only passivate the QD surface but also forms a barrier against exciton wandering by resonant energy transfer [342, 343], as the efficiency of this proces scales as $\sim 1/r^6$. Simultaneously, losses due to non-radiative Auger recombination of multiexciton states are reduced in core/shell structures. This many-body process is based on Coulomb interactions that are enhanced in small nanocrystalline QDs compared to a bulk material. Moreover, the abrupt step in the confinement potential at the QD surface, resulting in a large uncertainty in the electron and hole wave vectors, weakens the selection rule for Auger processes and therefore enhances the rate. Only after strong multiexciton emission was observed in self-organized epitaxial InGaAs quantum dots [344] with a shallow and gradual confinement potential, were colloidal analogues developed [345–349]. The same recipe that may prevent exciton energy transfer, *i.e.*, the growth of multiple shells around the nanocrystal, is used to make the confinement potential less abrupt, and in this way reduce the rate of Auger recombination. Recently, suppressed Auger recombination and related to that increased multiexciton emission have been reported for several types of specially engineered multishell nanocrystalline QDs [347, 350–355].

Here we report on the optical properties of a special type of QD solids that are assembled from CdSe (core) CdS/CdZnS/ZnS (multishell) QDs. These solids have a scalable spherical shape in the colloidal domain. Notwithstanding the (nearly) spherical shape, the QDs in the supraparticles are ordered. Provided that such supraparticles are still emitting, they would enable new designs for biological labels, light emitting diodes (LEDs) and lighting, lasing and optical switching [348, 356–358]. Supraparticles are in literature also referred to as superparticles, and have previously been made using roughly two pathways: one involves attractions such as hydrophobic forces between the articles [359–361], and the other uses drying emulsion droplets [362, 363]. With an emulsion based method in which self-assembly of nanoparticles takes place in droplets [364] we have prepared supraparticles of CdSe core/multishell QDs. The supraparticles had a perfectly spherical shape dictated by surface tension and their diameters ranged from 0.1 µm to several µm if the particles were deposited without drying effects e.g. by sublimation of the suspending solvent [364]. The shape was also retained when these supraparticles were deposited on a field of ZnO nanowires. However, when these supraparticles were deposited on a silica surface, drying forces distorted the spherical shape.

We investigated the light emission from these supraparticles, and how it depended on the supraparticle shape. In all cases, the supraparticles were photochemically stable in air up to high excitation intensities and showed a high photoluminescence quantum yield [365]. The supraparticles featured strong blue-shifted multiexciton emission at higher excitation intensities. Multiexciton emission was not observed when the particles were excited using two-photon excitation. Sufficiently large spherical supraparticles ($> 1.5\,\mu\text{m}$) showed a constant emission spectrum over five orders of excitation intensity with sharp peaks related to optical whispering gallery modes, while multiexciton emission was absent. It is clear that the optical properties of QD supraparticles depend both on the properties of the individual core-shell QDs and on collective related to the supraparticle size and shape.

7.2 Methods

Quantum Dot and Supraparticle Synthesis The QD synthesis and the assembly of QD's in supraparticles were done as described earlier [364, 365]. An approximation of the effective refractive index n_{eff} of the supraparticles (at 630 nm and 20 °C) was made based on the composition of the QD's, the thickness of the capping layer and the packing fraction of the QD's in the supraparticles. Based on the core-size of the CdSe core and the subsequent growth of monolayers of both CdS and ZnS, we assumed a refractive index of $n = 2.4$ (1.3% CdSe, 57.1% CdS, 41.6% ZnS) [366–368]. The QD's had a 6.2 nm radius and 1.1 nm thick oleic acid layer. The oleic acid layer took up 40% of the effective volume and the QD 60% of the effective volume. We asumed a refractive index $n = 1.46$ for the capping layer. The effective index of the QD was then calculated to be $n = 2.1$. We assumed an ideal packing of $\phi = 0.74$ of the QD's in the supraparticles. We assumed further that the remaining $\phi = 0.26$ in the supraparticles is cyclohexane $n = 1.43$ [369]. Therefore, we estimated the effective refractive index of the supraparticles as $n_{eff} = 1.89$.

Optical Measurements Optical measurements were performed on samples consisting of dilute nanocrystal chloroform solutions ($2 \times 10^{-6}\,\text{mol}\,\text{L}^{-1}$) in either a quartz cuvette or a capillary. We also investigated individual supraparticles lying on a 600 nm SiO_2 covered Si substrate and immersed in Leica immersion oil type F, and individual supraparticles in air lying on a bed of ZnO nanowires, that were deposited on the same Si substrate. Five different optical setups were used: (1) An Edinburgh instruments F900 double spectrometer (Fig. 7.3a). (2a) A home-built luminescence microscope fitted with pulsed laser excitation (Spectra Physics Explorer, 349 nm, 5 ns pulse duration, 5 kHz repetition rate) attenuated with neutral density filters and focused to a 50 µm full-width half-maximum (*fwhm*) spot coupled to a liquid nitrogen cooled spectrometer/charge-coupled device (CCD) (Princeton instruments) (Figs. 7.1c and 7.2 and 7.9). (2b) The same-home built microscope but fitted with a pulsed tunable fiber laser (Opotek Opolette 355, 10 ns, 10 Hz repetition rate) (Fig. 7.3b). (3a) A Leica TCS SP8 confocal microscope fitted with an pulsed super continuum source (NKT Photonics, 5 ps pulse duration, 78 MHz repetition rate), focused to a diffraction limited spot using a 63× 1.32 NA oil-immersion confocal-objective (Leica), and PMT detection (Figs. 7.3c-d and 7.10). (3b) The same

Leica TCS SP8 confocal microscope fitted with an ultrafast pulsed tunable IR laser (Coherent Chameleon Vision II, 140 fs pulse duration, 80 MHz repetition rate) (Fig. 7.4).

Electron Microscopy Scanning Electron Microscope (SEM) images were obtained with a FEI Nova 600 nanolab (Figs. 7.1a-b).

7.3 Results & Discussion

7.3.1 Assembly of Core/Multishell Quantum Dots into Supraparticles.

Self-assembly of the quantum dots in slowly drying oil droplets resulted in spherical supraparticles with a diameter between 100 nm and several µm (Fig. 7.1a). When these supraparticles were deposited on a silica substrate their shape was deformed by drying (Fig. 7.1b), but they still emited bright red light (Fig. 7.1c). Remarkably, when the QDs were self-assembled into supraparticles and dispersed in water, the photoluminescence (PL) quantum yield remained as high as 50–55%, similar to that of the individual QDs in suspension [365]. This is in contrast with the results obtained with solids of bare CdSe nanocrystals in which the luminescence gets nearly completely quenched [338, 370]. It means that when assembled in a (supraparticle) solid the emitting cores of our core/shell QDs are situated sufficiently far from each other such that quantum mechanical wave function overlap and Förster energy transfer between the QDs are absent.

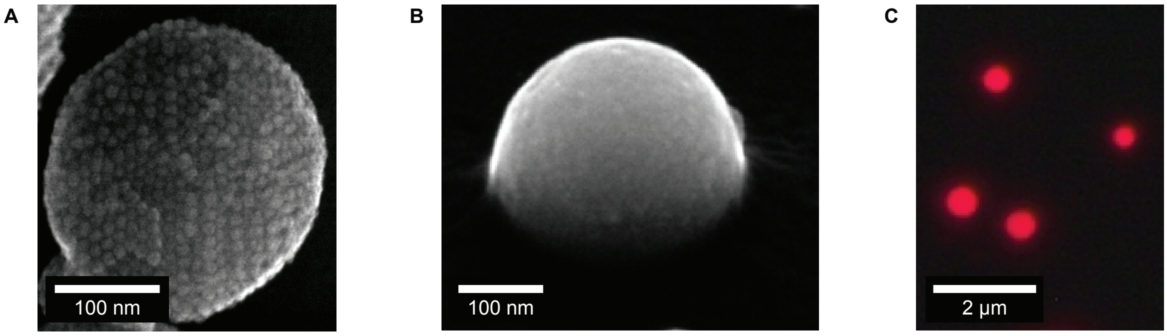

Figure 7.1 Structure of self-assembled supraparticles of CdSe (core) CdS/CdZnS/ZnS (multishell) quantum dots. **(a)** SEM image of an individual supraparticle, clearly showing the constituent nanocrystals. **(b)** A 52° side view image of an individual supraparticle on a SiO_2 substrate, showing that the shape is distorted from spherical due to drying forces. **(c)** Microscope image of the supraparticles on a SiO_2 substrate under UV excitation at 349 nm.

7.3.2 Multiexciton Emission.

Under high-intensity pulsed laser excitation (5 ns pulses at 349 nm), the PL emission spectrum of suspensions of the QDs or individual supraparticles on a silica substrate extends to higher energies by about 240 meV, (Figs. 7.2a-b). Aside from the original

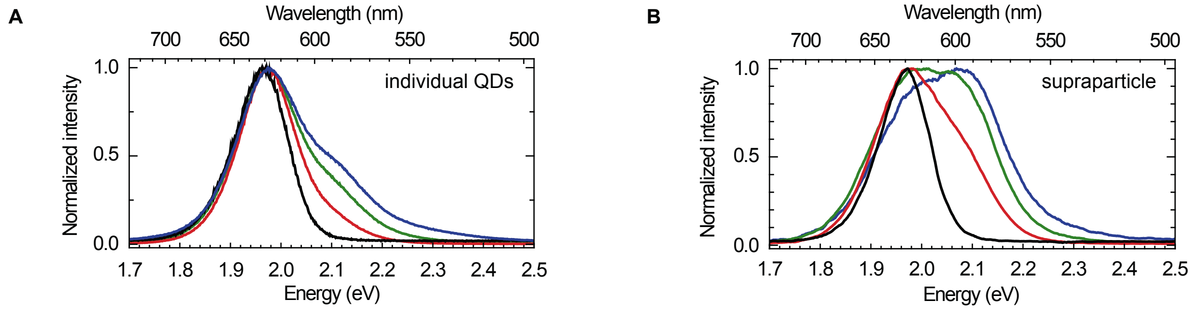

Figure 7.2 Excitation intensity dependent emission spectra of CdSe (core) CdS/CdZnS/ZnS (multishell) quantum dots in suspension, and self-assembled supraparticles. **(a)** PL emission spectra of a solution of multishell quantum dots at excitation fluences of $1.1 \times 10^{-6}\,\mathrm{J\,cm^{-2}}$ (black), $1.0 \times 10^{-4}\,\mathrm{J\,cm^{-2}}$ (red), $1.0 \times 10^{-3}\,\mathrm{J\,cm^{-2}}$ (green) and $1.9 \times 10^{-3}\,\mathrm{J\,cm^{-2}}$ (blue), demonstrating the emergence of high-energy peaks at 2.12 eV and 2.34 eV at intense excitation in addition to the peak at 1.98 eV already present at low excitation intensity. **(b)** Same as in a, but for an individual supraparticle of 1.3 µm diameter and at excitation fluences of $1.2 \times 10^{-4}\,\mathrm{J\,cm^{-2}}$ (black), $3.4 \times 10^{-3}\,\mathrm{J\,cm^{-2}}$ (red), $6.2 \times 10^{-3}\,\mathrm{J\,cm^{-2}}$ (green) and $8.2 \times 10^{-3}\,\mathrm{J\,cm^{-2}}$ (blue).

emission centered around 1.98 eV, now also distinct peaks at 2.12 eV and 2.34 eV appear with a remarkably high intensity. By again lowering the laser excitation intensity these peaks disappear and the spectrum reverts back to the spectrum corresponding to the lowest excitation fluence, Figs. 7.2a-b. This shows that the extension of the emission spectrum to higher energy is a reversible electronic effect and is not due to a structural modification. The reversible change in emission spectrum was observed for individual QDs in suspension as well as for supraparticles on a silica substrate. The supraparticles were photochemically stable and a gradual deterioration of the total intensity was only observed at very high fluences of $> 10^{-2}\,\mathrm{J\,cm^{-2}}$.

As we discuss in more detail below, the extension of the emission spectrum to higher energy is due to emission from several multiexciton states, enabled by the suppression of Auger rates in core/shell QDs. The fact that also in a scalable nano- to microsized colloid particle composed of QDs Auger recombination can be suppressed efficiently, is encouraging for high-intensity applications in lighting and biological research.

7.3.3 Excitation-Emission Properties of QDs and Supraparticles

In order to elucidate the microscopic nature of the emission bands, we performed detailed excitation-emission spectroscopy for variable excitation intensity. Figs. 7.3 a-d present the PL excitation-emission maps for the suspension of individual QDs (a-b) and a supraparticle (c-d). The dashed blue line in Fig. 7.3e presents the excitation spectrum of the QD solution at low intensity lamp excitation. In the energy range before the onset of CdS shell absorption (2.4 eV), a clear structure is seen originating from discrete optical transitions in the CdSe core. At higher excitation intensities, the excitation map (Fig. 7.3b) and spectrum (dashed red line in Fig. 7.3e) show the same resonances. Also the excitation-emission maps (Figs. 7.3c-d) and excitation spectra (solid lines in Fig. 7.3e) of a supraparticle show

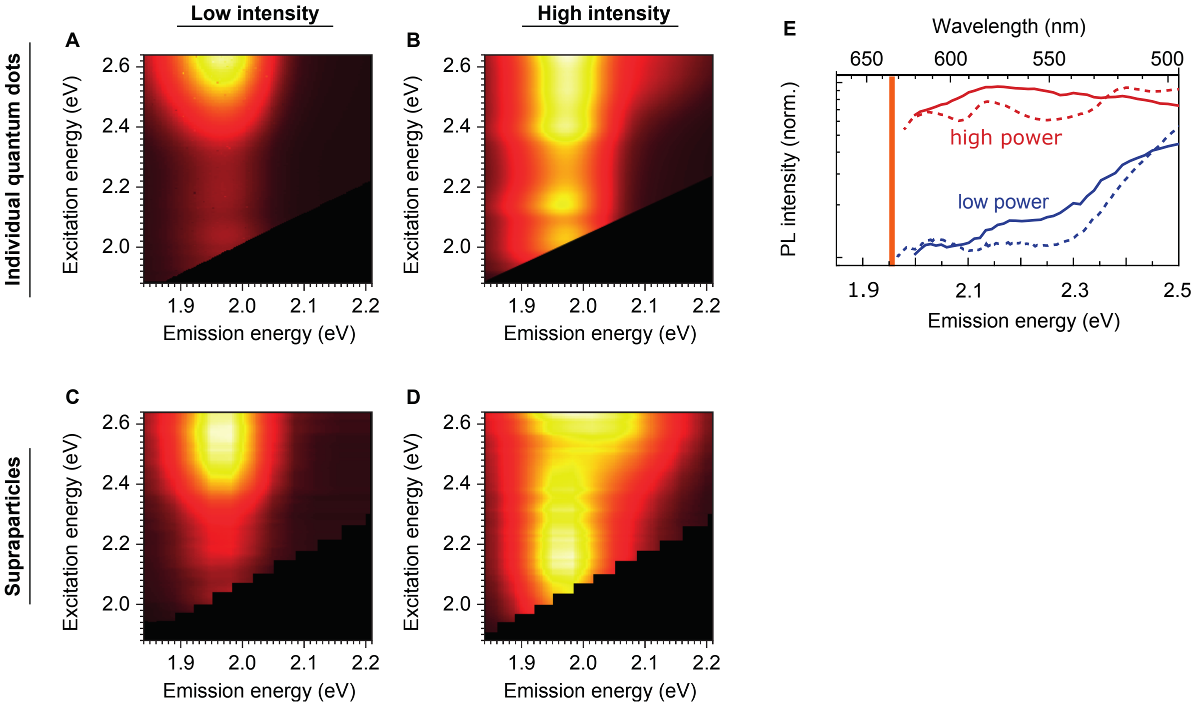

Figure 7.3 PL emission and excitation spectra as a function of excitation intensity. **(a-b)** Excitation-emission maps of a quantum-dot solution at **(a)** low and **(b)** high ($\sim 10 \times 10^{-3}\,\mathrm{J\,cm^{-2}}$) excitation intensity. **(c-d)** Same but for an individual supraparticle on a SiO_2 substrate. **(e)** Excitation spectra of the quantum dot solution (dashed lines) and the supraparticle (solid lines) for emission at 1.96 eV at low (blue) and high (red) excitation intensity, extracted from panels a-d.

qualitatively the same behavior as the QD solution. This demonstrates that the intrinsic exciton states are preserved when the QDs are assembled into supraparticles. We see in Fig. 7.3e that the apparent strength of the CdS interband transitions (above 2.4 eV) was lower at high excitation power (red) than at low power (blue). This can be understood because at high power we saturate the single-exciton emission. Consequently, spectral variations in absorption strength appear weaker in the high-power excitation spectrum. The additional emission bands at high pump power blueshifted from the exciton emission, must originate from multicarrier states. These can be simple multiexciton states of several electron-hole pairs per QD, but they can also be charged states. Multiexciton states can be generated at high pump powers, by rapid successive absorption of multiple photons. Indeed, the CdS shell strongly absorbs excitation light above 500 nm and funnels excitons to the core. At the same time, strong excitation conditions are known to be able to result in charge ejection (more precisely, Auger ejection from a multiexciton state [371, 372]) leaving the QD with a net charge. This is one of the mechanisms believed to be responsible for QD blinking.

Since the pronounced shoulders in the emission spectrum (Figs. 7.2a-b) are blueshifted by > 150 meV with respect to the exciton emission, we conclude that they are not simply due to S-shell biexcitons or charged single excitons (i.e. trions) because the binding energies of these are usually no more than a few 10 meV [373]. Instead, they must be higher multicarrier states involving the P-shell energy levels. In conventional QDs, emission from such states would be strongly quenched by Auger processes. We observe them in emission by virtue of suppressed Auger recombination in our core/multishell QDs. Indeed, emission from triexcitons and charged biexcitons [36, 349, 374–377] has been observed before in core/shell QDs.

7.3.4 Two-photon Excitation Emission Spectrum

While we observed state filling in supraparticles during laser excitation at high pump intensities, we did not observe any state filling using two-photon excitation (2PE), see Fig. 7.4. The red lines show the emission spectrum of a supraparticle, excited at 470 nm (5 ps pulse duration), at low excitation intensity (solid line, $\sim 1.1 \times 10^{-6}\,\mathrm{J\,cm^{-2}}$) and high excitation intensity (dashed line, $\sim 2.1 \times 10^{-4}\,\mathrm{J\,cm^{-2}}$). At high excitation intensity using single photon excitation the multiexciton emission is clearly visible. The black lines show the emission spectrum of the same supraparticle during 2PE excitation at 940 nm (140 fs pulse duration), at low laser intensity (solid line, $\sim 5 \times 10^{-3}\,\mathrm{J\,cm^{-2}}$) and at high laser intensity (dashed line, $\sim 2 \times 10^{-2}\,\mathrm{J\,cm^{-2}}$). At high excitation intensity during 2PE only a small increase in emission of the biexciton at 2.12 eV could be observed, in contrast to what was observed for single photon excitation. At even higher laser intensities $7 \times 10^{-2}\,\mathrm{J\,cm^{-2}}$ at 940 nm, the shape of the emission spectrum changed irreversibly and at even higher laser intensities the supraparticle was completely destroyed by the high laser power.

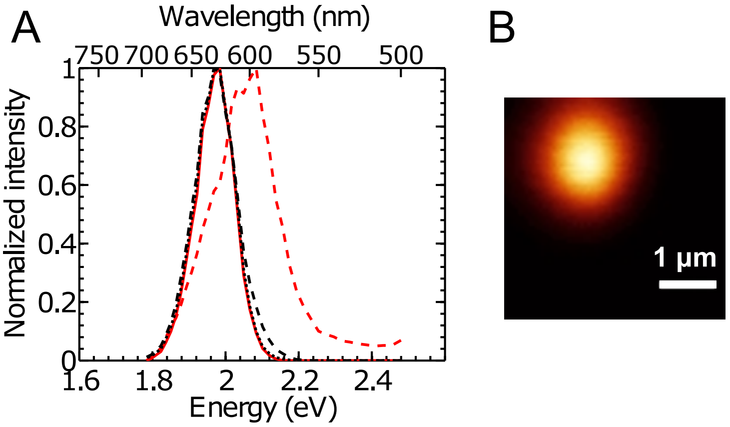

Figure 7.4 Two-photon excitation emission spectrum of supraparticles. **(a)** Emission spectra of a single supraparticle for excitation at 470 nm using high ($2 \times 10^{-4}\,\mathrm{J\,cm^{-2}}$, red dashed line) or low ($1 \times 10^{-6}\,\mathrm{J\,cm^{-2}}$, red solid line) excitation intensity and emission spectra for two photon excitation at 940 nm using an ultra fast laser, at high excitation energy ($J = 2 \times 10^{-2}\,\mathrm{J\,cm^{-2}}$, dashed black line) or low excitation energy ($J = 5 \times 10^{-3}\,\mathrm{J\,cm^{-2}}$, dotted black line). No state filling was observed at high two-photon excitation intensity. **(b)** Confocal image of a single supraparticle during excitation at 940 nm.

We tried to explain the difference in observed emission between 2PE and normal excitation using the Leica TCS SP8 confocal microscope set-up using a rate-equation model [365], which we adjusted for pulsed excitation, see Fig. 7.5. We modeled the pulsed excitation in two successive steps, first by an population decay of 12.5 ns (arrows k_1, k_2 and

k_3, in Fig. 7.5), the time between subsequent laser pulses, secondly with a laser excitation step (arrows P, in Fig. 7.5). The system is excited from the ground state G in to higher states X single exciton, X_2 biexciton, and X_3 triexciton, via non-resonant absorption followed by carrier cooling. We allow in the model for excited state absorption. The excited states, X, X_2 and X_3 decay at rates k_1, k_2, and k_3, respectively. We use values of $k_1 = 1/20\,\text{ns}$, $k_2 = 1/1\,\text{ns}$ and $k_3 = 1/500\,\text{ps}$ [378] [352]. The average number of electron-hole pairs for one-photon excitation $< N_1 >$ is given by $< N_1 > = J\sigma/h\nu$, with J the pump fluence ($\text{J}\,\text{cm}^{-2}$), $\sigma = 5 \times 10^{-15}\,\text{cm}^2$ the absorption cross section of the QDs, and $h\nu = 2.64\,\text{eV}$ the photon energy. For single-photon excitation we could show that a steady state was reached within 10 pulses, see Figs. 7.6a-b, This is well within the pixel dwell time during our measurements ($340\,\mu\text{s}$ or 2.7×10^5 pulses). At low laser fluences, Fig. 7.6a, only the single exciton state is populated. At high laser fluences, Fig. 7.6b, also the bi- and triexciton states and the population in these levels us higher compared to the single exciton state. Fig. 7.6c shows the modeled emission intensity from each of the three excited states as function of the excitation power. It shows that with the laser fluence used during confocal measurements, we were indeed able to explain the observed emission from multiexciton states. This is also clear if we look at the ratio in emission intensity between the different state (X_2/X_1 and X_3/X_1), Fig. 7.6d.

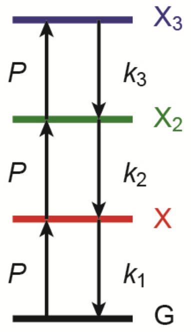

Figure 7.5 A four-level rate equation model is used to simulate the consecutive population of multiexciton states [365]. The system is excited from the ground state G in to higher states X single exciton, X_2 biexciton, and X_3 triexciton at a rate P, which is non-resonant absorption followed by carrier cooling. The excited state X, X_2 and X_3 decay at rates k_1, k_2, and k_3, respectively. We use values of $k_1 = 1/20\,\text{ns}$, $k_2 = 1/1\,\text{ns}$ and $k_3 = 1/500\,\text{ps}$ [352, 378]. We model the experiment with pulsed excitation of 78 MHz or 80 MHz (one-photon excitation or two-photon excitation). The average number of electron-hole pairs for one-photon excitation $< N_1 >$ is given by $< N_1 > = J\sigma/h\nu$, with J the pump fluence (photons/cm^2), $\sigma = 5 \times 10^{-15}\,\text{cm}^2$ the absorption cross section of the QDs, and $h\nu = 2.64\,\text{eV}$ the photon energy. The average number of electron-hole pares for two-photon excitation $< N_2 >$ is given by $< N_2 > = (J/h\nu)^2\sigma_2/\tau_p$, with $\sigma_2 = 2600\,\text{GM}$ (Göppert Mayer, $1\,\text{GM} = 10^{-50}\,\text{cm}^4\,\text{s}$), the estimated two-photon absorption cross section from literature values of similar QDs [379–381], $\tau_p = 140\,\text{fs}$ the pulse duration and $h\nu = 2.32\,\text{eV}$ the photon energy. We modeled the pulsed excitation in two successive steps, first by a population decay of 12.5 ns (arrows k_1, k_2 and k_3), the time between subsequent laser pulses, secondly with a laser excitation step (arrows P).

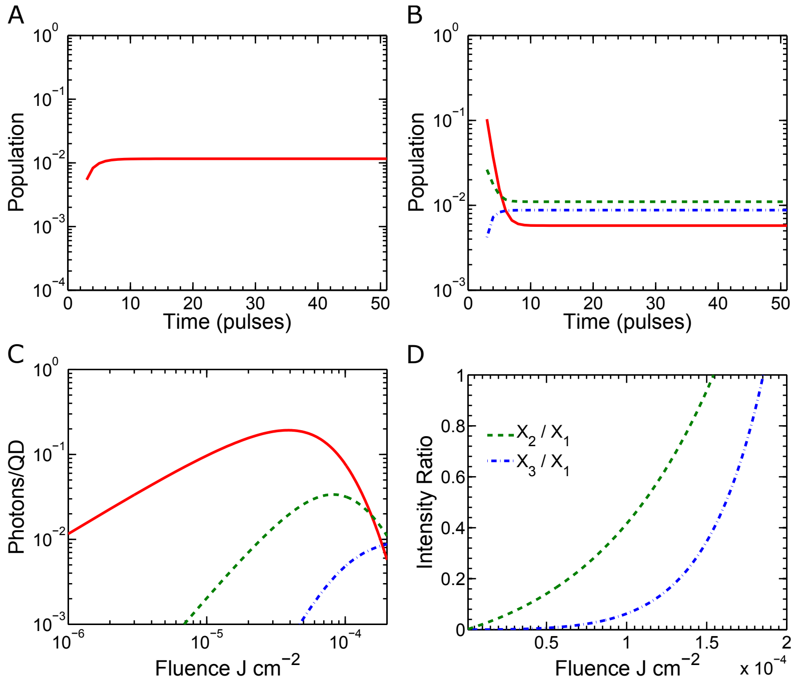

Figure 7.6 Rate-equation modeling of multiexciton populations. **(a)** The evolution of the population of multiexciton states simulated for normal pulsed excitation (470 nm) and a fluence of $J = 1 \times 10^{-6}\,\mathrm{J\,cm^{-2}}$. A steady state was reached after 5 laser pulses. **(b)** As **(a)**, but with a fluence of $J = 2 \times 10^{-4}\,\mathrm{J\,cm^{-2}}$. A steady state was reached after 10 laser pulses. **(c)** The simulated emission intensity for normal pulsed excitation (470 nm) at steady state per pulse, from each of the three levels as function of excitation power: $I_i = \eta_i k_i \int N_i(t)dt$, where I_i, η_i, k_i and N_i are the emission, the quantum efficiency, the decay rate and the population of level i, respectively. We assume the bright fraction of QDs in the ensemble $\eta_i = 1$, $\eta_2 = 0.1$, and $\eta_3 = 0.01$. The range of laser fluence plotted here, is similar as used in experiment. **(d)** The ratio in emission intensity from the different states (X_2/X_1 and X_3/X_1) plotted as function of laser fluence. The excited states are indicated in the following way: the single exciton (red solid line), of the biexcition (green dashed line), of the triexciton (blue dot-dashed line).

We employed the same rate-equation for 2PE to model the emission. We used the following relation to calculate the average electron-hole pairs created by 2PE

$$< N_2 > = \left(\frac{J}{h\nu}\right)^2 \frac{\sigma_2}{\tau_p}, \tag{7.1}$$

with $\sigma_2 = 2600\,\mathrm{GM}$ (Göppert Mayer, $1\,\mathrm{GM} = 10^{-50}\,\mathrm{cm^4\,s}$), the two-photon absorption cross section for QDs [379–381], $\tau_p = 140\,\mathrm{fs}$ the pulse duration, and $h\nu = 2.32\,\mathrm{eV}$ the photon energy. Two-photon excitation is different from one-photon excitation as it is dependent on the square of the fluence and the pulse duration.

Figs. 7.7a-b show that also with 2PE a steady state is reached within 10 laser pulses. Fig. 7.7c shows the emission of QDs under 2PE once a steady state is reached (after 50 pulses) as a function of the laser fluence, with the same range laser fluence used in experiments. In contrast to normal excitation the emission of the bi- and triexciton state stays below the single exciton state. If we then compare the calculated emission ratio from the different excited states (X_2/X_1 and X_3/X_1) for normal excitation and 2PE, we observe that using normal excitation, emission from the X_2 state becomes larger then emission form X_1 state at fluences above $1.5 \times 10^{-4}\,\mathrm{J\,cm^{-2}}$. On the other hand, in 2PE the calculated emission from X_2 stays below the emission from X_1 and is maximal 20% of the emission from X_1, see Fig. 7.7d. This is similar to what was found in the experiment, Fig. 7.4a, here we observe an emission from X_2 [365] at 2.12 eV at high fluences which is only slightly larger compared to emission at low fluences. This is in firm contrast with normal excitation, where at high fluences X_2 emission became about twice as high as X_1 emission, similar to what was predicted from calculations, Fig. 7.6d. From this we conclude that the model indeed explains the differences in multiexciton emission between normal excitation and 2PE under experimental conditions. Note, that differences between experiment and calculations may arise for instance, from errors in the measured laser power, the estimated two-photon absorption cross section σ_2, assumed quantum efficiencies η_i or decay rates k_i. Excitation at 800 nm, where σ_2 is larger [381], may result in more emission from bi- and triexciton states, provided that heating of the sample, due to the large fluences needed for 2PE, does not destroy the supraparticles.

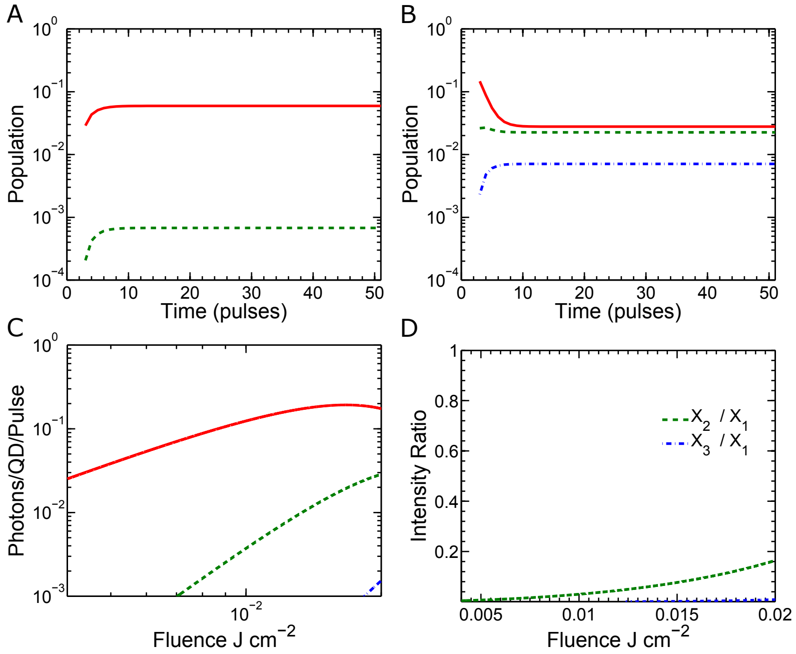

Figure 7.7 Rate-equation modeling of multiexciton populations for 2PE. **(a)** The evolution of the population of multiexciton states simulated for two-photon excitation (940 nm) and a fluence of $J = 4 \times 10^{-3}\,\mathrm{J\,cm^{-2}}$. A steady state was reached after 5 laser pulses. **(b)** As **(a)**, but with a fluence of $J = 2 \times 10^{-2}\,\mathrm{J\,cm^{-2}}$. A steady state was reached after 5 laser pulses. **(c)** The simulated emission intensity for two-photon excitation in steady state per pulse, from each of the three levels as function of excitation power. The range of laser fluence plotted here, is similar as used in experiment. **(d)** The ratio in emission intensity during 2PE from the different states (X_2/X_1 and X_3/X_1) plotted as function of laser fluence. The excited states are indicated in the following way: the single exciton (red solid line), of the biexcition (green dashed line), of the triexciton (blue dot-dashed line).

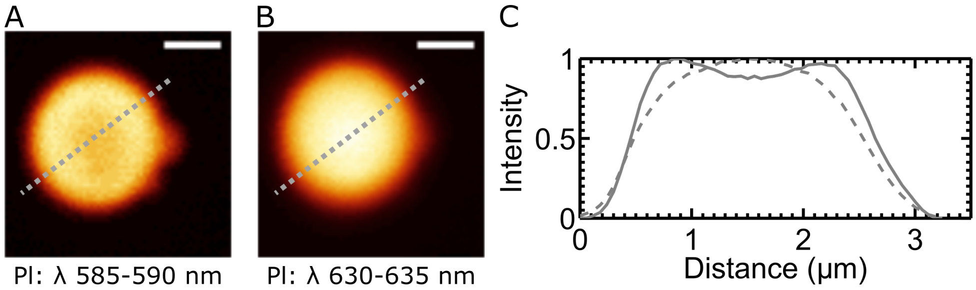

Figure 7.8 Onset of whispering gallery modes in a supraparticle. **(a)** Confocal image showing the recorded emission between λ 585–590 nm **(b)** and λ 630–635 nm (right) of a supraparticle with the size of 3 µm deposited on a silica waver, excited at 470 nm, 5 ps pulse duration and 78 MHz repitition rate, scale bar 1 µm. **(c)** Intensity profile of emission of emission between λ 585–590 nm (solid line) and emission between λ 630–635 nm (dashed line). Line profiles were taken from dashed lines in panels **(a-b)**. The fact that emission around 585 nm is preferentially present at the circumference, is an indication of the onset of whispering gallery modes. However, no spectral features in the emission spectrum could be observed for this sample.

7.3.5 Whispering Gallery Modes in Spherical Supraparticles.

Exciton and multiexciton emission was observed for supraparticles with a non-spherical shape deposited on a silica substrate. Supraparticles deposited on a silica substrate also showed the onset of whispering gallery modes in confocal microscope images when excited above 2.6 eV, see Fig. 7.8a. The confocal images show the luminescence from a supraparticle, with the size of 3 µm, from a small emission bandwidth ($\Delta\lambda = 5$ nm). At a bandwidth of $\lambda = 585$–590 nm, a higher emission intensity can be observed close to the circumference of the particle. This indicates that there was a whispering gallery mode present within that bandwidth. At a bandwidth of $\lambda = 630$–635 nm no whispering gallery modes were present in the confocal image. The line profile taken over the full width of the particle, presented in Fig. 7.8c, confirms that there was only a whispering gallery mode present around $\lambda = 585$–590 nm. In this emission bandwidth, a clear dip in intensity was observed in the center of the particle, while this was not observed for the other emission bandwidth. In this case, a whispering gallery mode was only observed from these confocal images. Conversely, we did not observe Mie modes in the emission spectrum. The exact reason for the absence of Mie modes is unclear. This can be due to several reasons: roughness of the surface of the supraparticle, dust around the particle, the outcoupling of light via the silica substrate $n \sim 1.46$, or irregularities in the dome-like shape.

In contrast, when the supraparticles particles were deposited on a field of upstanding ZnO nanowires their spherical shape was retained. Most likely, this is caused by the fact that as during drying the water was drained through the layer of rods (see Fig. 7.9a) avoiding deformation of the spherical supraparticles. Not only the microscope images of individual supraparticles showed the signs of whispering gallery modes (Fig. 7.9b), also their emission spectra showed sharp peaks in the energy region around 2 eV at all pump powers (Fig. 7.9c). Similar whispering gallery modes were observed previously with much larger silica microspheres on which quantum dots were adsorbed [382, 383].

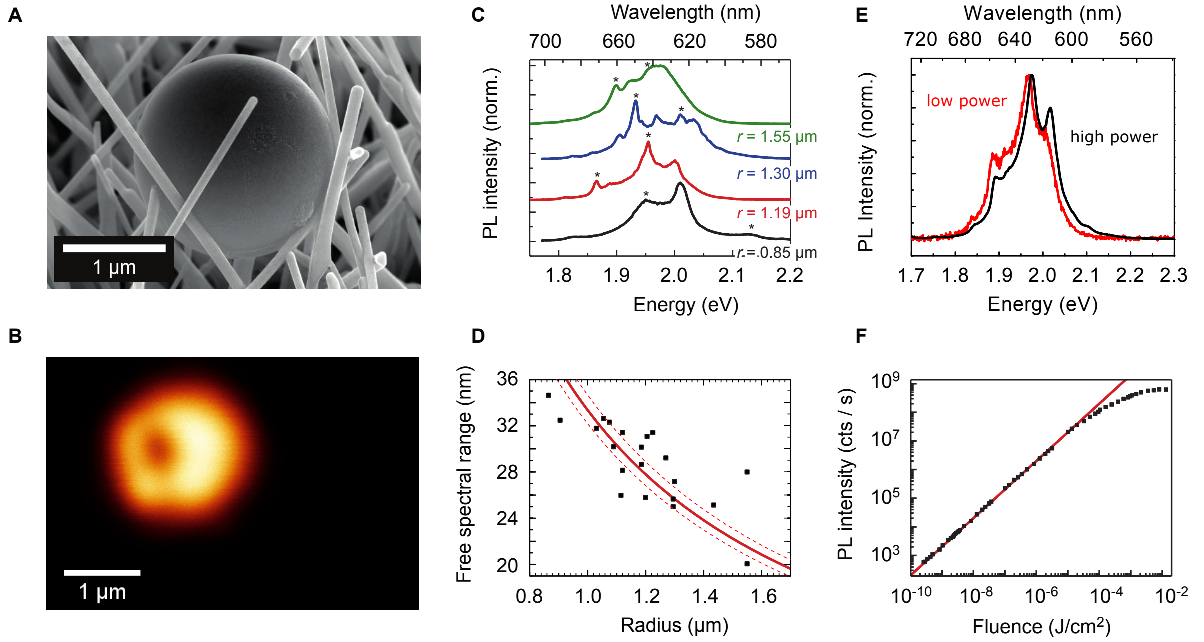

Figure 7.9 Mie whispering gallery modes in supraparticles. **(a)** SEM image of a supraparticle lying on a field of ZnO nanowires. **(b)** Microscope image of a supraparticle on ZnO nanowires under pulsed excitation (78 MHz, 140 ps pulse duration) at 485 nm, showing more intense emission at the circumference owing to whispering gallery modes. **(c)** PL emission spectra of four supraparticles of different radius, showing spectral features related to the whispering gallery mode structure. **(d)** Free spectral range $\Delta\lambda$ of the modes versus the supraparticle radius r_{ball}. The red lines are a fit to $\Delta\lambda = \lambda^2/(2\pi r_{ball} n_{eff})$, with an effective refractive index $n_{eff} = 1.89$ (solid line) or an effective refractive index of $n_{eff} = 1.82 \vee 1.96$ (dashed lines). The asterisks ($*$) in **(c)** indicate modes belonging to mode families with incremental quantum number. **(e)** Two emission spectra of an individual supraparticle, one at low excitation fluence ($1.06 \times 10^{-9}\,\mathrm{J\,cm^{-2}}$, blue) and one at orders of magnitude higher excitation intensity ($9.7 \times 10^{-4}\,\mathrm{J\,cm^{-2}}$, red). **(f)** The integrated PL emission intensity as a function of the pump fluence. There is a linear dependence over 6 orders of magnitude in fluence.

From the peak widths we derived a quality factor of the whispering gallery modes of $Q = fwhm/\lambda \sim 100$.

Fig. 7.9d presents the free spectral range of the modes (for instance, those indicated with asterisks ($*$) in Fig. 7.9c) plotted as function of the radius of the supraparticles. The line gives the free spectral range calculated for whispering gallery modes in spheres of varying diameter using $\Delta\lambda = \lambda^2/(2\pi r_{ball} n_{eff})$, with an effective refractive index $n_{eff} = 1.89$ and the emission wavelength $\lambda = 630\,\mathrm{nm}$.

We calculated the wavelength-dependent scattering using Mie theory, in order to get an idea of the whispering gallery modes that can be present in the particles. Figs. 7.10a-b present the wavelength-dependent scattering for sizes of supraparticles equal to those of which the PL emission spectra are shown in Fig. 7.9c, for a $n_{eff} = 1.89$. When we overlaid Figs. 7.9c and 7.10a, we concluded that the experimentally observed Mie modes do not exactly coincide with these theoretical calculations. Also, when a slightly different

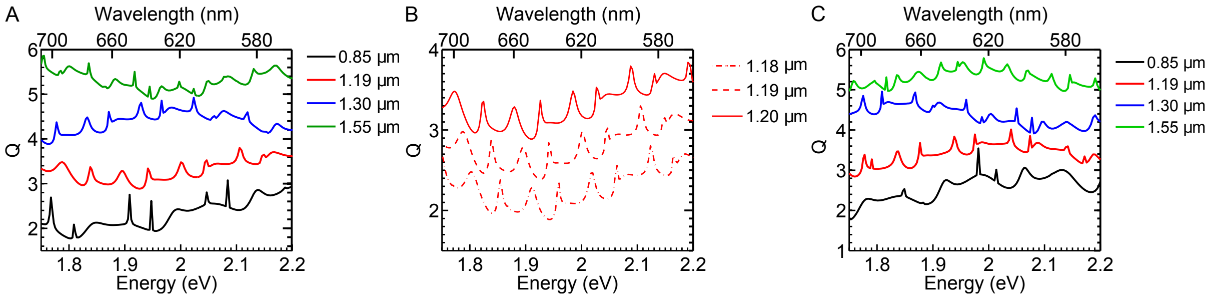

Figure 7.10 Calculations on the scattering of light of supraparticles using Mie theory. Calculations were done for supraparticles in air $n = 1.00$. **(a)** Calculations of the scattering of supraparticles for different particle sizes using an effective refractive index $n_{eff} = 1.89$. **(b)** Calculations of the scattering of supraparticles with a slight size difference using an effective refractive index $n_{eff} = 1.89$. **(c)** Calculations of the scattering of supraparticles for different particle sizes using an effective refractive index $n_{eff} = 1.96$.

effective refractive index $n_{eff} = 1.96$ was used to calculate Mie scattering, we obtained a complete different spectrum for the whispering gallery modes, presented in Fig. 7.10c. This shows how sensitive the calculations are for changes in n_{eff}. Moreover, sizes of supraparticles were determined using microscope images. The resolution of the microscope images is ~ 250 nm. This makes an accurate determination of the size of the particles (within ~ 20 nm) from these microscope images difficult. However, Fig. 7.10b shows that even small changes (~ 10 nm) in the size of the supraparticles result in considerable shifts in the position of the calculated whispering gallery modes of around ~ 10 nm, Fig. 7.10b. Therefore, in this case, predictions on the exact position of whispering gallery modes using Mie theory proved to be difficult.

Remarkably, the shape of the experimental emission spectrum remained perfectly constant over 5 orders of excitation intensity (Fig. 7.9e). This also means that, unlike for the deformed supraparticles, multiexciton emission did not occur at higher excitation intensities. This difference might be related to the higher density of optical states (DOS; averaged over the emission spectrum of the QDs) due to the Mie resonances in a supraparticle. A higher DOS leads to faster decay rates for all single and multiexciton states. Consequently, the fluence required to reach a considerable multiexciton population can become much higher. The unchanged shape of the emission spectrum with sharp peaks related to whispering gallery modes also shows that there is no gain for these modes. Indeed, Fig. 7.9f shows that the intensity of the entire spectrum increases linearly with the excitation intensity. The reason for the absence of gain and lasing is not yet clear. It might be related to the relatively small diameter of our supraparticles (maximum 3 µm), as radiative losses increase with decreasing diameter of spheres [384]. Moreover, surface absorption of contaminants, inhomogeneities, surface roughness can significantly decrease the quality factor of the whispering gallery modes [384]. It can also be due to optical coupling of the supraparticles with the supporting ZnO nanowires [385, 386]. In a recent publication, using similar core-shelled QDs, lasing of these QDs was observed [387]. This indicates that lasing from individual supraparticles is feasible and that it is a matter of times before lasing can be observed in these supraparticles. New experiments are currently performed.

7.4 Conclusion

In summary, we have demonstrated that quantum dot supraparticles with a non-spherical (and most likely less regular / smooth) shape show stable and bright broadband emission from exciton and multiexciton states. During 2PE, multiexciton emission was hardly observed due to the very low cross section for two-photon absorption at 940 nm. Spherical supraparticles emit from whispering gallery modes fed by the lowest exciton states. Individual supraparticles, which can be made with diameters from 100 nm to micrometers, can have high potential in applications varying from bio-labeling to integration with waveguides in silicon nitride opto-electronics. Moreover, although lasing from these supraparticles was not observed yet, we believe that finding the conditions such that the Mie modes, that we found, also show gain and finally lead to supraparticle lasing is a question of time. Finally, we remark that spherical supraparticles are colloids, for which microfluidic methods are available to reduce the size dispersion. This means that it should be possible to assemble the supraparticles in a third step in the hierarchy, to form photonic-crystals for optical wavelengths. Hence our results also open new versatile three-step routes for scalable fabrication of photonic structures.

7.5 Acknowledgements

I gratefully thank Relinde J. A. van Dijk-Moes for synthesis of the multi-shelled quantum dots. I gratefully thank Bart de Nijs for preparation of the supraparticles. I gratefully thank Lambert K. van Vugt for the spectroscopy measurements and SEM measurements. I thank Daniel Vanmaekelbergh, Freddy T. Rabouw and Lambert K. Van Vugt for co-interpretation of the data. I thank Freddy T. Rabouw with setting up the rate-equation model. Part of this chapter was published as a paper [365]: Shape-Dependent Multi-Exciton Emission and Whispering Gallery Modes in Supraparticles of CdSe/MultiShell Quantum Dots, *ACS Nano* **2015**, *9*, 3942-3950.

References

[1] P.-G. de Gennes, *Soft matter: more than words.* Soft Matter, 1(1):16, 2005.

[2] P.-G. de Gennes. *Nobel Lecture*, 1991. Nobelprize.org (accessed August 8, 2016).

[3] R. Brown, *XXVII. A brief account of microscopical observations made in the months of June, July and August* 1827*, on the particles contained in the pollen of plants; and on the general existence of active molecules in organic and inorganic bodies.* Philos. Mag. Series 2, 4(21):161–173, 1828.

[4] F. Selmi, *Studj sulla dimulsione di cloruro d'argento.* Nuovi Annali delle Scienze Naturali di Bologna, fasc. di agosto, 1845.

[5] T. Graham, *Liquid Diffusion Applied to Analysis.* Philos. Trans. Roy. Soc. London, 151(0):183–224, 1861.

[6] H. Siedentopf and R. Zsigmondy, *Uber Sichtbarmachung und Größenbestimmung ultramikroskopischer Teilchen, mit besonderer Anwendung auf Goldrubingläser.* Ann. Phys. (Berlin), 315(1):1–39, 1902.

[7] R. Zsigmondy. *Nobel Lecture*, 1926. Nobelprize.org (accessed August 8, 2016).

[8] J. Perrin, *Mouvement brownien et réalité moléculaire.* Ann. Chim. Phys., 18:5–114, 1909.

[9] A. Einstein, *Über die von der molekularkinetischen Theorie der Wärme geforderte Bewegung von in ruhenden Flüssigkeiten suspendierten Teilchen.* Ann. Phys. (Berlin), 322(8):549–560, 1905.

[10] A. Einstein, *Zur Theorie der Brownschen Bewegung.* Ann. Phys. (Berlin), 324(2):371–381, 1906.

[11] M. von Smoluchowski, *Zur kinetischen Theorie der Brownschen Molekularbewegung und der Suspensionen.* Ann. Phys. (Berlin), 326(14):756–780, 1906.

[12] A. Vrij, E. A. Nieuwenhuis, H. M. Fijnaut, and W. G. M. Agterof, *Application of modern concepts in liquid state theory to concentrated particle dispersions.* Farad. Discuss., 65(0):101, 1978.

[13] B. Alder and T. Wainwright, *Phase Transition for a Hard Sphere System.* J. Chem. Phys, 27(5):1208–1209, 1957.

[14] W. G. Hoover and F. H. Ree, *Melting Transition and Communal Entropy for Hard Spheres.* J. Chem. Phys, 49(8):3609, 1968.

[15] A. van Blaaderen, A. Imhof, W. Hage, and A. Vrij, *Three-dimensional imaging of submicrometer colloidal particles in concentrated suspensions using confocal scanning laser microscopy.* Langmuir, 8(6):1514–1517, 1992.

[16] A. van Blaaderen and P. Wiltzius, *Real-Space Structure of Colloidal Hard-Sphere Glasses.* Science, 270(5239):1177–1179, 1995.

[17] J. D. Bernal and J. Mason, *Packing of Spheres: Co-ordination of Randomly Packed Spheres.* Nature, 188(4754):910–911, 1960.

[18] P. N. Pusey and W. van Megen, *Phase behaviour of concentrated suspensions of nearly hard colloidal spheres.* Nature, 320(6060):340–342, 1986.

[19] D. J. W. Aastuen, N. A. Clark, L. K. Cotter, and B. J. Ackerson, *Nucleation and Growth of Colloidal Crystals.* Phys. Rev. Lett., 57(14):1733–1736, 1986.

[20] R. Piazza, T. Bellini, and V. Degiorgio, *Equilibrium sedimentation profiles of screened charged colloids: A test of the hard-sphere equation of state.* Phys. Rev. Lett., 71:4267–4270, 1993.

[21] M. A. Rutgers, J. H. Dunsmuir, J.-Z. Xue, W. B. Russel, and P. M. Chaikin, *Measurement of the hard-sphere equation of state using screened charged polystyrene colloids.* Phys. Rev. B, 53(9):5043–5046, 1996.

[22] R. Piazza, *Settled and unsettled issues in particle settling.* Rep. Prog. Phys., 77(5):056602, 2014.

[23] U. Gasser, E. R. Weeks, A. Schofield, P. N. Pusey, and D. a. Weitz, *Real-space imaging of nucleation and growth in colloidal crystallization.* Science, 292(5515):258–262, 2001.

[24] A. M. Alsayed, M. F. Islam, J. Zhang, P. J. Collings, and A. G. Yodh, *Premelting at defects within bulk colloidal crystals.* Science, 309(5738):1207–10, 2005.

[25] N. A. M. Verhaegh and A. van Blaaderen, *Dispersions of Rhodamine-Labeled Silica Spheres: Synthesis, Characterization, and Fluorescence Confocal Scanning Laser Microscopy.* Langmuir, 10:1427–1438, 1994.

[26] A. van Blaaderen and A. Vrij, *Synthesis and Characterization of Colloidal Dispersions of Fluorescent , Monodisperse Silica Spheres.* Langmuir, 81(2):2921–2931, 1992.

[27] G. Bosma, C. Pathmamanoharan, E. H. de Hoog, W. K. Kegel, A. van Blaaderen, and H. N. Lekkerkerker, *Preparation of Monodisperse, Fluorescent PMMA-Latex Colloids by Dispersion Polymerization.* J. Colloid Interface Sci., 245(2):292–300, 2002.

[28] R. P. A. Dullens, M. Claesson, D. Derks, A. van Blaaderen, and W. K. Kegel, *Monodisperse Core-Shell Poly(methyl methacrylate) Latex Colloids.* Langmuir, 19(15):5963–5966, 2003.

[29] C. P. Royall, W. C. K. Poon, and E. R. Weeks, *In search of colloidal hard spheres.* Soft Matter, 9(1):17–27, 2013.

[30] W. C. K. Poon, E. R. Weeks, and C. P. Royall, *On measuring colloidal volume fractions.* Soft Matter, 8(1):21–30, 2012.

[31] J. P. Hoogenboom, P. Vergeer, and A. van Blaaderen, *A real-space analysis of colloidal crystallization in a gravitational field at a flat bottom wall.* J. Chem. Phys., 119(6):3371–3383, 2003.

[32] P. Sollich and N. B. Wilding, *Polydispersity induced solid-solid transitions in model colloids.* Soft Matter, 7(9):4472, 2011.

[33] A. Yethiraj and A. van Blaaderen, *A colloidal model system with an interaction tunable from hard sphere to soft and dipolar.* Nature, 421(6922):513–7, 2003.

[34] S. C. Glotzer and M. J. Solomon, *Anisotropy of building blocks and their assembly into complex structures.* Nat. Mater., 6(7):557–562, 2007.

[35] S.-M. Yang, S.-H. Kim, J.-M. Lim, and G.-R. Yi, *Synthesis and assembly of structured colloidal particles.* J. Mater. Chem., 18(19):2177, 2008.

[36] J. Zhao, G. Nair, B. R. Fisher, and M. G. Bawendi, *Challenge to the Charging Model of Semiconductor-Nanocrystal Fluorescence Intermittency from Off-State Quantum Yields and Multiexciton Blinking.* Phys. Rev. Lett., 104(15):157403, 2010.

[37] P. Bolhuis and D. Frenkel, *Tracing the phase boundaries of hard spherocylinders.* J. Chem. Phys, 106(2):666–687, 1997.

[38] F. Reinitzer, *Beiträge zur Kenntniss des Cholesterins.* Monatsh. Chem., 9(1):421–441, 1888.

[39] O. Lehmann, *Über fliessende krystalle.* Z. Physik. Chem., 4:462–75, 1889.

[40] M. G. Friedel, *Les états mésomorphes de la matière.* Ann. Phys. (Paris), 18:273–474, 1922.

[41] S. Chandrasekhar, B. K. Sadashiva, and K. A. Suresh, *Liquid crystals of disc-like molecules.* Pramana, 9(5):471–480, 1977.

[42] L. Onsager, *The Effects of Shape on the Interaction of Colloidal Particles.* Ann. N. Y. Acad. Sci., 51(4):627–659, 1949.

[43] D. Frenkel, H. N. W. Lekkerkerker, and a. Stroobants, *Thermodynamic stability of a smectic phase in a system of hard rods.* Nature, 332(6167):822–823, 1988.

[44] A. Kuijk, A. van Blaaderen, and A. Imhof, *Synthesis of monodisperse, rodlike silica colloids with tunable aspect ratio.* J. Am. Chem. Soc., 133(8):2346–9, 2011.

[45] A. Kuijk, A. Imhof, M. H. W. Verkuijlen, T. H. Besseling, E. R. H. van Eck, and A. van Blaaderen, *Colloidal Silica Rods: Material Properties and Fluorescent Labeling.* Part. Part. Syst. Charact., 31(6):706–713, 2014.

[46] A. Kuijk. *Fluorescent Colloidal Silica Rods, Synthesis and Phase Behavior.* Phd-thesis, Universiteit Utrecht, The Netherlands, 2012. A digital version of this thesis is available at http://www.colloid.nl.

[47] M. A. Bates and D. Frenkel, *Influence of polydispersity on the phase behavior of colloidal liquid crystals: A Monte Carlo simulation study.* J. Chem. Phys., 109(14):6193–6199, 1998.

[48] P.-G. de Gennes. *The Physics of Liquid Crystals.* Clarendon Press, Oxford, 1974.

[49] H. Zocher, *Über freiwillige Strukturbildung in Solen. (Eine neue Art anisotrop flüssiger Medien.).* Z. Anorg. Allg. Chem., 147(1):91–110, 1925.

[50] F. C. Bawden, N. W. Pirie, J. D. Bernal, and I. Fankuchen, *Liquid crystalline substances from virus-infected plants.* Nature, 138:1051–1052, 1936.

[51] G. Oster, *Two-phase formation in solutions of tobacco mosaic virus and the problem of long-range forces.* J. Gen. Physiol., 33(5):445–473, 1950.

[52] Z. Dogic and S. Fraden, *Smectic phase in a colloidal suspension of semiflexible virus particles.* Phys. Rev. Lett., 78(12):2417–2420, 1997.

[53] K. M. Keville, E. I. Franses, and J. M. Caruthers, *Preparation and characterization of monodisperse polymer microspheroids.* J. Colloid Interface Sci., 144(1):103–126, 1991.

[54] C. C. Ho, A. Keller, J. A. Odell, and R. H. Ottewill, *Preparation of monodisperse ellipsoidal polystyrene particles.* Colloid Polym. Sci., 271(5):469–479, 1993.

[55] P. A. Buining and H. N. W. Lekkerkerker, *Isotropic-nematic phase separation of a dispersion of organophilic boehmite rods.* J. Phys. Chem., 97(44):11510–11516, 1993.

[56] F. M. van der Kooij and H. N. W. Lekkerkerker, *Formation of Nematic Liquid Crystals in Suspensions of Hard Colloidal Platelets.* J. Phys. Chem. B, 102(40):7829–7832, 1998.

[57] D. van der Beek, T. Schilling, and H. N. W. Lekkerkerker, *Gravity-induced liquid crystal phase transitions of colloidal platelets.* J. Chem. Phys., 121(11):5423–5426, 2004.

[58] H. Maeda and Y. Maeda, *Liquid crystal formation in suspensions of hard rodlike colloidal particles: direct observation of particle arrangement and self-ordering behavior.* Phys. Rev. Lett., 90(1):018303, 2003.

[59] A. Mohraz and M. J. Solomon, *Direct visualization of colloidal rod assembly by confocal microscopy.* Langmuir, 21(12):5298–5306, 2005.

[60] D. Mukhija and M. J. Solomon, *Nematic order in suspensions of colloidal rods by application of a centrifugal field.* Soft Matter, 7(2):540–545, 2011.

[61] J. J. Crassous, A. M. Mihut, E. Wernersson, P. Pfleiderer, J. Vermant, P. Linse, and P. Schurtenberger, *Field-induced assembly of colloidal ellipsoids into well-defined microtubules.* Nat. Commun., 5:5516, 2014.

[62] S. Sacanna, L. Rossi, B. W. M. Kuipers, and A. P. Philipse, *Fluorescent monodisperse silica ellipsoids for optical rotational diffusion studies.* Langmuir, 22(4):1822–1827, 2006.

[63] P. M. Johnson, C. M. van Kats, and A. van Blaaderen, *Synthesis of colloidal silica dumbbells.* Langmuir, 21(24):11510–11517, 2005.

[64] A. F. Demirörs, P. M. Johnson, C. M. van Kats, A. van Blaaderen, and A. Imhof, *Directed self-assembly of colloidal dumbbells with an electric field.* Langmuir, 26(18):14466–14471, 2010.

[65] T. H. Besseling. *Self-Assembly of colloidal spheres and rods in external fields.* Phd-thesis, Utrecht University, The Netherlands, 2014. A digital version of this thesis is available at http://www.colloid.nl.

[66] M. Mittal, R. K. Niles, and E. M. Furst, *Flow-directed assembly of nanostructured thin films from suspensions of anisotropic titania particles.* Nanoscale, 2(10):2237, 2010.

[67] B. J. Lemaire, P. Davidson, J. Ferré, J. P. Jamet, P. Panine, I. Dozov, and J. P. Jolivet, *Outstanding Magnetic Properties of Nematic Suspensions of Goethite (α-FeOOH) Nanorods.* Phys. Rev. Lett., 88(12):125507, 2002.

[68] J. Ge and Y. Yin, *Magnetically responsive colloidal photonic crystals.* J. Mater. Chem., 18(42):5041, 2008.

[69] E. van den Pol, A. V. Petukhov, D. V. Byelov, D. M. E. Thies-weesie, A. Snigirev, and G. J. Vroege, *Behavior of the smectic A phase of colloidal goethite in a magnetic field.* Soft Matter, 6(19):4895, 2010.

[70] A. Kuijk, T. Troppenz, L. Filion, A. Imhof, R. van Roij, M. Dijkstra, and A. van Blaaderen, *Effect of external electric fields on the phase behavior of colloidal silica rods.* Soft Matter, 10:6249–6255, 2014.

[71] J. D. Forster, J.-G. Park, M. Mittal, H. Noh, C. F. Schreck, C. S. O'Hern, H. Cao, E. M. Furst, and E. R. Dufresne, *Assembly of Optical-Scale Dumbbells into Dense Photonic Crystals.* ACS Nano, 5(8):6695–6700, 2011.

[72] M. Adams, Z. Dogic, S. L. Keller, and S. Fraden, *Entropically driven microphase transitions in mixtures of colloidal rods and spheres.* Nature, 393(6683):349–352, 1998.

[73] B. Comiskey, J. D. Albert, H. Yoshizawa, and J. Jacobson, *An electrophoretic ink for all-printed reflective electronic displays.* Nature, 394(6690):253–255, 1998.

[74] M. Kamp, N. A. Elbers, T. Troppenz, A. Imhof, M. Dijkstra, R. van Roij, and A. van Blaaderen, *Electric-Field-Induced Lock-and-Key Interactions between Colloidal Spheres and Bowls.* Chem. Mater., 28(4):1040–1048, 2016.

[75] H. R. Vutukuri, A. F. Demirörs, B. Peng, P. D. J. van Oostrum, A. Imhof, and A. van Blaaderen, *Colloidal Analogues of Charged and Uncharged Polymer Chains with Tunable Stiffness.* Angew. Chem. Int. Ed. (English), 51(45):11249–11253, 2012.

[76] J. P. Singh, P. P. Lele, F. Nettesheim, N. J. Wagner, and E. M. Furst, *One- and two-dimensional assembly of colloidal ellipsoids in ac electric fields.* Phys. Rev. E, 79(5):050401, 2009.

[77] U. Dassanayake, S. Fraden, and A. van Blaaderen, *The structure of electrorheological fluids.* J. Chem. Phys., 112(8):3851—-3858, 2000.

[78] A. A. Shah, H. Kang, K. L. Kohlstedt, K. H. Ahn, S. C. Glotzer, C. W. Monroe, and M. J. Solomon, *Liquid crystal order in colloidal suspensions of spheroidal particles by direct current electric field assembly.* Small, 8(10):1551–62, 2012.

[79] J. Vermant and M. J. Solomon, *Flow-induced structure in colloidal suspensions.* J. Phys.: Condens. Matter, 17(4):R187–R216, 2005.

[80] Y. L. Wu, D. Derks, A. van Blaaderen, and A. Imhof, *Melting and crystallization of colloidal hard-sphere suspensions under shear.* Proc. Natl. Acad. Sci. U. S. A., 106(26):10564–10569, 2009.

[81] D. Derks, Y. L. Wu, A. van Blaaderen, and A. Imhof, *Dynamics of colloidal crystals in shear flow.* Soft Matter, 5(5):1060, 2009.

[82] T. H. Besseling, M. Hermes, A. Fortini, M. Dijkstra, A. Imhof, and A. van Blaaderen, *Oscillatory shear-induced 3D crystalline order in colloidal hard-sphere fluids.* Soft Matter, 8(26):6931, 2012.

[83] P. Jiang and M. J. McFarland, *Large-Scale Fabrication of Wafer-Size Colloidal Crystals, Macroporous Polymers and Nanocomposites by Spin-Coating.* J. Am. Chem. Soc., 126(42):13778–13786, 2004.

[84] A. Mihi, M. Ocaña, and H. Míguez, *Oriented Colloidal-Crystal Thin Films by Spin-Coating Microspheres Dispersed in Volatile Media.* Adv. Mater., 18(17):2244–2249, 2006.

[85] Y. L. Wu. *Control over colloidal crystallization by shear and electric fields.* Phd-thesis, Utrecht University, The Netherlands, 2007. A digital version of this thesis is available at http://www.colloid.nl.

[86] H. Yang and P. Jiang, *Large-scale colloidal self-assembly by doctor blade coating.* Langmuir, 26(16):13173–13182, 2010.

[87] T. Ruhl, P. Spahn, and G. Hellmann, *Artificial opals prepared by melt compression.* Polymer, 44(25):7625–7634, 2003.

[88] O. L. J. Pursiainen, J. J. Baumberg, H. Winkler, B. Viel, P. Spahn, and T. Ruhl, *Shear-Induced Organization in Flexible Polymer Opals.* Adv. Mater., 20(8):1484–1487, 2008.

[89] Q. Zhao, C. E. Finlayson, D. R. E. Snoswell, A. Haines, C. Schäfer, P. Spahn, G. P. Hellmann, A. V. Petukhov, L. Herrmann, P. Burdet, P. A. Midgley, S. Butler, M. Mackley, Q. Guo, and J. J. Baumberg, *Large-scale ordering of nanoparticles using viscoelastic shear processing.* Nat. Commun., 7:11661, 2016.

[90] M. Doi and S. Edwards. *The Theory of Polymer Dynamics.* Oxford University Press, Oxford, Oxford, 1986.

[91] S. Hess, *Fokker-Planck-Equation Approach to Flow Alignment in Liquid Crystals.* Z. Naturforsch. A, 31(9):1034–1037, 1976.

[92] M. P. Lettinga and J. K. G. Dhont, *Non-equilibrium phase behaviour of rod-like viruses under shear flow.* J. Phys.: Condens. Matter, 16(38):S3929–S3939, 2004.

[93] M. P. Lettinga, Z. Dogic, H. Wang, and J. Vermant, *Flow behavior of colloidal rodlike viruses in the nematic phase.* Langmuir, 21(17):8048–8057, 2005.

[94] Y.-G. Tao, W. K. den Otter, and W. J. Briels, *Kayaking and wagging of liquid crystals under shear: Comparing director and mesogen motions.* EPL, 86(5):56005, 2009.

[95] Y.-G. Tao, W. K. den Otter, and W. J. Briels, *Kayaking and wagging of rods in shear flow.* Phys. Rev. Lett., 95(23):237802, 2005.

[96] G. von Freymann, V. Kitaev, B. V. Lotsch, and G. A. Ozin, *Bottom-up assembly of photonic crystals.* Chem Soc Rev, 42(7):2528–2554, 2013.

[97] J. V. Sanders, *Colour of Precious Opal.* Nature, 204(4964):1151–1153, 1964.

[98] R. Biswas, M. M. Sigalas, G. Subramania, C. M. Soukoulis, and K.-M. Ho, *Photonic band gaps of porous solids.* Phys. Rev. B, 61(7):4549–4553, 2000.

[99] E. Yablonovitch, *Inhibited spontaneous emission in solid-state physics and electronics.* Phys. Rev. Lett., 58(20):2059–2062, 1987.

[100] V. P. Bykov, *Spontaneous emission from a medium with a band spectrum.* Sov. J. Quantum Electron., 4(7):861–871, 1975.

[101] H. S. Sözüer, J. W. Haus, and R. Inguva, *Photonic bands: Convergence problems with the plane-wave method.* Phys. Rev. B, 45(24):13962–13972, 1992.

[102] A. A. Zakhidov, R. H. Baughman, Z. Iqbal, C. Cui, I. Khayrullin, S. O. Dantas, J. Marti, and V. G. Ralchenko, *Carbon structures with three-dimensional periodicity at optical wavelengths.* Science, 282(5390):897–901, 1998.

[103] Y. A. Vlasov, X.-Z. Bo, J. C. Sturm, and D. J. Norris, *On-chip natural assembly of silicon photonic bandgap crystals.* Nature, 414(6861):289–293, 2001.

[104] J. S. King, C. W. Neff, C. J. Summers, W. Park, S. Blomquist, E. Forsythe, and D. Morton, *High-filling-fraction inverted ZnS opals fabricated by atomic layer deposition.* Appl. Phys. Lett., 83(13):2566–2568, 2003.

[105] T. T. Ngo, C. M. Liddell, M. Ghebrebrhan, and J. D. Joannopoulos, *Tetrastack: Colloidal diamond-inspired structure with omnidirectional photonic band gap for low refractive index contrast.* Appl. Phys. Lett., 88(24):241920, 2006.

[106] I. D. Hosein, M. Ghebrebrhan, J. D. Joannopoulos, and C. M. Liddell, *Dimer shape anisotropy: A nonspherical colloidal approach to omnidirectonal photonic band gaps.* Langmuir, 26(3):2151–2159, 2010.

[107] S.-K. Lee, G.-R. Yi, J. Moon, S.-M. Yang, and D. Pine, *Pixellated Photonic Crystal Films by Selective Photopolymerization.* Adv. Mater., 18(16):2111–2116, 2006.

[108] A. C. Arsenault, D. P. Puzzo, I. Manners, and G. A. Ozin, *Photonic-crystal full-colour displays.* Nat. Photon., 1(8):468–472, 2007.

[109] S. A. Asher and J. H. Holtz, *Polymerized colloidal crystal hydrogel films as intelligent chemical sensing materials.* Nature, 389(6653):829–832, 1997.

[110] S. A. Asher, V. L. Alexeev, A. V. Goponenko, A. C. Sharma, I. K. Lednev, C. S. Wilcox, and D. N. Finegold, *Photonic Crystal Carbohydrate Sensors: Low Ionic Strength Sugar Sensing.* J. Am. Chem. Soc., 125(11):3322–3329, 2003.

[111] O. D. Velev and E. W. Kaler, *In Situ Assembly of Colloidal Particles into Miniaturized Biosensors.* Langmuir, 15(11):3693–3698, 1999.

[112] X. Hu, G. Li, J. Huang, D. Zhang, and Y. Qiu, *Construction of Self-Reporting Specific Chemical Sensors with High Sensitivity.* Adv. Mater., 19(24):4327–4332, 2007.

[113] W.-L. Min, P. Jiang, and B. Jiang, *Large-scale assembly of colloidal nanoparticles and fabrication of periodic subwavelength structures.* Nanotechnology, 19(47):475604, 2008.

[114] J. Zhu, Z. Yu, G. F. Burkhard, C.-M. Hsu, S. T. Connor, Y. Xu, Q. Wang, M. McGehee, S. Fan, and Y. Cui, *Optical Absorption Enhancement in Amorphous Silicon Nanowire and Nanocone Arrays.* Nano Lett., 9(1):279–282, 2009.

[115] S. Ji, J. Park, and H. Lim, *Improved antireflection properties of moth eye mimicking nanopillars on transparent glass: flat antireflection and color tuning.* Nanoscale, 4(15):4603, 2012.

[116] H. Fudouzi and Y. Xia, *Colloidal Crystals with Tunable Colors and Their Use as Photonic Papers.* Langmuir, 19(23):9653–9660, 2003.

[117] H. Pham, I. Gourevich, J. Oh, J. Jonkman, and E. Kumacheva, *A Multidye Nanostructured Material for Optical Data Storage and Security Data Encryption.* Adv. Mater., 16(6):516–520, 2004.

[118] G. S. Chai, I. S. Shin, and J.-S. Yu, *Synthesis of Ordered, Uniform, Macroporous Carbons with Mesoporous Walls Templated by Aggregates of Polystyrene Spheres and Silica Particles for Use as Catalyst Supports in Direct Methanol Fuel Cells.* Adv. Mater., 16(22):2057–2061, 2004.

[119] J. P. Bosco, K. Sasaki, M. Sadakane, W. Ueda, and J. G. Chen, *Synthesis and Characterization of Three-Dimensionally Ordered Macroporous (3DOM) Tungsten Carbide: Application to Direct Methanol Fuel Cells.* Chem. Mater., 22(3):966–973, 2010.

[120] W. L. Vos, M. Megens, C. M. van Kats, and P. Bösecke, *X-ray Diffraction of Photonic Colloidal Single Crystals.* Langmuir, 13(23):6004–6008, 1997.

[121] A. van Blaaderen, R. Ruel, and P. Wiltzius, *Template-directed colloidal crystallization.* Nature, 385(6614):321–324, 1997.

[122] A. S. Dimitrov and K. Nagayama, *Continuous Convective Assembling of Fine Particles into Two-Dimensional Arrays on Solid Surfaces.* Langmuir, 12(5):1303–1311, 1996.

[123] L. Malaquin, T. Kraus, H. Schmid, E. Delamarche, and H. Wolf, *Controlled Particle Placement through Convective and Capillary Assembly.* Langmuir, 23(23):11513–11521, 2007.

[124] P. Jiang, J. F. Bertone, , K. S. Hwang, and V. L. Colvin, *Single-Crystal Colloidal Multilayers of Controlled Thickness.* Chem. Mater., 11(8):2132–2140, 1999.

[125] C. Deleuze, B. Sarrat, F. Ehrenfeld, S. Perquis, C. Derail, and L. Billon, *Photonic properties of hybrid colloidal crystals fabricated by a rapid dip-coating process.* Phys. Chem. Chem. Phys., 13(22):10681, 2011.

[126] M. Bardosova, M. E. Pemble, I. M. Povey, and R. H. Tredgold, *The Langmuir-Blodgett approach to making colloidal photonic crystals from silica spheres.* Adv. Mater., 22(45):5081, 2010.

[127] R. C. Hayward, D. A. Saville, and I. A. Aksay, *Electrophoretic assembly of colloidal crystals with optically tunablemicropatterns.* Nature, 404(6773):56–59, 2000.

[128] M. Trau, D. A. Saville, and I. A. Aksay, *Field-Induced Layering of Colloidal Crystals.* Science, 272(5262):706–9, 1996.

[129] B. G. Prevo and O. D. Velev, *Controlled, Rapid Deposition of Structured Coatings from Micro- and Nanoparticle Suspensions.* Langmuir, 20(6):2099–2107, 2004.

[130] C. J. Barbe, F. Arendse, P. Comte, M. Jirousek, F. Lenzmann, V. Shklover, and M. Gra, *Nanocrystalline Titanium Oxide Electrodes for Photovoltaic Applications.* J. Am. Ceram. Soc., 71(12):3157–3171, 1997.

[131] M. M. Byranvand, A. N. Kharat, N. Taghavinia, and A. Dabirian, *Broadband and Low-Loss Plasmonic Light Trapping in Dye-Sensitized Solar Cells Using Micrometer-Scale Rodlike and Spherical Core-Shell Plasmonic Particles.* ACS Appl. Mater. Interfaces, 8(25):16359–16367, 2016.

[132] A. Dabirian, M. Malekshahi, N. Taghavinia, and A. Nemati, *Micron-scale rodlike scattering particles for light trapping in nanostructured thin film solar cells.* RSC Adv., 5:86050–86055, 2015.

[133] K. B. Singh and M. S. Tirumkudulu, *Cracking in Drying Colloidal Films.* Phys. Rev. Lett., 98(21):218302, 2007.

[134] P. Jiang. *Large-scale colloidal crystals and macroporous polymers and method for producing*, 2010. US Patent 7.767.720 (filed 13 Oct 2003).

[135] M. G. Bawendi, M. L. Steigerwald, and L. E. Brus, *The Quantum Mechanics of Larger Semiconductor Clusters ("Quantum Dots").* Annu. Rev. Phys. Chem., 41(1):477–496, 1990.

[136] A. I. Ekimov and A. A. Onushchenko, *Quantum size effect in three-dimensional microscopic semiconductor crystals.* ZhETF Pisma Redaktsiiu, 34:363, 1981.

[137] K.-S. Cho, E. K. Lee, W.-J. Joo, E. Jang, T.-H. Kim, S. J. Lee, S.-J. Kwon, J. Y. Han, B.-K. Kim, B. L. Choi, and J. M. Kim, *High-performance crosslinked colloidal quantum-dot light-emitting diodes.* Nat. Photon., 3(6):341–345, 2009.

[138] T.-H. Kim, K.-S. Cho, E. K. Lee, S. J. Lee, J. Chae, J. W. Kim, D. H. Kim, J.-Y. Kwon, G. Amaratunga, S. Y. Lee, B. L. Choi, Y. Kuk, J. M. Kim, and K. Kim, *Full-colour quantum dot displays fabricated by transfer printing.* Nat. Photon., 5(3):176–182, 2011.

[139] A. Rogach, N. Gaponik, J. Lupton, C. Bertoni, D. Gallardo, S. Dunn, N. Li Pira, M. Paderi, P. Repetto, S. Romanov, C. O'Dwyer, C. Sotomayor Torres, and A. Eychmüller, *Light-emitting diodes with semiconductor nanocrystals.* Angew. Chem. Int. Ed. (English), 47(35):6538–6549, 2008.

[140] Q. Dai, C. E. Duty, and M. Z. Hu, *Semiconductor-nanocrystals-based white light-emitting diodes.* Small, 6(15):1577–1588, 2010.

[141] X. Michalet, F. F. Pinaud, L. A. Bentolila, J. M. Tsay, S. Doose, J. J. Li, G. Sundaresan, A. M. Wu, S. S. Gambhir, and S. Weiss, *Quantum dots for live cells, in vivo imaging, and diagnostics.* Science, 307(5709):538–44, 2005.

[142] R. Gill, M. Zayats, and I. Willner, *Semiconductor quantum dots for bioanalysis.* Angew. Chem. Int. Ed. (English), 47(40):7602–7625, 2008.

[143] A. Nozik, *Quantum dot solar cells.* Physica E, 14(1-2):115–120, 2002.

[144] W. G. J. H. M. van Sark, K. W. J. Barnham, L. H. Slooff, A. J. Chatten, A. Büchtemann, A. Meyer, S. J. McCormack, R. Koole, D. J. Farrell, R. Bose, E. E. Bende, A. R. Burgers, T. Budel, J. Quilitz, M. Kennedy, T. Meyer, C. D. M. Donegá, A. Meijerink, and D. Vanmaekelbergh, *Luminescent Solar Concentrators–a review of recent results.* Opt. Express, 16(26):21773–21792, 2008.

[145] H. Giesche, *Synthesis of monodispersed silica powders II. Controlled growth reaction and continuous production process.* J. Eur. Ceram. Soc., 14(3):205–214, 1994.

[146] G. H. Bogush and C. F. Zukoski IV, *Studies of the kinetics of the precipitation of uniform silica particles through the hydrolysis and condensation of silicon alkoxides.* J. Colloid Interface Sci., 142(1):1–18, 1991.

[147] S. Dussi. *When shape is enough: from colloidal spheres to twisted polyhedras from icosahedral to chiral order.* Phd-thesis, Utrecht University, The Netherlands, 2016. A digital version of this thesis is available at http://www.colloid.nl.

[148] B. Liu, T. H. Besseling, M. Hermes, A. F. Demirörs, A. Imhof, and A. van Blaaderen, *Switching plastic crystals of colloidal rods with electric fields.* Nat. Commun., 5:3092, 2014.

[149] S. Rodríguez, C. Lafuente, P. Cea, F. M. Royo, and J. S. Urieta, *Densities and viscosities of binary mixtures of some cyclic ethers + chlorocyclohexane at 298.15 and 313.15 K.* J. Chem. Eng. Data, 42(6):1285–1289, 1997.

[150] C. P. Crowe, Robert W. and Smyth, *The Dielectric and Polymorphic Behavior of Cyclohexanol, Cyclohexanone, Chlorocyclohexane and Cyclohexane1,2.* J. Am. Chem. Soc., 73(11):5406–5411, 1951.

[151] J. W. Williams, *The dielectric constants of binary mixtures. X. The electric moments of simple derivatives of cyclohexane and of dioxan.* J. Am. Chem. Soc., 52(5):1831–1837, 1930.

[152] D. A. I. LeBel, R. G. and Goring, *Density, Viscosity, Refractive Index, and Hygroscopicity of Mixtures of Water and Dimethyl Sulfoxide.* J. Chem. Eng. Data, 7(1):100–101, 1962.

[153] S. M. Puranik, A. C. Kumbharkhane, and S. C. Mehrotra, *Dielectric study of dimethyl sulfoxide-water mixtures using the time-domain technique.* J. Chem. Soc. Faraday Trans., 88(3):433–435, 1992.

[154] Glycerine Producers' Association. *Physical properties of glycerine and its solutions.*, 1967.

[155] G. Akerlof, *Dielectric constants of some organic solvent-water mixtures at various temperatures.* J. Am. Chem. Soc., 54(11):4125–4139, 1932.

[156] N.-S. Cheng, *Formula for the Viscosity of a Glycerol-Water Mixture.* Ind. Eng. Chem. Res., 47(9):3285–3288, 2008.

[157] P. Jiang, T. Prasad, M. J. McFarland, and V. L. Colvin, *Two-dimensional nonclose-packed colloidal crystals formed by spincoating.* Appl. Phys. Lett., 89:011908, 2006.

[158] V. Prasad, D. Semwogerere, and E. R. Weeks, *Confocal microscopy of colloids.* J. Phys.: Condens. Matter, 19(11):113102, 2007.

[159] V. W. A. de Villeneuve, R. P. A. Dullens, D. G. A. L. Aarts, E. Groeneveld, J. H. Scherff, and W. K. Kegel, *Colloidal Hard-Sphere Crystal Growth Frustrated by Large Spherical Impurities.* Science, 309(5738):1231–1233, 2005.

[160] M. Minsky. *Microscopy Apparatus*, 1961. U.S. Patent 3.013.467 (filed 7 Nov 1957).

[161] M. Minsky, *Memoir on inventing the confocal scanning microscope.* Scanning, 10(4):128–138, 1988.

[162] P. Davidovits and M. D. Egger, *Scanning Laser Microscope.* Nature, 223(5208):831–831, 1969.

[163] W. B. Amos and J. G. White, *How the confocal laser scanning microscope entered biological research.* Biol. Cell, 95(6):335–342, 2003.

[164] K. Carlsson and N. Aslund, *Confocal imaging for 3-D digital microscopy.* Appl. Opt., 26(16):3232–3238, 1987.

[165] J. G. White. *Confocal Scanning Microscope*, 1988. GB Patent 2.184.321.A (filed 15 Dec 1986).

[166] A. Draaijer and P. M. Houpt, *A standard video-rate confocal laser-scanning reflection and fluorescence microscope.* Scanning, 10(4):139–145, 1988.

[167] G. J. Brakenhoff, P. Blom, and P. Barends, *Confocal scanning light microscopy with high aperture immersion lenses.* J. Microsc., 117(2):219–232, 1979.

[168] T. H. Besseling, M. Hermes, A. Kuijk, B. de Nijs, T. S. Deng, M. Dijkstra, A. Imhof, and A. van Blaaderen, *Determination of the positions and orientations of concentrated rod-like colloids from 3D microscopy data.* J. Phys.: Condens. Matter, 194109:1–12, 2014.

[169] J. Crocker and D. Grier, *Methods of Digital Video Microscopy for Colloidal Studies.* J. Colloid Interface Sci., 179:298–310, 1996.

[170] T. Wilson and C. Sheppard. *Theory and Practice of Scanning Optical Microscopy.* Academic Press, London, 1984.

[171] R. H. Webb, *Confocal optical microscopy.* Rep. Prog. Phys., 59(3):427, 1996.

[172] C. E. Shannon, *Communication in the Presence of Noise.* Proc. IRE, 37(1):10–21, 1949.

[173] J. B. Pawley. *Handbook of Biological Confocal Microscopy, Second Edition.* Springer Science & Business Media, 1996.

[174] H. T. M. van der Voort and K. C. Strasters, *Restoration of confocal images for quantitative image-analysis.* J. Microsc., 178(December 1994):165–181, 1995.

[175] E. Betzig, G. H. Patterson, R. Sougrat, O. W. Lindwasser, S. Olenych, J. S. Bonifacino, M. W. Davidson, J. Lippincott-Schwartz, and H. F. Hess, *Imaging intracellular fluorescent proteins at nanometer resolution.* Science, 313(5793):1642–5, 2006.

[176] M. J. Rust, M. Bates, and X. Zhuang, *Sub-diffraction-limit imaging by stochastic optical reconstruction microscopy (STORM).* Nat. Methods, 3(10):793–796, 2006.

[177] K. I. Willig, J. Keller, M. Bossi, and S. W. Hell, *STED microscopy resolves nanoparticle assemblies.* New J. Phys., 8(6):106–106, 2006.

[178] S. W. Hell, *Far-field optical nanoscopy.* Science, 316(5828):1153–8, 2007.

[179] S. W. Hell, *Microscopy and its focal switch.* Nat. Methods, 6(1):24–32, 2009.

[180] D. Wildanger, R. Medda, L. Kastrup, and S. Hell, *A compact STED microscope providing 3D nanoscale resolution.* J. Microsc., 236(1):35–43, 2009.

[181] W. Denk, J. H. Strickler, and W. W. Webb, *Two-photon laser scanning fluorescence microscopy.* Science, 248(4951):73–6, 1990.

[182] M. Göppert-Mayer, *Ueber Elementarakte mit Zwei Quantensprüngen.* Ann. Phys. (Berlin), 114:273–294, 1931.

[183] W. Kaiser and C. Garrett, *Two-Photon Excitation in* CaF_2*:*Eu^{2+}. Phys. Rev. Lett., 7(6):229–231, 1961.

[184] C. J. R. Sheppard and M. Gu, *Image formation in two-photon fluorescence microscopy.* Optik, 86(3):104–106, 1990.

[185] G. Moneron and S. W. Hell, *Two-photon excitation STED microscopy.* Opt. Express, 17(17):14567, 2009.

[186] J. H. Strickler and W. W. Webb, *Three-dimensional optical data storage in refractive media by two-photon point excitation.* Opt. Lett., 16(22):1780–1782, 1991.

[187] S. Maruo, O. Nakamura, and S. Kawata, *Three-dimensional microfabrication with two-photon-absorbed photopolymerization.* Opt. Lett., 22(2):132–134, 1997.

[188] B. H. Cumpston, S. P. Ananthavel, S. Barlow, D. L. Dyer, J. E. Ehrlich, L. L. Erskine, A. A. Heikal, S. M. Kuebler, I.-Y. S. Lee, D. McCord-Maughon, J. Qin, H. Röckel, M. Rumi, X.-L. Wu, S. R. Marder, and J. W. Perry, *Two-photon polymerization initiators for three-dimensional optical data storage and microfabrication.* Nature, 398(6722):51–54, 1999.

[189] W. Albrecht, T.-S. Deng, B. Goris, M. A. van Huis, S. Bals, and A. van Blaaderen, *Single Particle Deformation and Analysis of Silica-Coated Gold Nanorods before and after Femtosecond Laser Pulse Excitation.* Nano Lett., 16(3):1818–1825, 2016.

[190] P. Podsiadlo, G. V. Krylova, A. Demortière, and E. V. Shevchenko, *Multicomponent periodic nanoparticle superlattices.* J. Nanopart. Res., 13(1):15–32, 2010.

[191] A.-P. Hynninen, J. H. J. Thijssen, E. C. M. Vermolen, M. Dijkstra, and A. van Blaaderen, *Self-assembly route for photonic crystals with a bandgap in the visible region.* Nat. Mater., 6(3):202–205, 2007.

[192] F. X. Redl, K.-S. Cho, C. B. Murray, and S. O'Brien, *Three-dimensional binary superlattices of magnetic nanocrystals and semiconductor quantum dots.* Nature, 423(6943):968–71, 2003.

[193] Y. Kang, X. Ye, J. Chen, Y. Cai, R. E. Diaz, R. R. Adzic, E. A. Stach, and C. B. Murray, *Design of Pt-Pd binary superlattices exploiting shape effects and synergistic effects for oxygen reduction reactions.* J. Am. Chem. Soc., 135(1):42–5, 2013.

[194] H. N. W. Lekkerkerker and G. J. Vroege, *Liquid crystal phase transitions in suspensions of mineral colloids: new life from old roots.* Phil. Trans. R. Soc. A, 371(1988):20120263, 2013.

[195] X. Ye, J. a. Millan, M. Engel, J. Chen, B. T. Diroll, S. C. Glotzer, and C. B. Murray, *Shape Alloys of Nanorods and Nanospheres from Self-Assembly.* Nano Lett., 13:4980–4988, 2013.

[196] J. F. Galisteo-López, M. Ibisate, R. Sapienza, L. S. Froufe-Pérez, A. Blanco, and C. López, *Self-assembled photonic structures.* Adv. Mater., 23(1):30–69, 2011.

[197] S. Mühlig, A. Cunningham, J. Dintinger, T. Scharf, T. Bürgi, F. Lederer, and C. Rockstuhl, *Self-assembled plasmonic metamaterials.* Nanophotonics, 2(3):211–240, 2013.

[198] M. Adams and S. Fraden, *Phase behavior of mixtures of rods (tobacco mosaic virus) and spheres (polyethylene oxide, bovine serum albumin).* Biophys. J., 74(January):669–677, 1998.

[199] G. Cinacchi, E. Velasco, and L. Mederos, *Entropic segregation in smectic phases of hard-body mixtures.* J. Phys.: Condens. Matter, 16(19):S2003–S2014, 2004.

[200] A. Cuetos, B. Martínez-Haya, S. Lago, and L. F. Rull, *Use of Parsons-Lee and Onsager theories to predict nematic and demixing behavior in binary mixtures of hard rods and hard spheres.* Phys. Rev. E, 75(6 Pt 1):1–12, 2007.

[201] Z. Dogic, D. Frenkel, and S. Fraden, *Enhanced stability of layered phases in parallel hard spherocylinders due to addition of hard spheres.* Phys. Rev. E, 62(3 Pt B):3925–3933, 2000.

[202] R. van Roij, B. Mulder, and M. Dijkstra, *Phase behavior of binary mixtures of thick and thin hard rods.* Physica A, 261(3-4):374–390, 1998.

[203] S. K. Lai and X. Xiao, *Phase diagram of colloid-rod system.* J. Chem. Phys, 132(4):044905, 2010.

[204] S. Varga, K. Purdy, A. Galindo, S. Fraden, and G. Jackson, *Nematic-nematic phase separation in binary mixtures of thick and thin hard rods: Results from Onsager-like theories.* Phys. Rev. E, 72(5):1–19, 2005.

[205] S. Varga, E. Velasco, L. Mederos, and F. J. Vesely, *Stability of the columnar and smectic phases of length-bidisperse parallel hard cylinders.* Mol. Phys., 107(23-24):2481–2492, 2009.

[206] T. Koda, M. Numajiri, and S. Ikeda, *Smectic-A Phase of a Bidisperse System of Parallel Hard Rods and Hard Spheres.* J. Phys. Soc. Jpn., 65(11):3551–3556, 1996.

[207] Y. Martinez-Raton, G. Cinacchi, E. Velasco, and L. Mederos, *Depletion effects in smectic phases of hard-rod-hard-sphere mixtures.* Eur. Phys. J. E Soft Matter, 21(2):175–88, 2006.

[208] S. D. Peroukidis, A. G. Vanakaras, and D. J. Photinos, *Liquid crystalline phases and demixing in binary mixtures of shape-anisometric colloids.* J. Mater. Chem., 20(46):10495, 2010.

[209] D. Antypov and D. J. Cleaver, *Orientational and phase-coexistence behaviour of hard rod-sphere mixtures.* Chem. Phys. Lett., 377:311–316, 2003.

[210] S. Lago, A. Cuetos, B. Martínez-Haya, and L. F. Rull, *Crowding effects in binary mixtures of rod-like and spherical particles.* J. Mol. Recognit., 17(5):417–25, 2004.

[211] D. Antypov and D. J. Cleaver, *The role of attractive interactions in rod-sphere mixtures.* J. Chem. Phys, 120(21):10307–16, 2004.

[212] N. Urakami and M. Imai, *Dependence on sphere size of the phase behavior of mixtures of rods and spheres.* J. Chem. Phys, 119:2463, 2003.

[213] E. Grelet, *Hard-Rod Behavior in Dense Mesophases of Semiflexible and Rigid Charged Viruses.* Phys. Rev. X, 4(2):021053, 2014.

[214] T. Savin and P. S. Doyle, *Static and dynamic errors in particle tracking microrheology.* Biophys. J., 88(1):623–38, 2005.

[215] T. H. Besseling, J. Jose, and A. van Blaaderen, *Methods to calibrate and scale axial distances in confocal microscopy as a function of refractive index.* J. Microsc., 257(2):142–50, 2015.

[216] J. K. G. Dhont. *An Introduction to Dynamics of Colloids.* Elsevier, 1996.

[217] G. Cinacchi and L. De Gaetani, *Diffusion in the lamellar phase of a rod-sphere mixture.* J. Chem. Phys, 131(10):104908, 2009.

[218] H. E. Bakker, S. Dussi, B. L. Droste, T. H. Besseling, C. L. Kennedy, E. I. Wiegant, B. Liu, A. Imhof, M. Dijkstra, and A. van Blaaderen, *Phase diagram of binary colloidal rod-sphere mixtures from a 3D real-space analysis of sedimentation-diffusion equilibria.* Soft Matter, 12:9238–9245, 2016.

[219] M. Cifelli, G. Cinacchi, and L. De Gaetani, *Smectic order parameters from diffusion data.* J. Chem. Phys, 125(16):164912, 2006.

[220] W. L. McMillan, *Simple Molecular Model for the Smectic A Phase of Liquid Crystals.* Phys. Rev. A, 4(3):1238–1246, 1971.

[221] K. Kobayashi, *On the theory of translational and orientational melting with application to liquid crystals.* Phys. Lett. A, 31(3):125–126, 1970.

[222] P. Steinhardt, D. Nelson, and M. Ronchetti, *Bond-orientational order in liquids and glasses.* Phys. Rev. B, 28(2):784–805, 1983.

[223] W. Lechner and C. Dellago, *Accurate determination of crystal structures based on averaged local bond order parameters.* J. Chem. Phys, 129(11):114707, 2008.

[224] L. Wu, A. Malijevský, G. Jackson, E. A. Müller, and C. Avendaño, *Orientational ordering and phase behaviour of binary mixtures of hard spheres and hard spherocylinders.* J. Chem. Phys, 143(4):044906, 2015.

[225] A. Patti, D. El Masri, R. van Roij, and M. Dijkstra, *Collective diffusion of colloidal hard rods in smectic liquid crystals: Effect of particle anisotropy.* J. Chem. Phys, 132(22):224907, 2010.

[226] A. Kuijk, D. V. Byelov, A. V. Petukhov, A. van Blaaderen, and A. Imhof, *Phase behavior of colloidal silica rods.* Farad. Discuss., 159:181–199, 2012.

[227] W. B. Russel, D. A. Saville, and W. R. Schowalter. *Colloidal Dispersions*, volume 1st Edn. Cambridge University Press, 1995.

[228] K. Davis and W. Russel, *An asymptotic description of transient settling and ultrafiltration of colloidal dispersions.* Phys. Fluids A, 82:82–100, 1989.

[229] A. Cacciuto, S. Auer, and D. Frenkel, *Onset of heterogeneous crystal nucleation in colloidal suspensions.* Nature, 428(6981):404–6, 2004.

[230] D. Winter, P. Virnau, and K. Binder, *Monte Carlo test of the classical theory for heterogeneous nucleation barriers.* Phys. Rev. Lett., 103(22):225703, 2009.

[231] J. Russo, A. C. Maggs, D. Bonn, and H. Tanaka, *The interplay of sedimentation and crystallization in hard-sphere suspensions.* Soft Matter, 9(30):7369, 2013.

[232] B. J. Ackerson, S. E. Paulin, B. Johnson, W. van Megen, and S. Underwood, *Crystallization by settling in suspensions of hard spheres.* Phys. Rev. E, 59(6):6903–6913, 1999.

[233] J. S. van Duijneveldt, J. K. G. Dhont, and H. N. W. Lekkerkerker, *Expansion and crystallization of a sediment of charged colloidal spheres.* J. Chem. Phys, 99(9):6941, 1993.

[234] J. P. Hoogenboom, a. K. van Langen-Suurling, J. Romijn, and a. van Blaaderen, *Epitaxial growth of a colloidal hard-sphere hcp crystal and the effects of epitaxial mismatch on crystal structure.* Phys. Rev. E, 69(5 Pt 1):051602, 2004.

[235] R. Ni, S. Belli, R. van Roij, and M. Dijkstra, *Glassy dynamics, spinodal fluctuations, and the kinetic limit of nucleation in suspensions of colloidal hard rods.* Phys. Rev. Lett., 105(8):088302, 2010.

[236] T. Schilling and D. Frenkel, *Self-poisoning of crystal nuclei in hard-rod liquids.* Phys. Rev. Lett., 92(8):085505, 2004.

[237] A. Patti and M. Dijkstra, *Do multilayer crystals nucleate in suspensions of colloidal rods?* Phys. Rev. Lett., 102(12):128301, 2009.

[238] E. Spruijt and P. M. Biesheuvel, *Sedimentation dynamics and equilibrium profiles in multicomponent mixtures of colloidal particles.* J. Phys. Condens. Matter, 26:075101, 2014.

[239] D. de las Heras and M. Schmidt, *The phase stacking diagram of colloidal mixtures under gravity.* Soft Matter, 9(36):8636, 2013.

[240] H. Löwen and E. Allahyarov, *Doubled heterogeneous crystal nucleation in sediments of hard sphere binary-mass mixtures.* J. Chem. Phys, 135(13):134115, 2011.

[241] M. Kohl and M. Schmiedeberg, *Particle segregation in a sedimenting bidisperse soft sphere system.* Soft Matter, 10(24):4340, 2014.

[242] K. Milinković, J. T. Padding, and M. Dijkstra, *Hydrodynamic Rayleigh-Taylor-like instabilities in sedimenting colloidal mixtures.* Soft Matter, 7(23):11177, 2011.

[243] M. Leocmach, C. P. Royall, and H. Tanaka, *Novel zone formation due to interplay between sedimentation and phase ordering.* EPL, 89(3):38006, 2010.

[244] D. de las Heras, N. Doshi, T. Cosgrove, J. Phipps, D. I. Gittins, J. S. van Duijneveldt, and M. Schmidt, *Floating nematic phase in colloidal platelet-sphere mixtures.* Sci. Rep., 2:789, 2012.

[245] P. Woolston and J. S. van Duijneveldt, *Three-Phase Coexistence in Colloidal Rod-Plate Mixtures.* Langmuir, 31(34):9290–5, 2015.

[246] D. Kleshchanok, A. V. Petukhov, P. Holmqvist, D. V. Byelov, and H. N. W. Lekkerkerker, *Structures and phase behavior in mixtures of charged colloidal spheres and platelets.* Langmuir, 26(16):13614–21, 2010.

[247] C. Royall, E. Vermolen, A. van Blaaderen, and H. Tanaka, *Controlling competition between crystallization and glass formation in binary colloids with an external field.* J. Phys.: Condens. Matter, 20:404225, 2008.

[248] M. Chen, H. Cölfen, and S. Polarz, *Centrifugal Field-Induced Colloidal Assembly: From Chaos to Order.* ACS Nano, 9:6944–6950, 2015.

[249] C. G. Serrano, J. J. McDermott, and D. Velegol, *Sediments of soft spheres arranged by effective density.* Nat. Mater., 10(9):716–721, 2011.

[250] M. M. Tirado, C. L. Martínez, and J. G. de la Torre, *Comparison of theories for the translational and rotational diffusion coefficients of rod-like macromolecules. Application to short DNA fragments.* J. Chem. Phys, 81(4):2047, 1984.

[251] T. Svedberg and K. Predersen. *The Ultracentrifuge.* Oxford University Press, London, 1940.

[252] H. Brenner, *Taylor dispersion in systems of sedimenting nonspherical brownian particles. I. Homogeneous, centrosymmetric, axisymmetric particles.* J. Colloid Interface Sci., 71(2):189–208, 1979.

[253] G. K. Batchelor, *Sedimentation in a dilute dispersion of spheres.* J. Fluid Mech., 52(02):245, 1972.

[254] S. A. Allison and S. Mazur, *Modeling the free solution electrophoretic mobility of short DNA fragments.* Biopolymers, 46(6):359–373, 1998.

[255] D. H. Napper, *Steric stabilization.* J. Colloid Interface Sci., 58(2):390 – 407, 1977.

[256] M. N. van der Linden, K. M. Helfferich, P. H., J. E. G. J. Wijnhoven, H. E. Bakker, and A. van Blaaderen. *Reducing the effects of particle sedimentation in microelectrophoresis.* in preparation, 2016.

[257] M. N. van der Linden, J. C. P. Stiefelhagen, G. Heessels-Gürboğa, J. E. S. van der Hoeven, N. A. Elbers, M. Dijkstra, and A. van Blaaderen, *Charging of poly(methyl methacrylate) (PMMA) colloids in cyclohexyl bromide: Locking, size dependence, and particle mixtures.* Langmuir, 31(1):65–75, 2015.

[258] T. Vissers, A. Imhof, F. Carrique, Á. V. Delgado, and A. van Blaaderen, *Electrophoresis of concentrated colloidal dispersions in low-polar solvents.* J. Colloid Interface Sci., 361(2):443–455, 2011.

[259] A. Delgado, F. González-Caballero, R. Hunter, L. Koopal, and J. Lyklema, *Measurement and interpretation of electrokinetic phenomena.* J. Colloid Interface Sci., 309(2):194 – 224, 2007. Elkin 06, International Electrokinetics Conference, June 25-29, Nancy, France.

[260] R. Pelton, P. Miller, W. McPhee, and S. Rajaram, *Strategies for improving electrophoresis data from the Coulter DELSA.* Colloids Surf., A, 80(2-3):181–189, 1993.

[261] D. Yan, C. Yang, N.-T. Nguyen, and X. Huang, *A method for simultaneously determining the zeta potentials of the channel surface and the tracer particles using microparticle image velocimetry technique.* Electrophoresis, 27(3):620–7, 2006.

[262] C. Yang, T. Dabros, D. Li, J. Czarnecki, and J. H. Masliyah, *Measurement of the Zeta Potential of Gas Bubbles in Aqueous Solutions by Microelectrophoresis Method.* J. Colloid Interface Sci., 243(1):128–135, 2001.

[263] T. L. Doane, C.-H. Chuang, R. J. Hill, and C. Burda, *Nanoparticle* ζ *-potentials.* Acc. Chem. Res., 45(3):317–26, 2012.

[264] M. G. L. van den Heuvel, M. P. de Graaff, S. G. Lemay, and C. Dekker, *Electrophoresis of individual microtubules in microchannels.* Proc. Natl. Acad. Sci. U. S. A., 104(19):7770–5, 2007.

[265] G. Li, Q. Wen, and J. X. Tang, *Single filament electrophoresis of F-actin and filamentous virus fd.* J. Chem. Phys, 122(10):104708, 2005.

[266] N. C. Stellwagen, C. Gelfi, and P. G. Righetti, *The free solution mobility of DNA.* Biopolymers, 42(6):687–703, 1997.

[267] K. Strutz and N. C. Stellwagen, *Do DNA gel electrophoretic mobilities extrapolate to the free-solution mobility of DNA at zero gel concentration?* Electrophoresis, 19(5):635–42, 1998.

[268] P. van der Hoeven and J. Lyklema, *Electrostatic stabilization in non-aqueous media.* Adv. Colloid Interface Sci., 42:205–277, 1992.

[269] I. D. Morrison, *Electrical charges in nonaqueous media.* Colloids Surf., A, 71(1):1–37, 1993.

[270] G. H. Gelinck, H. E. A. Huitema, E. van Veenendaal, E. Cantatore, L. Schrijnemakers, J. B. P. H. van der Putten, T. C. T. Geuns, M. Beenhakkers, J. B. Giesbers, B.-H. Huisman, E. J. Meijer, E. M. Benito, F. J. Touwslager, A. W. Marsman, B. J. E. van Rens, and D. M. de Leeuw, *Flexible active-matrix displays and shift registers based on solution-processed organic transistors.* Nat. Mater., 3(2):106–10, 2004.

[271] P. Jenkins, S. Basu, R. Keir, J. Ralston, J. Thomas, and B. Wolffenbuttel, *The Electrochemistry of Nonaqueous Copper Phthalocyanine Dispersions in the Presence of a Metal Soap Surfactant: A Simple Equilibrium Site Binding Model.* J. Colloid Interface Sci., 211(2):252–263, 1999.

[272] F. Morrison, *Electrophoresis of a particle of arbitrary shape.* J. Colloid Interface Sci., 34(2):210–214, 1970.

[273] D. C. Henry, *The Cataphoresis of Suspended Particles. Part I. The Equation of Cataphoresis.* Proc. R. Soc. A, 133(821):106–129, 1931.

[274] D. Stigter, *Electrophoresis of highly charged colloidal cylinders in univalent salt solutions. 1. Mobility in transverse field.* J. Phys. Chem., 82(12):1417–1423, 1978.

[275] D. Stigter, *Electrophoresis of highly charged colloidal cylinders in univalent salt solutions. 2. Random orientation in external field and application to polyelectrolytes.* J. Phys. Chem., 82(12):1424–1429, 1978.

[276] S. Allison, C. Chen, and D. Stigter, *The length dependence of translational diffusion, free solution electrophoretic mobility, and electrophoretic tether force of rigid rod-like model duplex DNA.* Biophys. J., 81(5):2558–2568, 2001.

[277] J. Buitenhuis, *Electrophoresis of fd-virus particles: Experiments and an analysis of the effect of finite rod lengths.* Langmuir, 28:13354–13363, 2012.

[278] U. Hoss, S. Batzill, M. Deggelmann, C. Graf, M. Hagenbuechle, C. Johner, H. Kramer, C. Martin, E. Overbeck, and R. Weber, *Electrokinetic Properties of Aqueous Suspensions of Rodlike fd Virus Particles in the Gas- and Liquidlike Phase.* Macromolecules, 27(12):3429–3431, 1994.

[279] R. J. Hunter. *Zeta Potential in Colloid Science.* Elsevier, 1981.

[280] H. Ohshima, *Henry's Function for Electrophoresis of a Cylindrical Colloidal Particle.* J. Colloid Interface Sci., 180(1):299–301, 1996.

[281] A. de Keizer, W. van der Drift, and J. Overbeek, *Electrophoresis of randomly oriented cylindrical particles.* Biophys. Chem., 3(1):107–108, 1975.

[282] R. Besseling, L. Isa, E. R. Weeks, and W. C. K. Poon, *Quantitative imaging of colloidal flows.* Adv. Colloid Interface Sci., 146(1-2):1–17, 2009.

[283] M. Guizar-Sicairos, S. T. Thurman, and J. R. Fienup, *Efficient subpixel image registration algorithms.* Opt. Lett., 33(2):156–158, 2008.

[284] G. J. Janz and S. S. Danyluk, *Conductances of Hydrogen Halides in Anhydrous Polar Organic Solvents.* Chem. Rev., 60(2):209–234, 1960.

[285] A. Benouar, M. Kameche, and M. A. Bouhlala, *Molar conductivities of concentrated lithium chloride-glycerol solutions at low and high temperatures: application of a quasi-lattice model.* Phys. Chem. Liq., 54(1):62–73, 2015.

[286] T. Vissers. *Oppositely charged colloids out of equilibrium.* Phd-thesis, Utrecht University, The Netherlands, 2010. A digital version of this thesis is available at http://www.colloid.nl.

[287] D. El Masri, P. van Oostrum, F. Smallenburg, T. Vissers, A. Imhof, M. Dijkstra, and A. van Blaaderen, *Measuring colloidal forces from particle position deviations inside an optical trap.* Soft Matter, 7(7):3462–3466, 2011.

[288] G. Segré and a. Silberberg, *Behaviour of macroscopic rigid spheres in Poiseuille flow Part 2. Experimental results and interpretation.* J. Fluid Mech., 14(01):136, 1962.

[289] H. Ohshima, *Approximate Analytic Expression for the Electrophoretic Mobility of Moderately Charged Cylindrical Colloidal Particles.* Langmuir, 31(51):13633–8, 2015.

[290] A. Wysocki, C. P. Royall, R. G. Winkler, G. Gompper, H. Tanaka, A. van Blaaderen, and H. Löwen, *Direct observation of hydrodynamic instabilities in a driven non-uniform colloidal dispersion.* Soft Matter, 5(7):1340, 2009.

[291] J. M. Weissman, H. B. Sunkara, A. S. Tse, and S. A. Asher, *Thermally Switchable Periodicities and Diffraction from Mesoscopically Ordered Materials.* Science, 274(5289):959–60, 1996.

[292] S.-H. Kim, S.-H. Kim, W. C. Jeong, and S.-M. Yang, *Low-Threshold Lasing in 3D Dye-Doped Photonic Crystals Derived from Colloidal Self-Assemblies.* Chem. Mater., 21(20):4993–4999, 2009.

[293] E. A. Kamenetzky, L. G. Magliocco, and H. P. Panzer, *Structure of solidified colloidal array laser filters studied by cryogenic transmission electron microscopy.* Science, 263(5144):207–10, 1994.

[294] S.-H. Kim, H. S. Park, J. H. Choi, J. W. Shim, and S.-M. Yang, *Integration of colloidal photonic crystals toward miniaturized spectrometers.* Adv. Mater., 22(9):946–50, 2010.

[295] A. G. Emslie, F. T. Bonner, and L. G. Peck, *Flow of a Viscous Liquid on a Rotating Disk.* J. Appl. Phys., 29(5):858, 1958.

[296] P. Walker and J. Thompson, *Some physical properties of paints.* Proc. Amer. Soc. Test. Mater., Part 2, 22:464, 1922.

[297] L. Kleinschmidt, *Peparation of bituminous materials for spinning.* ASTM Bull., 193:53, 1953.

[298] K. Norrman, A. Ghanbari-Siahkali, and N. B. Larsen, *6 Studies of spin-coated polymer films.* Ann. Rep. Progr. Chem. C, 101(0):174, 2005.

[299] H. J. Kim, M. J. M. Krane, K. P. Trumble, and K. J. Bowman, *Analytical Fluid Flow Models for Tape Casting.* J. Am. Ceram. Soc., 89(9):2769–2775, 2006.

[300] Y. T. Chou, Y. T. Ko, and M. F. Yan, *Fluid Flow Model for Ceramic Tape Casting.* J. Am. Ceram. Soc., 70(10):C–280–C–282, 1987.

[301] H. Loest, R. Lipp, and E. Mitsoulis, *Numerical Flow Simulation of Viscoplastic Slurries and Design Criteria for a Tape Casting Unit.* J. Am. Ceram. Soc., 77(1):254–262, 1994.

[302] R. Pitchumani and V. M. Karbhari, *Generalized Fluid-Flow Model for Ceramic Tape Casting.* J. Am. Ceram. Soc., 78(9):2497–2503, 1995.

[303] K. J. Ruschak, *Coating flows.* Annu. Rev. Fluid Mech., 17:65–89, 1985.

[304] M. Pichumani, P. Bagheri, K. M. Poduska, W. Gonzalez-Vinas, and A. Yethiraj, *Dynamics, crystallization and structures in colloid spin coating.* Soft Matter, 9(12):3220–3229, 2013.

[305] M. Dijkstra, *Entropy-driven phase transitions in colloids: from spheres to anisotropic particles.* Adv. Chem. Phys., 156:35, 2014.

[306] M. Mittal and E. M. Furst, *Electric Field-Directed Convective Assembly of Ellipsoidal Colloidal Particles to Create Optically and Mechanically Anisotropic Thin Films.* Adv. Funct. Mater., 19:3271–3278, 2009.

[307] A. B. G. M. Leferink op Reinink, S. Belli, R. van Roij, M. Dijkstra, A. V. Petukhov, and G. J. Vroege, *Tuning biaxiality of nematic phases of board-like colloids by an external magnetic field.* Soft Matter, 10(3):446–456, 2013.

[308] M. Grzelczak, J. Vermant, E. M. Furst, and L. M. Liz-Marzán, *Directed self-assembly of nanoparticles.* ACS Nano, 4(7):3591–3605, 2010.

[309] H. Yang and P. Jiang, *Self-cleaning diffractive macroporous films by doctor blade coating.* Langmuir, 26(15):12598–12604, 2010.

[310] H. Yang and P. Jiang, *Macroporous photonic crystal-based vapor detectors created by doctor blade coating.* Appl. Phys. Lett., 98(1):011104, 2011.

[311] C. Y. Cai, K. Y. A. Lin, and H. Yang, *Superhydrophobic anti-ultraviolet films by doctor blade coating.* Appl. Phys. Lett., 105(20):201913, 2014.

[312] C.-Y. Cai, K.-Y. A. Lin, Y.-C. Chen, and H. Yang, *Macroporous photonic crystal-based anti-ultraviolet and anti-near-infrared materials by doctor blade coating.* Appl. Phys. Lett., 108(7):071906, 2016.

[313] W. Thielicke and E. J. Stamhuis, *PIVlab - Towards User-friendly, Affordable and Accurate Digital Particle Image Velocimetry in MATLAB.* JORS, 2(1):e30, 2014.

[314] W. Thielicke. *The Flapping Flight of Birds - Analysis and Application.* Phd-thesis, Rijksuniversiteit Groningen, The Netherlands, 2014.

[315] W. Thielicke and E. J. Stamhuis. *Pivlab - time-resolved digital particle image velocimetry tool for matlab (version: 1.41)*, 2014. http://dx.doi.org/10.6084/m9.figshare.1092508.

[316] L. D. Landau and B. Levich, *Dragging of a liquid by a moving plate.* Acta Physicochim.(USSR), 17:42, 1942.

[317] A. Acrivos, M. J. Shah, and E. E. Petersen, *On the flow of a non-newtonian liquid on a rotating disk.* J. Appl. Phys., 31(6):963–968, 1960.

[318] S. Matsumoto, Y. Takashima, T. Kamiya, A. Kayano, and Y. Ohta, *Film thickness of a Bingham liquid on a rotating disk.* Ind. Eng. Chem. Fundam., 21(3):198–202, 1982.

[319] D. Meyerhofer, *Characteristics of resist films produced by spinning.* J. Appl. Phys., 49(7):3993–3997, 1978.

[320] R. G. Larson. *The Structure and Rheology of Complex Fluids.* Oxford University Press, New York, NY, New York, 1999.

[321] R. G. Larson and H. C. Ottinger, *Effect of molecular elasticity on out-of-plane orientations in shearing flows of liquid-crystalline polymers.* Macromolecules, 24(23):6270–6282, 1991.

[322] L. Landau and E. M. Lifshitz. *Fluid Mechanics.* Pergamon, Oxford, 1975.

[323] Y. L. Wu, J. H. J. Brand, J. L. A. van Gemert, J. Verkerk, H. Wisman, A. van Blaaderen, and A. Imhof, *A new parallel plate shear cell for in situ real-space measurements of complex fluids under shear flow.* Rev. Sci. Instrum., 78(10):103902, 2007.

[324] R. Rezakhaniha, A. Agianniotis, J. T. C. Schrauwen, A. Griffa, D. Sage, C. V. C. Bouten, F. N. van de Vosse, M. Unser, and N. Stergiopulos, *Experimental investigation of collagen waviness and orientation in the arterial adventitia using confocal laser scanning microscopy.* Biomech. Model. Mechanobiol., 11(3-4):461–73, 2012.

[325] D. Sage. *OrientationJ*, 2016. http://bigwww.epfl.ch/demo/orientation/.

[326] G. Duclos, S. Garcia, H. G. Yevick, and P. Silberzan, *Perfect nematic order in confined monolayers of spindle-shaped cells.* Soft Matter, 10(14):2346–2353, 2014.

[327] D. P. Birnie, *A model for drying control cosolvent selection for spin-coating uniformity: The thin film.* Langmuir, 29(29):9072–9078, 2013.

[328] T. J. Rehg and G. Higgins, *Spin coating of colloidal suspensions.* AIChE J., 38(4):489–501, 1992.

[329] C. E. Colosqui, J. F. Morris, and H. A. Stone, *Hydrodynamically Driven Colloidal Assembly in Dip Coating.* Phys. Rev. Lett., 110(18):188302, 2013.

[330] R. Krechetnikov, *On application of lubrication approximations to nonunidirectional coating flows with clean and surfactant interfaces.* Phys. Fluids, 22(9):092102, 2010.

[331] H. C. Mayer and R. Krechetnikov, *Landau-Levich flow visualization: Revealing the flow topology responsible for the film thickening phenomena.* Phys. Fluids, 24(5):052103, 2012.

[332] B. Scheid, J. Delacotte, B. Dollet, E. Rio, F. Restagno, E. A. van Nierop, I. Cantat, D. Langevin, and H. A. Stone, *The role of surface rheology in liquid film formation.* EPL, 90(2):24002, 2010.

[333] B. J. Ackerson, *Shear induced order of hard sphere suspensions.* J. Phys.: Condens. Matter, 2(S):SA389–SA392, 1990.

[334] J. H. Snoeijer, J. Ziegler, B. Andreotti, M. Fermigier, and J. Eggers, *Thick Films of Viscous Fluid Coating a Plate Withdrawn from a Liquid Reservoir.* Phys. Rev. Lett., 100(24):244502, 2008.

[335] M. A. Green, J. Zhao, A. Wang, P. J. Reece, and M. Gal, *Efficient silicon light-emitting diodes.* Nature, 412(6849):805–808, 2001.

[336] M. A. Green, *Radiative efficiency of state-of-the-art photovoltaic cells.* Prog. Photovolt: Res. Appl., 20(4):472–476, 2012.

[337] I. Schnitzer, E. Yablonovitch, C. Caneau, and T. J. Gmitter, *Ultrahigh spontaneous emission quantum efficiency, 99.7% internally and 72% externally, from AlGaAs/GaAs/AlGaAs double heterostructures.* Appl. Phys. Lett., 62(2):131–133, 1993.

[338] S. A. Crooker, J. A. Hollingsworth, S. Tretiak, and V. I. Klimov, *Spectrally resolved dynamics of energy transfer in quantum-dot assemblies: towards engineered energy flows in artificial materials.* Phys. Rev. Lett., 89(18):186802, 2002.

[339] M. Achermann, M. A. Petruska, S. A. Crooker, and V. I. Klimov, *Picosecond Energy Transfer in Quantum Dot Langmuir-Blodgett Nanoassemblies.* J. Phys. Chem. B, 107(50):13782–13787, 2003.

[340] H. Song and S. Lee, *Red light emitting solid state hybrid quantum dot-near-UV GaN LED devices.* Nanotechnology, 18(25):255202, 2007.

[341] C. R. Kagan, C. B. Murray, M. Nirmal, and M. G. Bawendi, *Electronic Energy Transfer in CdSe Quantum Dot Solids.* Phys. Rev. Lett., 76(16):3043–3043, 1996.

[342] J. Zhao, O. Chen, D. B. Strasfeld, and M. G. Bawendi, *Biexciton quantum yield heterogeneities in single CdSe (CdS) core (shell) nanocrystals and its correlation to exciton blinking.* Nano Lett., 12(9):4477–83, 2012.

[343] M. A. Hines and P. Guyot-Sionnest, *Synthesis and Characterization of Strongly Luminescing ZnS-Capped CdSe Nanocrystals.* J. Phys. Chem., 100(2):468–471, 1996.

[344] E. Dekel, D. Gershoni, E. Ehrenfreund, D. Spektor, J. Garcia, and P. Petroff, *Multiexciton Spectroscopy of a Single Self-Assembled Quantum Dot.* Phys. Rev. Lett., 80(22):4991–4994, 1998.

[345] C. Javaux, B. Mahler, B. Dubertret, A. Shabaev, A. V. Rodina, A. L. Efros, D. R. Yakovlev, F. Liu, M. Bayer, G. Camps, L. Biadala, S. Buil, X. Quelin, and J.-P. Hermier, *Thermal activation of non-radiative Auger recombination in charged colloidal nanocrystals.* Nat. Nanotechnol., 8(3):206–12, 2013.

[346] G. E. Cragg and A. L. Efros, *Suppression of auger processes in confined structures.* Nano Lett., 10(1):313–7, 2010.

[347] Y.-S. Park, A. V. Malko, J. Vela, Y. Chen, Y. Ghosh, F. García-Santamaría, J. A. Hollingsworth, V. I. Klimov, and H. Htoon, *Near-Unity Quantum Yields of Biexciton Emission from CdSe / CdS Nanocrystals Measured Using Single-Particle Spectroscopy.* Phys. Rev. Lett., 106(18):187401, 2011.

[348] F. García-Santamaría, S. Brovelli, R. Viswanatha, J. A. Hollingsworth, H. Htoon, S. A. Crooker, and V. I. Klimov, *Breakdown of volume scaling in Auger recombination in CdSe/CdS heteronanocrystals: the role of the core-shell interface.* Nano Lett., 11(2):687–93, 2011.

[349] H. Htoon, A. V. Malko, D. Bussian, J. Vela, Y. Chen, J. A. Hollingsworth, and V. I. Klimov, *Highly emissive multiexcitons in steady-state photoluminescence of individual "giant" CdSe/CdS Core/Shell nanocrystals.* Nano Lett., 10(7):2401–7, 2010.

[350] O. Chen, H. Wei, A. Maurice, M. Bawendi, and P. Reiss, *Pure colors from core-shell quantum dots.* MRS Bulletin, 38(09):696–702, 2013.

[351] R. Osovsky, D. Cheskis, V. Kloper, A. Sashchiuk, M. Kroner, and E. Lifshitz, *Continuous-wave pumping of multiexciton bands in the photoluminescence spectrum of a single CdTe-CdSe core-shell colloidal quantum dot.* Phys. Rev. Lett., 102(19):197401, 2009.

[352] Y. S. Park, W. K. Bae, L. A. Padilha, J. M. Pietryga, and V. I. Klimov, *Effect of the core/shell interface on auger recombination evaluated by single-quantum-dot spectroscopy.* Nano Lett., 14(2):396–402, 2014.

[353] A. Minotto, F. Todescato, R. Signorini, J. J. Jasieniak, and R. Bozio. *Influence of core-shell interfaces on exciton and multi-exciton dynamics of CdSe-*$Cd_xZn1-xS$ *quantum dots.* In S. Cabrini, G. Lérondel, A. M. Schwartzberg, and T. Mokari, editors, *SPIE NanoScience + Engineering*, page 916103. International Society for Optics and Photonics, 2014.

[354] M. Marceddu, M. Saba, F. Quochi, A. Lai, J. Huang, D. V. Talapin, A. Mura, and G. Bongiovanni, *Charged excitons, Auger recombination and optical gain in CdSe/CdS nanocrystals.* Nanotechnology, 23(1):015201, 2012.

[355] A. A. Lutich, C. Mauser, E. Da Como, J. Huang, A. Vaneski, D. V. Talapin, A. L. Rogach, and J. Feldmann, *Multiexcitonic dual emission in CdSe/CdS tetrapods and nanorods.* Nano Lett., 10(11):4646–50, 2010.

[356] B. S. Mashford, M. Stevenson, Z. Popovic, C. Hamilton, Z. Zhou, C. Breen, J. Steckel, V. Bulovic, M. Bawendi, S. Coe-Sullivan, and P. T. Kazlas, *High-efficiency quantum-dot light-emitting devices with enhanced charge injection.* Nat. Photon., 7(5):407–412, 2013.

[357] B. S. Mashford, T.-L. Nguyen, G. J. Wilson, and P. Mulvaney, *All-inorganic quantum-dot light-emitting devices formed via low-cost, wet-chemical processing.* J. Mater. Chem., 20(1):167–172, 2010.

[358] F. García-Santamaría, Y. Chen, J. Vela, R. D. Schaller, J. A. Hollingsworth, and V. I. Klimov, *Suppressed auger recombination in "giant" nanocrystals boosts optical gain performance.* Nano Lett., 9(10):3482–8, 2009.

[359] A. Sánchez-Iglesias, M. Grzelczak, T. Altantzis, B. Goris, J. Pérez-Juste, S. Bals, G. van Tendeloo, S. H. Donaldson, B. F. Chmelka, J. N. Israelachvili, and L. M. Liz-Marzán, *Hydrophobic interactions modulate self-assembly of nanoparticles.* ACS Nano, 6(12):11059–11065, 2012.

[360] Y. Xia and Z. Tang, *Monodisperse inorganic supraparticles: formation mechanism, properties and applications.* Chem. Commun., 48(51):6320–6336, 2012.

[361] T. Wang, D. LaMontagne, J. Lynch, J. Zhuang, and Y. C. Cao, *Colloidal superparticles from nanoparticle assembly.* Chem Soc Rev, 42(7):2804–23, 2013.

[362] P. Qiu, C. Jensen, N. Charity, R. Towner, and C. Mao, *Oil phase evaporation-induced self-assembly of hydrophobic nanoparticles into spherical clusters with controlled surface chemistry in an oil-in-water dispersion and comparison of behaviors of individual and clustered iron oxide nanoparticles.* J. Am. Chem. Soc., 132(50):17724–32, 2010.

[363] S. Y. Lee, L. Gradon, S. Janeczko, F. Iskandar, and K. Okuyama, *Formation of highly ordered nanostructures by drying micrometer colloidal droplets.* ACS Nano, 4(8):4717–24, 2010.

[364] B. de Nijs, S. Dussi, F. Smallenburg, J. D. Meeldijk, D. J. Groenendijk, L. Filion, A. Imhof, A. van Blaaderen, and M. Dijkstra, *Entropy-driven formation of large icosahedral colloidal clusters by spherical confinement.* Nat. Mater., 14(1):56–60, 2015.

[365] D. Vanmaekelbergh, L. K. van Vugt, H. E. Bakker, F. T. Rabouw, B. de Nijs, R. J. A. van Dijk-Moes, M. A. van Huis, P. J. Baesjou, and A. van Blaaderen, *Shape-Dependent Multiexciton Emission and Whispering Gallery Modes in Supraparticles of CdSe/Multishell Quantum Dots.* ACS Nano, 9(4):3942–50, 2015.

[366] M. P. Lisitsa, L. F. Gudymenko, V. N. Malinko, and S. F. Terekhova, *Dispersion of the Refractive Indices and Birefringence of* CdS_xSe_{1-x} *Single Crystals.* Phys. Status Solidi B, 31(1):389–399, 1969.

[367] M. Debenham, *Refractive indices of zinc sulfide in the 0405-13-μm wavelength range.* Appl. Opt., 23(14):2238, 1984.

[368] T. M. Bieniewski and S. J. Czyzak, *Refractive Indexes of Single Hexagonal ZnS and CdS Crystals.* J. Opt. Soc. Am., 53(4):496, 1963.

[369] J. Rheims, J. Köser, and T. Wriedt, *Refractive-index measurements in the near-IR using an Abbe refractometer.* Meas. Sci. Technol., 8(6):601–605, 1997.

[370] E. Khon, S. Lambright, D. Khon, B. Smith, T. O'Connor, P. Moroz, M. Imboden, G. Diederich, C. Perez-Bolivar, P. Anzenbacher, and M. Zamkov, *Inorganic solids of CdSe nanocrystals exhibiting high emission quantum yield.* Adv. Funct. Mater., 22(17):3714–3722, 2012.

[371] C. Galland, Y. Ghosh, A. Steinbrück, M. Sykora, J. A. Hollingsworth, V. I. Klimov, and H. Htoon, *Two types of luminescence blinking revealed by spectroelectrochemistry of single quantum dots.* Nature, 479(7372):203–7, 2011.

[372] F. T. Rabouw, P. Lunnemann, R. J. A. van Dijk-Moes, M. Frimmer, F. Pietra, A. F. Koenderink, and D. Vanmaekelbergh, *Reduced Auger recombination in single CdSe/CdS nanorods by one-dimensional electron delocalization.* Nano Lett., 13(10):4884–92, 2013.

[373] V. I. Klimov, S. A. Ivanov, J. Nanda, M. Achermann, I. Bezel, J. A. McGuire, and A. Piryatinski, *Single-exciton optical gain in semiconductor nanocrystals.* Nature, 447(7143):441–6, 2007.

[374] M. Achermann, J. A. Hollingsworth, and V. I. Klimov, *Multiexcitons confined within a subexcitonic volume: Spectroscopic and dynamical signatures of neutral and charged biexcitons in ultrasmall semiconductor nanocrystals.* Phys. Rev. B, 68(24):245302, 2003.

[375] J.-M. Caruge, Y. Chan, V. Sundar, H. J. Eisler, and M. G. Bawendi, *Transient photoluminescence and simultaneous amplified spontaneous emission from multiexciton states in CdSe quantum dots.* Phys. Rev. B, 70(8):085316, 2004.

[376] B. Fisher, J. M. Caruge, D. Zehnder, and M. Bawendi, *Room-Temperature Ordered Photon Emission from Multiexciton States in Single CdSe Core-Shell Nanocrystals.* Phys. Rev. Lett., 94(8):087403, 2005.

[377] C. Bonati, M. B. Mohamed, D. Tonti, G. Zgrablic, S. Haacke, F. van Mourik, and M. Chergui, *Spectral and dynamical characterization of multiexcitons in colloidal CdSe semiconductor quantum dots.* Phys. Rev. B, 71(20):205317, 2005.

[378] V. I. Klimov, *Quantization of Multiparticle Auger Rates in Semiconductor Quantum Dots.* Science, 287(5455):1011–1013, 2000.

[379] Y. Liu, P. Chen, Z.-H. Wang, F. Bian, L. Lin, S.-J. Chang, and G.-G. Mu, *Efficient two-photon absorption of CdSe-CdS/ZnS core-multishell quantum dots under the excitation of near-infrared femtosecond pulsed laser.* Laser Phys., 19(9):1886–1890, 2009.

[380] J. Jasieniak, I. Fortunati, S. Gardin, R. Signorini, R. Bozio, A. Martucci, and P. Mulvaney, *Highly Efficient Amplified Stimulated Emission from CdSe-CdS-ZnS Quantum Dot Doped Waveguides with Two-Photon Infrared Optical Pumping.* Adv. Mater., 20(1):69–73, 2008.

[381] N. S. Makarov, P. C. Lau, C. Olson, K. A. Velizhanin, K. M. Solntsev, K. Kieu, S. Kilina, S. Tretiak, R. A. Norwood, N. Peyghambarian, and J. W. Perry, *Two-photon absorption in CdSe colloidal quantum dots compared to organic molecules.* ACS Nano, 8(12):12572–86, 2014.

[382] H. T. Beier, G. L. Coté, and K. E. Meissner, *Whispering gallery mode biosensors consisting of quantum dot-embedded microspheres.* Ann. Biomed. Eng., 37(10):1974–83, 2009.

[383] D. E. Gómez, I. Pastoriza-Santos, and P. Mulvaney, *Tunable whispering gallery mode emission from quantum-dot-doped microspheres.* Small, 1(2):238–41, 2005.

[384] A. Chiasera, Y. Dumeige, P. Féron, M. Ferrari, Y. Jestin, G. N. Conti, S. Pelli, S. Soria, and G. C. Righini, *Spherical whispering-gallery-mode microresonators.* Laser Photon. Rev., 4(3):457–482, 2010.

[385] L. K. van Vugt, B. Piccione, C.-H. Cho, P. Nukala, and R. Agarwal, *One-dimensional polaritons with size-tunable and enhanced coupling strengths in semiconductor nanowires.* Proc. Natl. Acad. Sci. U. S. A., 108(25):10050–5, 2011.

[386] H.-Y. Li, S. Rühle, R. Khedoe, A. F. Koenderink, and D. Vanmaekelbergh, *Polarization, microscopic origin, and mode structure of luminescence and lasing from single ZnO nanowires.* Nano Lett., 9(10):3515–20, 2009.

[387] C. Gollner, J. Ziegler, L. Protesescu, D. N. Dirin, R. T. Lechner, G. Fritz-Popovski, M. Sytnyk, S. Yakunin, S. Rotter, A. A. Yousefi Amin, C. Vidal, C. Hrelescu, T. A. Klar, M. V. Kovalenko, and W. Heiss, *Random Lasing with Systematic Threshold Behavior in Films of CdSe/CdS Core/Thick-Shell Colloidal Quantum Dots.* ACS Nano, 9(10):9792–801, 2015.

Summary

This thesis deals with the directed assembly of colloidal rods, spheres and their mixtures. *Colloids* are particles with a mesoscopic size which are dispersed in a continuous phase. Think of the fat droplets and proteins floating inside milk. Both the colloid and the continuous phase can be made of either a gas, a liquid or a solid. Self-assembly of colloids into colloidal crystals can be guided by external fields, to overcome kinetic barriers that prevent the system to reach the state of lowest free energy. This process is usually called *directed assembly.* In this thesis we study the directed assembly of colloids in external fields such as gravity, electric fields and shear flow.

Chapter 2 describes the colloidal synthesis, colloidal dispersions and the imaging techniques that are used in this thesis.

Chapter 3 and **Chapter 4** describe the sedimentation of a binary mixture of silica rods and spheres.

In **Chapter 3** we determine the experimental phase diagram, of a binary mixture of silica rods and spheres that form an Sm_2-phase. The phase diagram was determined from sedimentation-diffusion equilibria using confocal microscopy. In this way we were able to directly determine thermodynamic quantities such as osmotic pressure, and local and global order parameters. The results were compared with results from Monte Carlo simulations of hard spheres and hard rods in bulk. Next to that, we showed that we are able to align the Sm_2-phase with an ac electric field. Moreover, we measured the diffusion of spheres inside the Sm_2-phase and showed that the Sm_2-phase was a stable phase and not kinetically trapped.

In **Chapter 4**, the sedimentation dynamics of binary mixtures of silica rods and spheres were followed over time. We investigated two systems: in the first system the diameter of silica spheres σ is smaller than the diameter of the rods D, $\sigma/D = 0.66$, and the mixture forms a binary smectic phase; in the second system the diameter of the silica spheres is larger than the diameter of the rod $\sigma/D = 1.58$. The first system showed that the binary smectic phase nucleated from a nematic layer of rods at the bottom of the sample, once the pressure and volume fraction of rods were high enough. Moreover, we found an interplay between the sedimentation of rods and sedimentation of spheres. As the concentration of spheres increased at the bottom of the sample, the sedimentation of rods slowed down. The bottom rod-rich sediment then pushed the spheres upwards. In the second system a transition occurred upon sedimentation from a homogeneously mixture of colloids to a heterogeneously mixture. Here, bundles of aligned rods appeared inside the dense sediment and the overall bundles orientation was random. Over time the overall structure of the sediment did not change much. This indicated that perhaps the system was kinetically trapped.

In **Chapter 5** the electrophoresis of fluorescently labeled silica particles was investigated on the single particle level using confocal microscopy. We showed that using crosscorrelation as an image analysis technique, we can decrease the measurement time of micro-electrophoresis experiments. For silica rods this method is only valid $\kappa a \gg 10$, where κ^{-1} is the double layer thickness and a the radius of the rod associated with the diameter. We determined the electrophoretic mobility and the zeta-potential (ζ) of these particles. At lower κa, rod-like particles do not move uniformly in the electric field, but exhibit a velocity that depends on the angle between the long axis of the rod and the electric field. We measured this anisotropy in the electrophoretic mobility of individual silica rods during electrophoresis as function of κa and compared these results with theoretical predictions. We showed that even at already relatively high κa, when the Smoluchowski limiting law is assumed to be valid ($\kappa a > 10$), an orientation dependent velocity was found. Furthermore, we observed that at decreasing values of κa the anisotropy in the electrophoretic mobility of the rods increases. However, in low polar solvents with $\kappa a < 1$ this trend was reversed: the anisotropy in the electrophoretic mobility of the rods decreased. We argue that this decrease is due to the fact that end effects start to play a role, which was already predicted theoretically. When end effects are not taken into account, this will lead to strong underestimation of the experimentally determined zeta-potential.

In **Chapter 6** shear alignment was used to direct the assembly of thin films of ordered silica rods or spheres. In the first part of the chapter spin coating was used to obtain thin films of colloidal rods, whith the silica rods radially aligned along the direction of flow. This was done by using a dispersion of rods dispersed in a mixture of a liquid acrylate monomer and 1-propanol. In the second part of the chapter doctor blade coating was used to obtain crystalline colloidal films made of silica spheres, that were dispersed in a liquid acrylate monomer. The process of doctor blade coating was visualized in real-time with a confocal microscope, such that we were able to investigate shear alignment and the flow behavior of the dispersion during doctor blade coating. It was established that, in our case, capillary forces determined the properties of the obtained crystalline colloidal film and we observed Landau-Levich flow. Moreover, we were able to make the crystalline colloidal film permanent by polymerizing the liquid monomer using UV-light.

To conclude, in **Chapter 7** the optical properties of supraparticles consisting of core-multishell quantum dots were investigated. When quantum dots are packed together in a solid, they normally suffer from non-radiative recombination and their efficiency decreases. The supraparticles composed of CdSe/multishell nanocrystals did not suffer from non-radiative recombination, due to the additional shells of semiconductor grown around the particle, which have a larger energy gap E_g, reducing exciton energy transfer. All supraparticles showed stable and bright photoluminescence in ambient up to high excitation intensities. In addition to single-exciton emission, we observed bright emission from multiexciton states at high excitation powers. In contrast, supraparticles excited with two photon excitation did not show any bright emission from multiexciton states. Furthermore, the supraparticles exhibit shape-dependent optical properties. When the supraparticles were deposited on a silicon surface their spherical shape was deformed due to drying. These deformed supraparticles showed the onset of whispering gallery modes in microscope images, while sharp Mie modes in the spectrum were absent. Moreover, supraparticles that retained their perfectly spherical shape showed sharp Mie whispering gallery modes in their spectrum, while multiexciton emission was absent.

Samenvatting voor een breed publiek

De titel van dit proefschrift luidt ‘Gerichte organisatie van colloïdale staven, bollen en hun mengsels’. Hieronder zal ik proberen uit te leggen wat colloïden zijn en wat er zo interessant is aan de gerichte organisatie van colloïdale bollen en staven. En daarnaast kan je hier per onderzoeksproject een samenvatting vinden van de resultaten.

Colloïden Colloïden zijn deeltjes met een grootte van enkele nanometers ($1\,\mathrm{nm} = 10^{-9}\,\mathrm{m}$) tot enkele micrometers ($1\,\mu\mathrm{m} = 10^{-6}\,\mathrm{m}$). Vaak hebben colloïdale deeltjes de vorm van een bol, maar ze kunnen ook een andere vorm hebben, zoals een staaf of een kubus. Deze deeltjes ‘zweven’ rond in een medium, ook wel de continue fase genoemd. Zowel de colloïd als de continue fase kan bestaan uit een gas, vloeistof of vaste stof. Door de grootte van een colloïdaal deeltje hebben zowel krachten van buiten als de warmtebeweging van moleculen en atomen uit de continue fase een grote invloed op hun beweging. Samen vormen de colloïdale deeltjes en de continue fase een suspensie. Colloïdale deeltjes kom je dagelijks tegen. Je vindt ze in bloed, melk, mayonaise, verf en tandpasta. Kennis over suspensies is dus van groot belang in de levensmiddelenindustrie, maar ook voor verfproducenten en de medische sector.

Brownse beweging en diffusie In vergelijking met atomen en moleculen (1 atoom $\sim 0.1\,\mathrm{nm}$) zijn colloïdale deeltjes relatief groot en traag. Daardoor kunnen we colloïden goed waarnemen met optische microscopen. Als je met een microscoop naar een colloïdaal deeltje in een vloeistof zal kijken, zal je zien dat dit deeltje een *dronkemanswandeling* maakt. Door de warmtebeweging van moleculen en atomen uit de continue fase botsen deze voortdurend tegen de colloïden aan. Door fluctuaties in deze botsingen is de kracht op een deeltje niet altijd uniform, en dit resulteert in de *Brownse beweging.* De Brownse beweging veroorzaakt de *diffusie* van colloïden, de verplaatsing van een deeltje over de tijd. De afstand die een colloïdale deeltje aflegt door *diffusie* hangt af van de tijd, de grootte van het deeltje en de stroperigheid (viscositeit) van de continue fase.

Zelforganisatie en gerichte organisatie Colloïden kunnen dienen als modelsysteem voor atomen en moleculen. Dit komt doordat colloïden net als atomen en moleculen worden beïnvloed door de warmtebeweging en doordat we ze goed kunnen bestuderen met een optische microscoop. Colloïden kunnen ook net als atomen en moleculen zich ordenen in een regelmatig rooster als de concentratie van deeltjes hoog genoeg wordt. Dit heet *zelforganisatie.* Hiervoor dienen deze colloïden wel allemaal dezelfde grootte te hebben, ze zijn dan *monodisperse.* Doordat colloïden relatief groot zijn kunnen we ze ook relatief makkelijk manipuleren met krachten van buiten, zoals de zwaartekracht, elektrostatische krachten en krachten door stroming van de continue fase. We kunnen de zelforganisatie van colloïden in regelmatige structuren sturen met deze externe krachten, zodat ze zich ordenen in de gewenste structuur. Dit proces heet *gerichte organisatie.* In dit proefschrift gebruiken we zowel de zwaartekracht (hoofdstuk 3 & 4), elektrische velden (hoofdstuk 3) als ook stroming (hoofdstuk 6) voor de *gerichte organisatie* van colloïden in regelmatige structuren.

Dubbellaag De staafjes en bolletjes die ik gebruikt in dit proefschrift zijn gemaakt van silica (SiO_2), hetzelfde materiaal als waar zand uit bestaat en waar glas van is gemaakt. Silica staafjes en bolletjes hebben een negatief geladen oppervlak en wanneer ze elkaar raken plakken ze niet onomkeerbaar aan elkaar vast. Dit komt doordat twee gelijksoortige elektrische ladingen elkaar afstoten. Op welke afstand twee ladings gestabiliseerde deeltjes elkaar al kunnen voelen, hangt af van de reikwijdte van de oppervlakte lading. De reikwijdte van de oppervlakte lading wordt ook wel de elektrochemische *dubbellaag* genoemd. De dikte van de dubbellaag, hangt af van de polariteit van de continue fase en de concentratie ionen in de continue fase. Dit verschil in polariteit tussen water en olie betekent dat in olie de oppervlakte lading van een colloïdaal deeltje verder kan dragen dan in water. Twee gelijksoortige ladingen zullen elkaar dan al op een grotere afstand 'voelen' en dus afstoten. Als er zout aan de continue fase is toegevoegd, dan schermen de ionen van het zout de lading af en draagt de lading ook minder ver. Door het oplosmiddel te veranderen en de concentratie ionen te variëren, kan je de dikte van de dubbellaag variëren van enkele nanometers tot enkele micrometers dik. Dit hebben we gedaan in hoofdstuk 5.

Wanneer je een continue fase gebruiken die lijkt op water en je genoeg zout toevoegd om de lading van de deeltjes af te schermen dan wordt de afstand waarover de deeltjes elkaar afstoten relatief klein (over enkele nanometers) ten opzichte van de afmetingen van de deeltjes (rond de micrometer). Dit hebben we gedaan in hoofdstuk 3 & 4. De silica deeltjes gedragen zich dan als deeltjes met een hard-bollen potentiaal.

Harde-bollen Deeltjes met harde-bollen potentiaal 'voelen' elkaar niet als ze elkaar niet raken: er is geen aantrekkingskracht of afstotingskracht tussen de deeltjes. Echter, op het moment dat de deeltjes elkaar raken dan kunnen de deeltjes niet worden ingedrukt, net als biljart ballen. Aangezien de deeltjes elkaar alleen voelen als ze botsen met elkaar (ten gevolge van de Brownse beweging) hangt hun ordening alleen af van de dichtheid van de deeltjes (het aantal deeltjes per volume eenheid). Afhankelijk van de dichtheid van monodisperse bolvormige deeltjes zijn er twee fases: een vloeibare fase en een vaste kristal fase. In de vloeibare fase is er geen lange-afstand-ordening van de bolletjes. In de kristal fase organiseren de deeltjes zich daarentegen in een piramide rooster, zoals vroeger kanonskogels gestapeld werden. Dit kan op twee manieren, volgens een kubisch vlakgecentreerd rooster (Engels: *face center cubic latice, fcc*) of volgens een hexagonaal rooster (Engels: *hexagonal close packed latice, hcp*).

Vloeibare kristallen Door de niet ronde vorm van staafjes (anistrope vorm), bepaalt niet alleen de positie, maar ook de oriëntatie van de staafjes de structuur die wordt gevormd. Daarom kunnen staafjes met een harde-bollen potentiaal ook nog andere fases vormen dan alleen een vloeibare fase en een kristal fase. Tussen de vloeibare fase en de kristal fase vormen zich nog vloeibare kristallijne fases. Deze fases hebben eigenschappen van zowel de vloeibare als de kristal fase. Ook andere anisotrope deeltjes, zoals colloïdale schijfjes, vormen vloeibare kristallijne fases. Staafjes kunnen een nematische, smectische of een columnaire vloeibare kristallijne fase vormen. De vloeibare fase heet bij staven ook wel de isotrope fase, in deze fase is er geen ordering in positie of oriëntatie. In de nematische fase is er geen ordening in de positie, maar wel in de oriëntatie van de staafjes. De staafjes wijzen gemiddelde allemaal dezelfde kant op, deze voorkeursrichting wordt doorgaans aangeduid met $\hat{\boldsymbol{n}}$. In de smectische fase wijzen de staafjes ook allemaal dezelfde kant op, en daarnaast zijn ze ook geordend in smectische lagen. Binnen deze lagen is er geen ordening en gedragen de staafjes zich als een vloeistof. Daarnaast bestaat er ook een columnaire fase waarbij de staafjes hexagonaal geordend zijn in het vlak, maar waarbij de staafjes niet zijn geordend in lagen. De staafjes zijn uitgelijnd in 'treintjes' die langs elkaar heen kunnen glijden. In de kristal fase wijzen de staafjes allemaal dezelfde kant op en is er in drie richtingen lange-afstand-ordening. Een schematische weergave van deze fases is afgebeeld in figuur 1.

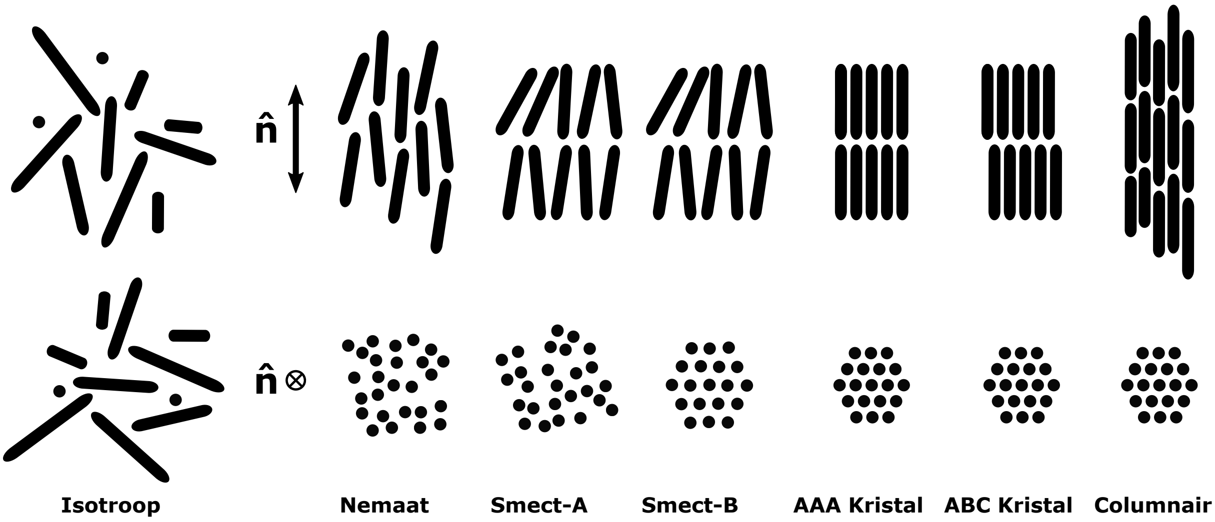

Figuur 1 Schematische weergave van staafjes in verschillende vloeibare kristallijne fases; boven zijn de staafjes weergeven parallel aan de voorkeursrichting $\hat{\boldsymbol{n}}$ van de staafjes, onder loodrecht op de voorkeursrichting $\hat{\boldsymbol{n}}$ van de staafjes.

Colloïdale fotonische kristallen Regelmatige structuren van colloïden kunnen een speciale interactie met het licht hebben, het zijn daardoor *fotonische kristallen.* Dit gebeurt wanneer de structuren variaties in de brekingsindex van het licht hebben ter grootte van de golflengte van het zichtbare licht. De golflengte van het licht bepaald de kleur die je ziet. Fotonische kristallen komen ook voor in de natuur. Zoals de vleugels van een Morpho vlinder, die een iriserende blauwe kleur hebben. De kleur en intensiteit van de vleugels verandert met de waarnemingshoek. Deze kleur wordt niet door een pigment (kleurstof) veroorzaakt (zoals de kleurstoffen die worden toegevoegd aan levensmiddelen, of welke gebruikt worden in verf), maar door de regelmatige structuur van de vleugel ter grootte van de golflengte van het licht. Door de regelmatige structuur kunnen niet alle golflengtes van het licht worden doorgelaten. Dit is afhankelijk van de hoek waarop het licht invalt. Hierdoor zie je onder bepaalde hoeken een verhoogde reflectie van licht wat niet wordt doorgelaten, zoals bijvoorbeeld de iriserende blauwe kleur van een Morpho vlinder. Ook het edelsteen opaal is een natuurlijk fotonische kristal. Opalen zijn colloïdale fotonische kristallen en zijn miljoenen jaren geleden gevormd door monodisperse bolletjes van amorfe silica (SiO_2). Ook bij een opaal zijn de kleuren die je waarneemt afhankelijk van de richting waarin je naar het opaal kijkt.

Colloïdale fotonische kristallen kunnen toegepast worden in bijvoorbeeld beeldschermen, chemische en biologische sensoren en antireflectie coatings. Er wordt daarom veel onderzoek gedaan om deze colloïdale kristallen ook in het laboratorium te maken door gebruik te maken van de zelforganisatie en gerichte organisatie van monodisperse colloïdale deeltjes.

Confocale microscopie In dit proefschrift gebruiken we confocale microscopie om colloïdale bollen en staven te bestuderen. Dit is een techniek waarbij een laser wordt gebruikt om een monster te belichten. Doordat er in de deeltjes die we gebruiken een fluorescerende stof is ingebouwd, gaan de deeltjes fluoresceren. Dit fluorescerend licht wordt vervolgens door een detector opgevangen. De bolletjes en staafjes konden goed worden onderscheiden omdat er in de bolletjes een andere fluorescerend stofje zit ingebouwd dan in de staafjes, ze fluoresceren daarom elk op een verschillende golflengte, zie figuur 2b. Bij een confocale microscope valt alleen fluorescerend licht op de detector wat uit het focale vlak komt. Hierdoor kunnen we op verschillende hoogtes dunne plakjes beeld opnemen van het monster. Door verschillende plakjes beeld achterelkaar op te nemen, kan er een 3D beeld worden gereconstrueerd van het monster. In dit proefschrift gebruiken we vaak computer algoritmes om beelden opgenomen met confocale microscopie te analyseren. Zo kunnen we bijvoorbeeld de locatie van de deeltjes en de orientatie van de staafjes bepalen uit 2D en 3D beeld, waardoor we bijvoorbeeld de precieze structuur van monsters kunnen bepalen, zie figuur 2a. Maar we kunnen ook aan de hand van filmpjes het pad volgen dat een deeltje aflegd in de tijd of de snelheid van een deeltje bepalen. Hierdoor kunnen we bijvoorbeeld volgen hoe deeltjes bewegen in een elektrisch veld (hoofdstuk 5) of hoe deeltjes bewegen als een suspensie wordt uitgesmeerd over een oppervlak (hoofdstuk 6).

Mengsel van colloïdale bollen en staven In hoofdstuk 3 & 4 hebben we onderzocht hoe mengsels van colloïdale staven en bollen zich ordenen in verschillende fases onder invloed van de zwaartekracht en wat voor een structuren er worden gevormd bij verschillende dichtheden en mengverhoudingen van bolletjes en staafjes. In hoofdstuk 3 laten we zien dat silica bolletjes en staafjes een binaire smectic fase kunnen vormen. In deze vloeibaar kristallijne fase vormen de staafjes smetische lagen en tussen de lagen bevinden zich de bolletjes in vloeibare fase. Een weergave van de binaire smectische fase is afgebeeld in figuur 2.

Mengsels van colloïdale bollen en staven onder de invloed van zwaartekracht In hoofdstuk 3 & 4 maken we gebruik van de zwaartekracht om de dichtheid van de deeltjes te variëren. Doordat de silica deeltjes een hogere dichtheid hebben dan de continue fase waarin ze in zitten, zakken de deeltjes naar de bodem. Na verloop van tijd onstaat er verdeling in dichtheid, op de bodem zijn de deeltjes heel erg geconcentreerd maar hogerop

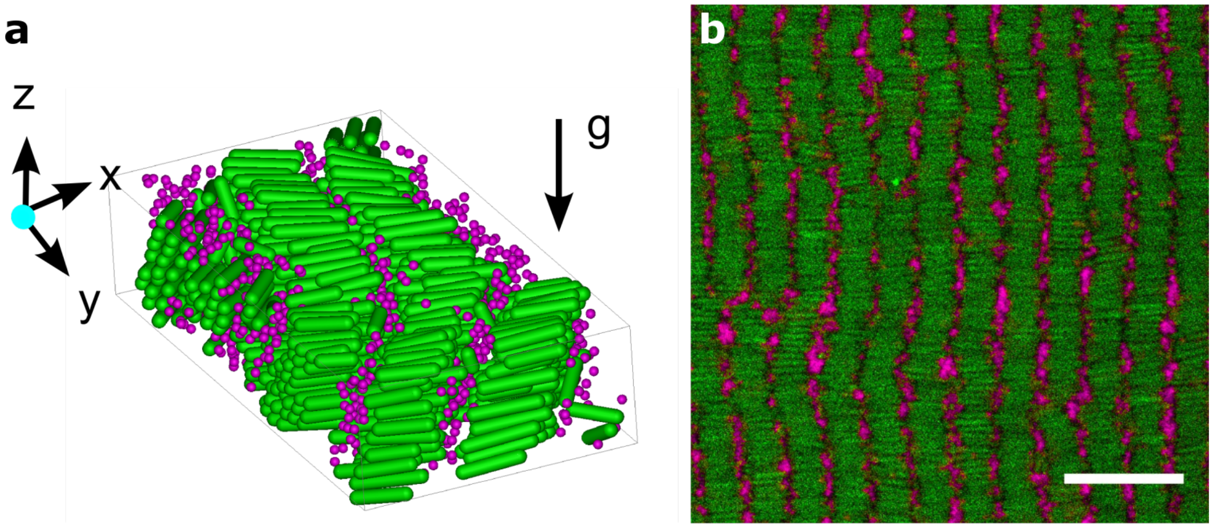

Figuur 2 De binaire smectische fase **(a)** getekend met de computer aan de hand van de coordinaten van de deeltjes verkregen uit confocale microscopie data. **(b)** Een confocaal microscopieplaatje van de binaire smectische fase, de silica staafjes zijn groen gekleurd, de silica bolletjes zijn roze gekleurd, net als in **(a)**.

neemt de dichtheid van deeltjes af. Dit komt omdat de deeltjes nog steeds onderhevig zijn aan de Brownse beweging, waardoor de deeltjes nog kunnen diffunderen. Dit is een sedimentatie-diffussie evenwicht, waarin de mate van diffussie langs de as van de zwaartekracht gelijk is aan de sedimentatie. Je kan deze dichtheidsverdeling vergelijken met de dichtheid van lucht in de atmosfeer (barometrische hoogteverdeling). De meeste mensen hebben deze barometrische hoogteverdeling van de aardse atmosfeer wel eens opgemerkt, in het hooggebergte is de lucht veel ijler waardoor je meer moeite hebt met ademen. Omdat de moleculen in lucht vele malen lichter zijn, is de zwaartekracht die er op werkt minder en is de dikte van de aardse atmosfeer wel $\sim 100\,\mathrm{km}$ in tegenstelling tot de hoogte van ons colloidaal sediment $\sim 150\,\mu\mathrm{m}$.

Nu hebben we eerder opgemerkt dat het fase gedrag, van de colloïden die worden gebruikt in dit proefschrift, alleen afhankelijk is van de dichtheid van de deeltjes. Hierdoor kan je je misschien wel voorstellen dat je in een sediment van enkel staaf- of bolvormige deeltjes alle mogelijke fases kan waarnemen. In het geval van een mengsel van staafjes en bolletjes ligt het wat complexer. Het fase gedrag is niet alleen afhankelijk van de dichtheid van deeltjes maar ook van de verhouding van staafjes en bolletjes op elke hoogte. In sedimentatie-diffusie evenwicht is de uiteindelijke verhouding bolletjes en staafjes in het sediment niet overal gelijk maar verschilt het per hoogte. Dit komt doordat bolletjes en staafjes niet hetzelfde gewicht hebben en daardoor ook een verschillende sedimentatie snelheid en diffussie snelheid (ten gevolge van de Brownse beweging) hebben.

In hoofdstuk 3 hebbben we het fase gedrag van bolletjes en staafjes onderzocht onder de invloed van de zwaarte kracht. Dit hebben we gedaan door mengsels van verschillende bol/staaf verhoudingen te laten sedimenteren en door van het resulterende sediment van $\sim 150\,\mu\mathrm{m}$ hoog in sedimentatie-diffussie evenwicht een 3D beeld met de confocale microscoop op te nemen. Uit het 3D beeld hebben we aan de hand van computer algoritmes de positie en oriëntatie van de deeltjes in het 3D beeld bepaald. Hierdoor konden we op elke hoogte vrij precies de structuur en fase bepalen (isotroop, nemaat en binair smectisch). Op deze manier konden we fysische grootheden bepalen, die normaal niet makkelijk uit experimenten te verkrijgen zijn. Door ons onderzoek konden we het experimentele fasediagram bepalen in het 2-dimensionale vlak van de druk P en de compositie x_{sph}. We weten zo onder welke omstandigheden de binaire smectische fase precies ontstaat. Daarnaast, konden we dit experimentele fasediagram vergelijken met een fasediagram verkregen uit computer simulaties. In de simulaties hebben we deeltjes voorgesteld als harde-bollen. Hierdoor hebben we kunnen bevestigen dat er geen aantrekkingskrachten nodig zijn om de binaire smectische fase te vormen. De harde-bollen afstoting alleen is genoeg om de binaire smectische fase te vormen.

Dynamica van mengsels van colloïdale bollen en staven Doordat we een viskeuze continue fase gebruiken, duurt het een paar weken voordat een sedimentatie-diffussie evenwicht is bereikt. In hoofdstuk 4 hebben we een monster van bolletjes en staafjes op verschillende tijdstippen onderzocht voordat een sedimentatie-diffussie evenwicht is bereikt. Zo hebben we kunnen onderzoeken hoe een binaire smectische fase zich in de tijd vormt. Uit het onderzoek is gebleken dat wanneer de staafjes dichtheid op de bodem groot genoeg is, we een fase overgang zien van een isotrope fase naar een nematische fase. Deze nematische fase vormde zich aan de bodem van het monster, dit proces heet *heterogene nucleatie*. Als de dichtheid van colloïdale deeltjes door sedimentatie dan nog groter wordt, dan vindt er een fase overgang plaats van een nematische fase naar een binaire smectische fase. De binaire smectische fase vormde zich op verschillende plekken binnen het al gevormde nemaat, dit proces heet *homogene nucleatie*. Ook hebben we in hoofdstuk 4 de sedimentatie onderzocht van een bolletjes en staafjes mengsel waarbij de diameter van de bolletjes groter was dan de staafjes diameter. Uit ons onderzoek bleek dat er dan geen binaire smectische fase werd gevormd, maar dat er een andere structuur werd gevormd. Doordat de dichtheid van deeltjes op de bodem langzaam groter werd, zagen we wel een overgang van een homogeen mengsel van bolletjes en staafjes, naar een heterogeen mengsel met daarin kleine clusters van staafjes. Over de tijd veranderde de heterogene structuur van het sediment niet naar een meer geordende structuur, maar vond er ook geen fase scheiding plaats. Daarom denken we dat in dit geval het systeem kinetisch vast zit. Hiermee wordt bedoeld dat de thermische fluctaties in de energie te klein zijn om via zelforganisatie een geordende structuur te vormen.

Elektroforese Als er met gelijkspanning een elektrisch veld op een suspensie met ladings gestabiliseerde colloïden wordt gezet, dan zullen de colloïden naar een tegenovergestelde geladen elektrode bewegen. Deze beweging heet elektroforese en deze techniek wordt gebruikt in laboratoria om eiwitten, DNA of RNA fragmenten te scheiden aan de hand van hun lading en grootte. In hoofdstuk 5 hebben we door middel van elektroforese de oppervlakte lading van colloïdale staven en bollen gemeten. De hoeveelheid lading aan het oppervlak is een mate voor de stabiliteit van het colloïdale deeltje in de oplossing en bepaald hoe sterk twee deeltjes elkaar afstoten. In hoofstuk 5 beschrijven een alternatieve manier om de oppervlakte lading van colloïdale deeltjes te bepalen met de confocale microscoop. Deze alternatieve manier is sneller dan de manier die voorheen werd gebruikt om electroforese metingen te doen met de confocale microscoop. Maar deze methode is voor staafjes alleen van toepassing als de dubbellaag relatief dun is ten opzichte van de staaf diameter.

Daarnaast hebben we in hoofdstuk 5 onderzocht hoe colloïdale staven zich bewegen in een elektrisch veld afhankelijk van de dikte van de dubbellaag. De dikte van de dubbellaag hebben we veranderd door het oplosmiddel te veranderen en de concentratie ionen in de continue fase te veranderen. We hebben gevonden dat wanneer de staafjes een dunne dubbellaag hebben ten op zichte hun diameter, de staafjes min of meer in een rechte lijn door het elektrisch veld bewegen. Maar als de dikte van de dubbellaag groter wordt, dan zien we dat de richting waar in het staafje beweegt afhankelijk is van de hoek die het staafje heeft met het elektrisch veld. Door de Brownse beweging kan het staafje vrij roteren en verandert de hoek die het staafje heeft met het elektrisch veld in de tijd. Daardoor verandert met de tijd dus ook de richting waarin het staafje beweegt. Het lijkt dan net alsof de staafjes een kant op zwemmen. De metingen van ons onderzoek kwamen grotendeels overeen met bestaande theorie van oneindig lange staven in een elektrisch veld. Alleen bij een relatief dikke dubbellaag kwamen de metingen met eindige staafjes niet meer overeen met de bestaande theorie. Deze afwijking konden we verklaren doordat, in het geval van een relatief dikke dubbellaag, de aanname van een oneindig lange staaf geen goede benadering is.

Gerichte organisatie door stroming In hoofdstuk 6 hebben we stroming gebruikt om organisatie te beïnvloeden van bolletjes en staafjes in een dunne film. In het eerste deel van het hoofdstuk gebruiken we spincoating om een zeer dun laagje van staafjes op een oppervlak te krijgen. Bij spincoaten wordt er door middel van snelle rotatie een druppel suspensie uitgesmeerd over een oppervlak tot een zeer dun laagje. Tijdens het spincoaten is de stroming naar buiten gericht. Wij hebben onderzocht hoe je het protocol moet veranderen zodat de silica staafjes in de uiteindelijke film gelijk aan de stromingsrichting naar buiten wijzen. In het tweede deel van het hoofdstuk gebruikten we doctor blade coating om een geordende dunne laag van bolletjes op een oppervlak te krijgen. Bij doctor blade coating smeert een dun mes een suspensie over een oppervlak uit tot een dunne laag. Dit gebeurt met een speciale opstelling, waarbij de snelheid van het mes constant is en waarbij ook de afstand van het mes tot het oppervlak constant is. Het bijzondere aan onze opstelling is dan we het proces van doctor blade coating in de tijd konden volgen met een confocale microscoop. We hebben onderzocht hoe de stroming van de suspensie tijdens het doctor blade coaten er uit ziet en we hebben dit vergeleken met bestaande theoriën. Zo kregen we een beter inzicht welke parameters van belang zijn tijdens het doctor blade coaten.

Supradeeltjes Tenslotte hebben we in hoofdstuk 7 de optische eigenschappen onderzocht van supradeeltjes, bolletjes van enkele micrometers groot die bestaan uit dicht op elkaar gepakte quantum dots. Quatum dots, ook wel luminescente nanokristallen genoemd, zijn deeltjes gemaakt uit halfgeleider materialen. De optische eigenschappen van deze nanokristallen zijn speciaal, omdat deze worden bepaald door hun grootte van enkele nanometers. Je zou verwachten dat de optische eigenschappen van op elkaar gepakte quantum dots, zoals in een supradeeltje, weer gaan lijken op de optische eigenschappen van bulk halfgeleider. In ons onderzoek gebruikten we quantum dots waar extra lagen van een andere halfgeleider materiaal omheen waren gegroeid. Hierdoor behielden de quantum dots in de supradeeltjes hun optische eigenschappen. Daarnaast is uit ons onderzoek gebleken dat de supradeeltjes optische eigenschappen hadden, die juist specifiek waren voor de micrometer grootte en de bolle vorm van de supradeeltjes: *whispering gallery modes*.

Dankwoord

Dit boekje is tot stand gekomen na vierenhalf jaar hard werk in de Soft-Condensed-Mattergroep in Utrecht. Maar in mijn eentje had ik dit proefschrift niet kunnen voltooien. Daarom wil ik op deze plaats een aantal mensen bedanken voor de begeleiding, steun en hulp die ze mij hebben gegeven.

Ten eerste wil ik mijn co-promotor Arnout Imhof en promotor Alfons van Blaaderen bedanken, zonder hen had ik niet aan dit project kunnen beginnen. Alfons, bedankt dat ik in je groep heb mogen werken. Je hebt een ongekend brede interesse en ongebreidelde kennis van de literatuur. Arnout bedankt voor al je enthousiasme, je hulp en je adviezen in de afgelopen jaren. Je drive om alles precies te willen begrijpen is erg inspirerend.

Ik wil ook graag Judith Wijnhoven, Peter Helfferich, Relinde van Dijk-Moes, Marion Wijburg en Thea Pozzi bedanken voor het draaiend houden van het lab en alle zaken er om heen. Peter bedankt voor alle technische hulp met computers, microscopen, elektrische velden en de doctor blade set-up. Judith en Relinde bedankt voor het draaiend houden van het lab en alle gezelligheid. Marion en Thea bedankt voor de organisatorische ondersteuning.

Verder wil ik al mijn collega's bedanken voor belangstelling, samenwerking en de open sfeer op het lab. In de Soft-Condensed-Mattergroep staat iedereen altijd open om elkaar te helpen en elkaar wegwijs te maken op het lab. Simone Dussi wil ik bedanken voor de samenwerking in het binaire smect project. Thijs Besseling wil ik bedanken voor alle hulp met het opzetten van de sedimentatie experimenten, de single deeltjes microscopie en de computercode om de staafjes te vinden en te volgen in tijd. Bart de Nijs en Bert van Vugt wil ik bedanken voor de samenwerking met de supradeeltjes experimenten. Tevens wil ik de studenten die ik heb begeleid, bedanken voor hun bijdrage aan het onderzoek. Dus bedankt Barbera Droste, Isabelle Palstra, Guy Frissen en Albert Grau Carbonell, ik heb ontzettend veel van jullie geleerd.

Daarnaast wil ik mijn kamergenoten van OL056 en later OL012 bedanken voor alle gezelligheid en (wetenschappelijke) discussies. Ten eerste, Bo Peng en Bas Kwaadgras gedurende het eerste jaar van mijn PhD. Bo voor zijn enthousiasme en goede raad. Bas voor alle computer hulp (als Peter niet in de buurt was). Later kwam de gezelligheid van Rik Koster, Fabian Hagemans, Vasileios Prymidis en Zdeněk Preisler. In OL012 wil ik Wessel Vlug, Jessi van der Hoeven en Pepijn Moerman bedanken voor alle koekjes, thee, gezelligheid en (wetenschappelijke) hulp bedanken.

Verder wil ik alle collega's van de Soft-Condensed-Mattergroep bedanken voor de leuke tijd die ik er heb gehad. Bedankt voor de borrels, congres bezoeken, groepsuitjes, diners, de Pheidippidesloop, het kanoën, het bioscoopbezoek, het schaatsen en alle activiteiten die ik ben vergeten te noemen. Biking buddies, met onder andere Nina Elbers, Sander van den Belt, Jessi van der Hoeven en Ramon Oord, bedankt voor alle racefietsavonturen.

De moleculairen Mieke Huijbers, Joseline Houwman, Bas van den Berg, Leonie van 't Hag en Antsje Nolles wil ik bedanken voor de gezamenlijk weg die we de afgelopen jaren hebben bewandeld. Na onze studie is ieder zijn eigen promotietraject ingeslagen, maar we hebben PhD lief en leed kunnen delen tijdens onze etentjes of tijdens het pubquizzen als team Marie Curie.

Ook wil ik mijn vrienden bedanken voor de steun en gezelligheid door de jaren heen. In het bijzonder Jan Joris, bedankt dat je één van mijn paranimfen wilt zijn!

Verder wil ik mijn familie bedanken voor alle steun de afgelopen jaren. Jenneke bedankt voor de steun die je me als ervaringsdeskundige hebt gegeven. Truuske bedankt voor alle nieuwsgierigheid en het corrigeren van mijn samenvatting. Anton bedankt voor het helpen bij het ontwerpen van de omslag van dit proefschrift. Als laatste wil ik Kees bedanken voor alle aanmoediging en steun die je me hebt gegeven in de afgelopen jaren. Ik hoop dat we elkaar nog tot in de lengte van dagen zullen aanmoedigen om het beste in onszelf naar boven te halen.

Iedereen die verder heeft bijgedragen aan dit proefschrift, maar die ik niet genoemd heb, bedankt!

List of Peer-Reviewed Publications

This thesis is partly based on the following publications

- Henriëtte E. Bakker, Simone Dussi, Barbera Droste, Thijs H. Besseling, Chris L. Kennedy, Evert I. Wiegant, Bing Liu, Arnout Imhof, Marjolein Dijkstra and Alfons van Blaaderen, *Phase diagram of binary colloidal rod-sphere mixtures from a 3D real-space analysis of sedimentation-diffusion equilibria*, Soft Matter 12, 9238-9245, 2016. (Chapter 3).
- Henriëtte E. Bakker, Simone Dussi, Arnout Imhof, Marjolein Dijkstra and Alfons van Blaaderen,*Dynamics of Sedimentation of Binary Colloidal Rod-Sphere Mixtures*, in preparation (Chapter 4).
- Henriëtte E. Bakker, Thijs H. Besseling, Judith Wijnhoven, Peter Helfferich, Alfons van Blaaderen and Arnout Imhof, *Micro-electrophoresis of silica rods using confocal microscopy*, submitted (Chapter 5).
- Daniël Vanmaekelbergh, Lambert K. Van Vugt, Henriëtte E. Bakker, Freddy T. Rabouw, Bart de Nijs, Relinde J.A. van Dijk-Moes, Marijn A. van Huis, Patrick J. Baesjou, Alfons van Blaaderen, *Shape-Dependent Multiexciton Emission and Whispering Gallery Modes in Supraparticles of CdSe/Multishell Quantum Dots*, ACS nano 9 (4), 3942-3950, 2015. (Chapter 7).

Other work

- Julius W. J. de Folter, Ping Liu, Lingxiang Jiang, Anke Kuijk, Henriëtte E. Bakker, Arnout Imhof, Alfons van Blaaderen, Jianbin Huang, Willem K. Kegel, Albert P. Philipse and Andrei V. Petukhov, *Self-Organization of Anisotropic and Binary Colloids in Thermo-Switchable 1D Microconfinement*, Particle & Particle Systems Characterization 32, 313-320, 2015.
- Yinghua Qiu, Preston Hinkle, Crystal Yang, Henriëtte E. Bakker, Matthew Schiel, Hong Wang, Dmitriy Melnikov, Maria Gracheva, Maria Eugenia Toimil-Molares, Arnout Imhof, Zuzanna S. Siwy, *Pores with Longitudinal Irregularities Distinguish Objects by Shape*, ACS nano 9 (4), 4390-4397, 2015.
- Henriëtte E. Bakker, Stefan B. Lindström and Joris Sprakel, *Geometry- and rate-dependent adhesive failure of micropatterned surfaces*, Journal of Physics: Condensed Matter, 24, 065103, 2012.
- Evan Spruijt, Henriëtte E. Bakker, Tom E. Kodger, Joris Sprakel, Martien A. Cohen Stuart and Jasper van der Gucht, *Reversible assembly of oppositely charged hairy colloids in water*, Soft Matter, 7, 8281-8290, 2011.

About the author

Henriëtte Bakker was born in Warnsveld, the Netherlands, on the fifteenth of January 1987. She attended secondary school (Gymnasium level) at 'Het Rhedens' in Dieren and Rozendaal from which she graduated in 2005. In 2006 she started her studies at Wageningen University and in 2010 she obtained her bachelor degree in Molecular Life Science (*with distinction*). She obtained her master's degree in Physical Chemistry at the same university in 2012. She carried out her thesis project in the Physical Chemistry and Colloid Science group of Martien Cohen Stuart in Wageningen under the daily supervision of Evan Spruijt. The project was entitled 'Controlled Aggregation of oppositely charged colloids'. In 2010 she went for five months to Cambridge (MA, USA) for her internship at Harvard University in the group of David Weitz under the supervision of Joris Sprakel. During her intership she worked on the project entitled 'Geometry- and rate-dependent adhesive failure of micropatterned surfaces'. On the 1^{st} of April in 2012 Henriëtte started her PhD research in the Soft Condensed Matter group at Utrecht University under the supervision of Alfons van Blaaderen and Arnout Imhof. The main results of this research are described in this thesis. Next to her studies and research, Henriëtte has been playing Ultimate frisbee and had to honor to be a member of the Dutch Women's team at the 2015 European Championships in Copenhagen.